DOCINADE

Doctorado en Ciencias Naturales para el Desarrollo

Énfasis en Tecnologías Electrónicas Aplicadas

Tesis de Doctorado

Experimental Validation of Plasma-Surface Interaction Models in High-Power Helicon Plasma Sources

Juan Ignacio Del Valle Gamboa

Dr. Franklin R. Chang Díaz
Director de Tesis

Dr. Iván Vargas Blanco
Asesor de Tesis

Dr. Víctor H. Granados Fernández
Asesor de Tesis

Liberia, Costa Rica, 30 de septiembre del 2022

MIEMBROS DEL TRIBUNAL EXAMINADOR

TEODOLITO GUILLEN GIRON (FIRMA)

Firmado digitalmente por TEODOLITO GUILLEN GIRON (FIRMA)
Fecha: 2022.10.21 09:31:33 -06'00'

Dr. Teodolito Guillén Girón
Director del Sistema de Posgrados del ITCR

Firmado por GIOVANNI SAENZ ARCE (FIRMA)
PERSONA FISICA, CPF-01-1153-0569.
Fecha declarada: 21/10/2022 02:46 PM

Dr. Giovanni Sáenz Arce
Coordinador del DOCINADE

FRANKLIN RAMON CHANG DIAZ (FIRMA)

Digitally signed by FRANKLIN RAMON CHANG DIAZ (FIRMA)
Date: 2022.10.27 11:12:28 -05'00'

Dr. Franklin R. Chang Díaz
Director de Tesis

VICTOR IVAN VARGAS BLANCO (FIRMA)

Firmado digitalmente por VICTOR IVAN VARGAS BLANCO (FIRMA)
Fecha: 2022.10.23 14:54:27 -06'00'

Dr. Iván Vargas Blanco
Miembro del Comité Asesor de Tesis

Digitally signed by VICTOR HUGO GRANADOS FERNANDEZ (FIRMA)
Date: 2022.10.24 11:03:18 -06'00'

Dr. Víctor H. Granados Fernández
Miembro del Comité Asesor de Tesis

Declaration of Authenticity

I, Juan Ignacio Del Valle Gamboa, student within the Doctorado en Ciencias Naturales para el Desarrollo program, hereby declare that this Doctoral Thesis I am submitting, titled "*Experimental Validation of Plasma-Surface Interaction Models in High-Power Helicon Plasma Sources*", is original work and that all sources consulted during its execution have been properly cited in this manuscript. This material has not been submitted, in partial or integral form, as a thesis to this or any other institution.

Declaración de Autenticidad

Yo, Juan Ignacio Del Valle Gamboa, estudiante del Doctorado en Ciencias Naturales para el Desarrollo, declaro que la Tesis Doctoral que presento para su exposición y defensa titulada "*Experimental Validation of Plasma-Surface Interaction Models in High-Power Helicon Plasma Sources*", cuyo Comité Asesor de Tesis está conformado por el Dr. Franklin R. Chang Díaz (Director de Tesis), Dr. Iván Vargas Blanco (Asesor de Tesis) y Dr. Víctor Hugo Granados Fernández (Asesor de Tesis), es original y que todas las fuentes utilizadas para su realización han sido debidamente citadas en el mismo. Este material no lo he presentado, en forma parcial o total, como una tesis en esta u otra institución.

Juan Ignacio Del Valle Gamboa
Liberia, Costa Rica, 20 de julio del 2022

Acknowledgements

The completion of this doctoral research project has been a long endeavor, which would have been impossible without the help of many people who supported me and made this task manageable.

Foremost, I wish to thank Dr. Franklin Chang Díaz for his support as my Thesis Director and mentor. It has been a privilege to work with him both within the academic as well as the professional fields. It is my sincere hope that my work may contribute in bringing his vision of a better world –and Solar System– into realization.

I would also like to acknowledge the invaluable support of my Thesis Committee. Dr. Iván Vargas has served both as an advisor and a teacher, and I am honored to have his endorsement of my work. Dr. Víctor Granados supported this project with a commitment beyond the ordinary; his help and motivation were essential for the completion of the final stages of this doctoral thesis for which I am extremely thankful.

I also extend my gratitude to all faculty members of the DOCINADE program who have contributed in one way or another to my journey. The existence of this particular academic program enabled me to achieve this goal while serving as a researcher embedded within the industrial sector, an aspect which I believe can serve to promote science-based development in our region.

I would also like to express my appreciation to my colleagues at Ad Astra Rocket Company, present and past. They have played the role of my research group, as well as that of an inspiration and support network. I would like to thank Drs. Jared Squire, Mark Carter, Tim Glover, Benjamin Longmier, Christopher Olsen and Matthew Giambusso, who at different stages provided me with explanations, support or encouragement directly related to this thesis work, and have shown me into the world of experimental plasma physics. I would also like to acknowledge Ing. Rónald Chang Díaz, who welcomed me into the Ad Astra team and has always believed in the potential of local talent to accept difficult challenges and achieve great results through honest, hard work. Many other colleagues at the company have supported me throughout these years with their friendship and support, and I extend my sincere gratitude to all of them.

I would finally like to acknowledge the incredible support I have received from my family, which has enabled me to work on this project and complete this thesis. I owe to my parents, Alfredo and Flory, the foundations of who I am and who I want to become in life. My brother Julio has always encouraged me throughout this long process. Lastly, my wife, Mary Anne, and my children, Emma and Antonio, have endured hard sacrifices in order to allow me the opportunity to work on this project. I am deeply indebted to the unlimited love and patience they have gifted me, and will now dedicate myself and my time to being there for them, for their goals and for their aspirations.

To my family

Contents

List of Tables

List of Figures

Abstract

This thesis analyzes the erosion phenomena present in helicon plasma sources. These are electrodeless radiofrequency plasma generators which are able to produce high-density plasmas with low and moderate input power levels. They have increasingly found research and industrial applications ranging from fundamental physics research, material processing, electric space propulsion and fusion-related research. The fact that they excite the plasma through an external antenna and possess an axial magnetic field containing the plasma is believed to prevent erosion interactions with the plasma-facing surfaces, yet this claim has not been critically assessed.

An analytical steady-state model is presented capable of estimating the 2D distribution of the plasma in cylindrical helicon plasma sources, as well as the acceleration of ions through the sheath and the corresponding sputtering phenomena in the boundary confinement surfaces. The model is validated through comparison with published experimental data from a variety of relevant helicon plasma sources, and is then used to estimate the erosion rates in the boundary surfaces of the VX-CR research helicon experiment. Results are analyzed and the strengths and limitations of the model are discussed. The highest erosion rate estimates were obtained for the upstream closed end of the cylindrical helicon device, followed by the erosion produced through RF capacitive coupling under the location of the external antenna straps, and then the erosion produced by the acceleration of ions through the DC sheath elsewhere in the inner surface of the cylindrical containment tube.

From these results, three main erosion modes in helicon plasma sources are identified and discussed. They are the acceleration of ions through the DC sheath, the effects of the RF capacitive coupling under the helicon antenna straps, and the contact or intersection of the magnetic field lines with the boundary surfaces. Potential mitigation strategies are introduced and discussed. These include the control of the distribution of key plasma parameters such as temperature and density, the proper configuration of the geometry and intensity of the magnetic field, and potentially the use of physical mitigation means such as Faraday shields. Perspectives are presented regarding remaining gaps in the understanding of these phenomena, and opportunities for future research.

Keywords: helicon plasma, surface, erosion, sputtering, model, simulation.

Resumen

Esta tesis analiza los fenómenos de erosión presentes en las fuentes helicoidales de plasma. Estas consisten en generadores de plasma mediante radiofrecuencia y carentes de electrodos, que son capaces de producir plasmas de alta densidad a partir de niveles de potencia de entrada bajos y medianos. En forma creciente, han encontrado aplicaciones industriales y académicas que abarcan desde la investigación en física básica, el procesamiento de materiales, la propulsión espacial eléctrica, e investigaciones relacionadas con la fusión nuclear. Se cree que el hecho de que excitan el plasma a través de una antena externa y que poseen un campo magnético axial conteniendo al plasma les permite reducir las interacciones de erosión con las superficies internas, sin embargo esta afirmación no ha sido evaluada críticamente.

Se presenta un modelo analítico de estado estable, capaz de estimar la distribución 2D del plasma en fuentes helicoidales de plasma cilíndricas, así como la aceleración de los iones a través de las regiones de apantallamiento eléctrico y los correspondientes fenómenos de pulverización catódica en las superficies de confinamiento. El modelo se validó a través de comparación con datos experimentales publicados provenientes de una variedad de fuentes helicoidales de plasma relevantes, y se utilizó posteriormente para estimar las tasas de erosión en las superficies de confinamiento de la fuente helicoidal experimental VX-CR. Los resultados fueron analizados, y las fortalezas y debilidades del modelo fueron discutidas. Las tasas de erosión estimadas más altas se obtuvieron para el extremo cerrado ubicado 'aguas arriba' en la fuente helicoidal cilíndrica, seguido de la erosión producida a través del acoplamiento capacitivo por radiofrecuencia (RF) bajo la ubicación de las terminales de la antena externa, y luego por la erosión producida gracias a la aceleración de los iones a través de la zona de apantallamiento de corriente directa (CD) en las restantes superficies internas del tubo de contención cilíndrico.

A partir de estos resultados, tres modos principales de erosión en las fuentes helicoidales de plasma se identificaron y se discutieron. Estos son: la aceleración de los iones a través del apantallmiento CD, los efectos del acoplamiento capacitivo por RF bajo las terminales de la antena helicoidal, y el contacto o intersección de las líneas del campo magnético con las superficies de frontera. Se introdujeron y discutieron potenciales mecanismos de mitigación. Estos incluyen el control de la distribución a parámetros claves del plasma como la temperatura y la densidad, la adecuada configuración de la geometría e intensidad del campo magnético, y potencialmente el uso de mecanismos físicos de mitigación como pantallas de Faraday. Se presentan perspectivas sobre las brechas remanentes en el entendimiento de estos fenómenos, así como oportunidades para futuras investigaciones.

Palabras clave: plasma helicoidal, superficie, erosión, pulverización catódica, modelo, simulación.

Chapter 1

Introduction

1.1. Context and Overview

Plasma is the scientific term used to describe the state of matter where a sufficient number of charged ionized particles coexist, large enough that the plasma exhibits collective behavior due to their presence. It is considered one of the fundamental states of matter, and the majority of the known universe exists as a plasma. The Sun, the stars and many other astronomical entities consist of plasmas of different configurations. On Earth, lightning and the auroras at the polar regions are some of the natural phenomena associated with plasmas and their particular behavior.

The ability to create artificial plasmas for research purposes and for practical applications has given birth to the fields of *plasma physics* and *plasma engineering*. Today, plasma technology is essential for a large variety of commercial and industrial applications. These include the manufacturing of most integrated circuits (ICs) for electronic devices such as smartphones, tablets and computers; material processing applications, including the treatment and cutting of metals and surface treatments for components of advanced medical devices; lightning applications, such as fluorescent and neon lamps; and automotive applications such as the ignition systems for internal combustion engines. Even newer applications of plasmas for practical purposes include their use to modify or affect organic living tissue, for applications in agriculture as well as the novel field of human *plasma medicine*. Within the energy industry, the development of sustainable *nuclear fusion* has been a long goal of the plasma physics community, with the promise of providing abundant, carbon-free energy in a high-density configuration without the existing drawbacks of nuclear fission reactors. Another promising application of this technology is the field of *electric space propulsion*, where plasmas are used for the production of thrust in spacecraft with efficiencies much higher than traditional chemical rocket engines.

In order to produce these artificial plasmas for terrestrial applications, a *plasma source* is required. They consist of a mechanism to couple energy into a neutral gas, in order to ionize it to a sufficient degree that it becomes a plasma. Most plasma sources couple electrical energy into the plasma discharge. This can be achieved through electrodes or cathodes that produce an electric arc, or through electromagnetic waves which resonate with the charged particles in the plasma.

This thesis focuses on a particular class of plasma sources, the *helicon plasma sources*. They exploit the specific properties of helicon plasma waves, one of the many categories of electromagnetic waves that can exist in plasmas when subjected to the presence of a magnetic field. Research on helicon waves began in the 1950s and 1960s, but the interest in helicon plasma sources surged in the 1980s and 1990s, when their ability to produce highly dense plasmas with low power inputs became clear. Since then, helicon sources have been employed in fundamental research, as well as in material processing applications, electric space propulsion designs and material science experiments within the fusion research community.

Typical helicon sources employ external radio frequency sources coupled to a particular type of antenna, which externally surrounds a cylindrical tube made of a non-conducting dielectric material. An external magnetic field is supplied, with the field lines aligned with the axis of the cylinder. The neutral gas (or mixture of gases) selected for creating the plasma flows inside the cylindrical element. When the radio frequency energy is conducted from the external source to the antenna, given the proper combination of physical and geometrical parameters (geometry of the device, electrical parameters of the wave, input power and mass flow rate of the neutral gas), a helicon plasma discharge will be initiated.

Since the antenna surrounds the cylindrical discharge tube in helicon plasma sources, it is not in direct contact with the plasma. This prevents the unwanted effects that energetic plasmas have upon electrodes, cathodes, grids and other elements used to create and sustain the discharge in other devices where direct contact does occur. This is an essential property that sets helicon plasma sources, and technologies based on them, apart from glow discharges, hollow cathodes, ion thrusters with biased grids, Hall-Effect thrusters and many other devices where elements degrade due to bombardment with the energetic plasma. The combination of the use of the external antenna and the presence of the axial magnetic field, has been cited as a reason enabling helicon plasma sources to have negligible erosion rates on its internal surfaces and long operational lifetimes. This statement is typical of the helicon plasma literature, yet it is a claim which has not been subjected to rigorous scrutiny. On the contrary, evidence does exist of relevant plasma-surface interactions in helicon sources, despite the advantages cited above. This issue has become more relevant in recent years, when helicon plasma sources have been chosen as components of high-power devices used for space propulsion applications and fusion science research.

This thesis aims to contribute to the understanding of the interactions between plasmas and their confinement surfaces within helicon plasma sources, particularly those operating at higher power levels, through the development of practical simulation tools which can be used to estimate these effects and help in the design, development or analysis of new and existing helicon plasma sources.

1.2. Research Objectives and Research Questions

This section will describe the fundamental objectives and questions guiding the research project described in this thesis and its methodological approach.

1.2.1. Research Objectives

Main Research Objective

To design an empirical and practical model which describes the distribution and intensity of erosion phenomena in the plasma-facing surfaces of boundary materials within high-power helicon plasma sources.

Specific Research Objectives

1. To review the existing body of knowledge regarding helicon plasma sources and plasma-material interactions, in order to identify elements suitable for the design of a model of plasma-surface interactions within helicon plasma sources.
2. To implement a practical simulation tool able to model plasma-surface interactions within helicon plasma sources and validate it against published experimental data.
3. To identify, based on the results provided by the simulation tool package, the main mechanisms for erosion of the material boundary surfaces in high-power helicon plasma sources.
4. To identify and postulate potential strategies to mitigate the effects of these erosion mechanisms.

1.2.2. Research Questions

Central Research Question

How are the distribution and intensity of erosion phenomena within the boundary surfaces of high-power helicon plasma sources determined?

Additional Research Questions

- Which are the critical factors and variables of erosion phenomena within helicon plasma sources?
- Which background theoretical work supports the understanding of erosion phenomena within helicon plasma sources?
- What are the relationships that exist between these factors and variables?
- Can these relationships be implemented as an empirical practical model, suitable of experimental validation?

1.3. Theoretical Background

This project stems out of the work carried out in Ad Astra Rocket Company Costa Rica (Liberia, Costa Rica), where a high-power research helicon plasma source, the VX-CR experiment ([26, 45]), has been implemented in order to study thermal management and lifetime issues in helicon sources. This research supports the development of the VASIMR® engine ([28, 29]), a high-power electric propulsion engine for in-space transportation applications developed by the Ad Astra Rocket Company of Webster, TX, USA. The design of the VASIMR® engine contains three interlinked magnetic cells. The first one of these is called the *Ionizer* stage and consists of a high-power helicon plasma source responsible for efficiently creating a high-density plasma from the neutral propellant gas and conducting it to the subsequent stages. The VX-CR experiment was designed as a practical test platform for trying out design solutions for thermal management, material erosion and lifetime issues pertinent to the Ionizer stage. Figure 1.1 shows an schematic diagram of the VASIMR® engine's design, and a photograph of the VX-CR experiment.

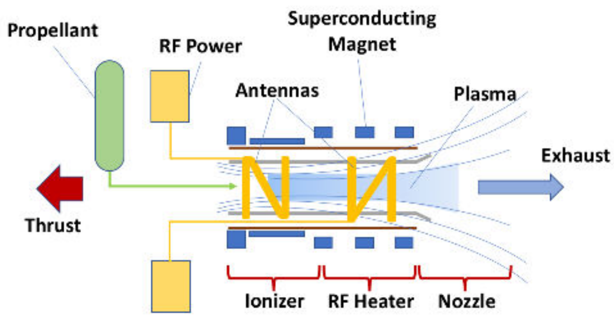

(a)

(b)

Figure 1.1: **(a)** Simplified diagram of the VASIMR® engine and its components. Courtesy of Ad Astra Rocket Company. **(b)** The VX-CR experiment in Ad Astra Rocket Company Costa Rica.

These issues concerning the VASIMR® engine's Ionizer stage are relevant for all helicon plasma sources ([35]). Their study dates to the 1960s, but in the 1980s and 1990s interest in their potential rose due to their ability to produce high-density plasmas with low input powers ([16, 37]).

One of the often-cited advantages of helicon plasma sources ([35, 92]) is the fact that since they rely on an external antenna to couple radio frequency waves into the plasma discharge and since they require an axial magnetic field that contains the plasma and prevents its radial diffusion towards the boundary wall, the erosion of their boundary materials is negligible and the antenna is not even in contact with the plasma. This is thought to provide them with long operational lifetimes. However, evidence suggests ([1, 6, 7]) that there are still plasma-surface interaction phenomena present in helicon sources, and that they increase as new devices are operated at higher power levels. One of these studies was published by Berisford et al. ([10, 11]), which includes experiments executed in the VX-CR device and is a predecessor of this thesis.

The research project presented in this thesis aims to comprehensively review the issue of plasma-surface interaction phenomena within helicon plasma sources, and develop validated simulation tools which can assist the design of helicon plasma source implementations in order to minimize unwanted erosion phenomena.

1.4. Methodology

In order to achieve the objectives of this research project, a comprehensive literature review has been carried out in the physics of helicon plasma sources, the modeling of cylindrical magnetized plasmas, DC plasma sheaths and RF sheaths, and the sputtering of solid materials by impacting ions at the low temperatures typical of helicon discharges.

Relevant analytical or empirical models have been developed combining a description of the helicon wave dispersion relation ([36]), a 2D fluid-based description of the dynamics of magnetized plasmas in cylindrical geometries ([3]), and the physics of plasma sheaths ([71]) and of sputtering reactions ([48, 71]). New correlations were obtained for the analysis of sputtering of dielectric ceramic compounds by argon gas, by adapting existing models for monoatomic targets and validating them against collected experimental data. A simulation of the power balance in a helicon plasma source based on the simplification of previous work was also developed ([3]).

These models were implemented as numerical simulations using the Python programming language and its NumPy and SciPy toolkit packages. These tools were then validated against published experimental data obtained from helicon plasma sources fitting the requirements and assumptions of these models. Simulation runs were then employed to explore the physics of plasma-surface interactions in helicon plasma sources, using the VX-CR experiment as a prototype model for investigation. The results were discussed and the main erosion mechanisms present in helicon plasma sources were identified. Potential mitigation strategies were presented and discussed, and suggestions for future related research projects were proposed.

1.5. Contributions to the Research Field

The integration of analytical and empirical models for the description of erosion phenomena in steady-state magnetized helicon plasma sources in a cylindrical configuration, and their implementation as computationally-inexpensive numerical simulations implemented in a widely-available open-source programming language, is the first major contribution of this thesis. The second relevant contribution is the comprehensive study of plasma-surface interaction phenomena in high-power helicon plasma sources and the analysis of the main erosion mechanisms. Both contributions add to the existing body of knowledge in the fields of helicon physics and plasma-material interactions, and could also be applied to other scenarios with similar configurations and characteristics.

Chapter 2

Research Summary and Thesis Structure

This chapter describes the structure of this thesis and provides a summary of the contents of each of its chapters.

Chapter 3 provides a literature review on the fields of helicon wave physics, the modeling of cylindrical magnetized plasmas, plasma sheaths, and plasma-surface interactions with an emphasis on sputtering of materials by energetic ions. Findings from recent experiments related to this topic are also reported and discussed. Chapter 3 was originally published as a peer-reviewed open-access article,

> Del Vale JI, Chang Díaz FR, Granados VH. (2022), *Plasma Surface Interactions Within Helicon Plasma Sources*. Front. Phys. 10:856221. doi: 10.3389/fphy.2022.856221
>
> https://www.frontiersin.org/articles/10.3389/fphy.2022.856221/

Chapter 4 presents the implementation of a simplified analytical model describing the 2D distribution of the plasma density in cylindrical magnetized plasmas, the physics of the DC and RF sheaths formed at the boundary surfaces, and an empirical submodel of the sputtering of these surfaces by energetic incident ions. This model was validated against published experimental data from relevant helicon plasma sources, and was then used to estimate and discuss erosion phenomena in the VX-CR research helicon plasma source. These results were used to identify and discuss the main mechanisms of erosion present in helicon plasma sources. Chapter 4 was originally published as a peer-reviewed open-access article,

> Del Valle JI, Granados VH and Chang Díaz FR (2022), *Estimation of erosion phenomena within helicon plasma sources through a steady-state explicit analytical model*. Front. Phys. 10:950472. doi: 10.3389/fphy.2022.950472
>
> https://www.frontiersin.org/articles/10.3389/fphy.2022.950472/

Chapter 5 presents a discussion of the topic of erosion phenomena within helicon plasma sources, based on the findings and results of chapters 3 and 4. The main erosion mechanisms of erosion in helicon plasma sources are identified and analyzed. A power balance model is introduced with the goal of relating the internal parameters of the plasma discharge with external physical inputs to the source; its results and limitations are discussed. A list of potential mitigation strategies are presented which may reduce the severity of these plasma-material interaction in helicon sources.

Chapter 6 summarizes the global conclusions of this thesis, and also presents an outlook of recommended future research avenues which may extend or complement its results.

Appendix A presents a summary of the derivation of the Cold Plasma Wave approximation, and also the derivation of the dispersion relations for both Helicon plasma waves as well as the Trivelpiece-Gould waves. Appendix B presents the complete derivation of the 2D fluid models for cylindrical magnetized plasmas which were introduced in chapter 3 and whose implementation is discussed in 4. Appendix C presents the complete derivation of the power balance model introduced in chapter 5, as well as the description of the model used to estimate the energy cost per ion-electron pair created in helicon discharges using argon gas. Appendix D presents the source code for the Python scripts implementing the models described in chapter 5. Appendix E contains the original publications corresponding to chapters 3 and 4, in their original layout from the corresponding journals.

Chapter 3

Plasma-Surface Interactions Within Helicon Plasma Sources

This chapter was originally published as a peer-reviewed open-access article,

> Del Vale JI, Chang Díaz FR, Granados VH. (2022), *Plasma Surface Interactions Within Helicon Plasma Sources*, Front. Phys. 10:856221, doi: 10.3389/fphy.2022.856221
> https://www.frontiersin.org/articles/10.3389/fphy.2022.856221/

Abstract: Helicon Plasma Sources do not require electrodes or grids directly immersed in the plasma, and also present an axial magnetic field confining the plasma discharge. These factors are believed to provide them with long operational lifetimes because of the reduced potential for surface etching. The physics of helicon waves, cylindrical magnetized plasmas, sheaths and plasma-surface interactions are discussed in the context of this claim. Practical implementation aspects are also reviewed, along with relevant experimental results. It is shown that understanding the distribution of ion density within the source, the presence of induced potentials in its surfaces and the physics of low-energy sputtering reactions is essential to properly model erosion phenomena within helicons, and consequently predict their performance in practical applications.

Keywords: helicon plasma, surface, erosion, sputtering, interactions.

3.1. Introduction

Helicon plasma sources (HPS) have attracted attention in recent decades because of their ability to produce high-density plasmas at low or moderate power levels and magnetic field intensities. For example, electron densities of more than 10^{12} cm^{-3} can be produced on helicon plasma sources operating at input power levels of around 1 kW$_e$ [92]. These properties make them suitable for practical applications in several fields. Within the research of plasma-material interactions at fusion-relevant conditions, HPSs have been used as part of test facilities where candidate wall materials are subjected to the typical operating conditions in projected fusion devices [87, 106], up to heat flux levels exceeding 20 MW/m^2 [23]. Helicons have also been used in the plasma-processing of commercial materials and products [82, 114]. Within the field of electric space propulsion, helicon plasma thrusters have been actively developed in recent years [31, 34, 89, 93, 100]; helicons are also essential components of more advanced electric propulsion systems such as the VASIMR engine [28]. Figure 3.1 shows some examples of devices based on helicon plasma sources.

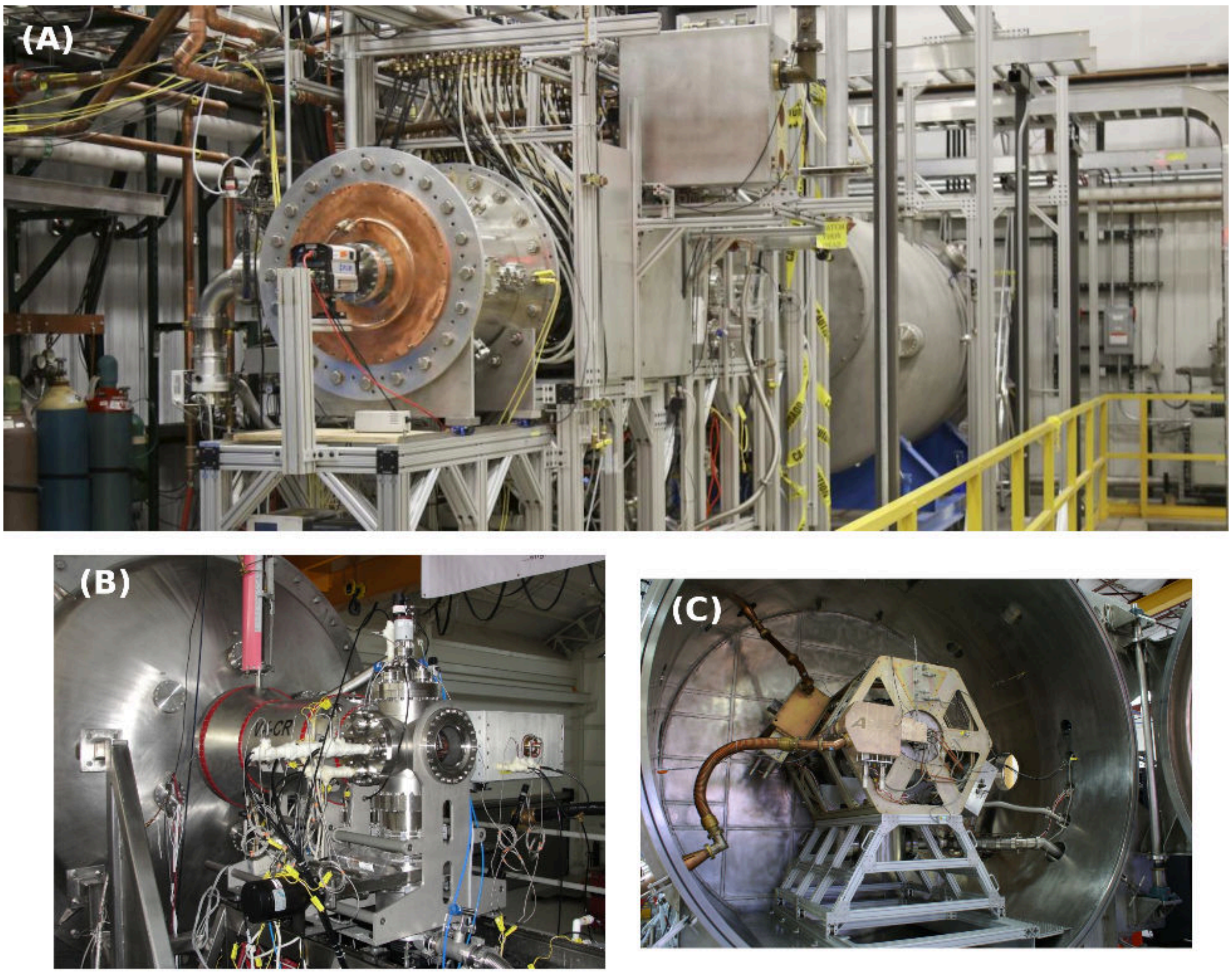

Figure 3.1: Examples of applications of Helicon Plasma Sources. (**A**) The Proto-MPEX linear device for the study of plasma-material interactions at fusion-relevant conditions [87]. Courtesy of Oak Ridge National Laboratory, U.S. Dept. of Energy. (**B**) The VX-CR research helicon plasma source [45]. Courtesy of Ad Astra Rocket Company Costa Rica, Liberia, Costa Rica. (**C**) The VASIMR VX-200SS high-power propulsion engine [28]. Courtesy of Ad Astra Rocket Company, Webster, TX, USA.

Another key feature of HPSs is that they typically do not have electrodes or cathodes in direct contact with the plasma, but rely instead on external radio frequency (RF) systems to launch and couple the corresponding waves within the medium and excite the discharge. This differs from other common plasma sources such as glow or DC discharges, where the plasma risks contamination from the release of electrode material or the source may fail altogether if this element erodes sufficiently. Avoiding direct contact between the plasma and such elements is particularly useful where a long operating lifetime is desired for the plasma source, either because long duty cycles will be required in the application (as in commercial plasma-processing devices), high power densities are required (as in linear devices used for the research of suitable materials for fusion-relevant conditions) or because these previous conditions combine with the impossibility to access the device in the case of component failure (as in electric space thrusters).

Despite this advantage particular to the discharge excitation mechanism, practical implementations of HPSs do contain other confinement surfaces which are in direct contact with the plasma. The performance of helicon sources depends on the specific properties of these surfaces as well, and their ability to withstand the conditions they are subjected to throughout the operating lifetime of the source. These issues are therefore also important when considering the long-term viability of helicon plasma sources in their intended applications, and are the subject of the present review.

This article is structured as follows. Section 3.2 discusses the physics behind helicon plasma waves and recent results on the modeling of cylindrical magnetized plasmas. Section 3.3 then reviews the theory of plasma-surface interactions as it applies to helicon plasma sources. Section 3.4 describes practical aspects of helicon plasma source design and implementation, as they relate to the plasma-surface interaction phenomena. Finally, section 3.5 summarizes this review's findings and offers perspectives for the advancement of the research and design of reliable, robust helicon plasma sources with long operational lifespans.

3.2. Physics of Helicon Plasma Sources

3.2.1. Helicon Plasma Waves

Helicon waves are a category of right-hand polarized (RHP) plasma waves which propagate along DC magnetic fields in bounded systems. They are related to so-called *whistler* waves, which have been studied in atmospheric physics since the early twentieth century. Whistlers and helicon waves belong to the group of right-hand polarized (RHP) waves propagating parallel to a magnetic field, in the frequency range $\omega_{ci} \ll \omega \ll \omega_{ce}$ (where ω_{ci} is the ion cyclotron frequency and ω_{ce} is the electron cyclotron frequency), together with electron cyclotron waves. Figure 3.2 shows the location of whistlers and helicon plasma waves within a w-k diagram representing RHP cold plasma waves.

A historical perspective for the first twenty years of helicon research has been given by Chen and Boswell [16, 37]. The following twenty-year period has been covered in more recent reviews by Chen [35] and Shinohara [92]. Theoretical treatments of the physics behind helicon waves have been produced, among others, by Klozenberg et al. [63], Chen [32], and Chen and Arnush [5, 36].

A basic dispersion relation can be obtained for helicon plasma waves from simplifying the Appleton-Hartree expression for quasi-longitudinal right-handed cold plasma waves [54, 98], propagating at an angle θ from an axial,

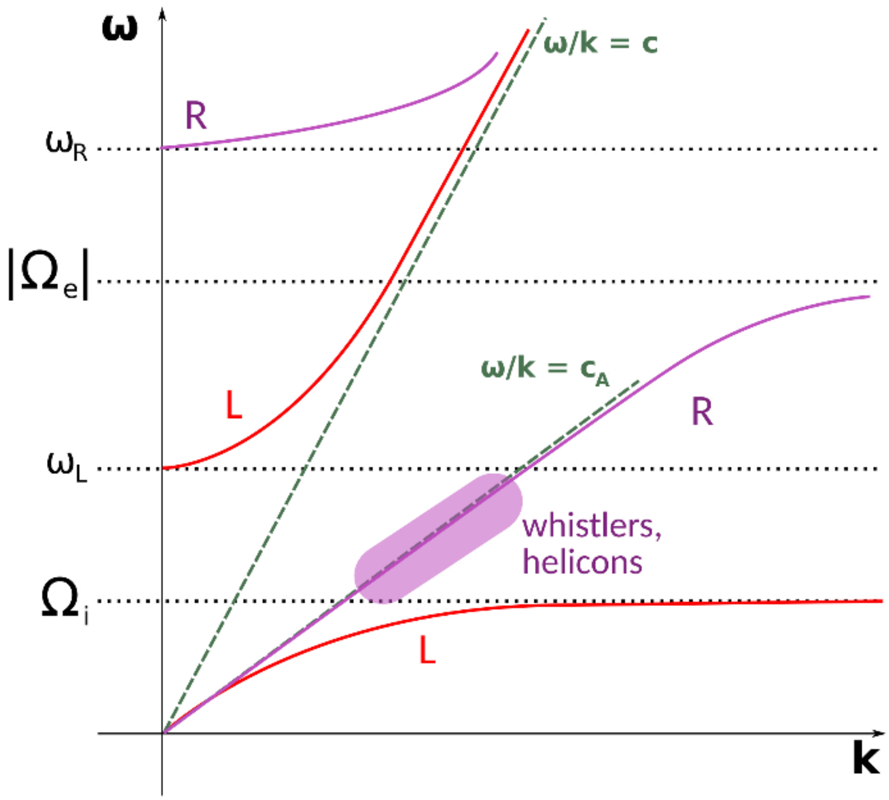

Figure 3.2: Location of whistlers and helicon plasma waves, among cold plasma waves propagating parallel to the externally-applied magnetic field.

static magnetic field $\mathbf{B} = B_0\hat{\mathbf{e}}_{\mathbf{z}}$,

$$\beta = \frac{\omega}{k}\frac{n_0 e\mu_0}{B_0} \tag{3.1}$$

where $\beta^2 = k^2 + k_\perp^2$ is the total wave number, $k = \beta\cos\theta$ and $k_\perp$ are the parallel and perpendicular components of the wave number, and n_0 is the plasma density. This expression, despite being a simplification, provides an intuitive insight on the relationship between the magnetic field B_0, the density n_0, the wave frequency ω and the wave number β, and can be used as a starting point when designing or analyzing a HPS.

A more detailed description of helicon waves can be obtained from Maxwell's equations by neglecting ion motions and the displacement current, as originally shown by Klozenberg et al. [63]. When the effects of electron inertia are retained within the analysis [36, 37, 83] two solutions are obtained for the dispersion relation,

$$\beta_{1,2} = \frac{k}{2\delta}\left[1 \mp \left(1 - \frac{4\delta k_w^2}{k^2}\right)^{1/2}\right] \tag{3.2}$$

where $\delta = \omega/\omega_{ce}$ is the ratio between the wave frequency and the electron cyclotron frequency $\omega_{ce} = eB_0/m_e$, and $k_w^2 = ww_p^2/w_c c^2 = wn_0 e\mu_0/B_0 \equiv \alpha k$ is the wavenumber for low-frequency whistler waves along B_0 in free space, with $\alpha = \beta$ the wave number previously described in equation 3.1. w_p is the electron plasma frequency at density n_0. δ is neglected when the effects of the electron mass are omitted or for frequencies $\omega \ll \omega_{ce}$.

Equation 3.2 describes two solutions for the wave dispersion relation, which can be simplified as shown in equation 3.3.

$$\beta_{1,2} \approx \frac{k}{2\delta}\left[1 \mp \left(1 - \frac{2\delta k_w^2}{k^2}\right)\right] \approx \begin{cases} k_w^2/k \\ k/\delta \end{cases} \tag{3.3}$$

Solution β_1 corresponds to the zero electron mass limit, and describes the helicon wave ("H") from equation 3.1. The second solution $\beta_2 = \beta_2\cos\theta\omega_{ce}/\omega$ describes a wave with frequency $\omega = \omega_{ce}\cos\theta$, which is an electron cyclotron wave propagating at an angle to the magnetic field. This is the Trivelpiece-Gould mode ("TG"), first described in bounded systems by Trivelpiece and Gould [109]. The TG mode co-exists with the H mode, and becomes relevant at lower values of B_0. The TG mode is thought to play a relevant role in the damping mechanism of helicon plasma sources and to contribute to its high ionization efficiency via mode-conversion processes [90].

Equation 3.3 describes the dispersion relation for both the H-mode and the TG mode. Expressions for the magnetic and electric fields ($\mathbf{B}$, $\mathbf{E}$) have been derived for different geometries as described in the early works on helicons [63, 70] as well as in more recent literature [32, 37, 83]. These expressions depend as well on the boundary conditions chosen for the analysis and on whether these boundaries are modelled as conductors or not [36]. Practical implementations of HPSs are typically linear devices implemented as cylindrical enclosures made of dielectric materials, as will be described in section 3.4.

The expressions obtained from equations 3.1 and 3.3, as well as the detailed derivations of the $\mathbf{B}$ and $\mathbf{E}$ fields that can be obtained for a particular configuration and geometry, can be used as an initial approximation to understand the regimes of H and TG modes that can be propagated in a given configuration, and establish a baseline estimation of the expected density distribution in a given HPS device.

One particular advantage of HPSs stemming from the fundamental physics of helicon waves is the ability of these devices to couple RF waves at the core of dense plasmas, enabled by the presence of the axial magnetic field and the propagation of the H-mode. This fact presents an advantage over other types of plasma sources, such as inductively-coupled plasmas (ICPs) where the penetration of RF waves into the plasma is limited by its skin-depth, or electron-cyclotron sources (ECR), where microwaves cannot propagate below the O-mode cutoff frequency (the electron plasma frequency ω_{pe}).

An investigation on the mechanisms which enable the initiation of the high-density helicon mode (the H-mode), based on modeling and experimental work, has been carried out by Carter et al. [25], including indirect evidence of the deposition of RF power at the high-density core in a helicon plasma source.

3.2.2. Cylindrical Magnetized Plasmas

Section 3.2.1 described helicon plasma waves and derived their dispersion relation in various scenarios. The general behavior of magnetized plasmas in cylindrical geometries will now be analyzed, which is relevant to the characterization of practical HPSs as described in section 3.4.

The problem of describing the bulk behavior of a plasma discharge has been addressed since the early stages of the development of plasma physics. In the classical paper by Tonks and Langmuir [108], expressions were derived for the distribution of the electric potential in an arc discharge, for various geometries including cylindrical coordinates. Scenarios were analyzed for different regimes of ion collisionality and ionization rates. This work also contains a treatment of the plasma-material boundary at the edge of the plasma discharge, pointing to the discontinuity of the bulk model within the plasma sheath.

In a later paper, Tonks [107] studied the effects of the magnetic field in an arc plasma. One of the cases described was the positive column plasma immersed within a longitudinal magnetic field, the same typical configuration applied nowadays to most helicon plasma sources. A radial model is developed based on classical diffusion theory. More recent models for cylindrical magnetized plasmas have been developed by Fruchtman et al. [50] and Sternberg et al. [97]. These works introduced the use of 2D fluid models in cylindrical coordinates (with the assumption of azimuthal symmetry), the separation of variables in order to decouple the expressions for the radial and axial coordinates, and the analysis of different degrees of magnetization. Differences between these authors rely on the assumptions chosen to simplify their models. The previous works were further adapted and extended by Ahedo et al. [2, 3], who developed a 2D model for cylindrical magnetized plasmas as part of their work on describing the plasma dynamics within helicon plasma thrusters. The properties of these models have been summarized in table 3.1.

These descriptions of cylindrical magnetized plasmas can be used to approximate the distribution of key pa-

Table 3.1: Relevant models developed for cylindrical magnetized plasmas which are applicable to the study of Helicon Plasma Sources.

Reference	**Tonks** [107]	**Ewald et al.** [49]	**Fruchtman et al.** [50]	**Sternberg et al.** [97]	**Ahedo et al.** [3]
Dimensionality	1D	1D	2D	1D	2D
Symmetry	Azimuthal, Longitudinal	Azimuthal, Longitudinal	Azimuthal	Azimuthal, Longitudinal	Azimuthal
Inertia					
Electrons	N/A	No	No	No	Yes, except longitudinal
Ions	N/A	Yes	Yes	Yes	Yes
Quasineutrality	Yes	Yes	Yes	Yes	Yes, except within sheath
Isothermality					
Electrons	Yes	Yes	Yes	Yes	Yes
Ions	Yes	Yes, $T_i \approx T_n$	Yes, $T_i = 0$	Yes, $T_i = 0$	Yes, $T_i \ll T_e$

rameters within the discharge, such as the density distribution, the velocity of ions and electrons, and the plasma potential. As an example, the complete model developed by Ahedo et al. [2, 3] is described by a set of four radial equations and five more for the axial dimension. These take as inputs information regarding the ion species taking part in the discharge, collisional rates related to the ionization and interactions between ions, electrons and neutrals, and constant parameters such as the magnitude of the axial magnetic field B_0 and the isothermal electron temperature T_e.

The dispersion relations found for helicon plasma waves in section 3.2.1 can be used to obtain reference values for parameters such as the peak density value in the discharge. This information can be coupled with the description obtained from a 2D fluid model in order to project the distribution of plasma density, kinetic energy and plasma potential througout the discharge. Understanding the values of these parameters at the boundaries of the system, where the plasma comes into contact with solid materials, is essential to describe the interaction phenomena taking place in this region. Figure 3.3 shows an example of the models from references [2, 3] being used to estimate the 2D plasma distribution within a particular HPS, the VX-CR device. Data from these models can be used to obtain the plasma conditions at the radial ($r \rightarrow R$) and axial ($z \rightarrow -L$) boundaries, which then enable the analysis of the interaction between the plasma discharges and the physical confinement materials.

3.3. Plasma-Surface Phenomena in HPS

Solid materials often constitute the physical boundaries of plasmas, and the interaction between the surface atoms and the bulk plasma can have a significant effect on the behaviour of the latter. In the case of typical HPSs, the dielectric containment surfaces are the only regions of direct interaction between the plasma and material surfaces. This is a particular advantage over other plasma generation technologies in which electrodes or cathodes have to be immersed within the plasma discharge, as they constitute additional regions of potential failure limiting the operational lifetime of the device. It is therefore relevant to understand the fundamental principles behind the

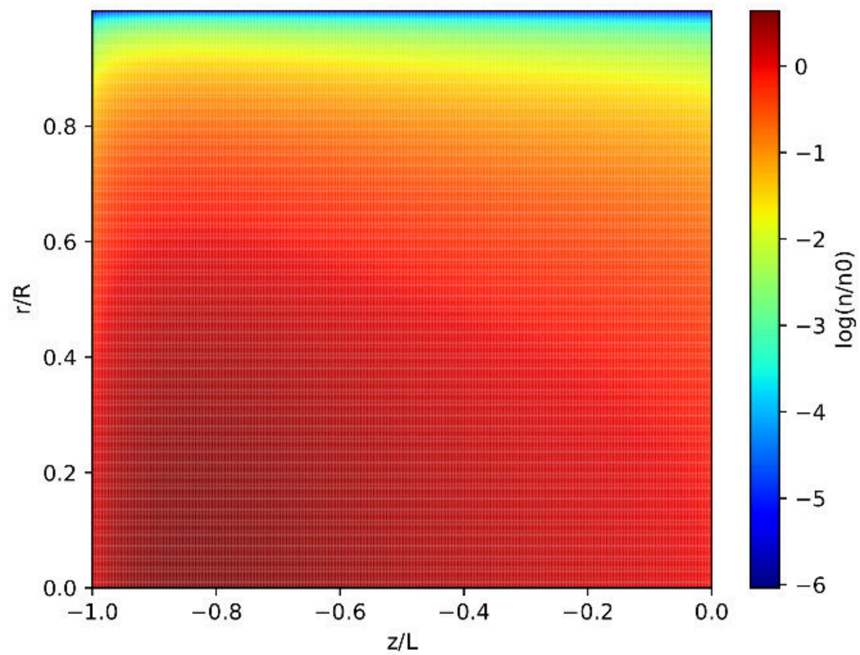

Figure 3.3: Estimation of 2D plasma density distribution in the VX-CR research HPS, obtained through the model developed by Ahedo et al. [2, 3]. Geometry and plasma parameters were obtained from [26, 43, 45]. Density values are normalized with respect to the background neutral Argon density, $n_{n0} \approx 2 \times 10^{20}$ m^{-3}. The VX-CR source is composed of a dielectric ceramic tube with $R = 0.045$ m and $L = 0.226$ m.

most typical plasma-surface interactions within HPSs, in order to characterize them and to design strategies for their control or mitigation.

3.3.1. Plasma Sheaths

DC Sheaths

Sheath is the region near a material boundary in contact with a plasma where the bulk quasineutrality breaks due to the buildup of charge at the surface. In low-temperature plasmas, such as those typically found in HPSs, the more mobile electrons produce a negative charge at the surface and, therefore, a positive sheath where the ion density is larger than the electron density, $n_i > n_e$. Sheaths typically have a scale in the order of the Debye length, $\lambda_D = (\epsilon_0 T_e/en_0)^{1/2}$. Sheaths have been studied since the early days of plasma physics, with the term originally coined by Irving Langmuir [68].

The process by which the quasineutrality in the bulk plasma transitions into the sheath is gradual, and three distinct regions can be identified as shown in figure 3.4. The quasineutral density within the bulk plasma ($n_i = n_e = n_0$) begins to decrease in the vicinity of the boundary, in a region called the pre-sheath where the bulk density and the plasma potential both decrease. The scale of the pre-sheath is of the order of the ion mean free path (λ_i). The plasma then enters the sheath proper, at which point the quasineutrality does break and the electron density diminishes at a much faster rate than the ion density. The plasma potential decreases until reaching the wall potential, which is typically lower than the bulk plasma potential.

An important property of the transition from the plasma to the sheath is the Bohm Sheath Criterion, which establishes a condition on the minimum energy of the ions as they enter the sheath. The derivation of this criterion is based upon the assumptions of negligible ionization within the sheath itself, negligible electric field at the plasma edge, Maxwellian electrons with a density given by the Boltzmann relation and cold ions with constant temperature [4, 71]. Its expression is provided by equation 3.4 and states that the energy of the ions within the sheath is comparable to that of the electrons in the bulk plasma, and that their thermal velocities surpass the Bohm velocity $u_B^2 = (k_B T_e)/m_i$.

$$eV_0 \geq \frac{T_e}{2} \Rightarrow v_i \geq u_B \tag{3.4}$$

It is possible to find expressions for the potential obtained by the surface wall due to the formation of the sheath. For the case of collisionless sheaths, equation 3.5 describes the wall potential with respect to the plasma potential at the sheath-presheath point of transition for the case of floating surfaces immersed within the plasma [71], a condition typical of certain types of probes as well as the boundary surfaces of HPSs.

$$\Phi_w = -\left(\frac{k_B T_e}{e}\right) \ln \sqrt{\frac{m_i}{2\pi m_e}} \tag{3.5}$$

This value is directly proportional to the electron temperature, and a constant factor related to the ion/electron

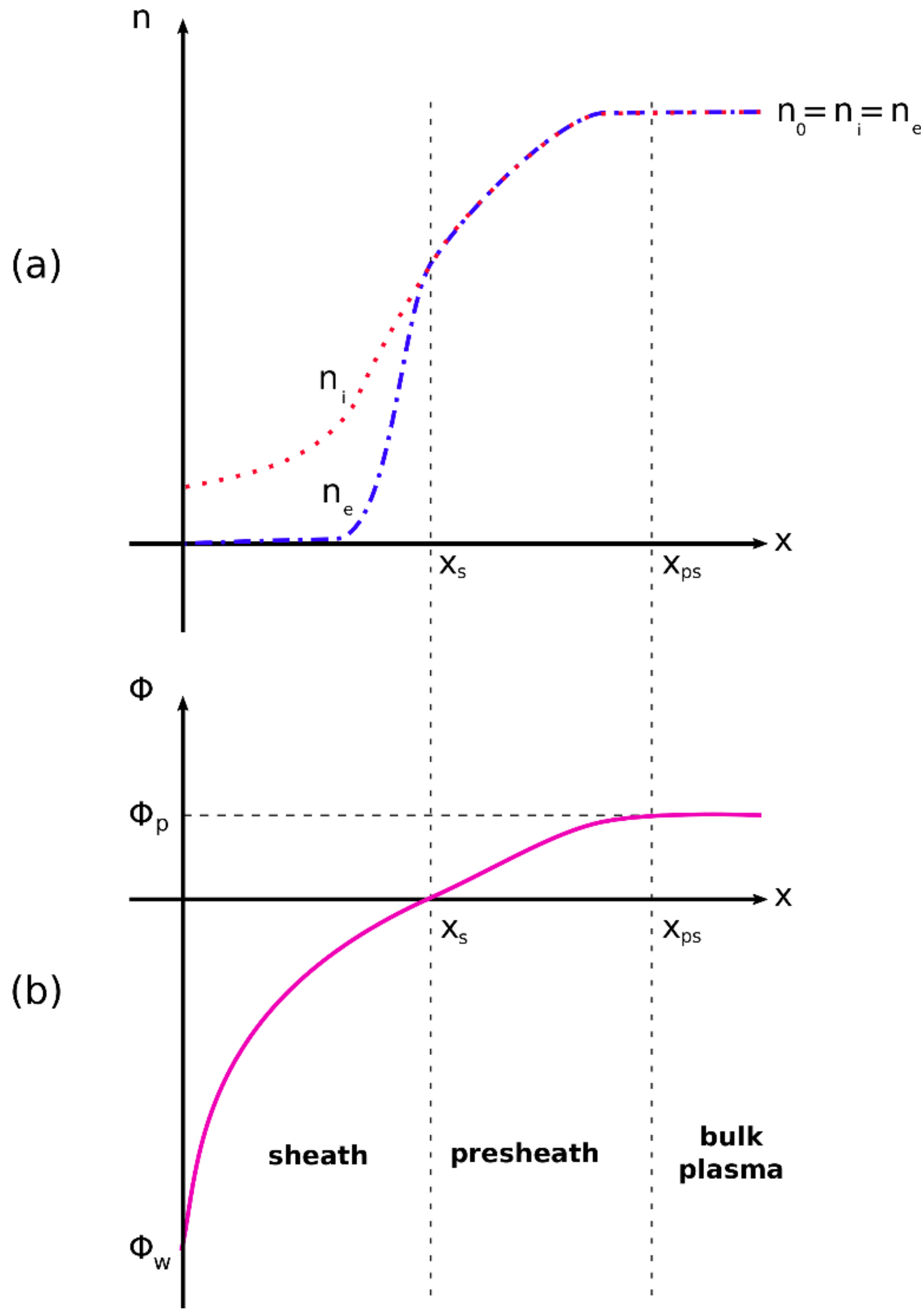

Figure 3.4: Regions in the transition between the bulk plasma and a surface in contact with a plasma, such as the inner confinement surfaces in a HPS or the surface of an electrostatic probe immersed in the plasma. Graph `(a)` shows the behavior of the electron and ion density, while graph `(b)` shows the electric potential. The surface is located at $x = 0$. The bulk plasma region is located at $x > x_{ps}$, where the plasma is quasineutral and its potential is the plasma potential Φ_p. The presheath is the region $x_s < x < x_{ps}$ where both the plasma density and potential decrease gradually as $x \to x_s$. The sheath properly begins at the point $x = x_s \approx \lambda_{De}$, where the ions acquire the Bohm velocity $u_i = u_B = -\left(k_B T_e / m_i\right)^{1/2}$. Quasineutrality is broken, the electron density quickly decreases to zero and the potential drops gradually towards the wall potential Φ_w at $x = 0$.

mass ratio. It is also possible to obtain expressions for the approximate width of the sheath, as well as expressions for these values when the sheath is collisional or the material surface is biased with a particular voltage [71].

The behavior of the plasma as it enters and traverses the sheath is critical to the understanding of the phenomena occuring at the boundary surfaces, as these depend on the energy of the ions and electrons reaching it.

RF or Capacitive Sheaths

In devices where radiofrequency (RF) waves, plasmas and materials coexist, the RF wave field dominates the formation and properties of the sheath near the boundary surfaces, allowing the appearance of potentials that surpass those typical of DC sheaths dominated by thermal effects. This phenomenon is defined as an RF plasma sheath, and it presents specific implications in the design of capacitive plasma sources, in material processing applications and within RF subsystems in fusion devices. An early treatise on this subject was presented by Butler and Kino [21], and a more recent review on this topic has been presented by Myra [78] with a particular emphasis on magnetically confined fusion systems.

RF sheaths present several features not found in the previously described DC sheaths. Plasmas interact with electrodes driven by oscillating currents I_{rf}, characterized by a frequency ω_{rf}. The sheaths created in the boundary region between the bulk plasma and these electrodes have a time-varying thickness correlated to the oscillation in the driving electrical parameters. Similar to the DC case, quasineutrality breaks within the sheath with the electron density becoming very low or even negligible. Lieberman and Lichtenberg [71] show simplified models for the case of simple, plane-parallel capacitive discharges, where assumptions help to gain a better understanding on the phenomena involved.

For idealized cases where the driving frequency is larger than the ion plasma frequency, $\omega_{\text{rf}}^2 \gg \omega_{pi}^2$, the ions react to the time-averaged potentials in the bulk plasma and not to the driving RF frequency. On the other hand, electrons do respond to the driving RF current, given the particular condition $\omega_{pe}^2 \gg \omega_{\text{rf}}^2(1+\nu_m^2/\omega_{\text{rf}}^2)$, with ν_m being the electron-neutral collision frequency. The current travelling through the RF sheaths is then mostly displacement current produced by the time-varying electric field (given the very low electron density within the sheaths); unlike inside the the bulk plasma where electrons react to the RF field and are able to carry the current through conduction. The analysis of an RF sheath depends on several factors, including the geometry of the problem, whether collisions are present within the sheath (when the ion mean free path, λ_i is smaller than the sheath thickness) and the frequency applied by the RF source. For the very high frequency (VHF) range, high ($n_e \approx 10^{17} m^{-3}$) plasma densities can be achieved with moderate power input, and this has been exploited in commercial devices used for materials processing [83].

In the particular case where $\omega_{\text{rf}} < \omega_i$, with $\omega_i = 2\pi/\tau_i$ and τ_i being the ion transit time through the sheath, the ions within the sheath are able to respond to the time-varying RF field and a low-frequency RF sheath is formed [71]. These differ from the high-frequency case since current conduction through the sheath is dominated by resistive effects and not by the displacement of the time-varying electric potential. Besides, the voltage at the capacitive electrodes becomes rectified within portions of the RF cycle, losing its sinusoidal character. In this low-frequency regime, ions react to the sheath as in the case of a high-voltage DC sheath, and the energy they obtain is a non-linear function of the time-varying voltage within the RF cycle [71].

RF sheaths are relevant to HPSs since they are present in the regions near the conductors of the antenna system used to produce the helicon discharge, where the plasma reacts to the time-varying field of the RF cycle. Despite the advantage presented by the fact that the antenna can be located outside of the discharge chamber, these RF sheaths are able to accelerate ions traversing the RF sheath with energies that can surpass those obtained in the boundary DC sheaths present in other regions within the source. This fact has critical implications for the subsequent analysis of plasma-material interactions within HPSs.

3.3.2. Plasma-surface interactions

Plasma-surface interactions (PSIs) or plasma-material interactions (PMIs) comprehend the different phenomena that occur when ions, electrons and neutrals within a plasma reach a material boundary. These interactions might produce effects on both the plasma itself as well as on the boundary. PSIs are essential in the field of plasma materials processing, and are also critical to the succesful development of practical fusion devices [75, 86], as most designs include open magnetic flux surfaces where the plasma directly impinges the physical boundaries. They are also crucial in the advancement of electric propulsion technologies, where the lifetime of the thrusters directly depends on the erosion rate of those critical surfaces directly in contact with the plasma discharge or the plume of the thruster [19, 84].

Several processes can occur at the physical boundaries of a helicon plasma. Positive ions traversing the sheath typically become neutralized, in a process that either produces an excited neutral, or a neutral plus the emission of a secondary electron (Auger emission, [71]). Secondary electron emission has been found to play a role in the sheath dynamics of certain types of low-energy plasma discharges, such as capacitively-coupled plasmas [59].

Another fundamental process is sputtering, the removal of material from a solid surface material due to the impact of an energetic impinging particle, typically ions in the case of plasma discharges. It is one of the most relevant phenomena occuring at the boundary surfaces of plasma discharges, since it can be responsible for significant erosion of said surfaces if the adequate conditions are met. Figure 3.5 depicts the basic mechanisms behind the most relevant PSI phenomena encountered in the study of HPSs.

Theoretical treatments of the phenomenon of sputtering are provided by Sigmund [95], Bohdansky [15], Yamamura [116], Eckstein [48] and Behrisch et al. [9]. Most models describe the process as the result of collisional cascades in the surface layer of the target material, in which the momentum of the impacting ion is transferred to an atom in the target material's lattice through ellastic collisions. The random arrangement of the position of both particles implies that an oblique collision is likely. The impacted target atom, in turn, collides with other neighboring particles triggering the cascade. With sufficient energy in the original impacting ion, eventually the collisional cascade will provide one of the atoms in the surface layer with an energy level surpassing the surface binding energy of the material [62], and a momentum directed outside of the surface. The atom will then be sputtered from the surface.

Simulation of the sputtering process based on the first principles from classical mechanics is possible, by using

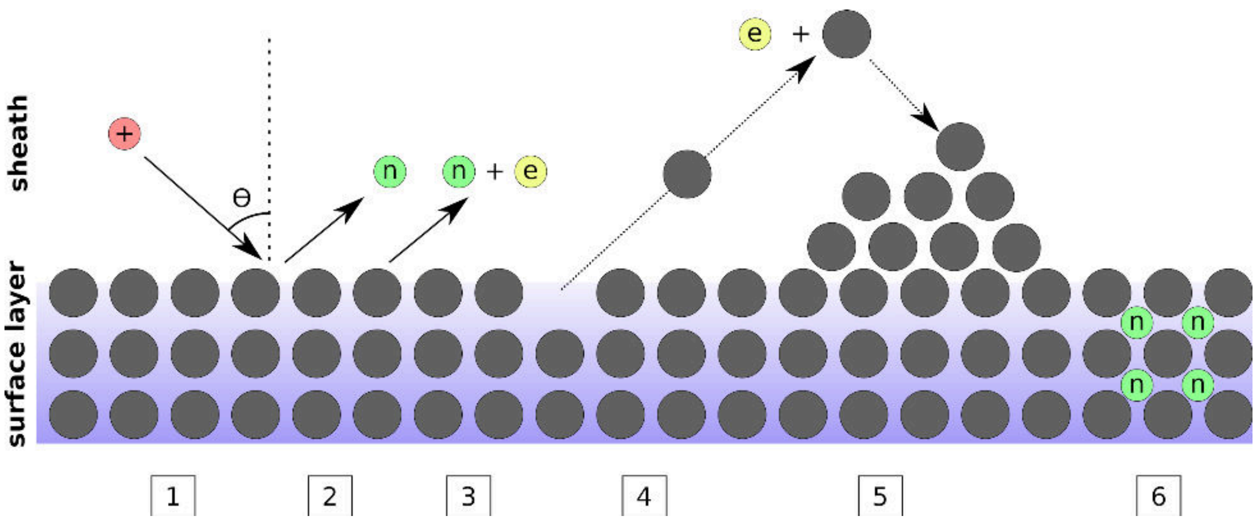

Figure 3.5: Simplified diagram of the plasma-surface interaction phenomena most relevant to the study of HPSs. The plasma sheath region is depicted at the top of the diagram, while the top layers of the plasma-facing surface lattice are represented at its bottom, where the surface atoms are represented by solid circles. (1) represents the impacting ion ⊕, approaching the surface at an angle θ with respect to its normal, and with an energy E_0. When the ion energy does not surpass the threshold energy for sputtering $E_0 < E_{thr}$, the ion may become neutralized by a surface electron releasing a reflected neutral ⓝ as shown in (2). In some cases, an additional electron ⓔ may be released (secondary or Auger emission, (3)). When $E_0 > E_{thr}$, collisional cascades within the top surface lattice are sufficient to expel a surface atom and sputtering occurs (4). The sputtered surface atoms might become ionized as they traverse the sheath, in which case they will be accelerated by the sheath potential back towards the surface and *redeposition* of material may occur (5). If the ion impact energy is sufficiently large, $E_0 >> E_{thr}$, the ions may become neutralized and *implanted* within the surface lattice (6).

the technique of Molecular Dynamics [64, 111]. Other popular simulation packages are based on the Monte Carlo statistical method, such as TRIM.SP [13] and SRIM [118]. Sputtering yield estimations obtained by the use of these software packages are strongly dependent on the chosen input parameters, and have been shown to differ from experimental values in certain ranges [115].

The fundamental parameter in sputtering models is the sputtering yield, Y_{sputt}, defined as the number of surface atoms sputtered off the surface per incident impacting ion. Y_{sputt} is mainly a function of the ion species and surface material, the ion energy and the angle of incidence between the surface normal and the ion's velocity vector. Below a particular threshold energy level, E_{thr}, ion impacts are not able to sputter surface atoms and $Y_{sputt} = 0$.

Several models have been developed to produce estimations for the sputtering yield, each particular to the species involved in the process, and the angle of incidence and energy E_0. Lieberman and Lichtenberg [71] report expressions valid for large atomic species within certain boundaries of their atomic number ratio. Eckstein and Preuss [48] proposed the model shown on equation 3.6, which is valid for ions impacting the surface at a normal angle of incidence.

$$Y(E_0) = q s_n^{KrC}(E_0) \frac{\left(\frac{E_0}{E_{thr}} - 1\right)^{\mu}}{\lambda + \left(\frac{E_0}{E_{thr}} - 1\right)^{\mu}} \tag{3.6}$$

where the krypton-carbon interaction potential s_n^{KrC} [48, 51] is used as an adequate mean value for different participating species and describes the nuclear stopping cross section[1]. This parameter is defined as follows,

$$s_n^{KrC}(\varepsilon) = \frac{0.5\ln(1 + 1.2288\varepsilon)}{\varepsilon + 0.1728\sqrt{\varepsilon} + 0.008\varepsilon^{0.1504}} \tag{3.7}$$

The reduced energy ε is obtained as follows,

$$\varepsilon = E_0 \frac{M_t}{M_i + M_t} \frac{a_L}{Z_i Z_t e^2} \tag{3.8}$$

where the subindexes i and t are used to describe the atomic numbers Z and atomic masses M of the projectile ion and target surface atoms, respectively. a_L is the Lindhard screening length [73],

$$a_L = \left(\frac{9\pi^2}{128}\right)^{1/3} a_B \left(Z_{ion}^{2/3} + Z_{tar}^{2/3}\right)^{-1/2} \tag{3.9}$$

where a_B is the Bohr atomic radius.

The remaining free parameters q and λ from equation 3.6 can be found in [9] for a variety of impacting ions,

[1]The parameter s_n^{KrC} corresponds to a fit to the krypton-carbon nuclear stopping cross section. It was proposed by Garcia-Rosales et al. ([51]) as an improvement to the sputtering formula from Bohdansky, which itself was an improvement on the Yamamura sputtering formula. It is not meant to represent the presence of either krypton or carbon in the sputtering phenomenon under analysis, but is instead a generic approximation of the particular sputtering nuclear cross section which is then used within the Eckstein sputtering formula.

target materials and ion energies.

When ions impact on a boundary surface not in a perpendicular direction, but instead at an angle α with respect to the surface normal, the calculation of the sputtering yield needs to take this geometry into account. Eckstein and Preuss [48] proposed the formula in equation 3.10,

$$Y(E_0,\alpha) = Y(E_0,0)\left\{\cos\left[\left(\frac{\alpha}{\alpha_0}\frac{\pi}{2}\right)^c\right]\right\}^{-f}\exp\left\{b\left(1-\frac{1}{\cos\left[\left(\frac{\alpha}{\alpha_0}\frac{\pi}{2}\right)^c\right]}\right)\right\} \tag{3.10}$$

where

$$\alpha_0 = \pi - \arccos\sqrt{\frac{1}{1+(E_0/E_{sp})}} \geq \frac{\pi}{2} \tag{3.11}$$

E_{sp} is a binding energy characteristic of impacting ions, and c and f are fitting parameters. Behrisch and Eckstein [9] have compiled tables for these formulae for the most common ions and target materials.

For the case of surface materials consisting of alloys or compounds of different elements, the sputtering yield will be different for each different species present in the target surface. For the steady state with a sufficiently high flux of incident ions, the sputtering yields will distribute according to the stochiometric concentration of each species within the target compound. However, this distribution is not kept for small fluences of impinging ions, and the phenomenon of preferential sputtering occurs.

For binary target materials, containing two elemental species i and j, the sputter preferentiality δ can be defined [9] as a ratio of the elemental sputtering yields Y_i, Y_j and their stochiometric concentrations c_i, c_j,

$$\delta = \frac{Y_i}{Y_j}\frac{c_j}{c_i} \tag{3.12}$$

δ can also be estimated as follows,

$$\delta = \left(\frac{M_j}{M_i}\right)^{2m}\left(\frac{U_j}{U_i}\right)^{1-2m} \tag{3.13}$$

where M_i, M_j are the atomic masses, U_i, U_j the surface binding energies and m is a power exponent describing the interaction potential.

When a plasma encounters a solid surface, such as at the boundaries provided by the containment surfaces of a HPS, a sheath will be formed and ions will be accelerated according to the potential present at the wall. If the ions are able to increase their energy beyond the threshold energy E_{thr}, sputtering will occur and the surface will be modified. Combining this information with the density distribution obtained through experimental measurements or simulations, such as the fluid models described in section 3.2.2, an *etch* rate or *erosion* rate can be calculated for the surface. This value can be used to project the behavior of the HPS and establish limits to its useful lifetime in a particular practical application.

In practical applications, the etch rate E of a surface bombarded with energetic ions, measured as a ratio of the etch depth per unit of time, is calculated as a function of the incident ion flux Γ_i, the particular sputtering yield Y and the mass density of the target surface ρ_t as shown in equation 3.14,

$$E = \frac{\Gamma_i Y M_{m,t}}{\rho_t N_A} \tag{3.14}$$

where $M_{m,t}$ is the molar mass of the target surface and N_A is Avogadro's constant. The calculation of the sputtering yield would take into account all the considerations discussed in this section. The incident ion flux Γ_i is determined by the particular conditions of the plasma discharge near the surface; for example, it can be approximated by applying the Bohm Sheath Criterion and specifying that $\Gamma_i = n_s u_B$ where n_s is the ion density at the entrance of the sheath and u_B the ion Bohm velocity.

3.4. Relevant Engineering Aspects

Figure 3.6 shows a simplified 2-D cross section of a typical HPS built in a cylindrical geometry (excluding auxiliary vacuum vessels, diagnostics or nozzle elements which may exist in laboratory or thruster applications). A cylindrical dielectric tube is sealed at one of its ends by an endcap or barrier. Neutral gas is fed inside the cylinder from an external source. An axial magnetic field, parallel to the dielectric cylinder axis, is created by using solenoid coils or permanent magnets. An antenna is used to launch the helicon waves into the neutral medium; this antenna is typically placed outside of the exterior surface of the dielectric tube. The open end of the cylinder is commonly attached to an external chamber and a gas extraction system capable of maintaining the vacuum pressure within the source at the required limits. Considerations for the design and implementation of practical HPSs are discussed in detail in [83].

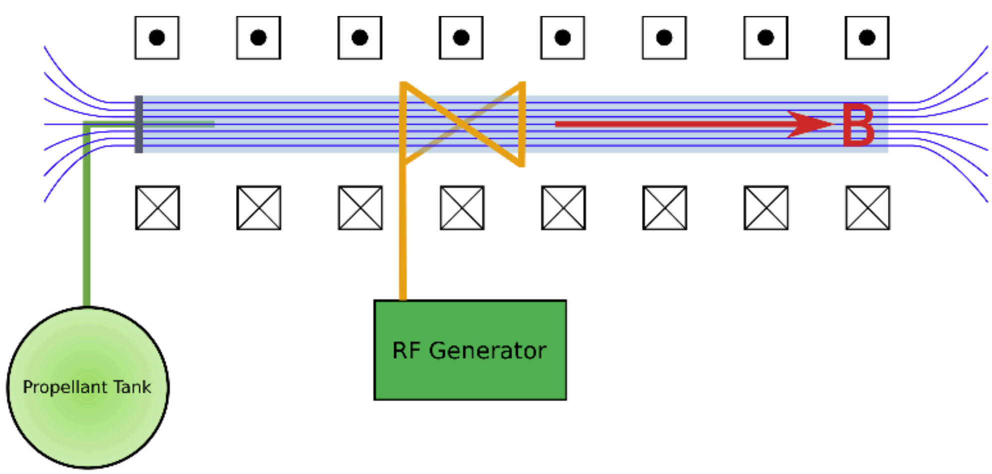

Figure 3.6: Simplified representation of a typical implementation of a Helicon Plasma Source.

Given the fact that the antenna used to launch the helicon waves can be placed outside the plasma medium, surrounding the external surface of the dielectric cylinder, the plasma-facing surfaces of the endcap, the dielectric cylinder and any other purposely-designed limiter inner walls are the only material boundaries in direct contact with the plasma, and therefore the only ones potentially subject to plasma-material interactions. The axial magnetic field limits the diffusion of particles toward the cylinder's inner surfaces. The *upstream* section of typical HPSs, shown at the left of figure 3.6, will usually contain another boundary surface and is a common location for the injection of the neutral gas required to sustain the plasma discharge. Depending on the specific geometry of a particular device, this section might be located in the vicinity of the helicon antenna or away from it, and the magnetic field might remain parallel to the axis of the source or diverge instead. The density of neutrals is usually higher in this region, promoting more frequent interactions with ions and removing momentum from them, which in turn has an effect on the energy they carry towards the boundary surfaces.

The careful selection of these materials interacting with the plasma discharge, as well as an adequate design of the HPS geometry, magnetic field and antenna, can reduce the plasma density and particle energies near the inner surfaces of these elements and therefore mitigate their erosion due to material sputtering. This in turn provides HPSs with the potential of long operational lifetimes. This is a critical property in fields such as in-space electric propulsion, where thrusters based on HPSs are among the leading candidate technologies within electrode-less thrusters [30].

3.4.1. Plasma-facing materials in HPSs

Materials used for the construction of HPSs must comply with a number of often conflicting properties. RF-transparent materials are commonly used to manufacture the cylindrical tube, allowing for the efficient transmission of the RF waves produced by the external antenna to the plasma medium. This requires materials with a low dissipation of RF energy, which is usually measured in terms of the loss tangent ($\tan \delta$). The amount of thermal energy dissipated by the boundary material is directly proportional to this loss tangent parameter, which is in itself proportional to the material temperature [27]. This can potentially create a positive feedback loop of RF energy losses within the boundary material, showing the importance of the material selection in practical HPSs.

From a practical engineering point of view, HPS materials should feature a high thermal conductivity, enabling the distribution and extraction of the heat loads produced by the inherent inefficiencies of the RF transmission and the ionization process within the source. Materials with a high thermal conductivity will allow the heat loads present in the material to spread axially and azimuthally, promoting the creation of a more even temperature distribution and reducing the appearance of thermal hotspots. This in turn contributes to the reduction of the amount of thermal energy dissipated as the RF energy traverses the boundary material. Thermal management of HPSs is a critical issue in practical implementations [11, 12, 41, 45, 77], and is essential for the development of high-power systems relying on HPSs, such as the VASIMR engine [96], the Proto-MPEX PMI research device [94] and the PISCES-RF steady-state helicon device [106].

De Faoite et al. [40] compiled a thorough review of the available data on the most relevant thermal and mechanical properties of dielectric technical ceramics commonly used in HPSs, focusing on those aspects relevant to the thermal management issues described above. The materials included in the analysis included alumina, aluminum nitride, berylia, quartz, sialon and silicon nitride. A later work [42] presents linear regressions of these properties as a function of temperature, where adequate fits were found for some of them while also highlighting the limits of the publicly available data sets.

In order to assess the reliability of these dielectric materials under the boundary conditions present in inner confinement surfaces of HPSs, their sputtering parameters would have to be evaluated under similar conditions, using the models and techniques discussed in section 3.3.2. As an example, figure 3.7 compiles experimental and simulated data for the sputtering yields of singly charged argon ions impacting some of these dielectric materials commonly used in HPSs, as a function of the impacting ion energy and at normal incidence. These choices are typical for the materials used in the VX-CR research HPS [45].

As an indicative example, erosion phenomena will be estimated for a typical HPS operating with an electron temperature of $T_e \approx 5$ eV and a density $n \approx 2 \times 10^{18}$ m^{-3} in the regions near the surface of a floating dielectric confinement wall [69]. Equation 3.5 estimates that the wall potential becomes $\Phi_w = -23.5$ V. If the ions enter the sheath with negligible kinetic energy, it can be assumed this will be the incident energy at the wall, slightly larger than the corresponding threshold energy for sputtering $E_{thr} \approx 19eV$. If the wall material is alumina, equation 3.6 produces a value of $Y \approx 0.06$ atoms/ion for the case of normal incidence to the surface and equation 3.14 produces an approximate etch rate of $E = 17.62$ nm/s. If the wall thickness of this material is $t = 2.5$ mm, this means it would take $\Delta t = 141.9 \times 10^3$ s $= 39.4$ hours for the wall to erode (in a scenario where all conditions remain constant). If the confinement surface is made of quartz glass (silicon dioxide), the wall potential Φ_w would be below the threshold energy for sputtering for argon ions impinging on SiO_2, $E_0 < E_{thr} \approx 35$ eV, and no sputtering would occur.

If these conditions exist in the vicinity of the antenna straps of the HPS, where the RF energy is transmitted as a 13.56 MHz signal with a peak-to-peak voltage amplitude of $V_{pp} = 1$ kV (and therefore a peak voltage of $V_p = 500$ V), the methods described by Berisford et al. [10] can be used to estimate an average sputtering rate given the ion energy distribution function for low-frequency RF sheaths [71]. In this particular case, an average sputtering yield of $Y_{avg} = 0.08$ is obtained for the case of Argon ions impacting the alumina surface. The corresponding etch rate would then be $E = 23.5$ nm/s, and it would take $\Delta t = 106\ 400$ s $= 29.56$ h for the wall to erode. If the material is quartz, the RF sheath would be able to produce sputtering, with an average yield of $Y_{avg} = 0.06$, an etch rate of $E = 18.85$ nm/s and the surface would be eroded in $\Delta t = 132\ 600$ s $= 36.84$ h. These are extremely simplified estimations, where conditions remain constant during the whole process, and no variations in the sputtering yield are introduced due to surface modification or deviations from normal incidence as the surface degrades.

3.4.2. Relevant experimental work regarding PSI within HPSs

HPSs have been used as part of plasma processing devices since early in their development [34, 82]), generating plasmas with the adequate parameters in order to modify the surfaces of samples or substrates subjected to their discharge. However, few studies have been conducted on the effects of the plasma discharge itself upon the inner confinement surfaces of HPSs.

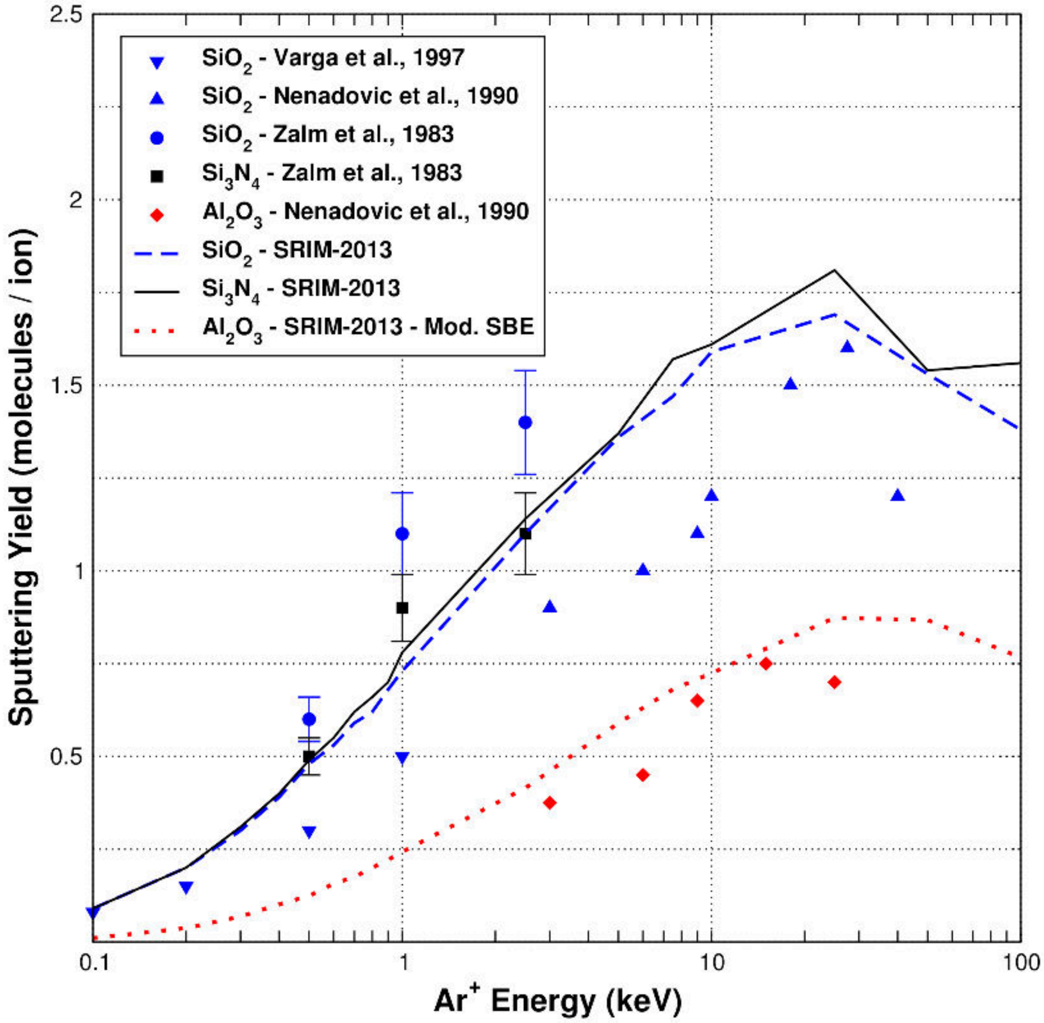

Figure 3.7: Sputtering yields for Ar^+ ions impacting perpendicularly onto some of the compounds commonly used in the construction of HPSs. Experimental data is shown for SiO_2 [81, 112, 117], Al_2O_3 [81] and Si_3N_4 [117]; as well as computational results obtained with the SRIM-2013 package.

Among these, Aanesland et al. [1] reported on the effects of an additional, floating copper antenna immersed within the discharge itself. They describe the sputtering of copper atoms from this additional antenna, which are then redeposited on the inner surface of the dielectric discharge tube. At high power levels, they describe how the areas in this dielectric tube located under the straps of the external helicon antenna remain clean due to the re-sputtering of the deposited copper layer. They suggest this is an effect of the RF sheath created on the plasma-surface boundary, as previously discussed in section 3.3.1.

This same mechanism was observed by Berisford et al. [11], when researching the power distribution and erosion within the dielectric tube of a linear helicon device. These authors developed expressions to estimate the etch rates observed at these regions under the straps of the extenal helicon antenna, modelling the sheath present in these areas as a low-frequency RF scenario (refer to section 3.3.1) and averaging the sputtering yield according to the ion energy distribution throughout the RF cycle [71]. These findings were validated through experimental observations of the actual erosion in the dielectric cylinder used in their experiment. These authors were able to estimate the required particle flux at the regions under the helicon antenna conductor from the measured etch rates, and also by analyzing IR thermal data measured at the same location; both estimations agreed within a factor of two.

Barada et al. [6] investigated this phenomenon more thoroughly, experimentally confirming the existence of an increased negative DC bias under the straps of the external antenna in the inner surfaces of a HPS, and investigating how this wall potential is affected by variations in the helicon discharge parameters. Infra-red (IR) thermography measurements taken on the inner surface of the dielectric ceramic window of the PISCES-RF device [106] also provided indirect evidence of this phenomena, showing increased values of the plasma heat flux under the straps of the helicon antenna, particularly the conductor connected to the live (non-grounded) terminal of the RF power supply.

The use of Faraday shields has been explored as a means to mitigate the effect of capacitive coupling within inductively-coupled plasmas (ICPs), and their application to HPSs has been suggested for the same purpose [99]. The Faraday shield has been implemented as a cylindrical jacket made of conducting material, installed between the dielectric plasma confinement surface and the helical antenna used in the ICP reactor [58]. Longitudinal slits have to be cut along this shield, to enable the inductive fields to penetrate the discharge. Specific experiments applying this technique to HPSs have yet to be performed. This method could potentially improve the performance of HPSs by reducing the erosion rate due to capacitive coupling under the antenna straps; however, its effects on other aspects of the source such as thermal management, and discharge efficiency, have to be investigated.

Recent experiments by Beers et al. [7, 8] describe the analysis of the helicon discharge section of the Proto-MPEX device, where they combined a finite-element model describing the helicon discharge, an ad-hoc sheath model and a transport code in order to analyze the production of impurities due to sputtering at the material boundaries. Their results confirm the experimental findings of Berisford et al. [11] and Barada et al. [6], showing the importance of the electrostatic potentials near the helicon antenna straps as a source of energetic ions impacting the radial boundaries. They also showed the difference between the operation in non-magnetized and magnetized regimes, as was also discussed by Ahedo et al. [3].

The effect of the strength and geometry of the magnetic field on the performance of HPSs has also been researched. The magnetic field has an effect on the density profile within the source. Lafleur et al. [66] show that its intensity affects the peak value of the plasma density in the helicon mode, and they show the existence of optimal configurations for given values of input RF power and magnetic field intensity. The axial magnetic configuration is also able to modify the performance of a HPS. Takahashi et al. [101, 103, 104] have described the distribution of momentum transfer between the plasma and different elements of the source, its relationship with the magnetic field configuration and how it can affect the total thrust of a helicon plasma thruster. These experiments describe how the ions are able to impart an axial momentum to the inner wall of the dielectric confinement material, due to the fact that their velocity vector is not completely normal to the wall surface [104]. This method could be used to indirectly estimate the incident angle with the confinement surface as the ions traverse the sheath, a critical factor in the calculation of the sputtering yield, although it is shown how the radial component is responsible of the energy transfer towards the wall.

The profile of the magnetic field within a HPS can be designed to mitigate the consequences of plasma-wall interactions within the source. Caneses et al. [22] describe experiments where two configurations of the magnetic field within the Proto-MPEX high-power helicon device were used to demonstrate the usefulness of controlling where the last uninterrupted magnetic flux surface (LUFS) makes contact with the inner confinment surfaces of the source. They relocated this contact point away from the dielectric ceramic window towards a purposely-designed stainless steel cylindrical limiter surface, an element with a function analog to that of divertors in fusion devices. This design change reduced the thermal heat loads under the dielectric window associated with direct impingement of the plasma, since the magnetic geometry maintains the LUFS at a minimum distance of approximately 1 cm away from the boundary surfaces. The plasma density decays rapidly beyond this point, as the magnetic lines intersect the material boundaries more often. This technique of magnetic field shaping allows the Proto-MPEX to reduce the heat loads on the dielectric window, but its effects on the sputtering and erosion related to plasma-surface interaction have not been thoroughly investigated. However, the careful design of magnetic geometries is commonly used for this purpose on electric propulsion devices [57, 76].

Figure 3.8 summarizes the findings of these experiments with regard to the appearance of sputtering phenomena within the internal dielectric confinement surfaces of HPSs. Region (1) in the figure represents areas within these internal surfaces in direct contact with the plasma, where a sheath forms and the dielectric surface obtains a negative electric potential Φ_w as described by equation 3.5. The positive ions are then accelerated towards the wall with a surface flux determined by the product of the bulk plasma density n_0 and the Bohm velocity u_B they obtain when entering the sheath. The effect of the impinging ions on the dielectric surface can then be analyzed according to the sputtering models discussed in subsection 3.3.2, and effective surface etch rates may be computed. Region (2) in figure 3.8 describes the particular phenomena observed by Berisford et al. [11], Aanesland et al. [1], Barada et al. [6] and Beers et al. [7, 8], where the creation of RF sheaths on the internal surfaces directly under the helical antenna straps may create the conditions for high-voltage DC sheaths in the negative part of the cycle. In this scenario, average sputtering yields can be computed through the ion energy distribution within the negative portion of the RF cycle [71], and hence etch rates can be computed as well.

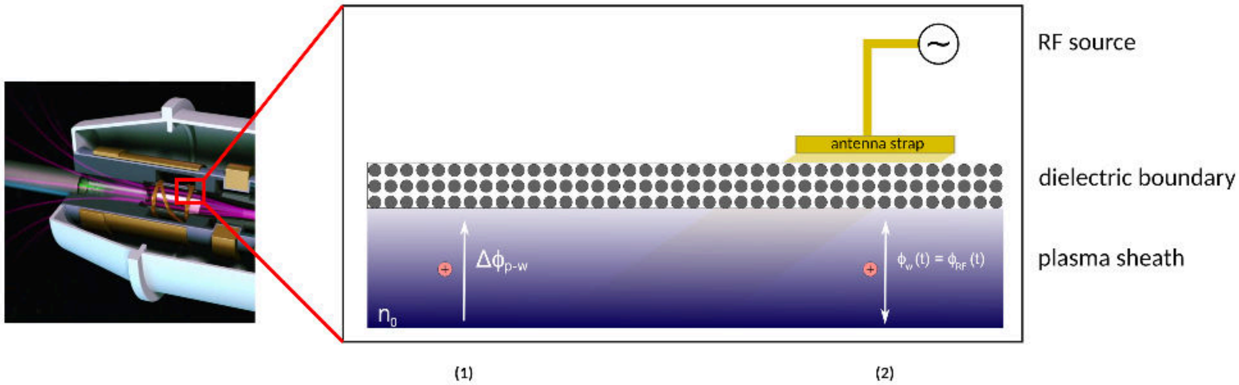

Figure 3.8: Representation of the two main sputtering regimes present in helicon plasma sources, as previously reported in literature. **(1)** shows the conditions present at the boundary between the bulk plasma, with density n_0, and the internal dielectric boundaries within a HPS. Parameters such as this density and the electron temperature T_e define the conditions present within the plasma sheath, which accelerate the positive ions towars the wall through the plasma-wall potential $\Delta\Phi_{p-w}$ [71]. If the energy obtained by the ions at the material boundary surpasses the threshold energy E_{thr}, sputtering will then occur. **(2)** describes the situation particular to the areas under the antenna straps, which may be subjected to high capacitive voltages driven by the external RF subsystem [6, 8, 11]. Given sufficiently large voltages, the negative part of the antenna's RF cycle will accelerate the ions towards the surface with enought time to traverse the sheath, essentially behaving as a high-voltage DC sheath [11]. Once again, if the energy obtained by the ions surpasses the threshold limit, sputtering will occur.

3.5. Summary and conclusion

Helicon Plasma Sources (HPSs) hold great potential for the development of efficient, high-density plasma sources. One of their widely quoted advantages is the absence of cathodes or electrodes directly in contact with the plasma discharge. This fact limits any plasma-surface interactions to the inner surfaces of the dielectric confinement surfaces, where the diffusion of the plasma is limited by the action and geometry of the axial magnetic field, thus reducing the expected material erosion rates and providing these devices with a potentially long operational lifetime. This proposed advantage of HPSs, among others, is still the subject of debate [53, 102].

The present review summarized the theory describing these interactions, beginning with the physics of helicon waves and cylindrical magnetized plasmas (section 3.2), followed by a description of the most relevant plasma-surface interacion phenomena within HPSs (section 3.3). Practical implementation aspects and relevant experimental results were presented in section 3.4.

Current research results point towards the existence of two main modes of plasma-surface interaction within HPSs. The first one is the diffusion of plasma towards the inner surfaces of these material boundaries, where the ions are then accelerated through DC sheaths and sputtering may occur if they are able to become energized above the corresponding threshold energy level. The eventual etch rate experienced by particular devices will depend on the plasma parameters near the boundaries, the species present in the plasma and the wall material, and the geometry of the magnetic field at each region. The second mode of interaction appears in the regions of the helicon dielectric window directly under the conductor straps of the antenna, where capacitive RF sheaths are created and accelerate the ions. Direct (profilometry and surface analysis) and indirect (IR thermography) evidence has confirmed the existence of this phenomenon, and it has also been investigated through modeling and simulations. Experimental results suggest that these RF sheaths appearing under the helicon antenna straps are responsible for the appearance of thermal hot spots and regions of concentrated erosion patterns in the inner surface of the dielectric windows of HPSs.

Despite recent advances in the description and understanding of these plasma-material interactions within helicon plasma sources, several topics are still open for research and experimentation. Current modeling efforts integrate different specific tools to simulate the interactions between the plasma discharge, the transport and diffusion of the plasma species throughout the simulation domain, the creation of DC and RF sheaths and the interaction phenomena occuring at the material boundaries. As usual within the simulation of plasma phenomena, varying timescales, lengths and energy levels are involved. Integrated simulation efforts for the specific purpose of studying sputtering and impurity transport within HPSs are recent, and they could benefit from the development of purposely-designed integrated simulation tools for this task.

Specific models for sputtering phenomena on the dielectric ceramics commonly used in HPSs should be developed and validated through experimentation. Additionally, the interaction between the sputtered species, the original plasma, external impurities and the boundary surfaces, including the formation of new compounds and molecules, appears to be a topic of relevance, as shown in the results obtained in the Proto-MPEX device [7] where these relationships where taken into account to better explain the observed experimental results.

The magnetic field geometry can be designed in order to displace the contact points between the plasma and its boundary surfaces and also to create a separation between the magnetic flux surface enveloping the plasma and the confinment materiales. This strategy appears to have a potential effect in reducing the erosion phenomena within the HPS, as suggested by the effect it has shown in modifying and reducing the heat flux distribution in the Proto-MPEX experiment [22]. Yet this claim has not been thoroughly investigated. This experiment also demonstrated how cylindrical liners can be placed at the locations where the plasma does contact the boundary surfaces; when this occurs outside of the section where the helicon antenna is located, the requirement for an RF-transparent dielectric window can be removed and other materials with lower sputtering yields can be selected. However, the exact interactions between these liner materials, the plasma, and the sputtered impurities have to be investigated. This technique could offer some critical advantages for the creation of impurity-free plasmas in high-power helicon devices used to research fusion-relevant material interactions; but they might introduce new unwanted issues in other applications where the physical lifetime of the hardware is the priority, such as in electric propulsion devices.

From an experimental perspective, the diagnostics able to measure the above-mentioned parameters can be improved. Given the linear nature of most helicon devices, access to the critical regions near the dielectric ceramic window and the RF antenna region is complex. High power density devices, such as the Proto-MPEX and Pisces-RF devices, or the VASIMR VX-200SS engine, create a hostile environment for most physical probes. Measurements have been done of the inner wall potential [6], the radial heat flux and the UV radiation [11], yet these experiments were not conducted inside high-power, steady-state devices.

Measurements of the effects of sputtering within the inner surface of helicon confinement surfaces have been studied through profilometry [11] and x-ray photoelectron spectroscopy [7]. Extensive experience in this particular field has been obtained in the simulation and execution of long-duration experimental runs of electric propulsion devices [18, 47, 84, 91], but not in those which employ HPSs. Diagnostics such as optical profilometry [52] and coordinate-measuring machines [43] could also be applied to HPSs, particularly for the measurement of surface erosion after long-duration tests in high-power devices.

The engineering problem of managing the heat fluxes transferred by the plasma onto the inner confinement surfaces of HPSs is partially related to the plasma-surface interaction issues discussed throughout this review, since the direct impingement of energetic ions onto these surfaces is one of the mechanisms of heat transfer present in the sources. Some mitigation techniques previously discussed, such as shaping the magnetic field to control the points of direct contact between the plasma and these inner surfaces, can be applied to both phenomena. The role of the temperature on the erosion rate of these surfaces in contact with the plasma has not been investigated in the particular case of HPSs. The formation of nanostructures has been studied in the case of candidate materials for the divertors of projected fusion devices [61]; similar conditions might be achievable in high-power HPSs operating at steady-state for long periods of time, and whether these phenomena affect the sputtering of these inner confinement surfaces remains to be investigated.

The physics concepts presented here can be combined to establish a framework for analyzing the impact of plasma-material interactions within HPSs, and explore mitigation strategies suited for the development of high-power helicon sources, particularly for those applications where an extended operational lifetime of the system is a critical requirement. These concepts can be used to model the density distribution within the HPS, and the existence of induced RF or DC bias voltages on its inner surfaces, which appear to be a significant factor in the appearance of local sputtering and deposition phenomena. A sufficient understanding of these phenomena will be required as the application of high-power, steady-state helicon sources continues to grow in the fields of materials processing, fusion research and in-space electric propulsion.

Chapter 4

Estimation of erosion phenomena within helicon plasma sources through a steady-state explicit analytical model

This chapter was originally published as a peer-reviewed open-access article,

> Del Valle JI, Granados VH and Chang-Diaz FR (2022), *Estimation of erosion phenomena within helicon plasma sources through a steady-state explicit analytical model*, Front. Phys. 10:950472, doi: 10.3389/fphy.2022.950472
> https://www.frontiersin.org/articles/10.3389/fphy.2022.950472/

Abstract: Helicon plasma sources produce high-density discharges without the need of electrodes in direct contact with the plasma, which is thought to provide them with long operational lifetimes. An explicit steady-state analytical model is described with the capability of depicting the 2D plasma density distribution, the sheath potentials and the estimated sputtering and etch rates along the plasma-facing components of the source. The individual constituting submodels are fitted against available experimental data, and the model is used to predict erosion rates within the VX-CR research helicon plasma source. Erosion within these components is dependent on the value of plasma density along the boundaries, the electron temperature and the particular ion-target material combination. The highest erosion rates are found along the upstream system boundary, followed by the regions near the helicon antenna straps where a capacitive RF sheath is formed. The assumptions and limitations of the model are discussed, and future improvements are proposed.

Keywords: helicon plasma, erosion, sputtering, model, etching.

4.1. Introduction

The use of helicon plasma sources (HPSs) ([35]) within different research and practical applications has gained traction because of their ability to produce high-density plasmas at low power levels and magnetic field intensities, and their capability to dissipate energy into the plasma deeper than other technologies such as capacitively-coupled (CC) or inductively-coupled (IC) discharges. Helicon sources have found usage within the materials processing industry, in electric propulsion devices, as ion sources for fusion systems, and within facilities researching the interactions between plasmas and materials at fusion-relevant conditions.

One of the claimed advantages of HPSs is the fact that the discharge is driven by radiofrequency (RF) waves emitted from an external helical antenna which does not contact the plasma directly, thereby discarding any damage to it as a potential failure mode. The erosion of electrodes and grids facing the plasma discharge is one of the key lifetime-limiting factors in practical devices relying on other plasma-generation techniques, and HPSs are therefore expected to exhibit long-lasting operational regimes. The presence of axial magnetic fields within HPSs also contributes to confine the plasma and reduce its diffusion towards the material boundaries. However, the erosion of these internal plasma-facing components due to the contact with the discharge has not been widely investigated in order to accurately estimate its effects. As these sources find their way into ever larger and more powerful devices, clearly understanding their limitations becomes key to the engineering of reliable and robust devices.

In a previous paper ([44]), we have contributed a review of this topic and the different phenomena involved in its analysis, and described past published work addressing erosion phenomena within HPS. Among those, Berisford et al. [11] conducted experimental measurements of the etching phenomena on the inside of a quartz tube used as dielectric boundary in a helicon source. They identified the voltages induced by the helicon antenna on the inner surface of the HPS dielectric cylindrical boundary as a key erosion mechanism, and correlated their predictions with experimental measurements to within an order of magnitude. Their work relied on simplified formulas for the sputtering of elemental targets by energetic ions and low-frequency RF sheaths, adapted for their particular HPS. Barada et al. [6] and Thakur et al. [106] also confirmed the relevance of this capacitive coupling phenomena in the regions near the location of the antenna straps. Recent work by Beers et al. [7, 8] developed a combined model integrating a finite-element simulation of the RF discharge, an ad-hoc sheath model and a transport code to estimate erosion and deposition rates in high-power deuterium discharges from the Proto-MPEX experiment, which were then compared to experimental measurements. Their approach to sputtering simplified the actual aluminum nitride (AlN) boundaries as pure aluminum, given their observations of aluminum enrichment in the surface after experimental runs. Their simulation provides an accurate and detailed prediction of sheath potentials, sputtering and deposition phenomena, and impurity transport within the HPS; its disadvantage is the complexity involved in the convergence of discrete 3D codes.

In the present work, we describe the development and validation of a modeling tool for the estimation of sputtering and etch rates within the plasma-facing components of a HPS. It combines individual analytical modules for analyzing the 2D distribution of plasma density within the source, the voltages produced by the sheaths in different regimes, and the sputtering phenomena and associated etching. The 2D plasma description and the sheath models adapt fluid-dynamic models previously published in the literature, while the sputtering package is also based on adapted empirical expressions developed to match available experimental data. The sputtering model was extended to provide the ability of simulating compound target materials. The combined model aims to simplify the estimation of average and peak erosion rates within HPSs, with the goal of providing a flexible tool that can be used to predict the performance of a particular device, to develop general erosion mitigation techniques for HPSs in general, and for the engineering analysis of practical helicon implementations.

This paper is organized as follows. Section 4.2 describes the individual components which form part of the simulation package. Section 4.3 describes the validation of each individual submodel against publicly-available experimental data sets; as well as the application of the combined tool to a particular HPS, the VX-CR device at Ad Astra Rocket Company Costa Rica. Section 4.4 analyzes these results and discusses the assumptions and limitations underlying the model, and section 4.5 summarizes the main findings of this work.

4.2. Mathematical Models

This section describes the first-principle models underlying the implementation of the analysis tools developed for the investigation of erosion phenomena within helicon plasma sources.

Figure 4.1a) presents an idealized diagram of a helicon plasma source (HPS), showing its main components in a typical cylindrical configuration, as well as the coordinate system defining the simulation domain. Figure 4.1b), reproduced from [44], describes the two main modes of erosion phenomena within the plasma-facing components of HPSs, as described in the literature.

The models presented in the following subsections are independent of the particular ion species present in the plasma, although they do assume the discharge is produced with a single gas (not a mixture of gasees), which is singly-ionized (a typical case in most low-temperature helicon sources).

4.2.1. Dispersion relation for helicon waves

Helicon waves fall into the category of right-hand polarized (RHP) plasma waves, which propagate along constant magnetic fields in bounded systems. They are related to atmospheric whistler waves, and typically appear in the frequency range $\omega_{ci} \ll \omega \ll \omega_{ce}$, where ω is the excitation frequency and ω_{ci} and ω_{ce} are, respectively, the ion and electron cyclotron frequencies for the given configuration.

A description of the relation dispersion describing helicon plasma waves can be obtained from Maxwell's equations, applying the cold plasma approximation (non-thermal ions) and neglecting the displacement current, as shown in detail by Chen and Arnush [5, 33, 36].

When electron inertia is retained in the derivation, the total wave number β of the wave is defined by

$$\beta_{1,2} = \frac{k}{2\delta}\left[1 \mp \left(1 - \frac{4\delta k_\omega^2}{k^2}\right)^{1/2}\right] \approx \frac{k_\parallel}{2\delta}\left[1 \mp \left(1 - \frac{2\delta k_\omega^2}{k_\parallel^2}\right)\right] \approx \left\{ \begin{array}{c} k_\omega^2/k_\parallel \\ k_\parallel/\delta \end{array} \right. \tag{4.1}$$

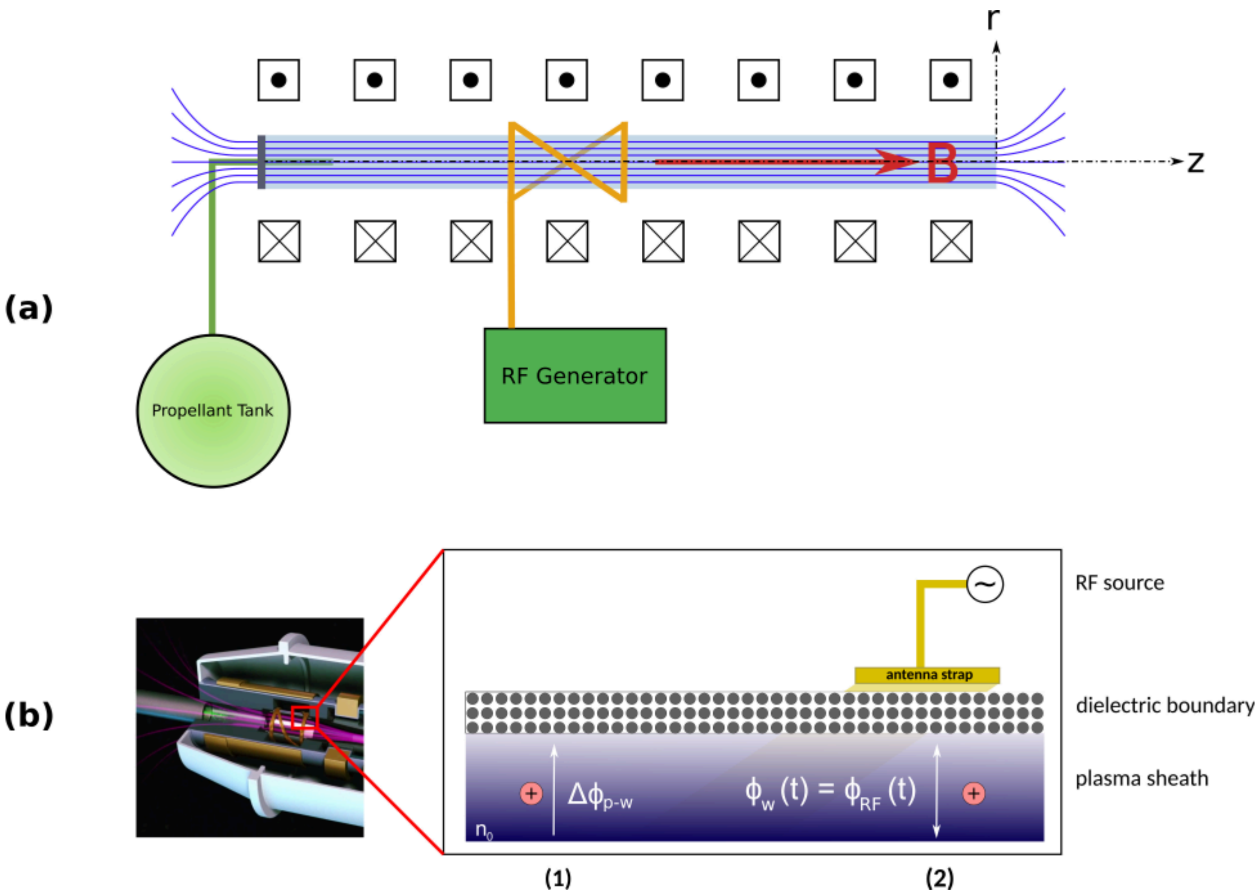

Figure 4.1: **(a)** A simplified diagram of a Helicon Plasma Source (HPS). **(b)** A representation of the main mechanisms of erosion present in Helicon Plasma Sources, reproduced from [44]. Region *(1)* describes the acceleration of ions towards the inner confinement surfaces due to the DC sheath and the floating negative potential present at the surface. Region *(2)* describes the acceleration of the ions due to the present of an external source of RF excitation, such as the terminals of the antenna used to excite the plasma discharge.

where θ is the angle of propagation of the wave with respect to the constant, axial magnetic field $\mathbf{B} = B_0\hat{\mathbf{e}}_\mathbf{z}$, with components parallel and perpendicular to $\mathbf{B}$: $\beta^2 = k_\parallel^2 + k_\perp^2$, where $k_\parallel = \beta\cos\theta$ and $k_\perp = \beta\sin\theta$. The ratio $\delta = \omega/\omega_{ce}$ is the ratio between the wave frequency and the electron cyclotron frequency $\omega_{ce} = eB_0/m_e$, and $k_\omega^2 = \omega\omega_p^2/\omega_{ce}c^2 = \omega n_0 e\mu_0/B_0 \equiv \beta k_\parallel$ is the wavenumber for low-frequency whistler waves along B_0 in free space.

The first solution to equation 4.1, β_1, corresponds to the helicon or H mode obtained in the zero electron mass limit, when electron inertia is neglected. Solution β_2 corresponds to the Trivelpiece-Gould or TG mode, an electron cyclotron wave propagating at an angle to the magnetic field and a relevant damping mechanism in helicon plasma sources, particularly at low values of B_0.

The expression for the H mode β_1 can be expanded as

$$\beta_1 = \frac{\omega}{k_\parallel}\frac{n_0 e\mu_0}{B_0} = \frac{\omega}{\beta_1\cos\theta}\frac{n_0 e\mu_0}{B_0} \tag{4.2}$$

where n_0 corresponds to the electron density of the plasma where the wave is propagating, with e the electron charge and μ_0 the permeability of free space.

The previous equation provides a means to estimate the maximum value of the expected plasma density for a given helicon device as a function of the axial magnetic field intensity B_0, for given values of the excitation frequency ω, the parallel wave number $k_\parallel$ and the angle θ between the wave propagation vector and B_0. These last parameters can be determined through the source's RF subsystem and the antenna geometry.

For the typical scenario of a helicon plasma source of cylindrical geometry of radius R and exciting mode $m = 1$, the previous equation can be simplified [32, 33] to

$$n_0 = \left(\frac{p_0 k_\parallel}{R\omega e\mu_0}\right) B_0 \tag{4.3}$$

where p_0 is the lowest root of the Bessel function of the first kind and order 0 ($J_1(p_0) = 0$, with $p_0 \approx 3.83$).

The actual distribution of plasma density within practical helicon plasma sources is seldom uniform, yet this expression enables the estimation of a reference value for the expected peak plasma density, which can be used with the subsequent models when describing the variation in all relevant plasma parameters.

4.2.2. 2D fluid description of cylindrical magnetized plasmas in steady-state

The description of the plasma behavior within a helicon plasma source is provided by a 2D, two-fluid description of cylindrical plasmas in the presence of an axial magnetic field using the cylindrical coordinate set (r, θ, z). The chosen model is an implementation of the asymptotic magnetized regime proposed by Ahedo and Navarro-Cavallé [3], which describes a quasineutral, isothermal plasma with azimuthal symmetry and where the ion temperature is much lower than the electron temperature, $T_i \ll T_e$. The model is based in a series of assumptions and simplifications, including: steady-state, azimuthal symmetry, cold neutrals whose velocity u_n and density distribution n_n only depend on the axial position, longitudinal ambipolarity where the axial and radial velocities of ions and electrons are constant ($u_{iz} = u_{ez}$ and $u_{ir} = u_{er}$) and the ion azimuthal velocity is negligible $u_{i\theta} \ll u_{e\theta} = u_\theta$, among others chosen by the authors.

The model is described by a set of radial and axial equations. The radial submodel describes the behavior of the plasma at a given axial location z. The ratio between the plasma density n_r and its value at the cylinder axis $n_r(z, 0)$ can be described by the expression

$$\frac{n_r(z,r)}{n_r(z,0)} = J_0\left(a_0 \frac{r}{R}\right) \tag{4.4}$$

where r is the radial coordinate, R is the maximum radius of the cylindrical plasma discharge, n_r is the quasineutral plasma density, J_0 is the Bessel function of the first kind of order 0 and $a_0 \approx 2.405$ is the first zero of J_0.

The radial component of the ion and electron velocity u_r is normalized by the ion sound speed $c_s = \sqrt{eT_e/m_i}$ and can be expressed as

$$\frac{u_r}{c_s} = a_0 \left(\frac{\nu_e \omega_r}{\omega_{lh}^2}\right) \left[\frac{J_1(a_0 r/R)}{J_0(a_0 r/R)}\right] \tag{4.5}$$

where the term $\nu_e = \nu_{en} + \nu_{ei} + \nu_{ion}$ is a linear combination of the electron-neutral ν_{en} and electron-ion ν_{ei} collision frequencies as well as the ionization frequency ν_{ion}, $\omega_r = c_s/R$ is the radial transit frequency; $\omega_{lh} = eB_0/\sqrt{m_e m_i}$ is the lower-hybrid frequency and J_1 is the Bessel function of the first kind of order 1. The collision rates composing the term ν_e can be approximated as a function of T_e, as described in [3].

The electron azimuthal velocity u_θ is normalized by the electron thermal velocity $c_e = \sqrt{eT_e/m_e}$ and is described by the expression

$$\frac{u_\theta}{c_e} = (u_r/c_s)(\omega_{lh}/\nu_e). \tag{4.6}$$

Boundary conditions for the radial model preclude null plasma velocities and plasma potential $u_r = u_\theta = \phi_p = 0$, and a known plasma density $n(z,r) = n(0,r)$ at the cylinder axis $r = 0$. At the $r = R$ physical boundary, the Bohm sheath criterion states that $u_r(z,R) = c_s$.

The axial submodel describes the plasma parameters at the $r = 0$ coordinate as a function of the axial coordinate z. For the limit of large T_e, large B_0 and with ideal plasma recombination at the system physical boundaries (producing neutrals with the same axial velocity u_n), the ideal asymptotic model from Ahedo et al. ([3]) can be applied.

The axial neutral velocity u_n remains constant throughout the source,

$$u_n = u_{n0}. \tag{4.7}$$

The axial velocity of both ions and electrons, u_z, is normalized by the ion sound velocity c_s and defined in terms of the auxiliary variable ξ as follows

$$u_z/c_s = \tan \xi. \tag{4.8}$$

The plasma density n is described by the following expression

$$n/n_0 = 2\eta_u \cos^2 \xi \tag{4.9}$$

where $n_0 = g_0/c_s$ is a reference plasma density, g_0 is the axial flow of heavy species (ions + neutrals) at the upstream boundary of the source $g_0 = \dot{m}/(m_i \pi R^2)$, $\dot{m}$ is the input mass flow to the system, and m_i is the mass of the ions. The parameter $\eta_u = n_{z=0}/n_0$ is the propellant utilization defined as the ratio between the plasma density at the downstream open boundary of the system, $n_{z=0}$, and n_0.

The axial neutral density n_n is defined as

$$n_n/n_{n0} = 1 - \eta_u \sin 2\xi \tag{4.10}$$

where $n_n 0 = g_0/u_{n0}$ is a reference neutral density.

The axial variation of the auxiliary variable ξ is defined implicitly by the integral expression

$$\frac{z+L}{L_\star} = \int_{-\pi/4}^{\xi} \frac{1 - \tan^2 \xi'}{1 - \eta_u \sin 2\xi'} d\xi' \tag{4.11}$$

where L is the axial length of the simulation space, $L_\star = c_s/(R_{ion} n_{n0})$ is an effective ionization mean free path, and R_{ion} is the ionization collision rate. An expressions for R_{ion} as a function of T_e is provided in [3].

The boundary conditions for the axial model include the given known values for the following parameters at both the upstream boundary $z = -L$ and the downstream exit plane $z = 0$: a given value for the flow of neutrals into the system, g_0; the reference neutral axial velocity $u_n(r, -L) = u_{n0}$; and the plasma velocity equal to the Bohm velocity at both the upstream and downstream axial boundaries, $u_z(r, -L) = -c_s$ and $u_z(r, 0) = c_s$. Setting $z = 0$ and $\xi = \pi/4$ in equation 4.11 defines the propellant utilization η_u as an implicit function of the ratio $L/L_\star$.

4.2.3. Sheath models

In the region where the plasma contacts a physical material boundary, the quasineutrality of the bulk discharges is broken due to the buildup of charge at the surface. This region is called a sheath, and its properties depend on both the parameters of the plasma as well as the material surface. The scale of the sheath is in the order of the Debye length, $\lambda_D = (\epsilon_0 T_e / e n_0)^{1/2}$, and is typically much smaller than the characteristic dimensions of practical laboratory plasmas.

The transition between the bulk plasma and the material surface occurs through different regions or regimes. Prior to the actual sheath, the *pre-sheath* is located, where the plasma density and potential decrease but quasineutrality is still preserved. At the point where the sheath begins, the Bohm sheath criterion must be met, $u_i \geq c_s$. Within the sheath, quasineutrality breaks and the electron density decreases rapidly towards zero. The potential at the material wall Φ_w is therefore lower than the bulk plasma.

For the case of a floating dielectric material immersed into the plasma, the potential obtained at the wall can be described ([71]) as

$$\Phi_w = -T_e \ln \sqrt{\frac{m_i}{2\pi m_e}}. \tag{4.12}$$

It is a function of constant properties of the plasma species (the ion and electron masses, m_i and m_e), and the electron temperature T_e expressed in units of electric potential. Under the assumption that $T_i \approx 0$, ions entering the sheath will be accelerated towards the wall due to the potential difference $\Phi_p - \Phi_w$, where Φ_p is the plasma potential.

Other conditions could be present in the boundary material, such as grounded or biased surfaces at a potential Φ_{bias}, in which case the analysis would need to take into account the effect of the potential difference $\Phi_p - \Phi_{bias}$ in the acceleration of the ions.

For the case where radiofrequency (RF) waves are present near the interface of plasmas and materials, such as near the location of the antenna straps providing the excitation source in helicon plasma sources, an *RF plasma sheath* is created. When the driving RF frequencies are sufficiently high ($\omega_{rf} \gg \omega_{pi}$, with $\omega_{pi}^2 = (e^2 n_0)/(\epsilon_0 m_i)$ the ion plasma frequency), the ions are able to respond only to the time-averaged variations in the DC plasma potentials and not the instantaneous RF wave. The electrons in the bulk plasma are able to react to the RF wave potentials, yet most of the current in the sheath is displacement current, given its low electron density.

When the frequency of the RF wave is low enough, ions are able to respond to the RF wave and a *low frequency sheath* is formed. This condition requires that $\omega \ll \omega_i = \pi \omega_{pi} (2T_e/V_0)^{1/4}$, with V_0 the transient voltage of the RF wave [71]. During the RF cycle, the ions will be accelerated towards the surface due to the time-varying potential.

The ion energy distribution function $g_i(E)$ for a low-frequency RF sheath [71] is given by the expression

$$g_i(E) = \begin{cases} \frac{1}{\pi}\left[V_{rf}^2 - (V_{bias} - E)^2\right]^{-1/2} & E \neq V_{bias} \\ \\ \frac{1}{2\pi}\left[\pi - 2\sin^{-1}\left(V_{bias}/V_{rf}\right)\right] & E = V_{bias} \end{cases} \tag{4.13}$$

where V_{rf} is the peak voltage amplitude of the RF wave, V_{bias} is any DC bias voltage applied to the surface, and E is the instantaneous voltage of the RF field. The distribution has a different expression for the case $E = V_{bias}$, to take into account the rectifying effect of the low-frequency sheath.

4.2.4. Sputtering phenomena

Plasma-surface interactions include all the phenomena that appear at the intersection between plasmas and a material boundary. Among those, sputtering is of significant interest to the fields of materials processing, fusion engineering and electric space propulsion. Sputtering is the removal of material from a solid surface due to the impact of energetic particles, and it plays a fundamental role in determining the lifetime of practical devices.

Sputtering depends on several parameters, including the properties of the impinging particles, the composition of the target material surface and the geometry of the impact. A simplified model for the geometry of the sputtering process ([44]) describes the incoming ion being accelerated by the potential drop on the sheath to an energy E_0 until it impacts the surface with an angle θ with respect to the surface normal. If the energy surpasses a threshold level for the occurrence of sputtering, $E_0 > E_{thr}$, a cascade of collisions within the target material will be able to provide sufficient momentum to one or several particles in the top layer of the target material, and allow them to overcome the surface binding energy E_{sb} and leave the surface.

Sputtering is described by the sputtering yield Y, defined as the number of surface particles sputtered from the target material surface per incoming ion. It depends on the properties of the impacting ion and the target material, the energy of the ion and the angle of incidence. Several models have been developed for the estimation of actual sputtering yields; the model chosen for this study is the one published by Eckstein and Preuss [48], which improves upon earlier work.

The sputtering yield Y when ions impact a surface at normal incidence ($\theta = 0$) is obtained with the expression

$$Y(E_0) = q s_n^{KrC}(E_0) \frac{\left(\frac{E_0}{E_{thr}} - 1\right)^{\mu}}{\lambda + \left(\frac{E_0}{E_{thr}} - 1\right)^{\mu}}. \tag{4.14}$$

It depends on three free parameters (q, λ and μ) used to fit the model to experimental data. Behrisch and Eckstein [9] have tabulated these parameters for a significant selection of sputtering scenarios involving monoatomic elemental targets. The term s_n^{KrC} is the krypton-carbon interaction potential,

$$s_n^{KrC}(\varepsilon) = \frac{0.5\ln(1+1.2288\varepsilon)}{\varepsilon + 0.1728\sqrt{\varepsilon} + 0.008\varepsilon^{0.1504}} \tag{4.15}$$

which is used as an adequate mean value to describe the nuclear stopping cross section for the problem, for any combination of ion species and target materials (not necessarily involving carbon or krypton)[1]. The term ε is the reduced potential, which is calculated as

$$\varepsilon = E_0 \frac{M_t}{M_i + M_t} \frac{a_L}{Z_i Z_t e^2} \tag{4.16}$$

and depends on the parameter a_L, the Lindhard screening length,

$$a_L = \left(\frac{9\pi^2}{128}\right)^{1/3} a_B \left(Z_{ion}^{2/3} + Z_{tar}^{2/3}\right)^{-1/2} \tag{4.17}$$

where a_B is the Bohr atomic radius.

When the ion impact occurs at an angle, $0 < \theta \leq \pi/2$, Y can be described by the expression

$$Y(E_0,\theta) = Y(E_0,0)\left\{\cos\left[\left(\frac{\theta}{\theta_0}\frac{\pi}{2}\right)^c\right]\right\}^{-f} \exp\left\{b\left(1 - \frac{1}{\cos\left[\left(\frac{\theta}{\theta_0}\frac{\pi}{2}\right)^c\right]}\right)\right\}. \tag{4.18}$$

It depends on the parameters b, c and f, which have also been tabulated in [9] for a variety of common scenarios.

The parameter θ_0 is calculated according to the expression

$$\theta_0 = \pi - \arccos\sqrt{\frac{1}{1+(E_0/E_{sp})}} \geq \frac{\pi}{2} \tag{4.19}$$

where E_{sp} corresponds to the surface binding energy of the impacting ions; it is equal to the surface binding energy of the projectiles in the case of self bombardment, $E_{sp} = 0$ for noble gas ions impacting on the target, and $E_{sp} \approx 1$ eV for ions of the hydrogen isotopes [48].

4.2.5. Implementation

The models described in the previous subsections were implemented as an object-oriented (OOP) toolkit in the Python programming language (version 3.9), with extensive use of routines from the NumPy and SciPy packages.

[1]See the footnote preceeding equation 3.7 in section 3.3.2.

The OOP approach enables a modular design, which allows for the substitution of a particular submodel with an alternative version. The approximate running time for the sensitivity analysis simulations presented in figures 4.9 and 4.10 is less than 5 minutes, on a PC computer having quad-core Intel Core i5-5200 CPU at 2.20 GHz, 8 GB of RAM and running the Debian GNU/Linux operating system.

4.3. Results

4.3.1. Model validation

In order to adjust the parameters in the models described in section 4.2 and to verify the accuracy of their estimations, publicly-available experimental data from a variety of suitable HPSs has been used for comparison. The chosen experimental data sets match the assumptions and configurations required by each submodel, and sufficient detail has been disclosed regarding the relevant physical and geometrical parameters of the source, enabling the use of the different mathematical expressions.

Figure 4.2 presents the estimations of n_e provided by equation 4.3 of section 4.2.1 as a function of the axial magnetic field B_0, together with experimental data published by Chen [38], Tysk et al. [110] and LaFleur et al. [65]. The parameters obtained for these three validation cases of figure 4.2 are listed in table 4.1. The chosen data sets are all helicon devices tested with argon gas, using Boswell-type double saddle antennas or half-helical antennas, which preferentially excite wavelengths of twice their lengths, $\lambda \approx 2 \times L_{ant}$. The parallel angular wave number $k_{\|}$ of equation 4.3 is then obtained as $k_{\|} = 2\pi/\lambda$. This estimation is only an approximation, and figure 4.2 shows the range of estimated density values accounting for variations in the wavelength λ of $\pm 50\%$ as suggested by Light and Chen [72]. The linear relationship between n and B_0 present in all experimental data sets is closely matched by the model estimations, particularly for the Chen and LaFleur data sets.

Table 4.1: Experimental parameters obtained for the data sets of figure 4.2, used for the validation of the simplified helicon wave dispersion model of equation 4.3.

	Chen, 1992 [38]	**Tysk, 2004** [110]	**LaFleur, 2010** [65]
Ion species	Ar^+	Ar^+	Ar^+
L_{ant} (m)	0.12	0.12	0.1
λ (m)	0.24	0.24	0.2
$k_{\|}$ (rad/m)	26.18	15.71	31.42
R (m)	0.02	0.05	0.068
f ($\times 10^6$ Hz)	27.12	13.56	13.56
ω ($\times 10^7$ rad/s)	17.04	8.52	8.52

The two separate fluid-models described in subsection 4.2.2 are compared to experimental measurements in figures 4.3 and 4.4. The chosen versions of these models are the asymptotic, magnetized regimes. For the case of the radial model [2, 3], figure 4.3 shows the normalized radial profile of the plasma density, compared to experimental data from the CSDX device published by Burin et al. [20], from the VX-CR device by Castro et al. [26] and from

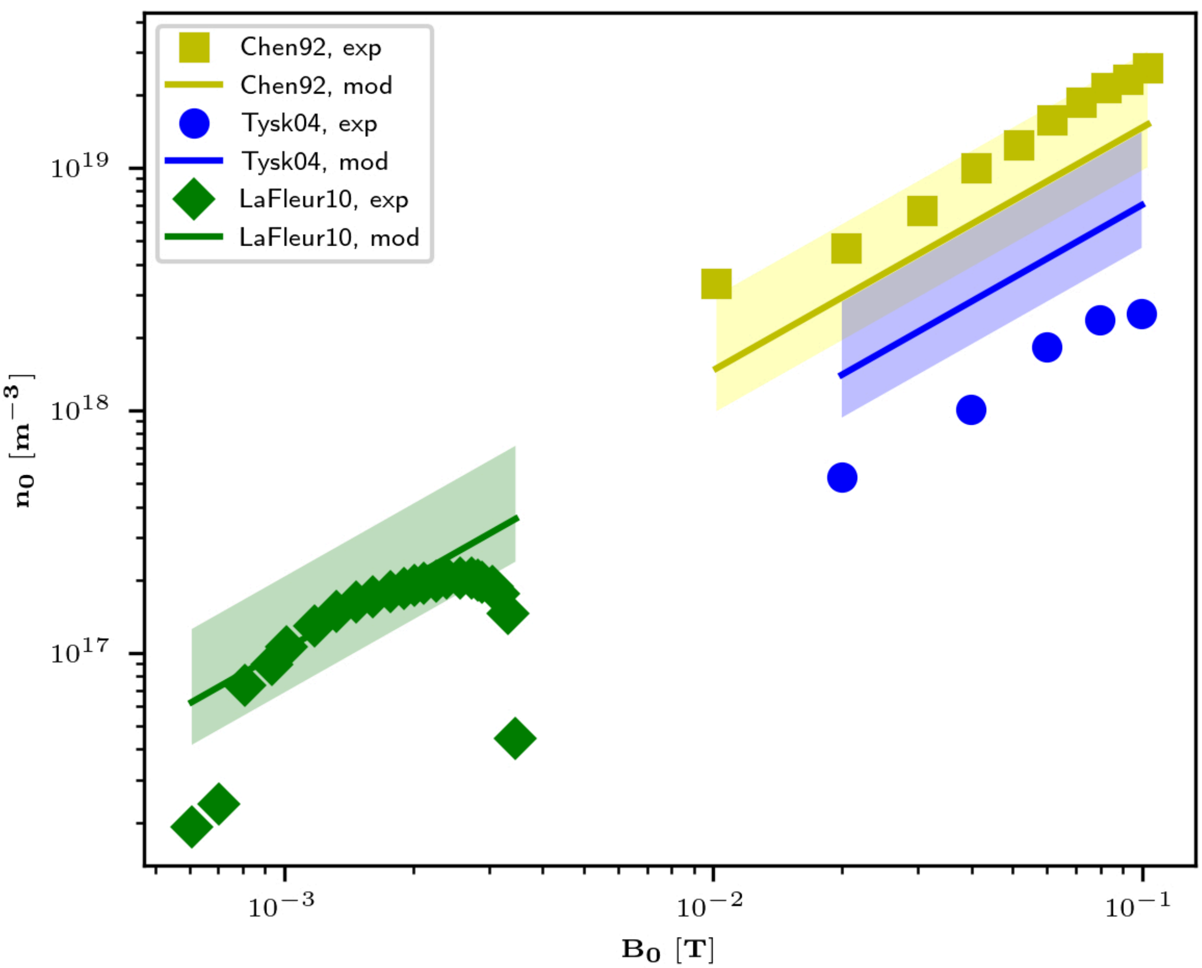

Figure 4.2: Comparison between the estimations provided by the helicon wave dispersion relation of equation 4.1 and experimental data published by Chen ([38]), Tysk et al. ([110]) and LaFleur [65]. The shaded regions correspond to variations in the estimation of n_e when considering the uncertainty in the estimation of λ, taken as $\pm 50\%$. Uncertainty data was only available for the experimental data points obtained from Tysk et al. ([110]), where the average uncertainty is $u(n_e) \approx 1.5 \times 10^{18}$ m^{-3}.

the PISCES-RF device by Thakur et al. [105, 106], from experimental runs using argon gas as the feedstock in all cases. The published experimental parameters obtained from these experimental data sets are described in table 4.2. The reference plasma density n_{r0} is obtained from the peak density value at $r = 0$. In the case of the VX-CR device, the radial coordinates of the published density values in [26] have been adjusted to account for the expansion of the magnetic field lines (and the plasma plume) as they exit the HPS towards the point of measurement. As described by the original authors, the magnetized version of this radial model describes a slow decay of the radial plasma density, which falls rapidly near the radial boundary of the HPS; the experimental data confirms this behavior, with only the VX-CR data approximating the estimated trend. For the purposes of this research, the fact that this magnetized regime of the radial model may overestimate the plasma density near the surface boundary, allows for a more conservative estimation of the boundary etch rates.

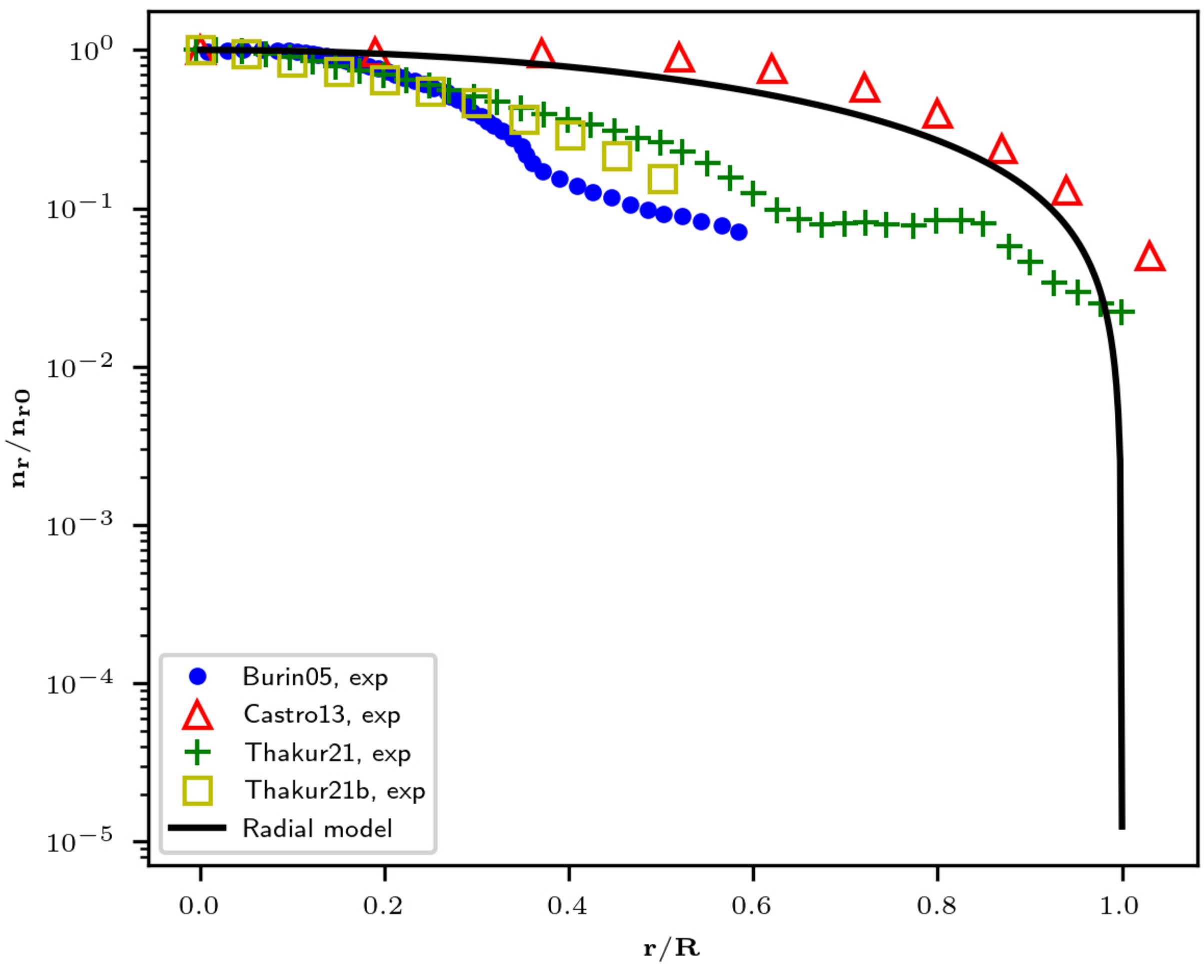

Figure 4.3: Comparison of the radial plasma density distribution estimated by Ahedo's radial model [2, 3] and experimental data published by Burin et al. [20], Castro et al. [26], and Thakur et al. [105, 106]. Uncertainty information was only available for the data sets from Burin et al. (where the uncertainty is deemed "*negligible*") and for Castro et al., where $u(n_r/n_{r0}) \approx 0.05$.

The validation of the axial model of equations 4.7 - 4.11 with experimental data is presented in figure 4.4, where

Table 4.2: Experimental parameters obtained for the validation data sets of figure 4.3, used for the validation of Ahedo's radial model in the magnetized case [2, 3], as shown in equations 4.4 - 4.6.

	Burin, 2005 [20]	**Castro, 2013** [26]	**Thakur, 2021** [106]	**Thakur, 2021b** [105]
Ion species	Ar^+	Ar^+	Ar^+	Ar^+
T_e (eV)	2.25	4.0	5.0	3.50
n_0 ($\times 10^{19}\ m^{-3}$)	2.35	0.388	2.45	1.93
R_0 (m)	0.1	0.045	0.1	0.1
B_0 (T)	0.1	0.1	0.09	0.09

the on-axis plasma density is presented as a function of the axial position inside the cylindrical dielectric containment surface. The experimental data sets are those published by Berisford et al. [11] and Takahashi et al. [101], which once again correspond to experiments running on argon gas. The source parameters used in the estimation are listed in table 4.3. It was found that the axial model was able to predict the behavior of the axial density profile, but an axial displacement $\Delta z = z_{exp} - z_{mod}$ was required to match the experimental data, where z_{exp} and z_{mod} are, respectively, the experimental axial coordinates and the ones used for the model calculations. The reference plasma density n_0 is obtained as the asymptotic on-axis density at the downstream boundary of the simulation domain (at the coordinate $z = 0$ following the convention of [3]). At this location, the Bohm criterion ($u_{z=0} = c_s$) is imposed as a boundary condition, setting the auxiliary variable $\xi = \pi/4$ according to equation 4.8. As the optimization process described for equation 4.11 when $z = 0$ converges to values $\eta_u \to 1$ for these two configurations (complete propellant utilization) equation 4.9 will tend towards a maximum value of 2 for the ratio n/n_0, which corresponds to the peak on-axis density and can be verified in the experimental data sets.

Table 4.3: Experimental parameters obtained for the data sets used in figure 4.4, for the validation of Ahedo's axial model in the asymptotic case [3].

	Berisford, 2010 [11]	**Takahashi, 2017** [101]
Ion species	Ar^+	Ar^+
L (m)	0.4	0.2
Δz (m)	-0.1	0.2
T_e (eV)	3.8	6.0
B_0 (T)	0.06	0.03
n_0 (m^{-3})	1.0×10^{19}	8.0×10^{17}

The sputtering model from [48] is compared to experimental data in figure 4.5, for the particular case of argon ions impacting SiO_2 [71, 81, 112, 117], Al_2O_3 [71, 81] and Si_3N_4 [117] target materials. The sputtering yield is presented as a function of incident ion energy. These materials were chosen as they are some of the most widely used in the construction of practical HPSs, including the VX-CR device analyzed in the next subsection. Eckstein's model, as described by equations 4.14 - 4.18, is designed to model the interaction between elemental ions and surface materials. The fitting parameters available in the literature for these equations [9] only account for this type of target materials. Therefore, some of the required parameters were obtained by averaging the values of the consti-

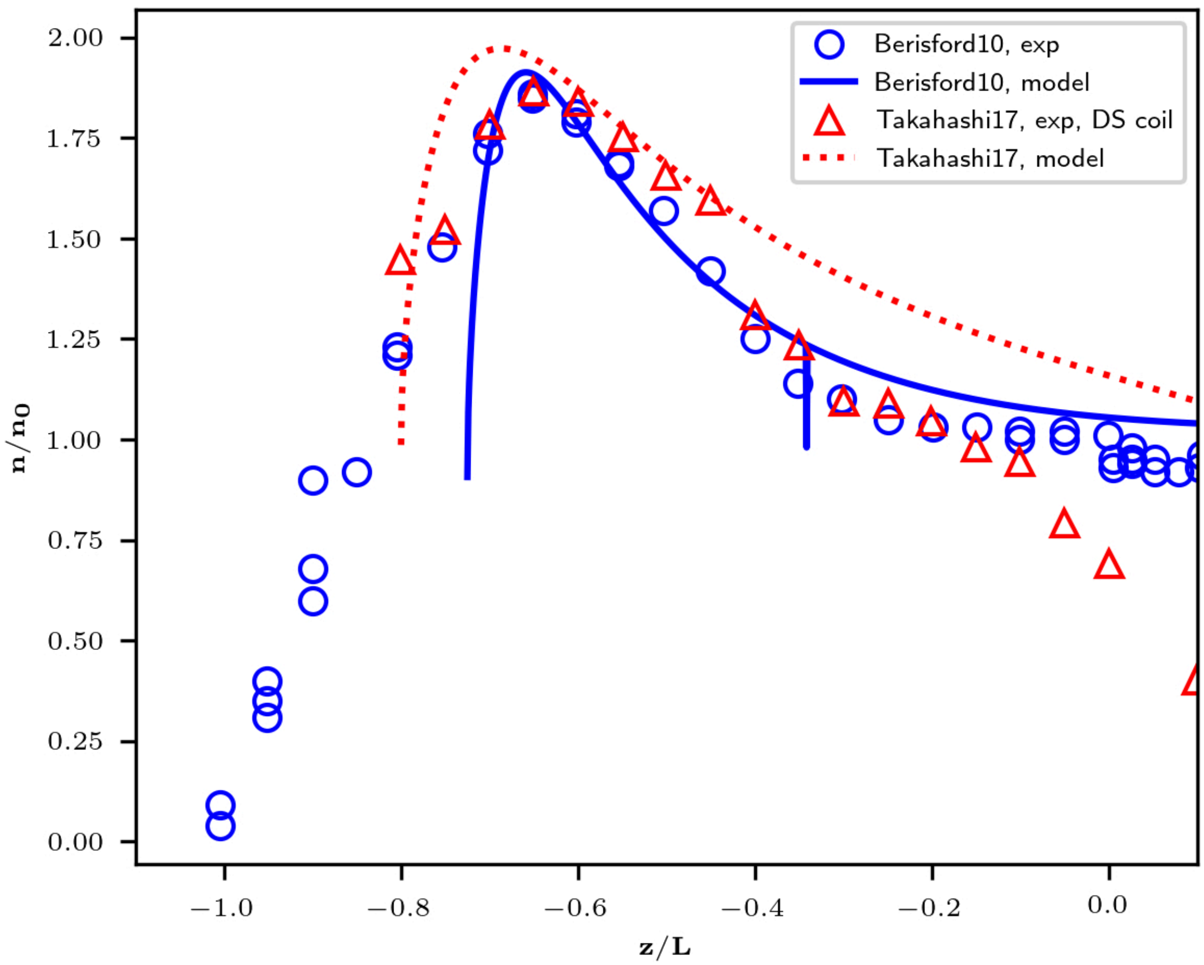

Figure 4.4: Comparison of the distribution of the on-axis plasma density as estimated by Ahedo's axial model [3] and experimental data published by Berisford et al. [11] and Takahashi et al. [101]. Uncertainty data was not available for these data sets.

tuting elements of the compound materials, following a technique originally proposed by Berisford et al. [11] when applying the particular sputtering model presented in [71]. Table 4.4 lists the parameters chosen to represent these compound materials. The atomic number Z_t, the atomic mass m_t and the surface binding energy SBE_t for each compound target material were found as a simple arithmetic average between the values corresponding to the two constituent elements in the lattice. SBE data was obtained from [71]. The threshold energy, a key parameter in the analysis of low-temperature devices such as typical laboratory HPSs, was selected as the corresponding value for argon atoms in normal incidence on pure Si in the case of SiO_2 and Si_3N_4, and that of pure Al for the case of Al_2O_3 [9]. The remaining fitting parameters λ, q and μ were obtained through a least-squares optimization algorithm.

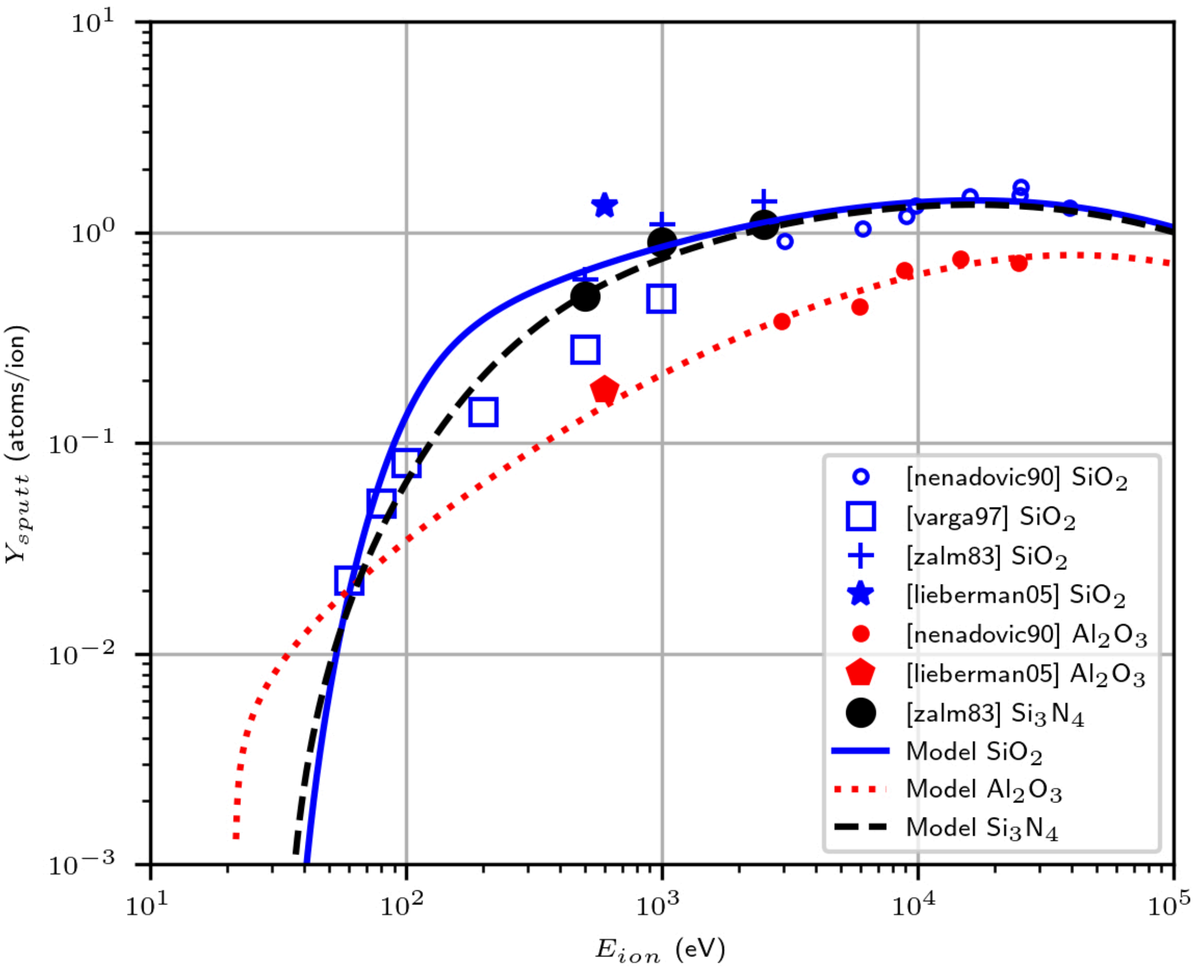

Figure 4.5: Estimation of the sputtering yield at normal incidence for argon ions impacting on different dielectric ceramic materials commonly used in HPSs, obtained from the model presented in subsection 4.2.4. The fitting parameters used are those described in table 4.4. The estimations are compared to the available experimental data points published for SiO_2 [71, 81, 112, 117], Al_2O_3 [71, 81] and Si_3N4 [117]. Uncertainty data was only available for the data sets obtained from Zalm et al. ([117]) where the average uncertainty is given as $\pm 10\,\%$, and for Varga et al. ([112]), where the average uncertainty is $u(Y_{sputt}) \approx 0.1$ atoms/ion.

Table 4.4: Fitting parameters chosen to represent SiO_2, Al_2O_3 and Si_3N_4 within the sputtering estimation models presented in figure 4.5. The values for the material properties and the fitting parameters were obtained through a combination of averaging and optimization techniques, as described in subsection 4.3.1.

	SiO_2	Al_2O_3	Si_3N_4
Z_t	11.0	10.5	10.5
m_t (amu)	22.042	21.485	21.045
SBE$_t$ (eV)	3.653	3.36	4.811
E_{thr} (eV)	32.8380	21.55	32.838
ρ (kg/m^3)	2648	3987	3170
λ	7.417	14.553	10.0
q	3.636	3.373	3.4777
μ	2.339	0.397	1.363

4.3.2. Analysis and investigation of the VX-CR HPS

The VX-CR experiment [26, 45] is a research helicon plasma source (HPS) located at Ad Astra Rocket Company Costa Rica, designed for the study of thermal management and component lifetime issues in the first stage of the VASIMR® [28] engine. Figure 4.6 (a) shows a simplified diagram of its operating configuration. It consists of a dielectric ceramic cylinder enclosed in a high vacuum chamber with a base pressure of 1.3×10^{-4} Pa. One end of this cylinder is sealed with a dielectric ceramic endcap, with openings to allow the injection of gas into the HPS. This cylinder is surrounded by a half-wavelength helical copper antenna, driven by an external RF subsystem able to deliver up to 13 kW$_e$ of radiofrequency energy to the plasma discharge. The open end of the dielectric cylinder is connected to a 14 m^3 exhaust vacuum chamber (not shown in figure 4.6), with a baseline pressure of 1.3×10^{-1} Pa. An axial magnetic field is created through two solenoid coils, with the resulting magnetic field intensity profile depicted in figure 4.6 (b). The dielectric boundary surfaces in the VX-CR are at a floating electric potential; this is not always the case for all HPSs, as these elements can be grounded ([11]) or biased to a particular voltage. Argon is the feedstock gas used in typical operations with the VX-CR and was used in the simulated results described in this subsection.

The models described in section 4.2 and validated in subsection 4.3.1 were used to estimate the erosion rates due to plasma-material interaction in the VX-CR device. Table 4.5 shows typical geometrical and operational parameters characteristic of experimental runs at the VX-CR device, at RF power levels between 1 kW$_e$ and 4 kW$_e$ and using argon gas. The three ceramic materials which have been used for the dielectric components of the device (the cylinder and its boundary endcap) are silicon dioxide (SiO_2), alumina (Al_2O_3) and silicon nitride (Si_3N_4). Figure 4.7*a* presents experimental measurements of the peak RF voltages at the helicon antenna straps as a function of the delivered RF forward power to the system; figure 4.7*b* (adapted from [26]) describes estimations of the electron temperature T_e obtained from Langmuir probe data, also as a function of RF forward power.

Figure 4.8 shows the distribution of normalized plasma density inside the VX-CR HPS, as predicted by the models described in subsection 4.2.2 for the scenario with $T_e = 5$ eV. A base density of $n_0 \approx 4.04 \times 10^{18}$ m^{-3} is predicted. The maximum estimated plasma density corresponds to $n_{\max} \approx 8.19 \times 10^{18}$ m^{-3}, while the mean

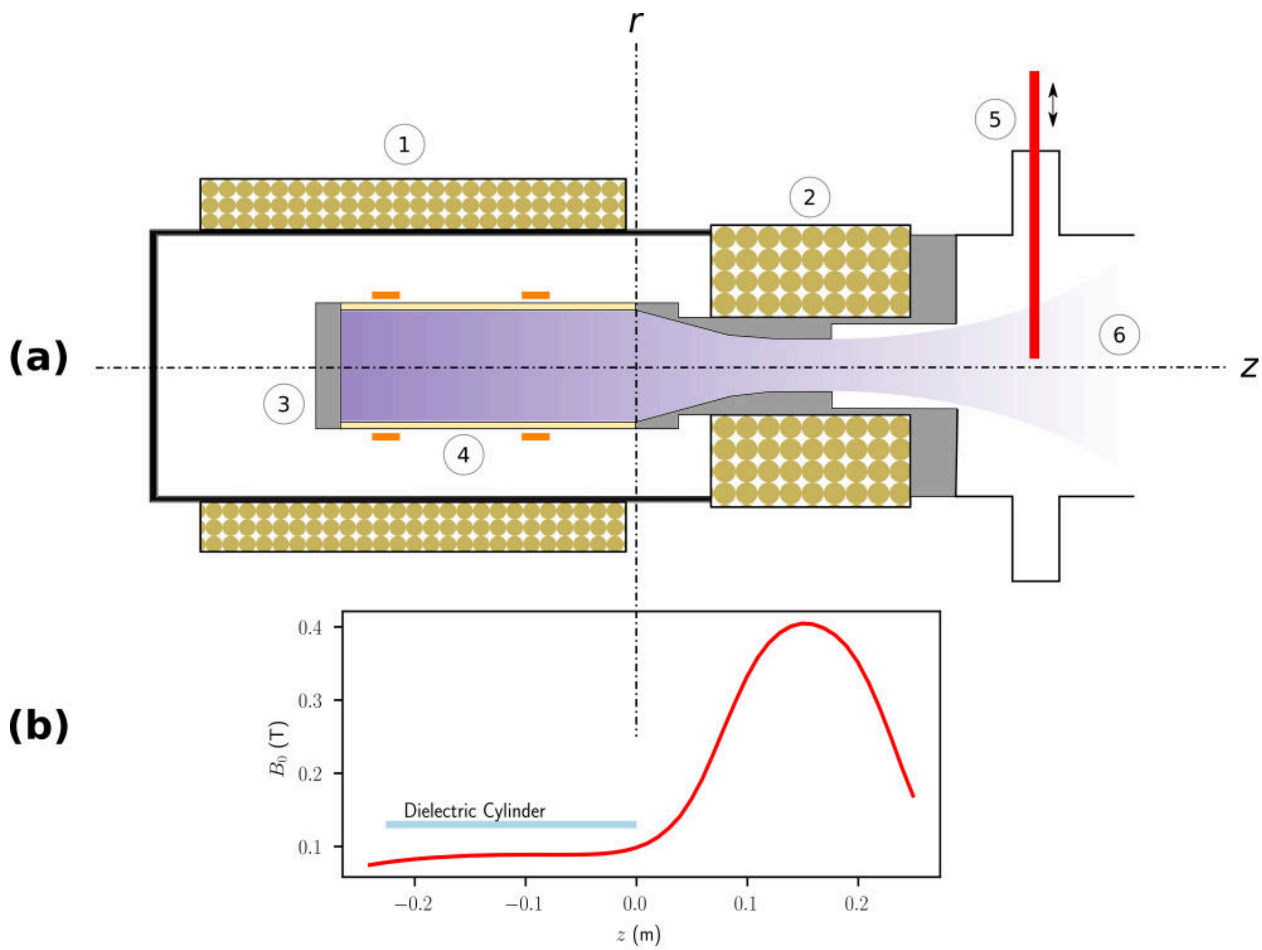

Figure 4.6: **(a)** Diagram of the VX-CR research helicon device. The axial magnetic field is produced through two solenoid coils, *1* in the HPS region and *2* located downstream of the source. The HPS itself is located inside a high-vacuum chamber to prevent arcing from the voltages present in the RF subsystem. *3* represents the upstream dielectric boundary of the source and this is the point where gas injection occurs (not shown). *4* represents the dielectric cylindrical boundary of the HPS, as well as the approximate location of the helicon antenna straps. *5* marks the location of a reciprocating Langmuir probe used to obtain ion current density and plasma density readings. *6* describes the downstream section of the HPS, interfaced to a vacuum chamber and a pumping system (not shown). **(b)** Experimental measurements of the magnetic field intensity B_0 at the HPS axis as a function of the z axial position. The coordinate system has its origin at the exit boundary of the HPS dielectric cylindrical boundary, following the convention established in section 4.2.2. Measurement uncertainties for the values of B_0 are less or equal than $0.0008\ T$.

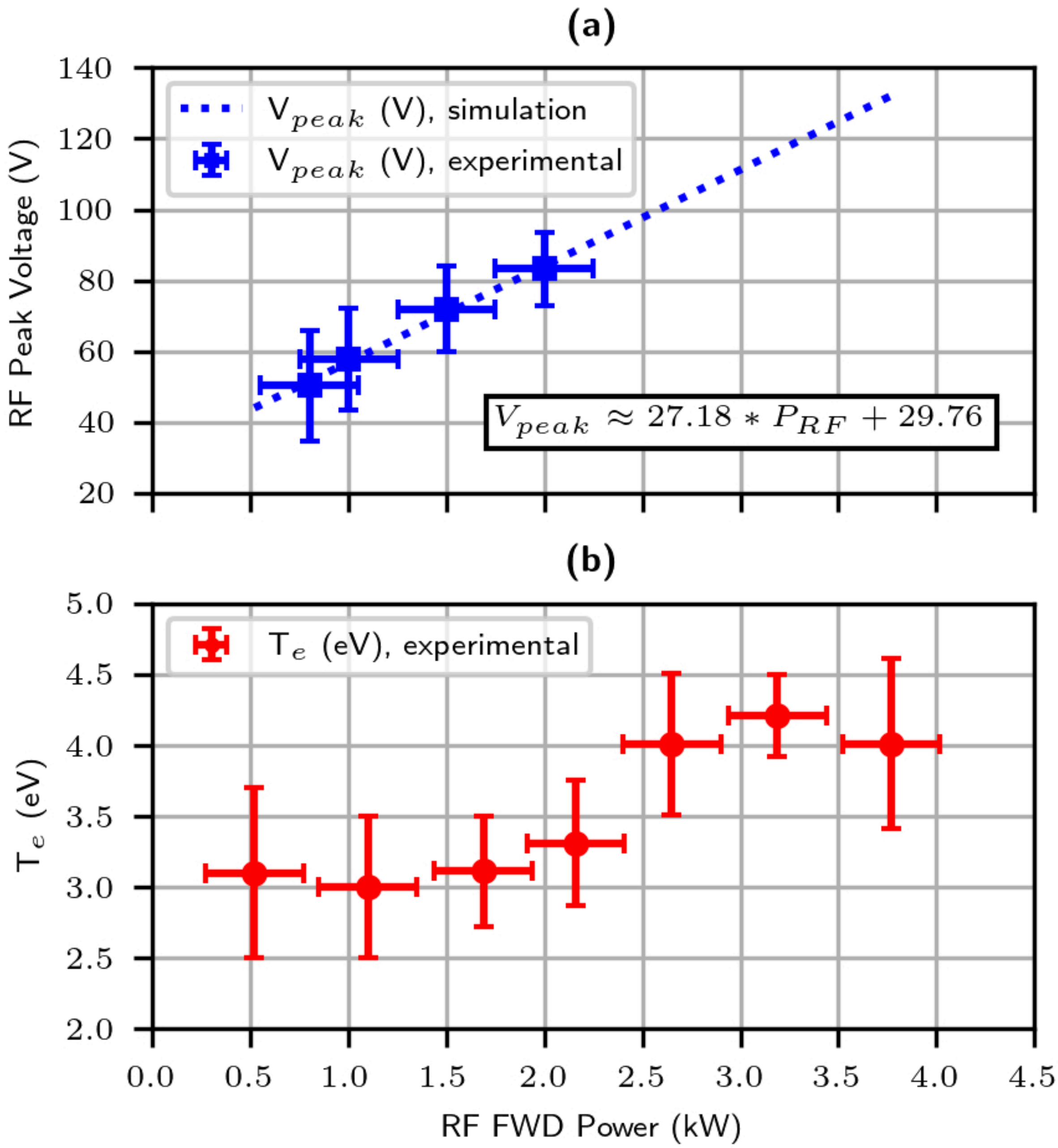

Figure 4.7: Experimental data obtained from the typical operation configuration of the VX-CR helicon plasma source, adapted from [26]. **(a)** shows the measurements of the peak voltage V_p in the VX-CR helicon antenna, measured at the external RF feed line, as a function of the measured RF forward power coupled into the system. A linear regression has been calculated for these data points, with the resulting expression shown in the plot. **(b)** shows the estimated values for the electron temperature T_e as a function of RF forward power, obtained from measurements with the reciprocating Langmuir probe. Experimental techniques and measurement uncertainties for these data points have been described in [26].

Table 4.5: Geometrical and physical parameters used for the simulation results of the VX-CR device presented in subsection 4.3.2. The values of T_e and $V_{\text{max,RF}}$ correspond to three separate scenarios, and were obtained from the regression described in figure 4.7.

Parameter	**Value**
R (m)	0.045
L (m)	0.226
B_0 (T)	0.1
T_e (eV)	$3.0, 5.0, 10.0$
$\dot{m}$ (kg/s)	1.785×10^{-3}
n_{n0} (m^{-3})	1.5×10^{20}
Δr (m)	9×10^{-5}
Δz (m)	2.26×10^{-4}
f_{RF} (Hz)	13.56×10^6
$V_{\text{max,RF}}$ (V)	$111.30, 165.66, 301.56$
Ion species	Ar^+
Dielectric materials	SiO_2, Al_2O_3, Si_3N_4

plasma density is $n_{\text{avg}} \approx 3.04 \times 10^{18}\ \text{m}^{-3}$.

The estimated plasma density values shown in figure 4.8 were used to obtain the approximate values along the upstream axial ($\hat{z} \to -1$) and radial ($\hat{r} \to 1$) boundaries of the dielectric cylinder. The radial and axial resolutions used in this particular simulation, Δr and Δz, are shown in table 4.5; although they exceed the Debye lengths present in both simulation boundaries, the density values obtained along these regions, $n_{\hat{z}\to-1} = n_r[\hat{r}, \hat{z} = -1 + (\Delta z/L)]$ and $n_{\hat{r}\to 1} = n_r[\hat{r} = 1 - (\Delta r/R), \hat{z}]$, have been used as reference values for the plasma density at these inner surfaces.

These density estimations along the radial and axial boundaries were used to calculate the etch rates along these surfaces due to the potential created at the wall by the sheath. The electron temperature T_e was used as an input to equation 4.12 in order to estimate the potential developed by the inner surfaces, under the assumption that they are floating (isolated from any induced voltages, as is the case in the VX-CR device). Under the cold ion approximation, this potential is taken as the energy obtained by the ions as they traverse the sheath. The sputtering yield was calculated for the case of normal incidence (equation 4.14) along the axial and radial boundaries. The etch rate E, defined as the ratio of surface etch depth per unit of time, was calculated through the expression

$$E = \frac{\Gamma_i Y M_m}{\rho_t N_A} \tag{4.20}$$

where $\Gamma_i = n_b u_B$ is the incident ion flux (with n_b the plasma density along the boundary), M_m and ρ_t are the molar mass and mass density of the surface material and N_A is Avogadro's constant.

The results of the etch rate calculations are shown in figure 4.9, where etch rate estimations are presented for the axial boundary (plots a, b, c) and the radial boundary (plots d, e, f). Results are shown for the three different dielectric materials previously analyzed (SiO_2, Al_2O_3 and Si_3N_4), and three chosen values of the electron tempera-

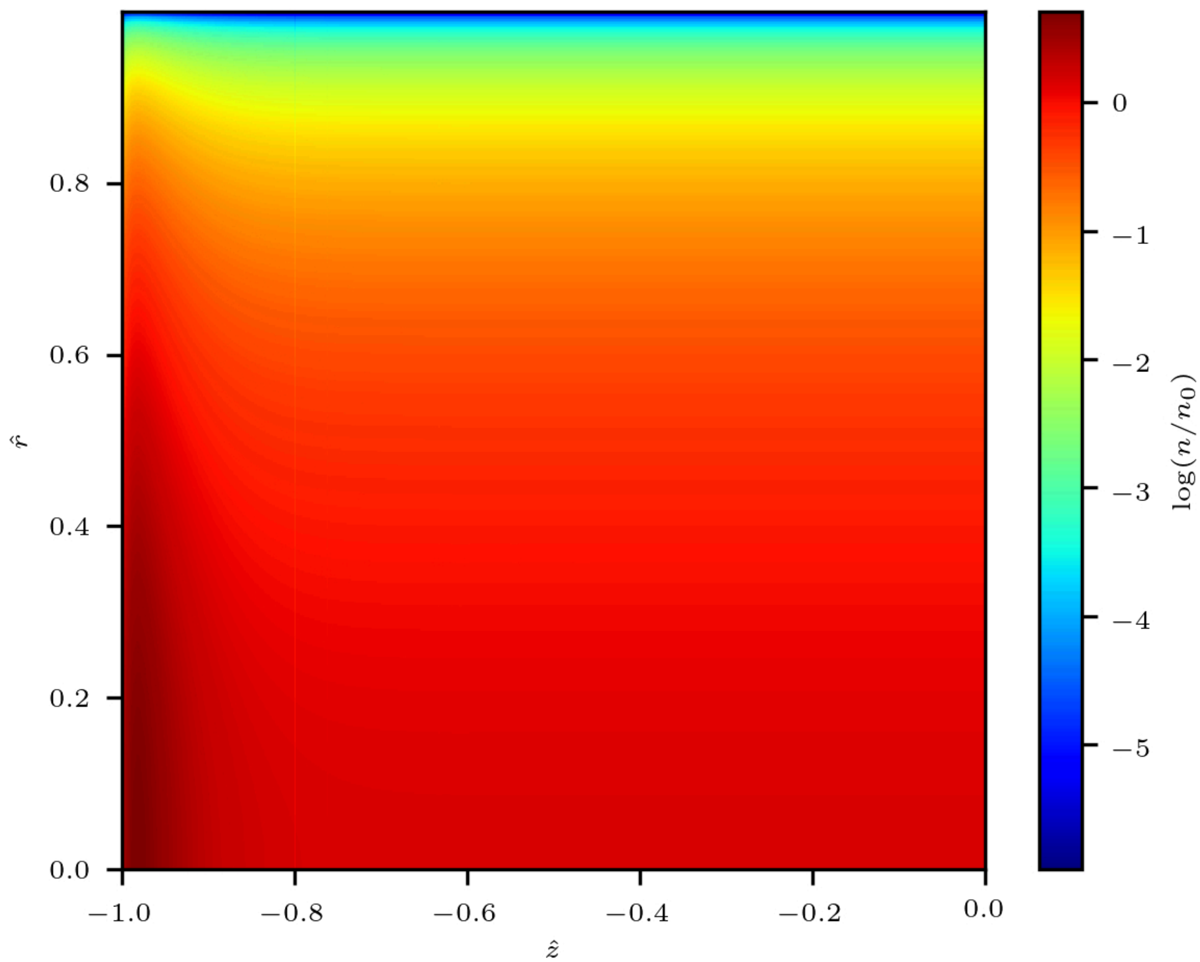

Figure 4.8: Estimated plasma density distribution in the VX-CR device [26, 45], as estimated by Ahedo's model [2, 3]. The relevant geometrical and physical parameters used for this simulation are listed in table 4.5. The reference plasma density n_0 is calculated as the ratio of the axial flow rate of heavy species per unit area g_0 and the ion Bohm velocity, $n_0 = g_0/c_s$, and has a value of $n_0 \approx 4.04 \times 10^{18}$ m^{-3} in this particular simulation.

ture. Since the simulation provides the ions with an energy equal to the floating potential obtained by the dielectric walls, the results depend on both T_e and the threshold energy for sputtering E_{thr} in each case. Figure 4.5 had shown that Al_2O_3 has a lower threshold energy than SiO_2 and Si_3N_4 according to the sputtering model, and that is the reason why the cases simulating silicon dioxide and silicon nitride present etching only at the higher values of the electron temperature, corresponding to the only scenarios where the wall floating potential produced by the plasma sheath is larger than E_{thr}. For the scenarios involving aluminum nitride, no sputtering occurs for the cases with $T_e = 3.0$ eV.

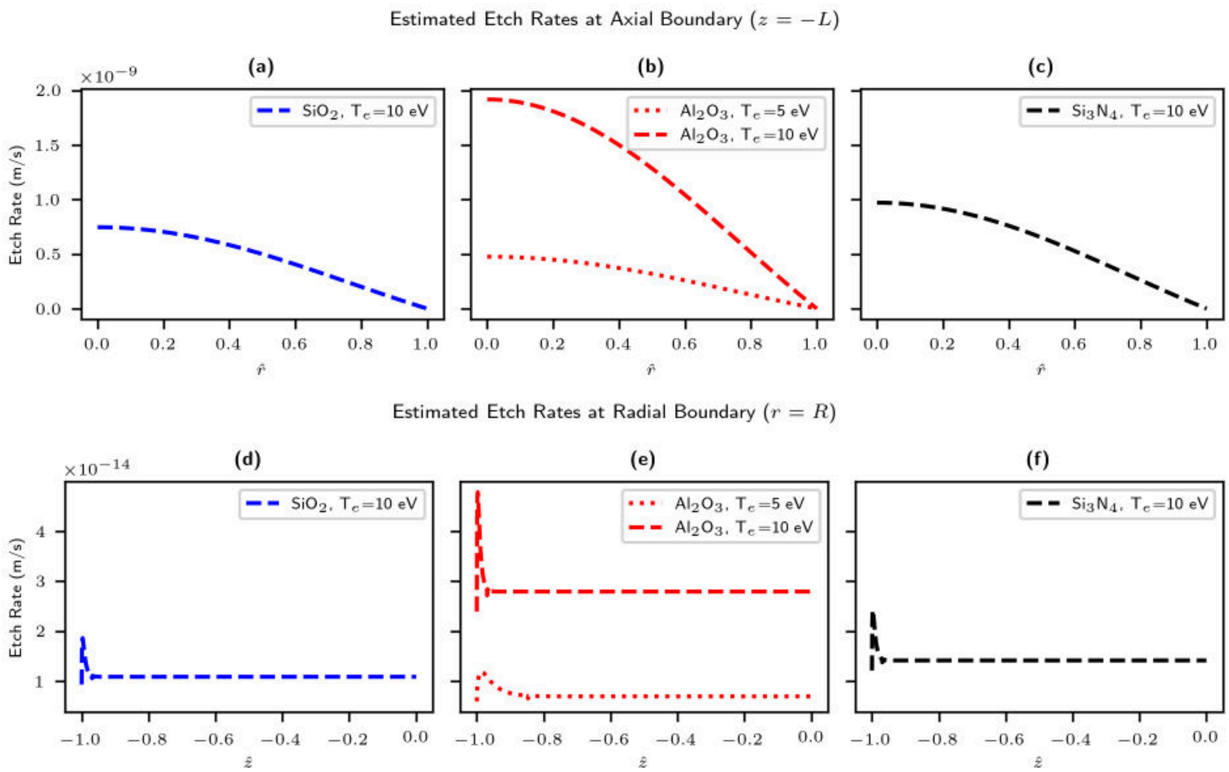

Figure 4.9: Estimated etch rates at the inner surfaces of the boundary dielectric containment material in the VX-CR device, as obtained through the combination of the density distribution, sheath and sputtering models described in section 4.2. The etch rates for the axial ($z = -L$) boundary, the endplate located at the upstream end of the dielectric cylinder, are presented in the top row in plots **(a)**, **(b)** and **(c)**; the corresponding etch rates for the radial ($r = R$) boundary, the inner surface of the dielectric cylinder, are presented in the bottom row in plots **(d)**, **(e)** and **(f)**. Estimations are presented for three different dielectric ceramic materials (SiO_2, Al_2O_3 and Si_3N_4) and three reference values for the electron temperature T_e. Plots are shown only for those scenarios where the ion energies surpass the corresponding threshold energy for sputtering, $E_0 \geq E_{thr}$.

The low-frequency RF sheath model from [71], presented in subsection 4.2.3, can be used to estimate the etch rate produced in certain regions of the radial boundary of the dielectric cylinder due to the vicinity of the helicon antenna straps. Table 4.5 presents the frequency f and peak voltage $V_{\mathrm{max,RF}}$ present in the helicon antenna straps of the VX-CR device. Using equation 4.13 and assuming that the voltages present in the copper terminals of the antenna are directly induced in the nearby inner surfaces of the dielectric cylinder of the HPS (as suggested by the results presented by [7, 11]), the incident ion energy distribution can be calculated. Once again using the cold ion approximation and assuming the ions are accelerated at normal incident only by the RF sheath voltage, the mean sputtering yield $\overline{Y}$ due to the low-frequency RF sheath can be obtained as a function of the axial position along the inner surface of the dielectric cylinder through the expression

$$\overline{Y}(\hat{r}=1,\hat{z}) = \int_0^{V_{\max,\mathrm{RF}}} Y(E) \cdot g_i(E,\hat{z}) \cdot dE. \tag{4.21}$$

The average value of the sputtering yield, $\overline{Y}$ can then be used within equation 4.20 to estimate the etch rate at any potential axial location of the helicon antenna straps along the radial boundary. The results are presented in figure 4.10 for the same three candidate materials and T_e values as in figure 4.9, where estimations are depicted for the etch rate along the entire radial boundary. Given the higher voltages induced by the RF subsystem in the helicon antenna, erosion is present in all configurations. These results are once again dependent on the sputtering threshold energy and the electron temperature. They are also a function of the voltages produced in the RF subsystem, which is an element external to the HPS and may differ between different practical implementations.

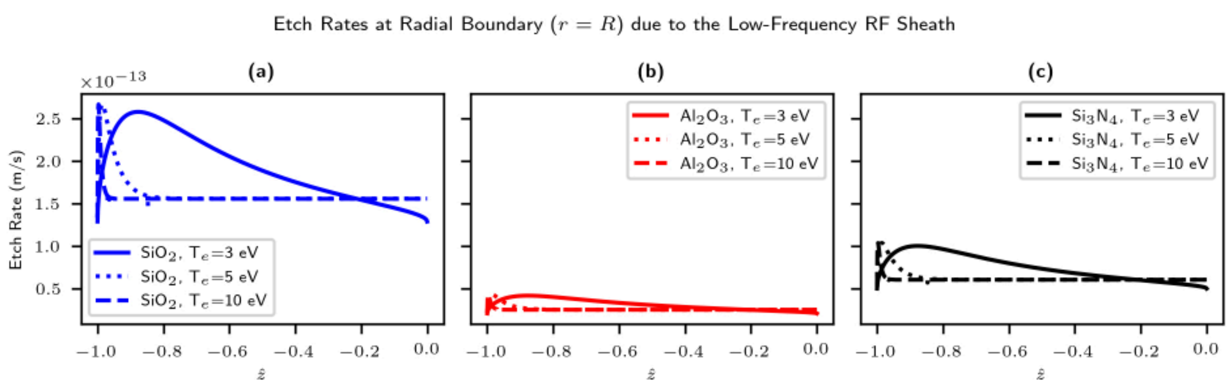

Figure 4.10: Estimation of the etch rate at the radial boundary $r = R$, the inner surface of the dielectric cylinder, due to the low-frequency RF sheath induced by the vicinity of the straps of the helicon antenna, using a method derived from the approach by Berisford et al. [11]. These plots represent the estimated etch rates for all possible locations of these external sources of RF excitation; actual devices typically have these antenna conductors at specific particular locations. Results are presented for three different candidate materials (SiO_2, Al_2O_3 and Si_3N_4), and three values of the electron temperature T_e.

4.4. Discussion

4.4.1. Practical estimation of erosion within HPSs

The analysis of sputtering and erosion phenomena within HPSs is dependent on understanding the behavior of key properties of the plasma throughout the source and particularly in the vicinity of the physical boundary surfaces of interest, with density and temperature being the most relevant parameters. Published experimental results identify two main modes of plasma-material interaction relevant to the estimation of erosion rates in the plasma-facing components of HPSs, which were shown in figure 4.1b. Region *(1)* in the figure describes the acceleration of ions towards the boundary surfaces due to the potential obtained by the floating wall due to the formation of the sheath; the ions will obtain the energy difference between the plasma potential and the wall potential, $\Delta\phi_{p-w} = \phi_p - \phi_w$. When using the cold ion approximation, $|\phi_p| \ll |\phi_w|$ is often assumed. This DC sheath is present along all plasma-facing boundary surfaces. Region (2) in the diagram describes the interaction between the ions and the RF sheath produced by the oscillation voltages induced in the vicinity of the location of the helicon antenna straps, dependent on the operation of the RF subsystem external to the HPS. This particular type of sheath, present at specific discrete locations along the radial ($r \to R$) boundary surface, is able to induce potentials ϕ_{RF} at the wall typically much larger than those produced by the DC sheath. Practical implementations of HPS commonly rely on RF generators operating in the high-frequency band (6.78 MHz, 13.56 MHz and other typical commercial frequencies), which enable the use of the low-frequency sheath model described in section 4.2.3 when the proper conditions are met.

The plasma density profile along the inner surfaces of the dielectric boundaries of a HPS has a direct influence on the magnitude of the rate of erosion throughout these regions, since the incident ion flow rate Γ_i is directly proportional to n_b. In the present approach, the distribution of plasma density has been obtained through the use of the uncoupled models of subsection 4.2.2 for cylindrical geometries, which correspond to the asymptotic limit of the models presented by Ahedo et al. [3]. The radial model (equations 4.4 - 4.6) produces the classical diffusion profile based on the zero-order Bessel function. Figure 4.3 shows how the simulated profile tends to overestimate the radial density value as $r \to R$ when compared to experimental data, which will produce conservative values of the ion flow rate towards the surface.

The axial model of equations 4.7 - 4.11 describes the axial distribution of plasma density along the central axis of the cylindrical geometry, as a function of the reference density $n_0 = g_0/c_s$ obtained from the axial flow rate of ions and/or neutrals $g_0 = \dot{m}/(m_i \pi R^2)$ and the Bohm velocity c_s. The axial density profile is dependent on the auxiliary coordinate ξ and the parameter $\eta_u = (n_{z=0}/n_0)$, which corresponds to the propellant utilization factor in electric propulsion applications. The mapping $\xi(z)$ to the physical dimension is obtained by analyzing equation 4.11 at the downstream boundary $z = 0$. The density distribution, provided by equation 4.9, presents a maximum value determined by the location of $\xi = 0$ and located towards the upstream boundary of the simulation domain. The axial spread of this density distribution is dependent on the parameter $L_\star$ appearing in equation 4.11. This parameter is inversely proportional to the ionization rate R_{ion}, which is a function of T_e; this rate and the collisional ones R_{ie}, R_{in} and R_{en} can be calculated following the formulas provided by [3].

The combination of the models discussed in section 4.2 allows for a computationally-inexpensive approximation to sputtering and erosion phenomena within HPSs, as they use uncoupled steady-state fluid expressions for the axial and radial distribution. These are then combined to produce a complete 2D map of the density distribution such as the one in figure 4.8. The density decay described by the radial model is combined with the density distribution profile along the cylinder axis provided by the axial model. The values at the cylinder boundaries can then be extracted and used as inputs to the sheath models of subsection 4.2.3, in order to estimate the energy obtained by the ions as they impact the wall. The sputtering models are then used to predict the sputtering yields and corresponding etch rates.

Figures 4.9 and 4.10 show how the estimated etch rates for the VX-CR device at the axial boundary (the upstream endplate at $z \to -L$) are about four orders of magnitude larger than the ones produced at the radial boundary for either the DC sheath scenario (plots d, e and f of figure 4.9) or the low-frequency RF sheath estimation (figure 4.10). This is a product of the larger density values present along that boundary surface, which is impacted along the whole range of the radial coordinate $0 < r < R$ at the axial location $z = -L$. For the case of the radial boundary ($r \to R$, the inner surface of the dielectric cylinder), the etching produced by the DC sheath potential (figure 4.9 d, e, f) is smaller than that produced by the voltages induced by the low-frequency RF sheath (figure 4.10). This depends on the particular electrical configuration of the external RF subsystem. In the case of the VX-CR, the RF subsystem is designed to operate at high current levels in order to reduce the voltage magnitude in the RF feed lines. Nevertheless, the average voltages during the negative part of the sinusoidal RF cycle weighted according to the distribution function described in equation 4.13 are larger than those produced by the sheath at the floating walls. For the case of helicon systems with grounded boundary surfaces, the energy of the ions reaching the wall would depend on the magnitude of the plasma potential ϕ_p and the ion energy distribution function within the plasma, and it is even less likely that the acceleration through the sheath can produce any etching as previously described by Berisford et al. [11].

4.4.2. Model limitations and potential improvements

The accuracy of the etch rate estimations provided by the model are conditioned by the validity of its assumptions. The simple magnetic field configuration of figure 4.1, with a constant axial B_0, is not the case for most practical HPS implementations. Devices with discrete solenoid cells might present a cusped profile, while other devices might include regions of higher intensity, mirror configurations and other scenarios. When the magnetic field lines intersect directly with the boundary surfaces, regions of direct impingement will produce localized spots of energy deposition and erosion [7, 8]. Since the radial model chosen is an asymptotic approximation for the magnetized regime, the radial density profile is not dependent on the magnetic field intensity and does not capture the effect of modifying B_0 on the radial ion diffusion.

The electron temperature T_e is assumed constant, and is an input parameter to both models. It plays a key role in defining the collisional rates and the sheath potentials. A constant T_e results from the steady-state condition of the discharge and sufficient electron confinement ([2]). This value of T_e can be estimated from global input and output parameters of the HPS, such as the total power coupled through the RF subsystem and the particle flow rate through the system boundaries, by using a power balance model (such as the ones described in [3, 67, 113]). This would also enable the use of engineering models of the external RF subsystem for the calculation of the voltages present at the helicon antenna terminals as a function of the coupled RF power. These values could then be used as inputs to the RF sheath models for the estimation of sputtering and etching in the locations near the antenna straps.

The condition of constant axial B_0 is rarely accomplished in practical helicon devices with a cylindrical geometry, either because the magnetic field is not produced through a single magnetic cell or due to the deliberate configuration of variable magnetic field intensities with the purpose of producing mirror effects or modifying the performance of the source. If the field lines diverge and intersect the inner surface of the dielectric cylinder, the kinetic energy of the ions along the direction parallel to the field lines is compounded with the acceleration due to the sheath potentials, and significant etching may occur at the impact points ([22]). A variable B_0 will also produce magnetic field lines which are not parallel to the dielectric cylinder axis at regions near the inner boundary surfaces, and the use of sheath models considering oblique magnetic fields [79] might be necessary.

The presence of a non-parallel magnetic field also contributes to the ions having an impact angle different than normal incidence, requiring the use of the angular sputtering formulas described in section 4.2.4 instead of the simpler normal-incidence scenarios used in figures 4.9 and 4.10. Another aspect of the sputtering models that needs further research is the lack of accurate experimental data, and therefore the corresponding fitting parameters required by the sputtering expressions, for dielectric ceramic compounds at the low energy ranges typical of HPSs. Parameters such as the threshold energy E_{thr} play a critical role in the estimation of etching rates, yet most of the available data and models such as the ones in subsection 4.2.4 have been developed in scenarios where ions impact monoatomic targets. The present approach averaged several parameters of equations 4.14-4.16 between the values corresponding to the constituting elements of the dielectric compounds; however the values for the threshold energy E_{thr} were obtained from those corresponding to argon ions impacting monoatomic silicon and aluminum, which resulted in the best correlations with published experimental sputtering data.

4.5. Conclusion

The development and validation of a set of modeling tools designed for the investigation of sputtering and erosion phenomena within the plasma-facing surfaces of a helicon plasma source (HPS) has been presented. It is based on the combination of a 2D fluid-based model for the distribution of plasma density within the HPS (based on the work of Ahedo et al. [3]), sheath models for the estimation of the wall potential in the case of floating surfaces and low-frequency RF fields ([71]), and a sputtering model based on the work of Eckstein et al. [48]. Relying on the use of steady-state analytical expressions derived from first-principles approximations or empirical models, it aims to provide computationally-inexpensive estimations of the etch rates along the inner boundary surfaces of a HPS. This information is critical for applications of HPSs where long operational times are desired, such as electric propulsion engines or high-power sources for the research of fusion-relevant plasma-material interactions.

The individual components of the model have been validated against published experimental data, centering on the case of argon discharges in sources using silicon dioxide, alumina and silicon nitride components as boundary surfaces. Since the chosen sputtering model was not developed to simulate compound materials, average values were used for the properties of the target material atoms, and the fitting parameters in the model were obtained through an optimization algorithm. The threshold energy for sputtering was selected as that of argon atoms impacting monoatomic silicon or aluminum. This approach yielded the best correlation with published data. This strategy can be adapted to other ion species and target materials, and represents an improvement of previously published techniques using empirical analytical models for the analysis of sputtering on dielectric compound materials such as the approach described in [11]. The subsequent analysis showed how the threshold energy for sputtering E_{thr} is a critical parameter for the analysis of etching within low-temperature devices such as HPSs.

Estimations of the etch rates due to particle sputtering were obtained for the VX-CR helicon plasma source, as a representative device conforming to the model's assumptions. The highest expected values were found at the upstream boundary, the circular endcap surface, where etch rates between 0.5 and 2.0 nm/s were obtained due to the acceleration of ions through the sheath at the axial upstream boundary. For the radial boundary (the inner plasma-facing surface of the dielectric cylinder), these values ranged between 0.5 and 5.0 $\times 10^{-14}$ m/s. Along this same boundary surface, etch rates produced by the low-frequency RF sheath acceleration are one order of magnitude higher, with averages between 0.25 and 2.5 $\times 10^{-13}$ m/s. These results confirm previous findings pointing towards the relevance of the voltages induced by the RF sheath under the antenna straps; but also point towards the importance of controlling the plasma density values in the regions near the upstream axial boundary of the system.

The model presented in this study can potentially be used to guide the physics and engineering design of more robust helicon sources with longer operational lifetime. A discussion is also presented regarding the limitations and possible improvements of this modeling approach, including the estimation of electron temperature from the power balance in the system, the consideration of variable magnetic field intensities and more refined sputtering models for the compounds of interest.

Chapter 5

Assessment and mitigation of plasma-surface effects in high-power helicon plasmas

5.1. Chapter Introduction

The study of plasma-surface interactions as the cause of unwanted erosion phenomena has been actively researched for fusion devices, electric propulsion engines and other applications of plasma physics. In the case of fusion reactors such as tokamaks and stellerators, regions around the edge of their high-temperature plasmas impinge directly on boundary material surfaces where the open magnetic flux surfaces (the so-called "scrape-off layer" or SOL) intersect the containment wall. These sections, defined as divertors in typical tokamaks, play a key role in achieving a stable fusion reaction as well as in extracting the reactor's thermal energy for practical engineering purposes [39]. The phenomena that take place in these sections still pose great challenges for the development of practical fusion reactors, such as large thermal loads on the plasma-facing surfaces and high rates of sputtering and other types of plasma-material interactions [74, 85].

In the field of electric space propulsion, erosion has been actively studied for two of the most commonly-used technologies: ion thrusters and Hall-effect thrusters (HETs). Ion thrusters are electrostatic devices where a negatively-charged grid accelerates positive ions to create thrust; this grid will degrade over time because of the direct impact of ions not aligned with the spaces on it. HETs consist of two concentric dielectric cylinders which combine an axial and a radial magnetic field, creating an azimuthal Hall current within the plasma. The magnetic configuration of some HET designs include magnetic field lines which intersect the boundary material surfaces at specific points, thereby eroding them and constraining the useful lifetime of the device.

Recent advances in HET design have enabled the implementation of magnetic field configurations that minimize erosion down to a point where the undesired effects are negligible. These are the Magnetically-Shielded Hall-Effect Thrusters, or MS-HETs ([57, 76]). Previous research ([19, 84]) has identified two main modes for mitigating erosion effects within HETs: reducing the plasma density at key locations within the HET discharge chamber, and displacing the acceleration region downstream so that the ion energy is reduced at the material boundaries.

Erosion within helicon plasma sources (HPSs) has also become an important topic of research, due to the integration of these devices for the production of low-temperature, high-density plasmas within electric propulsion and fusion research applications. HPSs lack electrodes, antennas or grids in direct contact with the plasma. They are also typically implemented as linear devices with axial magnetic fields, which promotes the magnetization of the plasma and reduces its radial diffusion towards the boundary walls. These two facts have often been cited as reasons to expect reduced erosion and long operational lifetimes in HPSs ([35, 92]). However, unwanted sputtering and erosion of the plasma-facing surfaces in HPSs can still create impurities which affect their use in material science research ([7, 8]). The reduction of the wall thickness in these boundary materials can eventually become a cause of failure for these sources and affect the lifetime of the systems they are integrated with, a critical issue for electric space propulsion applications.

These concerns are of particular relevance for the category of *high-power helicon plasma sources* or HP-HPSs. This range of HPSs can be defined through several figures of merit, with threshold values indicating the definition of the high-power category. The most relevant of these include,

- Total RF input power coupled into the HPS, $P_{RF,in}$, with the high-power range defined as $P_{RF,in} \geq P_{RF,thr}$.
- Plasma density above a density threshold, $n_e \geq n_{thr}$.
- Surface power density absorbed by the lateral wall of the helicon dielectric window, $P_{surf} = P_{RF,in}/(2\pi RL) \geq P_{surf,thr}$.

The most commonly chosen threshold values used in the definition of HP-HPSs are described in table 5.1. For the purpose of this study, the volumetric power density P_{vol} has been chosen for the definition.

Table 5.1: Typical values selected for the threshold values of the figures of merit used to define high-power helicon plasma sources.

Parameter	**Value**	**Source Reference**
$P_{RF,thr}$	10 kW	[24]
$n_{e,thr}$	10^{19} m^{-3}	[92]
$P_{surf,thr}$	12 kW/m^2	[106]

The remainder of this chapter is organized as follows. Section 5.2 will describe and analyze the main drivers of erosion phenomena within HPSs, as identified through the modeling tools described in the previous chapters. Section 5.3 presents the results of modeling the power balance model with the goal of better relating the internal plasma parameters of the helicon source to the external input parameters of the system. Section 5.4 will introduce strategies for the mitigation of these undesirable plasma-material interactions, based on physics and engineering principles. Section 5.5 will summarize the findings and the main conclusions of this analysis.

5.2. Main Erosion mechanisms within Helicon Plasma Sources

Based upon the findings and modeling tools presented in previous chapters, this section classifies and describes the most relevant processes by which energetic ions might come into contact with the inner plasma-facing surfaces of Helicon Plasma Sources, and the physical principles that govern them. Three main modes of interaction have been identified, depending on the region within the source where they are present.

5.2.1. Direct Plasma Diffusion towards the Boundary Surfaces

Helicon sources contain and constrain the internal distribution of the plasma through their axial magnetic field. The ions and electrons can travel towards the material surfaces by diffusing through the magnetic field, radially across the magnetic field lines or following them until they intersect a boundary wall.

Diffusion of a plasma in the presence of a magnetic field can be described by diffusion and mobility coefficients for the directions perpendicular and parallel to the axial magnetic field, as shown by Lieberman and Lichtenberg [71]. Vidal et al. [113] implemented these expressions when describing the behaviour of cylindrical argon plasmas in the presence of axial magnetic fields. The rate of cross-field diffusion can sometimes increase above the estimations provided by these ambipolar models, as in the case of the anomalous or Bohm diffusion [56].

The results presented in this section use the models described in chapter 3 when describing the axial and radial distribution of the plasma density within a Helicon Plasma Source, as they were designed for the particular scenarios under study.

The upstream boundary in typical cylindrical helicon plasma sources serves the function of sealing this end of the dielectric vacuum vessel, and sometimes contains ports for the injection of neutral gas or diagnostics. Depending on the specific configuration of the helicon device, the axial magnetic field lines running along the cylindrical source may intersect this surface, therefore allowing the plasma to diffuse along them and impact the boundary. The deposition of energetic ions into the material can produce significant deposition of thermal energy as well as erosion of the surface due to plasma sputtering. In his historical perspective on helicon plasmas, Boswell reports [16] on the early high-density helicon experiments at Flinders University in the late 1960s [17], commenting that the closed end of the glass dielectric window would melt due to the energy deposition from the plasma. This anecdote provides evidence of the importance of this phenomenon since the initial development of helicon sources.

The models developed by Ahedo et al. [3] for the case of cylindrical magnetized plasmas describe the distribution of the plasma at the upstream boundary as a function of the radial and axial coordinates (r, z). The radial model describes the radial distribution of the plasma density with respect to the reference density on-axis for a particular axial position, as shown in equation 4.4. This central density distribution is in turn provided by equation 4.10 from the axial model. These axial density values depend on the reference density value n_0, which is calculated as the ratio between the input flow of heavy particles $g_0 = \dot{m}/(m_i \pi R^2)$ and the ion sound speed (its Bohm velocity)

$u_B = \sqrt{T_e/m_i}$,

$$n_0 = g_0/u_B = \frac{\dot{m}}{(\pi R^2 \sqrt{m_i T_e})} \tag{5.1}$$

where $\dot{m}$ is the input mass flow of neutral gas into the system, m_i is the mass of the ions, T_e is the constant and uniform electron temperature and R is the radius of the cylindrical plasma discharge.

Previously, section 3.3.2 described how the etch rate experienced by a surface depends on the magnitude of the sputtering yield, and the flow of particles impacting on it. The sputtering yield is in turn a function of the ion species, the target material, the angle of impact, and the energy of the ions; while the particle flow is a function of the plasma density at the edge of the sheath and the ion velocity at the same location. Therefore, the key in controlling erosion phenomena in the upstream axial boundary lies in reducing both the density n and the ion impact energy E_0.

The distribution of the plasma density within the helicon plasma source is dependent on different parameters described in the cylindrical plasma models of section 4.2.2. These parameters ultimately depend on the reference plasma density n_0. Figure 5.1 illustrates the relationship between the reference plasma density n_0 and the electron temperature T_e as expressed by equation 5.1, showing the relationship $n_0 \propto 1/\sqrt{T_e}$.

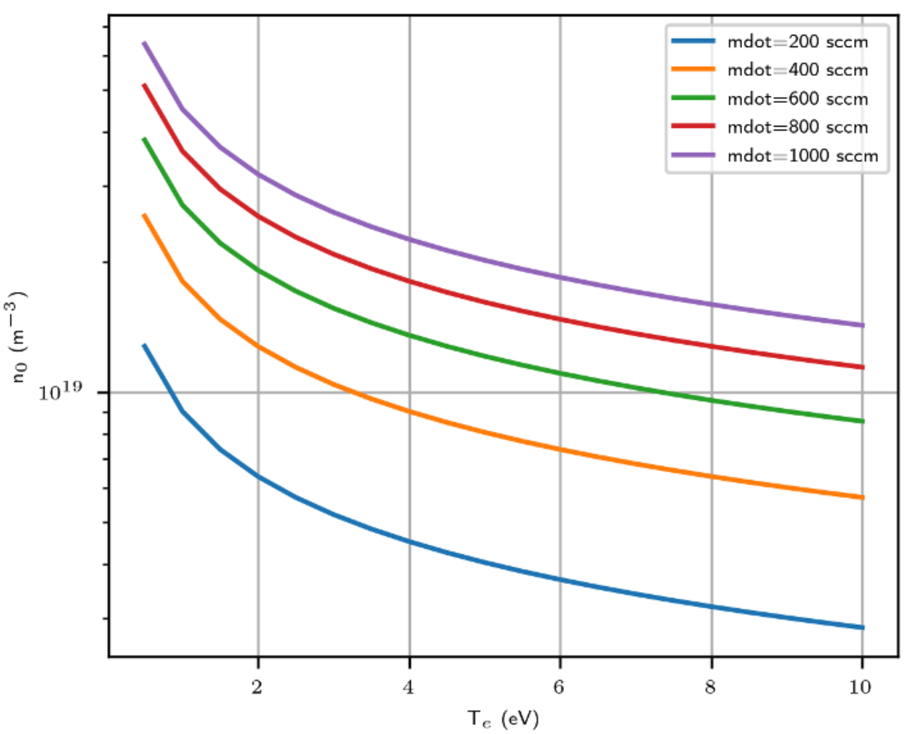

Figure 5.1: Relationship between n_0 and T_e for the axial model from [3], as described by equation 5.1, for a set of input mass flow rates of argon gas. The geometrical parameters of the source are those representative of the VX-CR device as already described in Table 4.5.

The actual etching of the material boundary surface depends on the incident ion flux arriving at the surface, previously defined as $\Gamma_i = n_s u_B$ in chapter 3. n_s is the plasma density value at the sheath edge, and $u_B = \sqrt{T_e/m_i}$ is the ion Bohm velocity. The exact density values can be estimated through the radial and axial models described previously. In order to assess the effect of these parameters on the surface boundary etch rates within a helicon plasma source, the density distribution at the plasma-surface interfaces will be described as

$$n_b \approx h(\hat{r}, \hat{z}) n_0 \tag{5.2}$$

where $h(\hat{r}, \hat{z})$ is an arbitrary non-dimensional function obtained from the composition of the expressions provided by equations 4.4 and 4.9,

$$h(\hat{r}, \hat{z}) = J_0\left(a_0 \hat{r}\right)\left(2\eta_u \cos^2 \xi\right) \tag{5.3}$$

All the variables in the previous equations have been described in the description of the radial and axial models from section 4.2.2. n_0 is provided by the expression from equation 5.1. The exact form of $h(\hat{r}, \hat{z})$ will depend on the particular boundary surface. In the case of the upstream boundary surface, $\hat{z} = -1$, $\xi = -\pi/4$ and $h(\hat{r}, -1) = \eta_u J_0(a_0 \hat{r})$. For the longitudinal inner surface of the dielectric cylinder, $\hat{r} \approx 1$ and $h(1, \hat{z}) = J_0\left(a_0 \hat{r}\right)_{\hat{r}\approx 1}\left(2\eta_u \cos^2 \xi\right)$; at this boundary surface, the actual plasma density values will depend on the approximation used for the limit $\hat{r} \approx 1$ since $J_0(a_0) = 0$.

The plasma density near the surface boundaries n_b is a key parameter in defining the surface flux of incident ions into the surface, $\Gamma_i = n_b u_{i,b}$, where the Bohm sheath criterion states that the ion velocity at the boundary $u_{i,b}$ satisfies the relationship $u_{i,b} \geq u_B = \sqrt{T_e/m_i}$. Substituting the expressions from equations 5.1 and 5.3 into the definition of n_b and the result into the expression for Γ_i, it can be found that

$$\Gamma_i \geq \left(\frac{\dot{m}/m_i}{\pi R^2}\right) J_0\left(a_0 \hat{r}\right)\left(2\eta_u \cos^2 \xi\right) \tag{5.4}$$

which implies that, for the simplified models considered in chapters 3 and 4, the lower value for the incident ion flux at the inner plasma-facing boundary surfaces of a helicon plasma source does not depend on the electron temperature of the plasma, nor the electron energy distribution within the plasma. It is instead dependent on the plasma density distribution at the boundary, and in other constant input parameters such as the incident mass flow rate $\dot{m}$, the mass of the particular ion species m_i and the plasma radius R.

The second factor influencing the etch rate of the boundary surfaces in helicon sources is the sputtering yield Y_i, which is itself a function of the ion impact energy E_0, the ion species, the particular composition of the target surface and the impact angle. Ions obtain their impact energy E_0 through a combination of their thermal energy (given by their temperature T_i) and the electrostatic potentials present in the plasma. In the cold plasma assumption, $T_i \approx 0$ and the ion impact energy is a function of the plasma potential ϕ_p and the wall potential

ϕ_w, as previously described in section 3.3.1. For the typical configuration of helicon sources with floating dielectric boundary surfaces, equation 3.5 describes how ϕ_w is directly proportional to the electron temperature T_e. These boundaries could also be biased at a specific voltage, either to ground potential (where $\phi_w = 0$) or to a specific bias voltage. The typical scenario of floating dielectric boundary walls will be considered in the present analysis, since voltages induced on these surfaces could create conditions that affect the behavior of the plasma itself, and promote etching of the wall materials instead of reducing it.

Since the wall potential ϕ_w in the case of a floating dielectric boundary is directly proportional to T_e, reducing the etch rate on these boundary surfaces implies that, for a given source geometry (with radius R) with a fixed input mass flow $\dot{m}$, T_e should be as low as possible to minimize the ion impact energy E_0 to the walls.

5.2.2. Erosion due to Ion Acceleration through RF Sheath near Antenna Terminals

High capacitive voltages can be induced on regions of the plasma-facing surfaces of the dielectric cylindrical boundaries of helicon plasma sources, induced by the vicinity of the terminals or straps of the helicon antenna on the external side of the material. This phenomenon has been observed as one of the most common causes of etching and erosion in helicon sources ([7, 11]), and is also associated with the presence of regions of concentrated thermal energy deposition.

The physics governing these capacitive plasma sheaths has already been discussed in section 3.3.1. Under appropriate conditions, the oscillating voltages from the external RF subsystem of the plasma source can induce capacitive coupling in the plasma near the location of the antenna terminals, and the associated RF sheath could accelerate the ions towards the dielectric wall at energies higher than those induced by the DC sheath.

In order to better understand the variables involved in this process, figure 5.2 shows a simplified diagram of the area near the location of one of the straps of the helical antenna, depicting it as a classical plane-parallel capacitor. The antenna strap (of thickness t_{ant}) and the plasma itself play the role of the capacitor plates. The dielectric materials between them, represented by the material boundary (of thickness t_b) and a vacuum gap (with separation d_g) in the figure, correspond to the dielectric medium. Oscillating voltages are induced into the helicon antenna by the external RF subsystem, which typically is more complex than the figure's simplified representation (possibly including impedance-matching circuits, instrumentation and other elements). The electric charge Q stored in the terminals of capacitors is proportional to the potential drop V between them, with the capacitance C being the proportionality constant in an ideal capacitor, $Q = CV$.

In the simplest plane-parallel scenario, the capacitance is given by $C = \epsilon_d A/d$, where A is the area of the parallel plates, d is the gap between them (filled by a vacuum or a dielectric) and ϵ_d is the dielectric material's permittivity. The ratio between a specific material's permittivity and the constant vacuum permittivity ϵ_0 is defined as its relative permittivity $\epsilon_r = \epsilon_d/\epsilon_0$. The model depicted in figure 5.2 depicts instead the case of a capacitor with a compound dielectric material, formed by the series coupling of the capacitance of the vacuum gap and the dielectric cylindrical

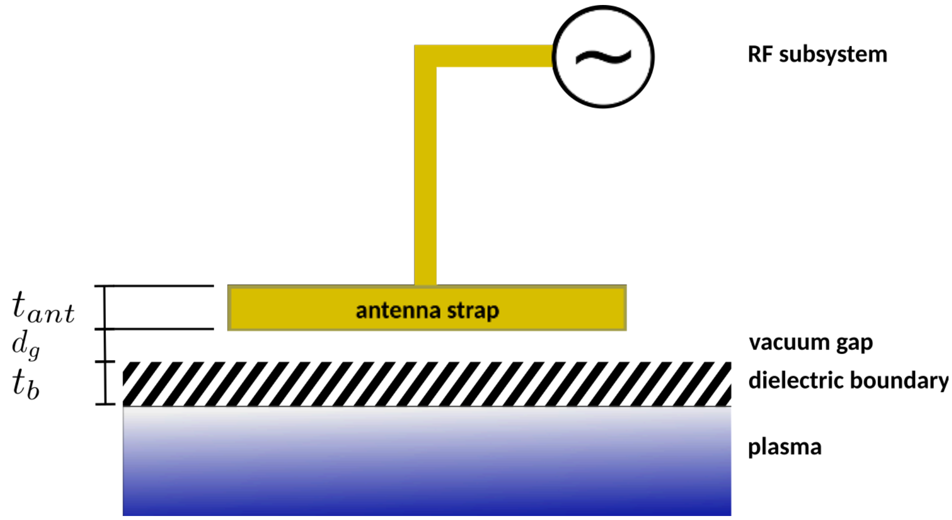

Figure 5.2: Simplified model depicting the elements relevant in the description of capacitive coupling phenomena in the regions near the antenna terminals in a helicon plasma source.

material boundary. The corresponding expression for the equivalence capacitance in this example is

$$C_{eq} = \frac{\epsilon_{rb}\epsilon_0 A}{\epsilon_{rb} d_g + t_b} \tag{5.5}$$

where ϵ_{rb} is the relative permittivity of the dielectric material boundary. Since the charge stored by the ideal capacitor is the product of the applied voltage V and its capacitance C_{eq}, reducing any of these two parameters would decrease Q. Applying this argument to the present simplified analogy of the capacitive coupling near the antenna terminals of a helicon source, a reduction of the equivalent capacitance would diminish the capability of storing charge in the plasma sheath on the inner dielectric surface, and therefore reduce the possibility of related plasma-surface interactions such as sputtering and etching. Reducing the applied voltage to the antenna terminals would also produce the same effect.

The simplified scenario depicted in figure 5.2 must be modified for helicon source configurations where additional material layers exist between the helicon antenna and the plasma. One such example is the use of hollow dielectric cylindrical windows with the purpose of circulating cooling fluids inside them, as has been tested in the PISCES-RF linear helicon device by Thakur et al. ([106]). The authors reported negligible effects on the absorption of the helicon wave or the production of high-density plasmas for this high-power device, when using deionized water as a cooling fluid on a composite helicon window made of alumina and quartz coaxial cylinders.

In practical implementations of helicon sources, reducing the capacitance for a given choice of dielectric boundary material can then be achieved by increasing the thickness of the material and the vacuum gap between it and the antenna terminal. This may not always be feasible, as practical considerations such as weight and cost of the material might preclude it. Some helicon source designs rely instead on direct contact between the antenna and the dielectric boundary, for mechanical, thermal or electrical purposes. Besides, capacitive coupling plays a role in starting the helicon discharge ([25]); diminishing it may impair the performance of the source.

Electrical parameters in the external RF subsystem of the source can also be controlled in order to diminish plasma-surface interactions due to undesired capacitive coupling. Diminishing the applied voltage at the antenna terminals can reduce the potential within the RF sheath. However, this could create high RF currents within the circuit which may not be feasible in practice. The other electrical parameter that has a significant effect on the behavior of capacitive coupling phenomena is the applied RF frequency. Figure 3.2 from section 3.2.1 described how helicon and whistler waves exist in a defined range of the ω-k space as right-hand polarized (RHP) cold plasma waves. Section 4.2.3 discussed how lower RF frequencies enable the ions to react to the voltage oscillations and become accelerated towards the material boundary during the transient phase of the wave with negative potential. Therefore, frequencies which lie within the helicon wave range but are larger than the threshold frequency $\omega_i = \pi\omega_{pi}(2T_e/V_0)^{1/4}$ may significantly reduce plasma-surface capacitive effects.

A thorough discussion of the practical engineering implications of modifying these operating parameters in the RF subsystem of a helicon plasma source is beyond the scope of the present discussion. A discussion of practical design considerations is presented by Popov ([83]).

A common technique to reduce the effect of undesired capacitive effects in inductively-coupled plasma sources ([58]) is the use of Faraday shields or cages, as already described in section 3.4.2. Few results have been published regarding their specific application to helicon plasma sources. Blackwell and Chen ([14]) described the effects of an external aluminum Faraday shield on a helicon source using two different configurations of antennas (Nagoya type-III, and helical). They were able to conclude that inductive coupling effects were associated with the production of symmetrical, centrally-peaked dense plasmas. More recently, Rauner et al. ([88]) reported on the effects of introducing a cylindrical copper jacket with azimuthal slits inside a quartz cylinder used as part of a low magnetic field helicon plasma source. The shield becomes then the new plasma-facing surface. The contribution of the edge localized TG-mode, previously described in section 3.2.1, is significantly reduced and the deposition of RF power within the discharge is diminished. The authors attribute this effect to the modification of the boundary condition of the plasma-facing surface of the cylindrical boundary, which becomes a conductor when the Faraday shield is introduced.

5.2.3. Contact between Magnetic Flux Surfaces and Boundary Materials

The third erosion mechanism identified in helicon plasma sources is the direct contact between magnetic field lines and the source boundary surfaces. The axial magnetic field in helicon sources is required for the excitation of the H-mode (the helicon wave). It also serves the purpose of containing the discharge by preventing the radial diffusion of the plasma towards the boundaries.

This contact between the field lines and the boundaries may be a tangential interaction or the direct intersection of a field line with one of the boundaries. An ideal implementation of a cylindrical magnetized helicon source, such as the one depicted in figure 3.6, may present an intersection of the field lines with the upstream boundary surface. The plasma will then directly impinge upon the surface and the methods of section 5.2.1 can be applied to estimate the distribution of ion flux and ion energies on the surface, and the corresponding plasma-surface interactions can be estimated. If the magnetic field is properly aligned with the axis of the dielectric cylinder, and the source of the magnetic field has been designed to prevent any divergence of the field lines within the length of the cylindrical boundary, then no contact should occur between the plasma and the plasma-facing surface of this cylinder.

Real implementations of helicon sources are more complex than these simplified models. The generation of perfectly uniform axial magnetic fields may require complex engineering solutions which may not be practical or feasible. As an example, large solenoid electromagnetic coils would be needed to create high field intensities that continuously expand the length of the source. In some scenarios such as space electric propulsion, the practical context of the application of the helicon source might constrain the geometry or power consumption of the external magnetic field subsystem. Other applications might in fact require non-uniform magnetic fields, where regions or high and low intensities coexist; this is the case of the Ionizer stage in the VASIMR®.

These variations of helicon sources might present locations where the magnetic field lines intersect or tangentially contact the boundary surfaces. The erosion caused by this type of interactions between the material boundaries and the magnetic field geometry are a well-studied issue in Hall-Effect electric thrusters ([19, 84]). Recently, solutions have been proposed based on optimizing the geometry of both the magnetic field profile and of the dielectric boundary surfaces ([57, 76]). The technique relies on the careful design of what Mikellides et al. define as the "grazing line", the last complete magnetic field line that extends from the external magnetic circuit to the back of the annular acceleration channel.

A very similar strategy to that used in magnetically-shielded Hall thrusters has been investigated by Caneses et al. ([22]) in their analysis of the magnetic field lines in the Proto-MPEX linear helicon device. They define the "last uninterrupted flux surface" or LUFS as the complete magnetic flux surface that tangentially makes contact with the material boundary of the helicon source. At radial coordinates larger than those of the LUFS, the magnetic field lines intersect the boundary surfaces at several points and create short-length paths between these points. Caneses et al. report that the plasma density decays rapidly in these regions, in a manner analog to the scrape-off layer (SOL) in magnetic fusion devices.

Figure 5.3 depicts the 2D cross section of the VX-CR helicon device (previously shown in figure 4.6), highlighting the LUFS corresponding to its magnetic field configuration. The relevant material boundary surfaces have been labeled in this diagram. The VX-CR's axial magnetic field is not of uniform intensity, with a value of $B \approx 0.1$ T in the region of the cylindrical alumina helicon window (labeled **B** in the figure), and $B \approx 0.4$ T in the downstream choke region (inside the downstream limiter labeled **C**). Apart from the direct intersection of all magnetic field lines with the upstream dielectric material boundary (labeled **A** in the diagram), the geometry of all boundary surfaces closely match the shape of the LUFS. There are no points of tangential contact between them, and the corners of the vacuum chamber interface port (labeled **D**) have been chamfered to perfectly match the divergence of the field.

Identifying potential points of contact or intersection between the magnetic field and the boundary surfaces in a helicon source is critical, as the ions could potentially impact these regions with a combination of their translational kinetic energy along the field lines, and the acceleration obtained as they enter the sheath at the surface boundary. The geometry of the magnetic field at these contact points can also define the angle of impact of the ions on the surface, requiring the use of the corresponding expressions for sputtering from ions not impacting at normal incidence (as previously described in section 3.3.2).

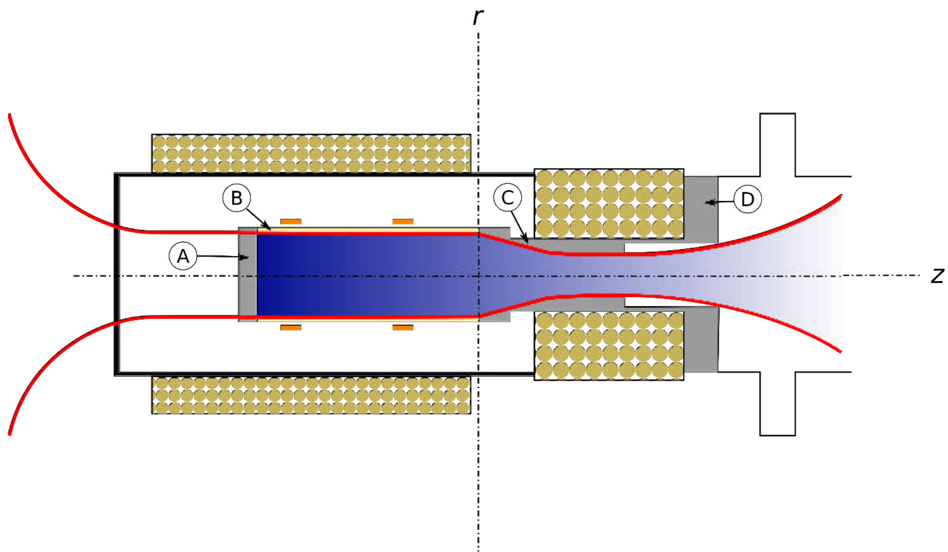

Figure 5.3: 2D schematic cross section of the VX-CR helicon device ([26, 45]), with the last uninterrupted flux surface or LUFS highlighted in red. The main elements of the helicon source have already been identified and labeled in figure 4.6. Boundary material surfaces have been labeled as follows: **(A)** the upstream boundary surface, **(B)** the dielectric cylindrical tube, **(C)** the downstream limiter, and **(D)** the interface port from the downstream vacuum chamber.

5.3. Power Balance Model of a Helicon Plasma Source

In order to properly estimate the relationship between these two key parameters n_0 and T_e for a given source geometry and the specific operational configuration of a helicon source implementation, expressions for the power balance of the complete helicon source are required in order to obtain the parameter values at steady-state for a given input power into the system. The electron temperature T_e will no longer need to be an input variable for the magnetized cylindrical plasma simulation of chapter 3, but can instead be found through an iterative optimization.

The relationship between the power balance model and the cylindrical magnetized plasma models from section 4.2.2 is depicted in the diagram shown in figure 5.4. The combination of both models enables a simulation where the external input parameters are the RF input power to the system P_{inp}, the input mass flow rate of neutral gas $\dot{m}$ and the geometry of the cylindrical plasma source defined by the parameters R and L. The electron temperature of the plasma T_e, the plasma density distribution n, the neutral density distribution n_n and the velocity distribution for all particle species $\mathbf{u}_j$ (for $j = i, e, n$) become internal state variables of the system. The optimization algorithm consists of an iteration between both models until the calculation of the power dissipated by the source through collisional processes and the flux of particles through its boundaries matches the external input power P_{inp} within a pre-defined tolerance level.

The selected power balance criterion is a modification of the expression proposed by Ahedo et al. [3], including some concepts expressed by Vidal et al. [113]. It describes the power distribution within the helicon plasma source itself, and does not analyze the magnetic nozzle present in the case of helicon thrusters. It can be expressed as the equality between the external RF input power into the system, and the sum of the power dissipated in ionization

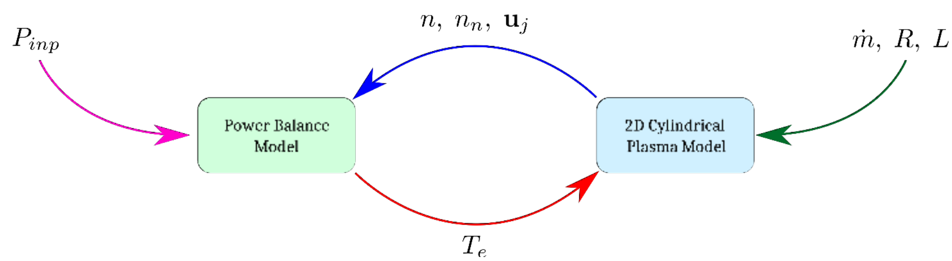

Figure 5.4: Relationship between the internal and external variables of the Power Balance model ([3, 113]) and the 2D Cylindrical Plasma model ([3]).

and excitation processes P_{ion}, the power deposited by the plasma in the boundary surfaces P_{wall} and the ejected power through the downstream open boundary of the helicon source P_{beam}. This is shown in the expression

$$\begin{aligned} P_{in} &= P_{out} \\ P_{RF} &= P_{ion} + P_{wall} + P_{beam} \end{aligned} \tag{5.6}$$

The expressions on the right-hand side this equation are dependent on the electron temperature T_e and the distribution of the plasma density n within the source, as well as on other fixed parameters such as the source geometry, the particular species and the input mass flow. The parameter P_{RF} on the left-hand side is an external input parameter into the system. A brief description of these terms will be presented, and the complete derivation of all these terms is detailed in appendix C.

P_{ion} represents the power dissipated within the helicon source due to collisional processes, which is estimated as the product of the total flow of ions leaving the source through its boundaries and an term representing the combination of excitation and collisional processes within the source. This second term is a key factor in the power balance model as it determines the bulk of the power dissipation within the source and the convergence of the optimization algorithm.

Ahedo and Navarro ([3]) describe this term as the *effective ionization energy* E'_{ion}, and they use the correlation to the data derived by Dugan ([46]) for the case of argon plasmas. The present analysis will follow the more recent study by Gudmundsson ([55]) and referenced by Lieberman and Lichtenberg ([71]), which contains collision rate data for argon ions at the low electron temperatures relevant for typical helicon plasma sources (1 eV $< T_e <$ 10 eV). These later authors define this term as the *collisional energy lost per ion-electron pair created* ε_c, and define it as

$$\varepsilon_c = \varepsilon_{iz} + \sum_j \varepsilon_{ex,j} \frac{k_{ex,j}}{k_{iz}} + \frac{k_{el}}{k_{iz}} \frac{3m_e}{m_i} T_e \tag{5.7}$$

where ε_{iz} is the ionization energy for singly-charged ions ($\varepsilon_{iz} \approx 15.76$ eV for Ar^+ ions), $\varepsilon_{ex,j}$ and $k_{ex,j}$ are respectively the threshold energies and rate coefficients for the different excitation processes (represented by the subindex j), k_{iz} is the ionization rate coefficient, and k_{el} is the rate coefficient for elastic collisions between electrons and ions. The rate coefficients $k_{ex,j}$, k_{iz} and k_{el} are a function of the electron temperature T_e; their formulas, as compiled and reported by Gudmundsson, are presented in appendix C. Figure 5.5 shows the estimated values for ε_c as a function of the electron temperature for the case of singly-ionized argon plasmas, obtained from the expression in equation 5.7. The plot clearly shows how the values of ε_c increase at lower electron temperatures, as the excitation and elastic collisions are more dominant than ionization processes ([71]).

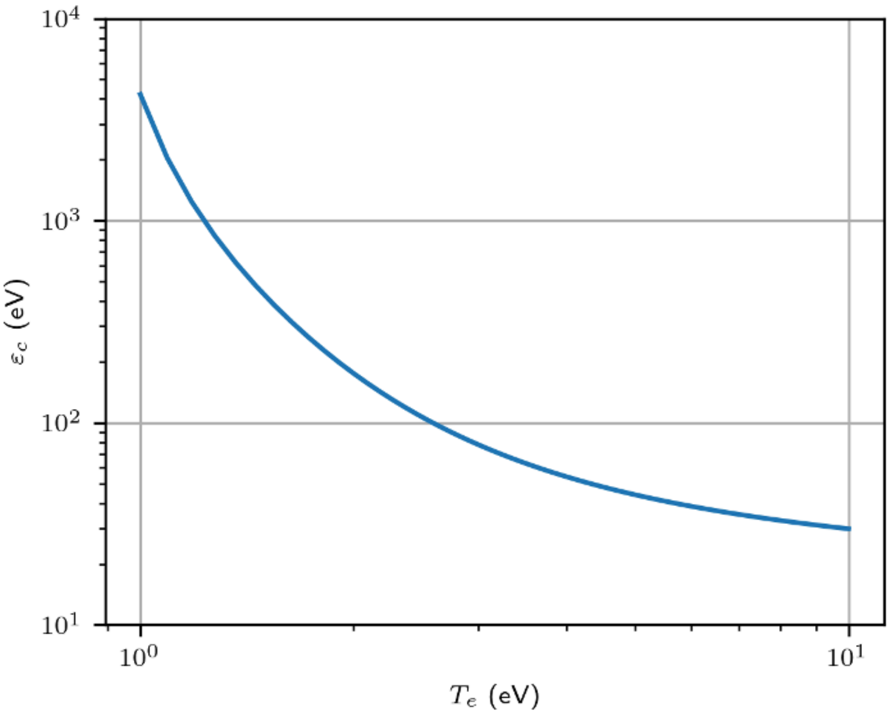

Figure 5.5: Dependence of the collisional energy lost per ion-electron pair created, ε_c, on the electron temperature T_e for singly-ionized argon plasmas according to Gudmundsson [55].

The term P_{ion} from equation 5.6 can then be calculated as

$$P_{ion} = \varepsilon_c \left(\frac{\dot{m}_T}{m_i} \right) \tag{5.8}$$

where $\dot{m}_T$ represents the total mass flow through the system boundaries, and $\dot{m}_T/m_i$ is then the total flow of ions through the boundaries. The calculation of m_T involves the calculation of surface integrals through each system boundary (the upstream wall, the inner surface of the dielectric cylindrical boundary and the downstream open end); they are detailed in appendix C.

The remaining two terms from equation 5.6, P_{wall} and P_{beam}, represent respectively the transfer of momentum from the different plasma species to the system material boundaries and the downstream open end. Their calculation, derived from the plasma momentum equation, is also presented in appendix C.

In order to assess the accuracy and performance of the power balance model, a calculation was run with parameters corresponding to the VX-CR helicon plasma source (previously presented in table 4.5). The geometrical input parameters of the simulation, R and L, remained constant. The other two external parameters depicted in figure 5.4 did not. The mass flow rate of neutral argon into the system is varied between the values of 200 sccm Ar $< \dot{m} <$ 500 sccm Ar, which correspond to flow rates in the range 5.95 μg/s Ar $< \dot{m} <$ 29.7 μg/s Ar. The range of RF input power levels was chosen as 2000 W $< P_{inp} <$ 5000 W. Figure 5.6 presents the result of the optimization algorithm for these configurations. Both the equilibrium plasma temperature T_e and the reference plasma density n_0 are shown as a function of the RF input power P_{inp}, with separate plots for each value of the neutral argon mass flow rate $\dot{m}$.

The results shown in figure 5.6 predict a reduction in the electron temperature T_e as the RF input power P_{inp} is increased. This trend contradicts the expected behavior of increasing temperature as more energy is injected into the system by the RF source, which is confirmed by the experimental data from the VX-CR shown in figure 5.7.

These results provided by the simulation, while not in agreement with experimental data, can be explained from the limitations of the models involved. The bulk of the energy dissipation is provided by the term P_{ion}, whose magnitude is typically much larger than the contributions provided by the momentum transfer terms P_{wall} and P_{beam}. The contribution of the P_{ion} term is larger for lower electron temperatures, given the increased effect of excitation collisions as already shown in figure 5.5. Since the simulated plasma is composed of only three distinct species (neutrals, electrons and *singly-ionized* ions), as the energy input into the system (the RF input power P_{in}) is increased for given a fixed input neutral mass flow rate $\dot{m}$, the simulation converges to a lower equilibrium temperature T_e in order to balance the additional energy input.

Other power-dissipation mechanisms are either not available or not implemented in this particular simulation. The axial submodel, part of the 2D cylindrical plasma model, tends to converge to configurations where $\eta_u \rightarrow 1$. This implies that the neutral density at the downstream open end of the helicon source is null and the plasma is fully ionized in that location. Therefore, an additional increase in the power input to the system cannot be dissipated as an increment in the plasma ionization. The other mechanism which might absorb the additional energy is higher ionization states in the positive ions. However doubly-ionized ions, which would imply the existence of four different species within the plasma, are not taken into account by either the 2D cylindrical plasma model of section 4.2.2 or by the power balance model of appendix C.

5.4. Potential Mitigation Strategies

Section 5.2 identified three main mechanisms capable of producing significant erosion phenomena within helicon plasma sources, when the proper conditions are met. They include the diffusion of ions toward the boundary surfaces, the acceleration of ions due to capacitive coupling produced by the helicon antenna terminals and the direct contact between magnetic field lines and the material boundaries. The present section will discuss potential strategies able to mitigate these phenomena and their effects, with a focus on the issues relevant for high-power helicon plasma sources. They combine both adequate selection of the physical properties of the components of the source, as well as design choices that reduce the potential unwanted erosion effects.

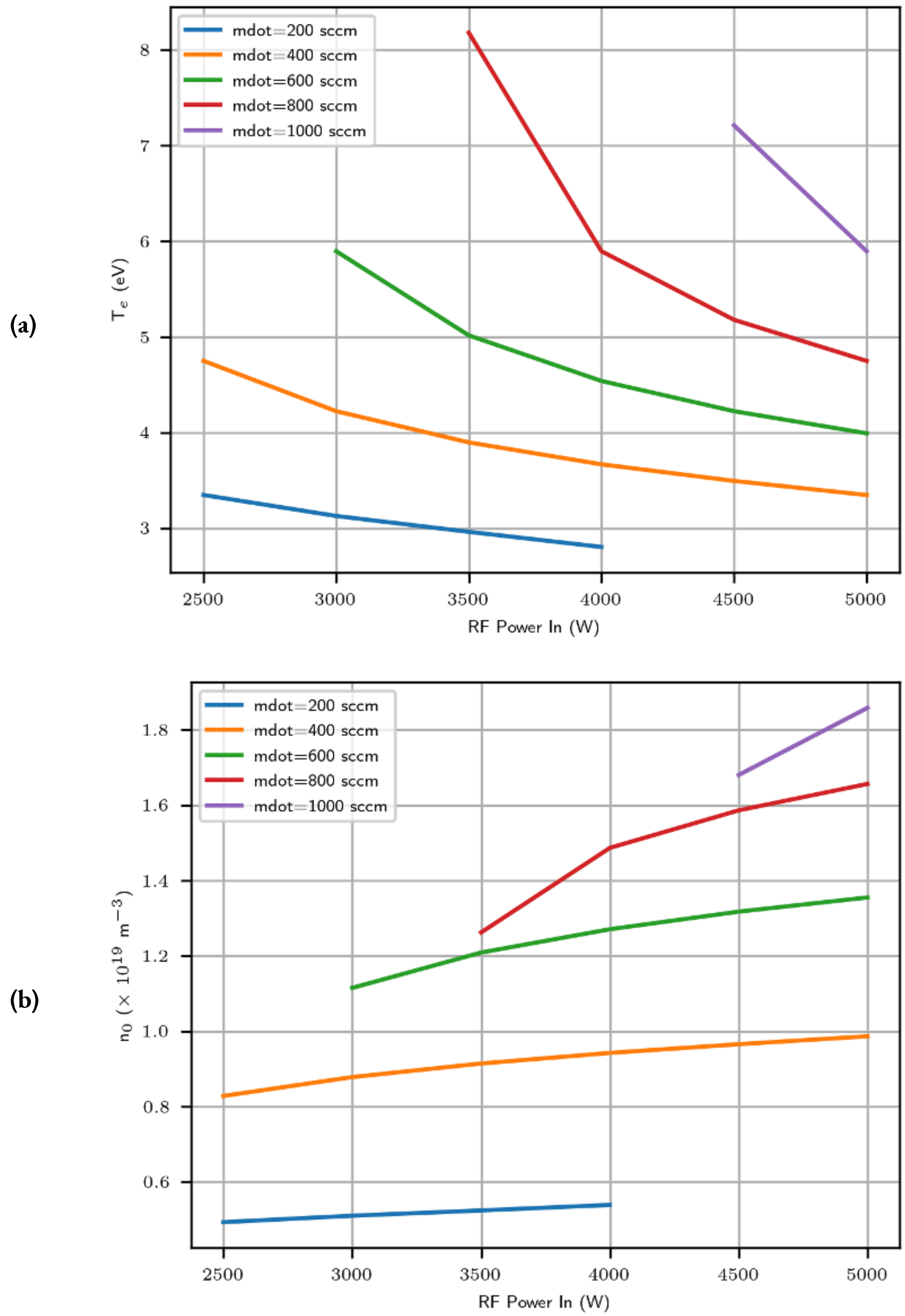

Figure 5.6: Results obtained with the optimization algorithm relating the Power Balance and 2D Cylindrical Plasma models. (a) shows the relationship between the electron temperature T_e and the RF input power level P_{inp}, and (b) presents the reference plasma density n_0 as a function of P_{inp}. Plots are shown for different values of the neutral argon mass flow rate, and for those configurations where the optimization algorithm converged according to the established condition.

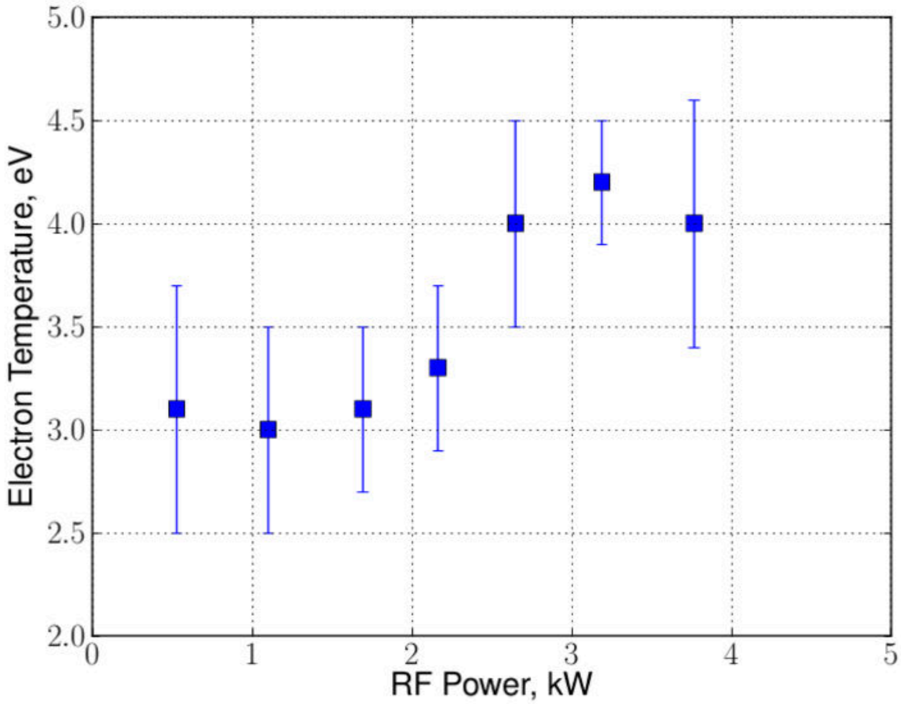

Figure 5.7: Experimental measurements of the electron temperature T_e as a function of the input RF power in the VX-CR device, as published by Castro et al. ([26]). The operational configuration of the system is that described in table 4.5, with a neutral argon mass flow rate of $\dot{m} = 200$ sccm.

5.4.1. Selection of Optimal Dielectric Materials

The proper material selection for all plasma-facing surfaces within a helicon plasma source can have a significant effect on sputtering and erosion phenomena. However, the choice of materials must also consider many other practical aspects of the implementation of the source and these requirements are not always aligned.

The properties of these boundary materials relevant for the design of helicon plasma sources can be organized in three overall categories. They are electrical properties, mechanical and thermal properties and plasma interaction properties.

Electrical Properties

The electrical requirements for candidate boundary materials are related to the need to transmit the radiofrequency waves from the external helicon antenna into the inner volume where the plasma discharge is produced. The material's relative permittivity must be high ($\varepsilon_r \gg 1$), making the material an insulating dielectric. This prevents the shielding of the propagation of the radio frequency waves through the boundary. The second electrical property of relevance is the loss tangent $\tan\delta$, which quantifies the energy losses in the material when the radio frequency waves are propagating through it. Caughman ([27]) presents the calculation of the power losses P_{loss} in the material as

$$P_{loss} = \frac{1}{2}\omega\varepsilon_d\left(\tan\delta\right)E^2 \tag{5.9}$$

where ω is the frequency of the waves and E is the applied electric field. Both the material permittivity ε_d and the loss tangent $\tan\delta$ are functions of the temperature. Therefore, as losses occur the temperature of the dielectric material increases, which leads to an increment in the rate of power loss and could potentially produce a positive feedback loop of increased loss of radio frequency energy. A solution to this issue is the selection of materials with low values of the loss tangent, coupled with proper mechanisms of heat dissipation as will be discussed below for the thermal properties.

Mechanical and Thermal Properties

Dielectric boundary materials for helicon plasma sources should exhibit adequate resistance to fracture, good tensile strength, low coefficients of thermal expansion and good thermal conductivity, among other relevant properties. Despite the fact that most plasma sources do not contain mechanical moving parts, these properties enable helicon sources to resist the mechanical loads created when the residual heat from the plasma discharge is distributed among all boundary materials, and potential mechanical loads may be imposed on the boundary materials due to uneven thermal expansion.

DeFaoite et al. ([40, 41]) published a thorough review of the mechanical and thermal properties of engineering ceramics suitable for application in the VASIMR® engine, a high-power electric propulsion device which contains a helicon plasma source as its first stage. Their review considers the following mechanical properties: density, Young's modulus, bulk modulus, shear modulus, Poisson's ratio, tensile strength, flexural strength and compressive strength. The thermal properties included in the analysis are the thermal conductivity, the specific heat capacity and the thermal expansion coefficient. The candidate materials studied include alumina, aluminum nitride, beryllium, fused quartz, sialon and silicon nitride. These parameters are presented as a function of the material's temperature, and mathematical regressions are produced to be used in engineering analysis.

From a thermal point of view, the boundary materials should also be able to withstand high temperatures of operation. High-power helicon sources, such as the one used in the VASIMR® ([29]), the Pisces-RF experiment ([106]) or the Proto-MPEX device ([7, 22]) can easily reach steady-state operational temperatures above 500° C even with advanced thermal management systems in place.

The combination of these mechanical and thermal properties, with the electrical requirements discussed above, typically constrain the selection of helicon source boundary materials to engineered ceramic materials with adequate mechanical strength, tolerance to high temperatures, high thermal conductivity and low coefficients of thermal expansion. As practical examples of material choices in high-power helicon sources, the VX-CR device has operated with alumina and silicon nitride boundary surfaces, the Pisces-RF experiment uses a composite alumina and quartz cylindrical helicon window including an annular channel for the circulation of cooling deionized water ([106]) and the Proto-MPEX device uses aluminum nitride for its dielectric helicon window section ([22]).

Plasma Interaction Properties

The mechanical and electrical material constraints previously discussed are related mostly to practical engineering issues in the design of helicon plasma sources. They typically limit the selection of boundary materials to dielectric technical ceramics with good mechanical resistance and thermal conductivities.

Beyond this category of properties, the sputtering parameters of the particular combination of boundary materials and plasma species are another factor that could influence this selection. As previously discussed in chapter 3, the sputtering yield is a factor of the particular combination of target material and the species of impacting ion, as well as other parameters such as the incident energy and the angle of impact. The species present in the plasma, and consequently the selection of neutral gas used for the discharge, are typically dependent on the specific application of the helicon source. Therefore, the plasma species are normally considered a given constraint, and the selection of boundary materials should comply with all the previously described mechanical and thermal properties, while minimizing the potential sputtering yield values if possible.

5.4.2. Reduction of Plasma Density at the Material Boundaries

The distribution of plasma density along the source's material boundaries is a key parameter to control the potential rate of etching along these surfaces. It is in fact one of the parameters which are controlled in systems design to intentionally etch surfaces, such as those used in the manufacturing of integrated circuits and microelectronics.

In order to illustrate the discussion regarding the distribution of plasma density throughout the source, Figure 5.8 presents the basic results from the simulation of the VX-CR device according to the models presented in Chapters 3 and 4, following the same configuration described in table 4.5.

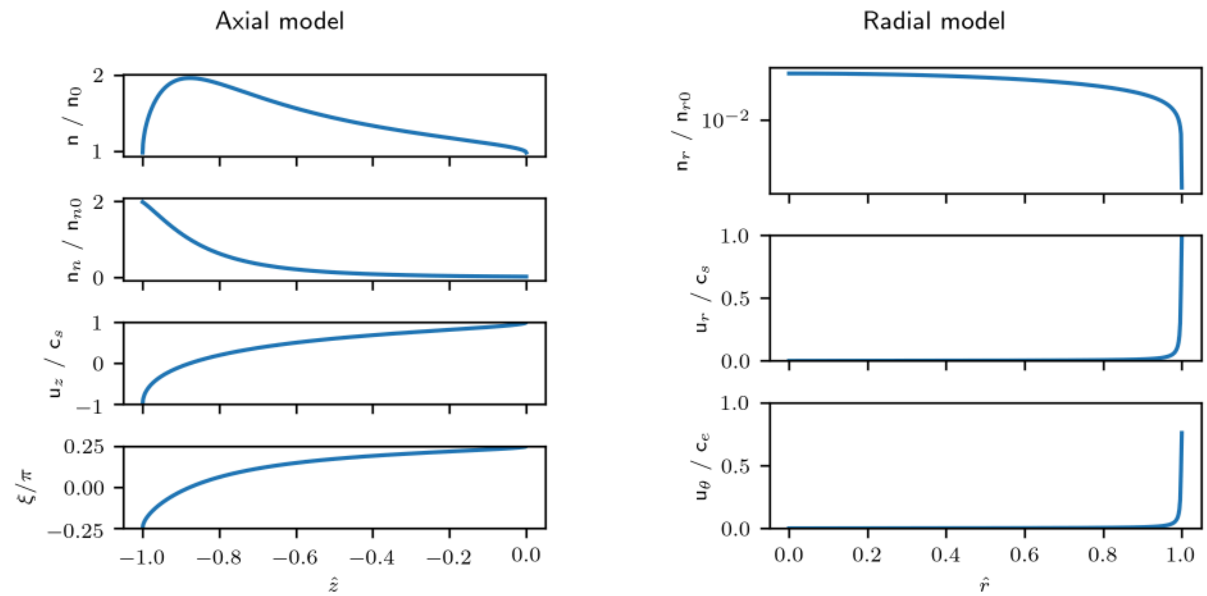

Figure 5.8: Simulation of the distribution of the main plasma parameters in the VX-CR device according to the Axial and Radial models described in Chapters 3 and 4. Simulation input parameters are those of table 4.5 with an electron temperature of $T_e = 3.0$ eV.

For reducing the plasma density along the inner surface of the cylindrical boundary of a helicon source, the key approach is the control of the radial density profile. The radial submodel from the 2D cylindrical plasma model presented in Chapter 3 and Appendix B describes the radial distribution of the plasma density towards the boundary from the on-axis reference value, depicting a centrally-peaked distribution. The radial diffusion of the plasma is determined by the magnitude of the axial magnetic field B, and appears within the lower-hybrid frequency parameter $\omega_{lh} = eB(m_i m_e)^{-1/2}$. The analysis presented in Chapters 3 and 4 made use of the asymptotic form of the distribution for the magnetized regime, where $\hat{\omega}_{lh} \gg u_B/R$; in this particular case, the radial distribution is provided by a Bessel function of the first kind of order zero, and is independent of the value of the magnetic field. Nevertheless, the geometry and magnitude of $\mathbf{B}$ is the key parameter that affects the radial diffusion across the magnetic field. As an indication of its critical relevance, the diffusion coefficient across a magnetic field can be estimated ([71]) as

$$D_{\perp} = \frac{eT_e\nu_m}{m_e\Omega_e^2} = \frac{m_eT_e\nu_m}{eB_0^2} \tag{5.10}$$

where ν_m is the frequency of collisions of the electrons with the static background ions. Clearly, the effect of the magnetic field in limiting cross-field diffusion is evident as $D_{\perp} \propto 1/B_0^2$. Even in the case when the anomalous or *Bohm* diffusion is present,

$$D_{\perp,B} = \frac{T_e}{16B_0} \tag{5.11}$$

still $D_{\perp,B} \propto 1/B_0$. Controlling the magnetic field intensity is key in reducing cross-field diffusion.

At the upstream end of a helicon source, the plasma impacts directly with the boundary surface as the magnetic field lines typically intersect it. According to the cylindrical plasma models as depicted in Figure 5.8, the plasma density distribution along this surface will be determined by the value of the on-axis density at the location $z = -L$, since the radial distribution will depend on this particular value (as described by equation 5.2). The $n/n0$ plot in figure 5.8 shows that this on-axis density approaches the reference value $n_0 = g_0/u_B$ at the upstream end of the source (where $z = -L$ or $\hat{z} = -1$). For the case of the VX-CR, the propellant utilization parameter in the simulation tends to unity, $\eta_u \rightarrow 1$, since the neutrals are mostly depleted at the downstream open end of the simulation domain. This is a consequence of the asymptotic expressions used for the case of magnetized cylindrical plasmas. However, Ahedo et al. ([3]) present results using the complete, non-asymptotic, solution of the axial model where $n/n_0 < 1$ at the upstream boundary of the simulation domain. Also, the actual experimental data from measurements of on-axis plasma density previously presented in Figure 4.4 indicates that density values lower than the reference plasma density n_0 do appear on practical implementations of helicon plasma sources. Therefore, this is a topic that requires further investigation and experimental validation. Nevertheless, these partial results seem to suggest that a reduction of the on-axis plasma density below the reference value of n_0 is possible. As an indicative example, data published for the Proto-MPEX experiment by Kafle et al. ([60]) shows that the on-axis plasma density at the upstream boundary is 20% of the corresponding value at the location of the helicon antenna (as estimated using the 3D kinetic Monte Carlo particle code B2.5-Eirene).

A recent innovation in the design of helicon plasma thrusters related to diminishing the effects of plasma impingement upon the upstream boundary of the source, is the Magnetic Arch thruster developed by the Zarathustra project of the Carlos III University in Madrid, Spain. Figure 5.9 shows a sketch of its operational concept. It consists of a non-linear helicon plasma source, in which the usual cylindrical dielectric tube is bent into a circular arc producing a source with two open ends (an no upstream boundary). This concept is still under development. The removal of the upstream boundary eliminates the afore-mentioned issues of direct impact of ions, but the new arch configuration includes curved magnetic field lines and its effect on the plasma dynamics will require further testing and research. Besides, topics related to the detachment of the plasma from the magnetic arch configuration will require to be addressed in order to demonstrate a reliable thruster design.

5.4.3. Reduction of RF Sheath Voltages

The acceleration of ions due to the capacitive coupling effects produced by the terminals of the helicon antenna has been identified as one of the critical sources of unintended etching phenomena in the helicon plasma literature ([1, 6, 7, 11]).

Three approaches exist to mitigate these effects. The first one relates to the operational parameters of the ex-

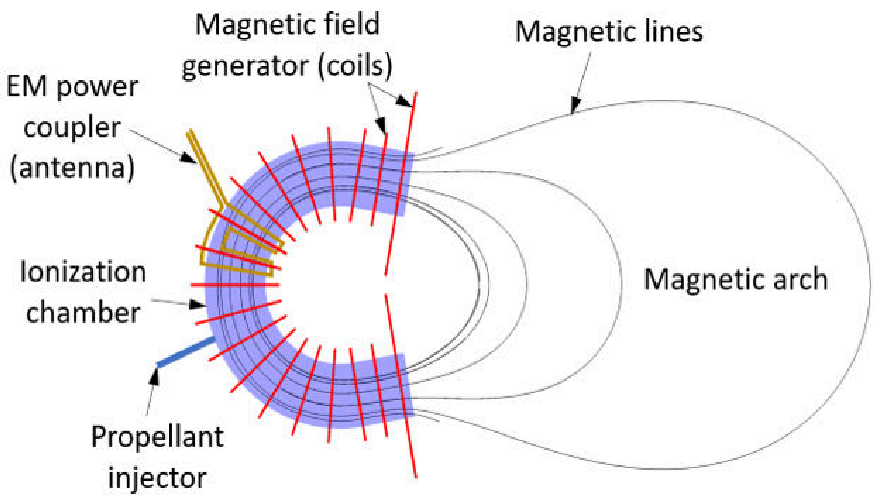

Figure 5.9: Sketch of the Magnetic Arch thruster from the Zarathustra project at the Carlos III University (Madrid, Spain). *Source:* `https://erc-zarathustra.uc3m.es/zarathustra/`

ternal radio frequency (RF) subsystem of the helicon source, responsible for generating and transmitting the electromagnetic waves to the helicon antenna itself. As previously described in section 5.2, lowering the RF voltage or increasing the operating frequency of the RF generator can reduce the capacitive coupling effects. The energy obtained by the ions from the RF sheath is proportional to the potential induced in the dielectric material surface. However, practical engineering considerations must be taken into account as reducing the voltage would increase the current transmitted through the RF subsystem to levels which might be unfeasible in high-power devices. Increasing the operating frequency of the RF subsystem reduces the ability of the ions to react to the oscillating electric field, and the low-frequency RF sheath approximation is then no longer valid. However, the chosen frequency range must be adequate for an efficient coupling of the RF energy to the plasma in the H-mode and this might constraint the frequency range to specific intervals for each particular implementation.

The second potential approach to mitigate capacitive coupling phenomena is the optimization of both the material selection and the geometry of the source, in particular with respect to the configuration of the helicon antenna with respect to the cylindrical material boundary. As previously described in section 5.2, increasing the thickness of the dielectric material and the gap between the dielectric window and the antenna terminals can decrease their combined equivalent capacitance, and potentially reduced the magnitude of the induced voltages in the plasma-facing surface. However, once again these modifications have to be weighed against constraints related to other aspects of the operation of the source such as RF coupling efficiency, thermal and mechanical considerations, and others.

Finally, the use of Faraday shields is a promising technique which may significantly reduce capacitive coupling effects in helicon sources. The study of their application for this particular purpose is incipient ([14, 88]) and further research is needed to understand the effects of these shields in the overall efficiency and performance of the source. An optimal design pattern or technique has not been identified yet.

5.4.4. Magnetic Field Shaping

The geometry and magnitude of the external magnetic field has a critical relevance in the operation of helicon plasma sources, including erosion phenomena. As described above, the magnitude of the axial magnetic field has a dominant effect in reducing the cross-field radial diffusion of the plasma towards the cylindrical boundary wall. Similar to the other parameters discussed in the preceding paragraphs, increasing the magnetic field intensity has to be weighed against the effect of this action in the performance of the helicon source or its implementation.

In devices operating with non-uniform fields, the points of contact or intersection between the magnetic field lines and the material boundary surfaces have the potential to create localized spots of increased erosion. Careful mapping of the magnetic flux surfaces and its relationship with the geometry of the material boundary surfaces can be used to intentionally place these contact points at regions where adequate conditions exist in order to reduce unwanted plasma-surface effects.

This is the approach followed with the Proto-MPEX high-power helicon device ([22]), where the geometry of the magnetic field was modified to ensure that the tangential contact point between the last uninterrupted flux surface (LUFS) and the material boundary surfaces occurs away from the dielectric cylinder. The particular contact point was moved downstream from the helicon antenna region where the coupling of the RF waves takes place, to a region where the ceramic material is replaced by a metallic (stainless steel) limiter. The use of this alternate material reduces the problems associated with the direct contact of the field lines in the antenna region within the source, reducing the plasma density in this critical area. The stainless steel limiter also acts as a sacrificial material, which can then be replaced when the etching depth becomes unacceptable. This particular study did not analyze the effects of the transport of the sputtered atoms from this stainless steel limiter along the magnetic field lines, which are in effect impurities which may hinder the performance of this device for its intended purpose of plasma-surface interaction studies. This particular issue has been analyzed by Beers et al. ([8]) for the same Proto-MPEX experiment.

5.5. Chapter Conclusion

Based on the theoretical developments and simulation techniques presented in Chapters 3 and 4, the most important erosion mechanisms affecting helicon plasma sources have been identified and discussed.

Potential mitigation approaches have been presented for most of them, based on these findings and on practical results published in the available literature. Opportunities for further research work have been identified and discussed, which may contribute to advancing the study of plasma-surface interactions within helicon plasma sources.

Chapter 6

Conclusions and Recommendations

This chapter summarizes and the main research conclusions obtained during the course of this research work. A concluding section will propose future avenues of research which may be pursued as a continuation or a complement of the present work.

6.1. Summary of Conclusions

The present work focused on the study of internal plasma-surface interactions in a particular kind of plasma-generating device, the helicon plasma source. These belong to the family of radiofrequency-based plasma sources which do not require electrodes immersed within the discharge, and have the capability of producing high-density plasmas with low input powers. The fact that the plasma discharge is excited through an external antenna, a trait shared with other technologies such as inductively-coupled plasma (ICP) sources and capacitive-coupled plasma (CCP) sources, is thought to reduce the problems associated with the erosion of cathodes and electrodes inside the plasma. Given these promising features, helicon sources have gained recent interest as plasma sources in the semiconductor and material processing industry, in the field of electric space propulsion, as plasma sources for fusion-related research studies or as ion sources in large-scale fusion devices. However, as the technology evolves and higher-power devices are tested, a thorough understanding of all interactions between the plasma and the boundary material surfaces in helicon sources has become relevant. These phenomena are essential in defining the lifetime of practical helicon implementations, as well as optimizing the ability to produce impurity-free plasmas for many industrial and research applications.

Chapter 3 presented the background theory supporting the framework developed to address the objectives of this project. Four main areas within the plasma physics literature were identified as essential foundations for the objectives of this research. The first is the body of theoretical work on helicon plasma waves, which began with preliminary work in the 1960s but was developed and organized by Rod Boswell, Francis Chen and their research groups in the 1980s and 1990s ([16, 37]). The physics of helicon waves and the mechanisms through which they couple and deposit their energy into the plasma discharge is still an active topic of research in the present day.

However, the currently-accepted models of the two main coupling modes ([5, 36]), the H-mode and the TG-mode, can be used to understand the relationship between some of the key parameters in a helicon discharge (frequency, density, magnetic field intensity) and can be used to inform the design of practical implementations. The second area studied is the modeling of cylindrical plasma discharges within an axial magnetic field. The initial work in this field was produced in the early days of plasma physics by Langmuir and his research on arc discharges ([107, 108]). The recent work by Ahedo's research group ([2, 3]) was selected as the basis of a 2D steady-state model of cylindrical magnetized plasmas, capable of depicting the distribution of all relevant plasma parameters without requiring computationally-expensive operations. The third and fourth topics identified are related to the subfield of plasma-surface interactions. Plasma sheaths are an essential phenomena for the understanding of how plasmas react to the presence of material surfaces, and also determine critical aspects of how ions might get accelerated towards the surface. Models for DC and RF sheaths were described based on the work of Lieberman and Lichtenberg ([71]) among others. Finally, plasma-surface interaction phenomena were analyzed with a specific emphasis on sputtering and erosion phenomena. The current theories describing sputtering phenomena were reviewed. Recent empirical models describing sputtering at low temperatures and in ceramic materials were discussed. The chapter concluded with a review of recent experimental work in this particular subject and other related fields, highlighting the general scarcity of specific work in this specific area in both the simulation and experimental fronts.

Chapter 4 described the development of simulation tools based on the theories previously introduced. Steady-state analytical expressions were developed for each one of the four topics identified in chapter 3, and these numerical models were implemented in the Python programming language making use of the NumPy and SciPy toolkits. Estimations provided by these models were compared, and validated, against available experimental data from relevant helicon plasma sources matching the assumptions and constraints of the simulation. New correlations for the sputtering of composite ceramic materials by argon atoms at low impact energies were developed, by adapting the existing empirical models developed for the case of monoatomic target materials. Estimations were produced for the density distribution and etch rates of the VX-CR helicon plasma source, as a test of the capabilities of the model. Etch rates were calculated for the two main modes of erosion related to the diffusion of ions toward the boundary surfaces and the acceleration through the sheaths, both for the DC sheath and the low-frequency capacitive RF sheath. Within the assumptions of the simulation models, it was found that the higher erosion rates appear at the upstream boundary surface, since the magnetic field lines intersect this whole surface and the average density over it is higher than in other boundaries. The maximum etch rate estimated at this surface was of 2.0×10^{-9} m/s. The second most relevant erosion mechanism found is the etching due to capacitive coupling under the antenna straps, with maximum values of 2.5×10^{-13} m/s. Etching on the plasma-facing surface of the cylindrical boundary is an order of magnitude smaller, with maximum estimated etch rates of 5.0×10^{-14} m/s. These results were discussed and analyzed, highlighting the model limitations and the areas were further research is needed in order to improve the accuracy of these predictions.

Chapter 5 discussed the modeling results obtained in chapters 3 and 4 with the purpose of describing the main mechanisms for erosion of the internal boundary surfaces in helicon plasma sources. Three global modes of plasma-surface interactions capable of producing sputtering of the material surfaces were identified: a) the direct diffusion of the plasma towards the boundary surfaces (across and along the magnetic field lines) with the ions being accelerated by the potential drop across the DC sheath at the boundary; b) acceleration of the ions due to the low-frequency RF sheath under the terminals of the external helicon antenna; and c) the direct contact or intersection between the magnetic flux surfaces and the material boundary surfaces. Each one of these modes was discussed thoroughly, identifying their key parameters, the effects of modifying them, and the practical engineering and physics implications of these approaches. Since both the plasma density n and the electron temperature T_e were identified as key plasma parameters with an influence on all these erosion mechanisms but T_e is a fixed input parameter in the simulations developed in chapter 4, a global power balance model was introduced which complements the cylindrical plasma simulation. This addition enables the calculation of both T_e and n as internal state variables of a combined simulation depending on external parameters such as the RF input power, the neutral mass flow rate and the source geometry. Simulations were performed for the VX-CR device, where it was found that the bulk of the dissipated energy was allocated to the ionization and excitation reactions, favoring lower electron temperatures as the input power is increased. The limitations of the power balance model were discussed, and future potential improvements were identified. Finally, general mitigation strategies were presented and briefly discussed for the mitigation of unwanted erosion phenomena within helicon plasma sources. These include a discussion on the optimal selection of dielectric boundary materials, the reduction of the plasma density along the sheath edges near the boundary surfaces, the minimization of capacitive coupling effects due to the creation of RF sheaths near the terminals of the helicon antenna, and the proper design of the magnetic field geometry. The practical implications of each one of these strategies was analyzed and balanced with all other constraints related to the design of high-power helicon plasma sources.

The study of erosion phenomena for the three candidate materials selected discussed in chapter 5 clearly shows how those combinations where the sputtering yield is lower, present lower rates of surface etching. Among the three simulated materials, silicon dioxide presents the lower values of Y_{sputt} while alumina presents the highest. However, the additional considerations discussed in section 5.4, regarding the mechanical and thermal properties of the dielectric materials used in helicon plasma sources, suggest the conclusion that silicon nitride is a better choice than silicon dioxide, given its higher mechanical strength and thermal conductivity among other factors. The key plasma parameters that contribute to erosion phenomena are the electron temperature T_e and the plasma density at the boundary surface n_b. The plasma temperature contributes to determining the wall potential ϕ_w and the plasma potential ϕ_p, and sputtering will only occur if the potential difference between the plasma and the wall surface is larger than the threshold energy for sputtering, $(\phi_p - \phi_w) > E_{thr}$. If this condition is met, the plasma density at the boundary n_b then becomes the main parameter driving the surface etch rate, as it the ion flux to the wall is proportional to it: $\Gamma_i \geq n_b u_B$, and u_B is the boundary condition at the surface sheath given by the Bohm Sheath Criterion.

Helicon plasma sources are increasingly finding applications in fields ranging from material interaction experiments within the fusion community, space electric propulsion and basic plasma physics research. An accurate understanding of all issues constraining their performance or limiting their practical lifetime will be required in order to further advance the development of these technologies. Beyond the specific focus in helicon plasma sources, the models developed in the present work can also be applied in several fields involving plasma-surface interactions at low temperatures and in the presence of magnetic fields. These include industrial material processing applications, the development of practical fusion devices where the scrape-off layer (SOL) presents plasma parameters with values overlapping the operational regimes of high-power helicon plasmas, and other types of electric plasma thrusters. These domains can also benefit from the development of computationally-inexpensive simulation tools which can guide practical design decisions.

6.2. Recommendations for Future Research Work

Throughout the course of this research project, undeveloped topics were identified in several fields lying outside of the scope of the present work. Several potential improvements to the modeling work presented in this thesis were also evident from the discussion of the results obtained. The present section summarizes these areas where the results presented in this work can be expanded or improved. They are organized according to their relationship to experimental or simulation research.

6.2.1. Experimental Research Work

Within the helicon community, few experimental devices have been dedicated to the study of plasma-surface interactions within the source. The relevant experimental work which exists has been typically carried out as part of broader, unrelated research campaigns. Experiments could be carried out in flexible helicon-based plasma sources, where detailed measurements of the internal distribution of the plasma parameters can be carried out along the internal boundary surfaces. Besides the classical plasma physics probes (Langmuir probes, RPAs and Faraday cups), non-invasive techniques such as optical emission spectrometry (OES), laser-induced fluorescence (LIF) and IR thermography can produce relevant information on the distribution of excitation reactions throughout the plasma and the distribution of power deposition in these internal surfaces.

A particular topic where a clear need of relevant experimental data was identified is sputtering yield values for the dielectric ceramic materials impacted by ion species commonly used both in low-temperature plasma sources and electric propulsion devices, and at their typical low-temperature intervals. Existing data is scarce, and collected using different techniques and at different energy ranges. The research community would greatly benefit from a consolidated effort of collecting and compiling accurate data for the low-temperature energy range of 10 eV $< T_e < 200$ eV.

Among the different mitigation strategies for addressing erosion phenomena within helicon plasma sources, Faraday shields are widely cited in the literature due to previous successful results in inductively-coupled plasma (ICP) sources. Very little experience has been accumulated regarding their usefulness in helicon plasma sources. Questions remain open regarding their effects on the efficiency and performance of the plasma discharge, and specific research related to the eventual mitigation of capacitive coupling phenomena in helicon sources is non-existing.

6.2.2. Simulation Research Work

The current research aimed to develop a practical model of the erosion phenomena within high-power helicon sources. The approach selected was based on 2D fluid-dynamic models for magnetized cylindrical plasmas. However, several assumptions exist in the model which may affect the estimations of the distribution of plasma parameters; exploring these alternative configurations may provide further insights into the plasma behavior which better match actual experimental measurements. Among them, the magnetic field is taken as a constant axial value throughout the source; the model could be improved to include the possibility of non-uniform magnetic fields. The electron temperature, a key parameter in defining the momentum transferred by all species in their mutual collisions and interactions with the boundary surfaces, is assumed a constant value throughout the simulation domain. Non-uniform T_e values could be introduced into the model, as well as non-Maxwellian temperature distributions. Of particular interest is the study of edge-localized modes such as the TG-mode present in helicon sources; their role in the deposition of RF energy becomes relevant at low magnetic field intensities, and they could also influence the plasma-surface interactions in DC and RF sheaths. The chosen model for cylindrical plasmas is the asymptotical magnetized case of the model proposed by Ahedo and Navarro-Cavallé ([3]); although the magnetized scenario is typical of the high-power helicon devices under study in the present work, further insights could be obtained by implementing the complete, non-simplified model. The effects of some key parameters such as the magnetic field $\mathbf{B}$ could be further understood.

Another possible research path is the substitution of the chosen 2D fluid-based model for cylindrical magnetized plasmas with particle-based codes, which could be coupled to the sheath and sputtering submodels developed in the present work. Several alternatives are available, including open-source particle-in-cell (PIC) implementations such as XOOPIC or commercial packages such as COMSOL®.

The power balance model introduced in Chapter 5 is also based in the work proposed by Ahedo and Navarro-Cavallé. While their particular configuration included a model for the magnetic nozzle of a helicon plasma thruster, the modified version presented here includes only a static downstream simulation boundary. This minimizes the effects associated to the fact the plasma in the helicon source is a *flowing* plasma, and this may contribute to the dominance of the ionization and excitation term as the main energy deposition mechanism in this simulation. Improving this power balance model, by better representing the boundary conditions at the downstream open end of the source could significantly improve the results obtained from this simulation. Including dissipation mechanisms associated with high-power devices such as the possibility of doubly-ionized ions could better represent actual experimental devices; this would require updating the cylindrical plasma simulation to include this fourth species of particle.

Bibliography

[1] Aanesland, A., Charles, C., Boswell, R., and Fredriksen, A. Sputtering effects in a helicon plasma with an additional immersed antenna. *Plasma Sources Science and Technology 12* (2003), 85–88.

[2] Ahedo, E. Parametric analysis of a magnetized cylindrical plasma. *Physics of Plasmas 16*, 11 (2009), 113503.

[3] Ahedo, E., and Navarro-Cavallé, J. Helicon thruster plasma modeling: two-dimensional fluiddynamics and propulsive performances. *Physics of Plasmas 20* (2013), 043512.

[4] Allen, J. The plasma-sheath boundary: its history and Langmuir's definition of the sheath edge. *Plasma Sources Science and Technology 18* (2009), 014004.

[5] Arnush, D., and Chen, F. Generalized theory of helicon waves - II - excitation and absorption. *Phyisics of Plasmas 5*, 5 (1998), 1239–1254.

[6] Barada, K. K., Chattopadhyay, P., Ghosh, J., Saxena, Y., and Bora, D. Wall charging of a helicon antenna wrapped plasma filled dielectric tube. *Physics of Plasmas 22*, 1 (2015), 013507.

[7] Beers, C., Lau, C., Rapp, J., Younkin, T., Biewer, T., Bigelow, T., Caneses, J., Caughman, J., Green, D., Meyer III, H., et al. RF sheath induced sputtering on Proto-MPEX part 2: Impurity transport modeling and experimental comparison. *Physics of Plasmas 28*, 10 (2021), 103508.

[8] Beers, C. J., Green, D. L., Lau, C., Myra, J., Rapp, J., Younkin, T. R., and Zinkle, S. J. RF sheath induced sputtering on Proto-MPEX. I. sheath equivalent dielectric layer for modeling the RF sheath. *Physics of Plasmas 28*, 9 (2021), 093503.

[9] Behrisch, R., and Eckstein, W., Eds. *Sputtering by Particle Bombardment: Experiments and Computer Calculations from Threshold to MeV Energies*. Springer-Verlag, 2007.

[10] Berisford, D. *Thermal Phenomena and Power Balance in a Helicon Plasma*. PhD thesis, University of Texas at Austin, May 2009.

[11] Berisford, D., Bengston, R., and Raja, L. Power balance and wall erosion measurements in a helicon plasma. *Physics of Plasmas 17* (2010), 033503.

[12] Berisford, D., Bengston, R., Raja, L., Cassady, L., and Chancery, W. Heat flow diagnostics for helicon plasmas. *Review of Scientific Instruments 79* (2008).

[13] Biersack, J., and Eckstein, W. Sputtering studies with the monte carlo program trim. sp. *Applied Physics A 34*, 2 (1984), 73–94.

[14] Blackwell, D., and Chen, F. Two-dimensional imaging of a helicon discharge. *Plasma Sources Science and Technology 6* (1997), 569–576.

[15] Bohdansky, J. A universal relation for the sputtering yield of monatomic solids at normal ion incidence. *Nuclear Instruments and Methods in Physics Research Section B: Beam Interactions with Materials and Atoms 2*, 1-3 (1984), 587–591.

[16] Boswell, R., and Chen, F. Helicons: The early years. *IEEE Transactions on Plasma Science 25*, 06 (1997), 1229–1244.

[17] Boswell, R. W. Very efficient plasma generation by whistler waves near the lower hybrid frequency. *Plasma Physics and Controlled Fusion 26*, 10 (1984), 1147.

[18] Boyd, I., and Falk, M. A review of spacecraft material sputtering by hall thruster plumes. In *AIAA 37th Joint Propulsion Conference, Salt Lake City, Utah (USA)* (2001).

[19] Brown, N. P., and Walker, M. L. Review of plasma-induced hall thruster erosion. *Applied Sciences 10*, 11 (2020), 3775.

[20] Burin, M., Tynan, G., Antar, G., Crocker, N., and Holland, C. On the transition to drift turbulence in a magnetized plasma column. *Physics of Plasmas 12*, 5 (2005), 052320.

[21] Butler, H., and Kino, G. Plasma sheath formation by radio-frequency fields. *The physics of fluids 6*, 9 (1963), 1346–1355.

[22] Caneses, J. F., Beers, C., Thakur, S. C., Simmonds, M. J., Goulding, R. H., Lau, C., Caughman, J. B., Biewer, T. M., Meitner, S. J., Rapp, J., et al. Characterizing the plasma-induced thermal loads on a 200-kW light-ion helicon plasma source via infra-red thermography. *Plasma Sources Science and Technology 30*, 7 (2021), 075022.

[23] Caneses, J. F., Lau, C., Goulding, R. H., Bigelow, T. S., Biewer, T. M., Caughman, J. B., and Rapp, J. Power transport efficiency during O-X-B 2nd harmonic electron cyclotron heating in a helicon linear plasma device. *Plasma Physics and Controlled Fusion 64* (2021), 025005.

[24] Carter, M., Squire, J., Chang-Diaz, F., Corrigan, A., Dean, L., Farrias, J., Giambusso, M., McCaskill, G., and Yao, T. Physics foundations and testing of a vasimr® engine. In *2018 Joint Propulsion Conference* (2018), p. 4504.

[25] Carter, M. D., Batity Jr., F., Barber, G. C., Goulding, R., Mori, Y., Sparks, D., White, K., Jaeger, E., Chang-Díaz, F., and Squire, J. Comparing experiments with modeling for light ion helicon plasma sources. *Physics of Plasmas 9* (2002), 5097–5110.

[26] Castro, J., Del Valle, J., Arce, N., Chinchilla, E., Echeverría, E., Lezama, D., Martínez, C., Oguilve-Araya, J., Rivera, A., Rodríguez, M., Valverde, J.and Chang-Díaz, R., Carter, M., Olsen, C., Squire, J., and Chang-Díaz, F. VASIMR VX-CR experiment: Status, diagnostics and plasma plume characterization. In *The 33rd International Electric Propulsion Conference, The George Washington University, Washington DC, USA* (2013), no. IEPC-2013-202.

[27] Caughman, J., Baity, F., Bigelow, T., Gardner, W., Hoffman, D., Forrester, S., and White, T. Non-fusion applications of rf and microwave technology. In *AIP Conference Proceedings: The 11th topical conference on radio frequency power in plasmas, Palm Springs, California (USA)* (1996), vol. 355, American Institute of Physics, pp. 449–458.

[28] Chang Diaz, F., Squire, J. P., Carter, M., Corrigan, A., Dean, L., Farrias, J., Giambusso, M., McCaskill, G., and Yao, T. An overview of the VASIMR® engine. In *2018 Joint Propulsion Conference, Cincinnati, OH* (2018), p. 4416.

[29] Chang Díaz, F., Giambusso, M., Corrigan, A., Dean, L., and Warrayat, M. Recent progress on the VASIMR(R) engine. In *37th International Electric Propulsion Conference, Boston, MA* (2022), pp. IEPC–2022–525.

[30] Charles, C. Plasmas for spacecraft propulsion. *Journal of Physics D: Applied Physics 42* (2009), 163001.

[31] Charles, C., Boswell, R., Alexander, P., Costa, C., Sutherland, O., Pfitzner, L., Franzen, R., Kingwell, J., Parfitt, A., Frigot, P.-E., Del Amo, J., and Saccoccia, G. Operating the helicon double-layer thruster in a space simulation chamber. *IEEE Transactions on Plasma Science 36* (2008), 1196–1197.

[32] Chen, F. Plasma ionization by helicon waves. *Plasma Physics and Controlled Fusion 33* (1991), 339–364.

[33] Chen, F. Physics of helicon discharges. *Physics of Plasmas 3* (1996), 1783–1793.

[34] Chen, F. A compact permanent-magnet helicon thruster. *IEEE Transactions on Plasma Science 43* (2015), 195–197.

[35] Chen, F. Helicon discharges and sources: a review. *Plasma Sources Science and Technology 14* (2015), 014001.

[36] Chen, F., and Arnush, D. Generalized theory of helicon waves - I - normal modes. *Physics of Plasmas 4*, 9 (1997), 3411.

[37] Chen, F., and Boswell, R. Helicons: The past decade. *IEEE Transactions on Plasma Science 25*, 6 (December 1997), 1245–1257.

[38] Chen, F. F. Experiments on helicon plasma sources. *Journal of Vacuum Science & Technology A: Vacuum, Surfaces, and Films 10*, 4 (1992), 1389–1401.

[39] Counsell, G. The plasma-wall interaction region: a key low-temperature plasma for controlled fusion. *Plasma Sources Science and Technology 11* (2002), A80–A85.

[40] De Faoite, D., Browne, D., Chang-Diaz, F., and Stanton, K. A review of the processing, composition and temperature-dependent mechanical and thermal properties of dielectric technical ceramics. *Journal of Material Science 47* (2011), 4211–4235.

[41] De Faoite, D., Browne, D., Del Valle Gamboa, J., and Stanton, K. Inverse estimate of heat flux on a plasma discharge tube to steady-state conditions using thermocouple data and a radiation boundary condition. *International Journal of Heat and Mass Transfer 77* (April 2014), 564–576.

[42] De Faoite, D., Browne, D., and Stanton, K. Regression analysis of temperature-dependent and thermal properties of dielectric technical ceramics. *Journal of Material Science 48* (2012), 451–461.

[43] Del Valle, J. I., Castro, J., Arce, N., Chinchilla, E., Echeverría, E., Lezama, D., Martínez, C., Oguilve-Araya, J., Rivera, A., Rodríguez, M., Valverde, J., Chang-Díaz, R., Olsen, C., Illin, A., Giambusso, M., Carter, M., Squire, J., and Chang-Diaz, F. Measurement of the dielectric wall erosion in helicon plasma thrusters: an application to the VASIMR VX-CR experiment. In *33rd International Electric Propulsion Conference, The George Washington University, Washington, D.C., USA* (2013).

[44] Del Valle, J. I., Chang Diaz, F. R., and Granados, V. H. Plasma-surface interactions within helicon plasma sources, review. *Frontiers in Physics 10* (2022), 856221.

[45] Del Valle, J. I., Cortés, S., Fonseca, L., Oguilve-Araya, J., Valverde, J., Martínez, C., Ixcamparij, D., Chang-Díaz, R., Longmier, B., Glover, T., Squire, J., and Chang-Díaz, F. The VX-CR experiment: A thermal and lifetime testbed for the VASIMR^{TM} engine. In *32nd International Electric Propulsion Conference, Wiesbaden, Germany* (2011), no. IEPC-2011-155.

[46] Dugan, J. V., and Sovie, R. J. Volume ion production costs in tenuous plasmas: a general atom theory and detailed results for helium, argon, and cesium. Tech. rep., 1967.

[47] Eagle, W., Boyd, I., Trepp, S., and Sedwick, R. The erosion prediction impact on current Hall thruster model development. In *44th AIAA/ASME/SAE/ASEE Joint Propulsion Conference & Exhibit, Hartford, CT* (2008).

[48] Eckstein, W., and Preuss, R. New fit formulae for the sputtering yield. *Journal of Nuclear Materials 320* (2003), 209–213.

[49] Ewald, H., Crawford, F., and Self, S. Steady-state theory of an intermediate-pressure discharge column in a magnetic field. *Journal of Applied Physics 38*, 7 (1967), 2753–2761.

[50] Fruchtman, A., Makrinich, G., and Ashkenazy, J. Two-dimensional equilibrium of a low temperature magnetized plasma. *Plasma Sources Science and Technology 14* (2005), 152–167.

[51] Garcia-Rosales, C., Eckstein, W., and Roth, J. Revised formulae for sputtering data. *Journal of Nuclear Materials 218*, 1 (1995), 8–17.

[52] Gildea, S., Matlock, T., and Martinez-Sanchez, M.and Hargus, W. J. Erosion measurements in a diverging cusped-field thruster. In *32nd International Electric Propulsion Conference, Wiesbaden, Germany* (2011), no. IEPC-2011-149.

[53] Godyak, V. On helicon thrusters: Will they ever fly? *Journal of Applied Physics 127*, 10 (2020), 103301.

[54] Goldston, R. J., and Rutherford, P. H. *Introduction to plasma physics*. IOP Publishing, 1995.

[55] Gudmundsson, J. T. Notes on the electron excitation rate coefficients for argon and oxygen discharge. Tech. Rep. RH-21-2002, Science Institute, University of Iceland, 2002.

[56] Guthrie, A., and Wakerling, R. K. *The characteristics of electrical discharges in magnetic fields*, vol. 5. McGraw-Hill, 1949.

[57] Hofer, R. R., Goebel, D. M., Mikellides, I. G., and Katz, I. Magnetic shielding of a laboratory Hall thruster: II. experiments,. *Journal of Applied Physics 115*, 4 (2014), 043304.

[58] Hopwood, J. Review of inductively coupled plasmas for plasma processing. *Plasma Sources Science and Technology 1*, 2 (1992), 109.

[59] Horváth, B., Daksha, M., Korolov, I., Derzsi, A., and Schulze, J. The role of electron induced secondary electron emission from sio2 surfaces in capacitively coupled radio frequency plasmas operated at low pressures. *Plasma Sources Science and Technology 26*, 12 (2017), 124001.

[60] Kafle, N., Owen, L., Caneses, J., Biewer, T., Caughman, J., Donovan, D., Goulding, R., and Rapp, J. Plasma flow measurements in the prototype-material plasma exposure experiment (proto-mpex) and comparison with b2. 5-eirene modeling. *Physics of Plasmas 25*, 5 (2018), 052508.

[61] Kajita, S., Sakaguchi, W., Ohno, N., Yoshida, N., and Saeki, T. Formation process of tungsten nanostructure by the exposure to helium plasma under fusion relevant plasma conditions. *Nuclear Fusion 49*, 9 (2009), 095005.

[62] Kelly, R. The surface binding energy in slow collisional sputtering. *Nuclear Instruments and Methods in Physics Research Section B: Beam Interactions with Materials and Atoms 18*, 1-6 (1986), 388–398.

[63] Klozenberg, J., McNamara, B., and Thonemann, P. The dispersion and attenuation of helicon waves in a uniform cylindrical plasma. *Journal of Fluid Mechanics 21*, 3 (1965), 545–563.

[64] Kubota, N., Economou, D., and Plimpton, S. Molecular dynamics simulations of low-energy (25–200 ev) argon ion interactions with silicon surfaces: Sputter yields and product formation pathways, sputtering. *Journal of Applied Physics 83* (1998), 4055–4063.

[65] Lafleur, T., Charles, C., and Boswell, R. Plasma control by modification of helicon wave propagation in low magnetic fields. *Physics of Plasmas 17*, 7 (2010), 073508.

[66] Lafleur, T., Charles, C., and Boswell, R. Characterization of a helicon plasma source in low diverging magnetic fields. *Journal of Physics D: Applied Physics 44*, 5 (2011), 055202.

[67] Lafleur, T., Charles, C., and Boswell, R. Electron temperature characterization and power balance in a low magnetic field helicon mode. *Journal of Physics D: Applied Physics 44*, 18 (2011), 185204.

[68] Langmuir, I. Oscillations in ionized gases. *Proceedings of the National Academy of Sciences of the United States of America 14*, 8 (1928), 627.

[69] Lee, C., Chen, G., Arefiev, A., Bengston, R., and Breizman, B. Measurements and modeling of radio frequency field structures in a helicon plasma. *Physics of Plasmas 18* (2011), 013501.

[70] Legéndy, C. R. Macroscopic theory of helicons. *The Physical Review 135* (1964), A1713–A1724.

[71] Lieberman, M., and Lichtenberg, A. *Principles of plasma discharges and materials processing*. Wiley-Interscience, 2005.

[72] Light, M., and Chen, F. Helicon wave excitation with helical antennas. *Physics of Plasmas 2*, 4 (1995), 1084 – 1093.

[73] Lindhard, J., and Scharff, M. Energy dissipation by ions in the kev region. *Physical Review 124*, 1 (1961), 128.

[74] Linke, J., Du, J., Loewenhoff, T., Pintsuk, G., Spilker, B., Steudel, I., and Wirtz, M. Challenges for plasma-facing components in nuclear fusion. *Matter and Radiation at Extremes 4*, 5 (2019), 056201.

[75] Linsmeier, C., Unterberg, B., Coenen, J., Doerner, R., Greuner, H., Kreter, A., Linke, J., and Maier, H. Material testing facilities and programs for plasma-facing component testing. *Nuclear Fusion 57*, 9 (2017), 092012.

[76] Mikellides, I. G., Katz, I., Hofer, R. R., and Goebel, D. M. Magnetic shielding of a laboratory Hall thruster: I. theory and validation,. *Journal of Applied Physics 115*, 4 (2014), 043303.

[77] Mulcahy, J., Browne, D., Stanton, K., Chang-Díaz, F., Cassady, L., Berisford, D., and Bengston, R. Heat flux estimation of a plasma rocket helicon source by solution of the inverse heat conduction problem. *International Journal of Heat and Mass Transfer 59* (2009), 2343–2357.

[78] Myra, J. A tutorial on radio frequency sheath physics for magnetically confined fusion devices. *Journal of Plasma Physics 87*, 5 (2021), 905870504.

[79] Myra, J. R., and D'Ippolito, D. A. Radio frequency sheaths in an oblique magnetic field. *Physics of Plasmas 22*, 6 (2015), 062507.

[80] Navarro-Cavallé, J. *Plasma simulation in space propulsion: the helicon plasma thruster*. PhD thesis, Universidad Politécnica de Madrid, 2016.

[81] Nenadovic, T., Perraillon, B., Bogdanov, Z., Djordjevic, Z., and Milic, M. Sputtering and surface topography of oxides. *Nuclear Instruments and Methods in Physics Research B 48*, 1-4 (1990), 538–543.

[82] Perry, A., Vender, D., and Boswell, R. The application of the helicon source to plasma processing. *Journal of Vacuum Science and Technology 9*, 2 (1991), 310–317.

[83] Popov, O. A., Ed. *High Density Plasma Sources: Design, Physics and Performance*. Noyes Publications, 1995.

[84] Pérez-Grande, D., Fajardo, P., and Ahedo, E. Evaluation of erosion reduction mechanisms in a hall effect thruster. In *Joint Conference of 30th International Symposium on Space Technology and Science, 34th International Electric Propulsion Conference and 6th Nano-satellite Symposium, Hyogo-Kobe, Japan* (2015).

[85] Rapp, J. The challenges of plasma material interactions in nuclear fusion devices and potential solutions. *Fusion Science and Technology 72*, 3 (2017), 211–221.

[86] Rapp, J., Biewer, T., Bigelow, T., Caneses, J., Caughman, J., Diem, S., Goulding, R., Isler, R., Lumsdaine, A., Beers, C., et al. Developing the science and technology for the material plasma exposure experiment. *Nuclear Fusion 57*, 11 (2017), 116001.

[87] Rapp, J., Biewer, T. M., Bigelow, T. S., Caughman, J., Duckworth, R. C., Ellis, R. J., Giuliano, D. R., Goulding, R. H., Hillis, D., Howard, R., et al. The development of the material plasma exposure experiment. *IEEE Transactions on Plasma Science 44*, 12 (2016), 3456–3464.

[88] Rauner, D., Zielke, D., Briefi, S., and Fantz, U. Impact of internal faraday shields on rf driven hydrogen discharges. *Plasma 5*, 3 (2022), 280–294.

[89] Shabshelowitz, A., and Gallimore, A. D. Performance and probe measurements of a radio-frequency plasma thruster. *Journal of Propulsion and Power 29*, 4 (2013), 919–929.

[90] Shamrai, K. P., and Taranov, V. B. Volume and surface rf power absorption in a helicon plasma source. *Plasma Sources Science and Technology 5*, 3 (1996), 474.

[91] Shastry, R., Herman, D., Soulas, G., and Patterson, M. NASA's evolutionary xenon thruster (NEXT) long-duration test as of 736 kg of propellant throughput. In *48th AIAA/AME/SAE/ASEE Joint Propulsion Conference and Exhibit, Atlanta, GA* (2012).

[92] Shinohara, S. Helicon high-density plasma sources: physics and applications. *Advances in Physics: X 3*, 1 (2018), 1420424.

[93] Shinohara, S., Nishida, H., Tanikawa, T., Hada, T., Funaki, I., and Shamrai, K. Development of electrodeless plasma thrusters with high-density helicon plasma sources. *IEEE Transactions on Plasma Science 42* (2014), 1245–1254.

[94] Showers, M., Piotrowicz, P., Beers, C., Biewer, T., Caneses, J., Canik, J., Caughman, J., Donovan, D., Goulding, R., Lumsdaine, A., et al. Power accounting of plasma discharges in the linear device proto-mpex. *Plasma Physics and Controlled Fusion 60*, 6 (2018), 065001.

[95] Sigmund, P. Theory of sputtering. I. Sputtering yield of amorphous and polycrystalline targets. *Physical Review 184* (1969), 383–416.

[96] Squire, J. P., Carter, M., Chang Diaz, F. R., Corrigan, A., Dean, L., Farrias, J., Giambusso, M., McCaskill, G., and Yao, T. Steady-state testing at 100 kW in the VASIMR® VX-200SS project. In *AIAA Propulsion and Energy 2019 Forum, Indianapolis, IN, USA* (2019), p. 3810.

[97] Sternberg, N., Godyak, V., and Hoffman, D. Magnetic field effects on gas discharge plasmas. *Physics of Plasmas 13* (2006), 063511.

[98] Stix, T. H. *Waves in plasmas*. Springer Science & Business Media, 1992.

[99] Takahashi, K. Helicon-type radiofrequency plasma thrusters and magnetic plasma nozzles. *Reviews of Modern Plasma Physics 3*, 1 (2019), 1–61.

[100] Takahashi, K. Magnetic nozzle radiofrequency plasma thruster approaching twenty percent thruster efficiency. *Scientific reports 11*, 1 (2021), 1–12.

[101] Takahashi, K., and Ando, A. Enhancement of axial momentum lost to the radial wall by the upstream magnetic field in a helicon source. *Plasma Physics and Controlled Fusion 59*, 5 (2017), 054007.

[102] Takahashi, K., Charles, C., Boswell, R. W., Takao, Y., Fruchtman, A., Navarro-Cavallé, J., and Merino, M. Commentary: On helicon thrusters: Will they ever fly? *Frontiers in Physics 8* (2020), 277.

[103] Takahashi, K., Chiba, A., Komuro, A., and Ando, A. Axial momentum lost to a lateral wall of a helicon plasma source. *Physical review letters 114*, 19 (2015), 195001.

[104] Takahashi, K., Sugawara, T., and Ando, A. Spatially-and vector-resolved momentum flux lost to a wall in a magnetic nozzle rf plasma thruster. *Scientific reports 10*, 1 (2020), 1–11.

[105] Thakur, S. C., Paul, M., Hollmann, E., Lister, E., Scime, E., Sadhu, S., Steinberger, T., and Tynan, G. Ion heating in the pisces-rf liquid-cooled high-power, steady-state, helicon plasma device. *Plasma Sources Science and Technology 30*, 6 (2021), 065010.

[106] Thakur, S. C., Simmonds, M. J., Caneses, J. F., Chang, F., Hollmann, E. M., Doerner, R. P., Goulding, R., Lumsdaine, A., Rapp, J., and Tynan, G. R. PISCES-RF: a liquid-cooled high-power steady-state helicon plasma device. *Plasma Sources Science and Technology 30*, 5 (may 2021), 055014.

[107] Tonks, L. Theory of magnetic effects in the plasma of an arc. *Physical Review 56* (1939), 360–373.

[108] Tonks, L., and Langmuir, I. A general theory of the plasma of an arc. *Physical Review 34* (1929), 876–922.

[109] Trivelpiece, A., and Gould, R. Space charge waves in cylindrical plasma columns. *Journal of Applied Physics 30*, 11 (1959), 1784–1793.

[110] Tysk, S., Denning, M., Scharer, J., and Akhtar, K. Optical, wave measurements of helicon plasmas for a wide range of magnetic fields. *Physics of Plasmas 11*, 3 (2004), 878–887.

[111] Urbassek, H. M. Molecular-dynamics simulation of sputtering. *Nuclear Instruments and Methods in Physics Research Section B: Beam Interactions with Materials and Atoms 122*, 3 (1997), 427–441.

[112] Varga, P., Neidhart, T., Sporn, M., Libiselle, G., Schmid, M., Aumayr, F., and Winter, H. Sputter yields of insulators bombarded with hyperthermal multiply charged ions. *Physica Scripta T73* (1997), 307–310.

[113] Vidal, F., Johnston, T. W., Margot, J., Chaker, M., and Pauna, O. Diffusion modeling of an hf argon plasma discharge in a magnetic field. *IEEE transactions on plasma science 27*, 3 (1999), 727–745.

[114] Wang, S.-B., and Wendt, A. Control of ion energy distribution at substrates during plasma processing. *Journal of Applied Physics 88* (2000), 643–646.

[115] Wittmaack, K. Reliability of a popular simulation code for predicting sputtering yields of solids and ranges of low-energy ions. *Journal of applied physics 96*, 5 (2004), 2632–2637.

[116] Yamamura, Y., and Tawara, H. Energy dependence of ion-induced sputtering yields from monoatomic solids at normal incidence. Tech. rep., National Institute for Fusion Science, Japan, 1995.

[117] Zalm, P., Beckers, L., and Sanders, F. On the role of physical sputtering in reactive ion beam etching. *Nuclear Instruments and Methods 209/210* (1983), 561–565.

[118] Ziegler, J. F., Ziegler, M. D., and Biersack, J. P. Srim -the stopping and range of ions in matter (2010). *Nuclear Instruments and Methods in Physics Research Section B: Beam Interactions with Materials and Atoms 268*, 11-12 (2010), 1818–1823.

Appendix A

Derivation of Dispersion Relation for Helicon and Trivelpiece-Gould Waves

A.1. Introduction

Helicon waves are a category of righ-hand polarized (RHP) plasma waves which propagate along dc magnetic fields in bounded systems. They are related to so-called *whistler* waves which have been studied in atmospheric physics since the early XX century. A historical perspective on the early development of the theory and research related to helicon plasma waves is provided in the review paper from Boswell ([16]).

This section describes the behavior of helicon plasma waves through the derivation of their corresponding dispersion relation, with a particular emphasis on cylindrical geometries. This derivation will be obtained both from the simplified description of cold plasma waves in magnetic fields, as well as a more general approach based on Maxwell's equations and the equation of motion.

A.2. Cold Plasma Wave Approximation

This description of cold plasma waves in dc magnetic fields follows loosely the terminology and approach presented in Stix ([98]).

Equation set A.1 presents Maxwell's equations in differential form.

$$\begin{aligned}\nabla \cdot \mathbf{E} &= \frac{\rho}{\epsilon_0} \\ \nabla \times \mathbf{E} &= -\frac{\partial \mathbf{B}}{\partial t} \\ \nabla \cdot \mathbf{B} &= 0 \\ \nabla \times \mathbf{B} &= \mu_0 \mathbf{j} + \left(\frac{1}{c^2}\right)\left(\frac{\partial \mathbf{E}}{\partial t}\right)\end{aligned} \tag{A.1}$$

The magnetic field is aligned with the z axis, $\mathbf{B} = B_0\mathbf{k}$. The electric and magnetic fields will be linearized as $\mathbf{E} = \mathbf{E}_0 + \tilde{\mathbf{E}}_\mathbf{1}(\mathbf{r}, t)$ and $\mathbf{B} = \mathbf{B}_0 + \tilde{\mathbf{B}}_\mathbf{1}(\mathbf{r}, t)$, where $\mathbf{E}_0$ and $\mathbf{B}_0$ are the values at equilibrium and $\tilde{\mathbf{E}}_1$ and $\tilde{\mathbf{B}}_1$ are perturbations of type $e^{\omega t + m\theta + kz}$.

Application of the Fourier transform to set A.1 yields the following linearized expressions,

$$\imath \mathbf{k} \times \tilde{\mathbf{E}}_\mathbf{1} = \imath\omega \tilde{\mathbf{B}}_\mathbf{1} \tag{A.2}$$

$$\imath \mathbf{k} \times \tilde{\mathbf{B}}_\mathbf{1} = \mu_0 \tilde{\mathbf{j}}_\mathbf{1} + \left(-\frac{\imath\omega}{c^2}\right) \tilde{\mathbf{E}}_\mathbf{1} \tag{A.3}$$

Combining these expressions produces

$$\mathbf{k} \times \mathbf{k} \times \tilde{\mathbf{E}}_\mathbf{1} = \left(\frac{\mu_0 \omega}{\imath}\right) \tilde{\mathbf{j}}_\mathbf{1} - \left(\frac{\omega^2}{c^2}\right) \tilde{\mathbf{E}}_\mathbf{1} \tag{A.4}$$

The expression on the left side can be expanded as,

$$\begin{aligned}\mathbf{k} \times \mathbf{k} \times \tilde{\mathbf{E}}_\mathbf{1} = & \left(E_y k_x k_y - E_x k_y^2 - E_x k_z^2 + E_z k_x k_z\right) \mathbf{e_x} \\ & + \left(E_z k_z k_y - E_y k_z^2 - E_y k_x^2 + E_x k_x k_y\right) \mathbf{e_y} \\ & + \left(E_x k_x k_z - E_z k_x^2 - E_z k_y^2 + E_y k_y k_z\right) \mathbf{e_z}\end{aligned} \tag{A.5}$$

and then compacted to,

$$\mathbf{k} \times \mathbf{k} \times \tilde{\mathbf{E}}_\mathbf{1} = k^2 \left[\frac{\mathbf{kk}}{k^2} - \mathbb{1}\right] \cdot \tilde{\mathbf{E}}_\mathbf{1} \tag{A.6}$$

where $\mathbf{kk} = [k_i k_j]$ and $\mathbb{1} = [\delta_{ij}]$ is the unit tensor. Substituting expression A.6 in equation A.4 produces the general dispersion relation

$$-N^2\left[\frac{\mathbf{kk}}{k^2}-\mathbb{1}\right]\cdot\tilde{\mathbf{E}}_\mathbf{1}=\left(\frac{\imath}{\epsilon_0\omega}\right)\tilde{\mathbf{j}}_\mathbf{1}+\tilde{\mathbf{E}}_\mathbf{1} \tag{A.7}$$

where $N=\frac{ck}{\omega}$ is the *index of refraction* and $c^2=(\epsilon_0\mu_0)^{-1}$ has been applied.

Equation A.8 shows the two-species momentum equation, where $s=\{i,e\}$ stands for ions and electrons.

$$n_s m_s\left[\frac{\partial\mathbf{u}_s}{\partial t}+(\mathbf{u}_s\cdot\nabla)\,\mathbf{u}_s\right]=n_s q_s\left(\mathbf{E}_s+\mathbf{u}_s\times\mathbf{B}\right) \tag{A.8}$$

Several assumptions regarding the plasma at equilibrium are required to obtain the cold plasma approximation.

1. The plasma is quasineutral, therefore $n_{s0}=n_0$ for both species.
2. The plasma is isothermal, therefore $\nabla p_s=0$ for both species.
3. The electric field at equilibrium is null, $\mathbf{E}_0=\mathbf{0}$.
4. The magnetic field is uniform and constant, $\mathbf{B}=B_0\mathbf{e}_z$.

Linearizing equation A.8 while applying these assumptions yields,

$$m_s\left(\frac{\partial\mathbf{u}_{s1}}{\partial t}\right)=q_s\mathbf{E}_1+q_s\mathbf{u}_{s1}\times\mathbf{B} \tag{A.9}$$

Applying the Fourier transform to this result then produces,

$$-\imath\omega m_s\tilde{\mathbf{u}}_{\mathbf{s1}}=q_s\tilde{\mathbf{E}}_\mathbf{1}+q_s\tilde{\mathbf{u}}_{\mathbf{s1}}\times\tilde{\mathbf{B}} \tag{A.10}$$

For the sake of simplicity, tildes will be dropped from now on (all magnitudes represent their frequency-domain transformations). Noting that $\mathbf{u}_{s1}\times\mathbf{B}=(B_0u_{s1,y})\,\mathbf{e}_x-(B_0u_{s1,x})\,\mathbf{e}_y$, the previous expression can be simplified as

$$\mathbf{u}_{s1}=\left(\frac{q_s}{m_s}\right)\begin{pmatrix}-\imath\omega & -\Omega_s & 0\\ \Omega_s & -\imath\omega & 0\\ 0 & 0 & -\imath\omega\end{pmatrix}^{-1}\cdot\mathbf{E}_1 \tag{A.11}$$

where $\Omega_s=\frac{-|q_s|B_0}{m_s}$ is the *cyclotron frequency* for each species. Inversion of the matrix produces,

$$\mathbf{u}_{s1}=\left(\frac{q_s}{m_s}\right)\begin{pmatrix}\frac{\imath\omega}{\omega^2-\Omega_s^2} & -\frac{\Omega_s}{\omega^2-\Omega_s^2} & 0\\ \frac{\Omega_s}{\omega^2-\Omega_s^2} & \frac{\imath\omega}{\omega^2-\Omega_s^2} & 0\\ 0 & 0 & \frac{\imath}{\omega}\end{pmatrix}\cdot\mathbf{E}_1 \tag{A.12}$$

Defining the *mobility tensor* $\overline{\mu}_s$ as

$$\overline{\mu}_s = \left(\frac{q_s}{m_s}\right) \begin{pmatrix} \frac{\imath\omega}{\omega^2-\Omega_s^2} & -\frac{\Omega_s}{\omega^2-\Omega_s^2} & 0 \\ \frac{\Omega_s}{\omega^2-\Omega_s^2} & \frac{\imath\omega}{\omega^2-\Omega_s^2} & 0 \\ 0 & 0 & \frac{\imath}{\omega} \end{pmatrix} \tag{A.13}$$

equation A.12 becomes,

$$\mathbf{u}_{s1} = \overline{\mu}_s \cdot \mathbf{E}_1 \tag{A.14}$$

The total current density for the two-fluid plasma can be expressed as

$$\mathbf{j}_1 = \sum_s \left(q_s n_s \mathbf{u}_{s1}\right) = \sum_s \left[q_s n_s \left(\overline{\mu}_s \cdot \mathbf{E}_1\right)\right] \tag{A.15}$$

which can be condensed as the expression for *Ohm's Law* for the cold-plasma approximation,

$$\mathbf{j}_1 = \overline{\overline{\sigma}} \cdot \mathbf{E}_1 \tag{A.16}$$

where $\overline{\overline{\sigma}} = \sum_s q_s n_s \overline{\mu}_s$ is the *conductivity tensor*.

Now, substituting the expression for the current density in the general dispersion relation of electromagnetic waves, equation A.7, with that from Ohm's Law for the cold-plasma approxiomation, equation A.16, the nature of cold plasma waves can be further investigated.

$$-N^2 \left[\frac{\mathbf{kk}}{k^2} - \mathbb{1}\right] \cdot \mathbf{E_1} = \left(\frac{\imath\overline{\overline{\sigma}}}{\epsilon_0\omega}\right) \mathbf{E_1} + \mathbf{E_1} \tag{A.17}$$

which can be simplified as

$$\left\{N^2 \left[\frac{\mathbf{kk}}{k^2} - \mathbb{1}\right] + \overline{\overline{\epsilon}}\right\} \cdot \mathbf{E_1} = \mathbf{0} \tag{A.18}$$

where the *dielectric tensor*, $\overline{\overline{\epsilon}} = \left(\frac{\imath\overline{\overline{\sigma}}}{\epsilon_0\omega}\right) + \mathbb{1}$ has been defined. The terms of this dielectric tensor will be defined and analyzed, once again following the terminology established by Stix ([98]).

$$\bar{\bar{\epsilon}} = \begin{pmatrix} \epsilon_1 & -\imath\epsilon_2 & 0 \\ \imath\epsilon_2 & \epsilon_1 & 0 \\ 0 & 0 & \epsilon_3 \end{pmatrix} = \begin{pmatrix} S & -\imath D & 0 \\ \imath D & S & 0 \\ 0 & 0 & P \end{pmatrix} \tag{A.19}$$

where S, D and P are respectively the *sum*, *difference* and *plasma* terms which can be defined as follows when the corresponding terms are expanded.

$$S = 1 - \sum_s \frac{\omega_{p,s}^2}{\omega^2 - \Omega_s^2} \tag{A.20}$$

$$D = \sum_s \left(\frac{\Omega_s}{\omega}\right)\left(\frac{\omega_{p,s}^2}{\omega^2 - \Omega_s^2}\right) \tag{A.21}$$

$$P = 1 - \sum_s \left(\frac{\omega_{p,s}^2}{\omega^2}\right) \tag{A.22}$$

where use has been made of the expression for the *plasma frequency*, $\omega_{p,s}^2 = \dfrac{q_s^2 n_s}{m_s \epsilon_0}$.

In the absence of an externally-applied magnetic field, $\mathbf{B} = \mathbf{0}$, the cyclotron frequency for each species becomes null, $\Omega_s = 0$, and therefore the sum and plasma terms become equal while the difference term becomes null. This produces a symmetric dielectric tensor, essentially describing an *isotropic* plasma.

$$S = P = 1 - \sum_s \left(\frac{\omega_{p,s}^2}{\omega^2}\right) \tag{A.23}$$

$$D = 0 \tag{A.24}$$

$$\Rightarrow \bar{\bar{\epsilon}} = P\mathbb{1} \tag{A.25}$$

For the case when an external magnetic field is applied and without loss of generality, the magnetic field vector will be considered parallel to the z direction and the wave vector located within the xz plane, $\mathbf{k} = (k\sin\theta)\mathbf{e_x} + (k\cos\theta)\mathbf{e_z}$, as depicted in figure A.1.

The introduction of the angle θ between the wave vector $\mathbf{k}$ and the magnetic field vector $\mathbf{B}$ allows the simplification of equation A.18 as

$$\begin{pmatrix} S - N^2\cos^2\theta & -\imath D & N^2\sin\theta\cos\theta \\ \imath D & S - N^2 & 0 \\ N^2\sin\theta\cos\theta & 0 & P - N^2\sin^2\theta \end{pmatrix} \cdot \mathbf{E}_1 = 0 \tag{A.26}$$

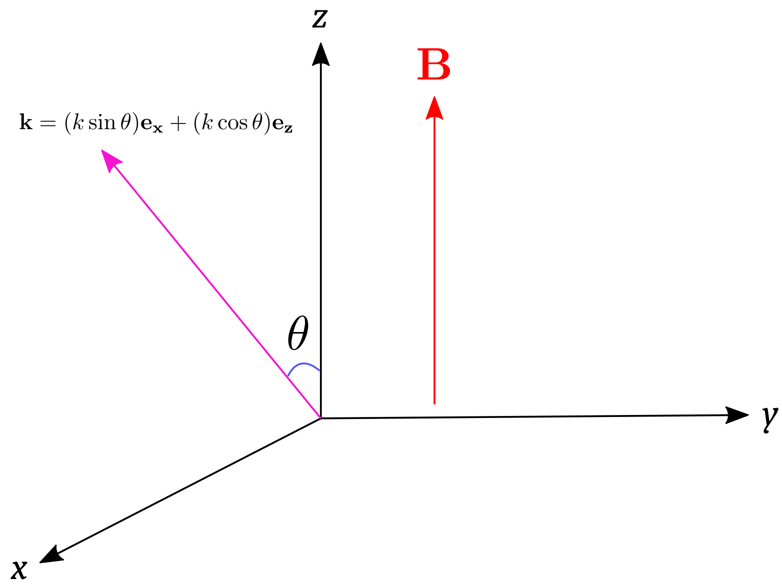

Figure A.1: Vector quantities involved in the description of cold plasma waves in the presence of an external magnetic field.

The conditions for the propagation of the cold plasma wave will be those that satisfy equation A.26. Beyond the obvious solution $\mathbf{E}_1 = \mathbf{0}$, the *determinant* of the matrix in this equation must become null in order for the expression to be valid.

Let $R = S + D$, $L = S - D$, and therefore $S^2 - D^2 = RL$, $S = (1/2)(R + L)$ and $D = (1/2)(R - L)$. Introducing these quantities into the expression for the determinant of the matrix in equation A.26, produces the following quadratic expression in N^2,

$$\left(S\sin^2\theta + P\cos^2\theta\right)N^4 - \left[RL\sin^2\theta + SP\left(1+\cos^2\theta\right)\right]N^2 + PRL = 0 \tag{A.27}$$

Solutions for these equation could be found using the general formula for quadratic equations

$$N^2 = \frac{B \pm \sqrt{\Delta}}{2A}$$

where the coefficients A, B and the discriminant Δ are defined as follows,

$$\begin{aligned}
A &= S\sin^2\theta + P\cos^2\theta \\
B &= RL\sin^2\theta + SP\left(1+\cos^2\theta\right) \\
C &= PRL \\
\Delta^2 &= B^2 - 4AC
\end{aligned}$$

However, a more practical approach for the analysis of this equation can be obtained by manipulating the trigonometrical expressions contained in equation A.27. Following [54], expressions can be found for $\sin^2\theta$ and $\cos^2\theta$ which can be combined to produce equation A.28 for $\tan^2\theta$.

$$\tan^2\theta = \frac{-P\left(N^2-R\right)\left(N^2-L\right)}{\left(SN^2-RL\right)\left(N^2-P\right)} \tag{A.28}$$

The advantage of the expression in equation A.28 is that the analysis of the angle θ and the corresponding terms in its numerator and denominator easily produces simple expressions for the desired dispersion relations, without the need of solving the quadratic expression in equation A.27.

For the case of parallel cold plasma waves, $\theta = 0$ and therefore $\tan^2\theta = 0$. This can only happen if $N^2 = R$ or $N^2 = L$, which respectively produce the so-called **right-handed** waves and **left-handed** waves.

For the case of perpendicular cold plasma waves, $\theta = \pi/2$ and therefore $\tan^2\theta \to \infty$. This is produced when $N^2 = RL/S$, termed the **extraordinary wave**, or when $N^2 = P$ which is called the **ordinary wave**.

Equation A.28 also depicts the conditions present at *resonances*, in the limit where $N \to \infty$. This produces $\tan^2\theta \approx -P/S$. For the case of waves parallel to the magnetic field, $\theta = 0$ and resonances are produced if $P = 0$ or if $S \to \infty$; this last condition is equivalent to the cases when $R \to \infty$ or $L \to \infty$.

A.3. Derivation from Maxwell Equations

This section derives the dispersion equation for the helicon ("H") and Trivelpiece-Gould ("TG") modes following the approach published by Chen and Arnush ([36]).

Maxwell's equations can be stated as

$$\begin{aligned}
\nabla \cdot \mathbf{B} &= \mathbf{0} && \text{(A.29)}\\
\nabla \times \mathbf{E} &= \imath\omega\mathbf{B} && \text{(A.30)}\\
\nabla \times \mathbf{B} &= \mu 0\left(\mathbf{j} - \imath\omega\epsilon_0\mathbf{E}\right) = -\imath\omega\epsilon_0\mu_0\epsilon \cdot \mathbf{E} && \text{(A.31)}
\end{aligned}$$

where all symbols maintain their usual meaning in the field of electrodynamics. The momentum equation for the electrons can be expressed as

$$-\imath\omega m_e\mathbf{u_e} = -e\left(\mathbf{E} + \mathbf{u_e} \times \mathbf{B}\right) - m_e\nu\mathbf{u_e} \tag{A.32}$$

where ν is the collisional frequency for the electrons. By applying the cold plasma approximation ($\mathbf{u_i} \approx \mathbf{0}$), the current can be defined as $\mathbf{j} = -en\mathbf{u_e}$.

The substitutions $\Omega_e = eB_0/m_e$, $\delta_r = \omega/\Omega_e$ and $\delta = (\omega + \imath\nu)/\Omega_e$ transform A.32 into

$$\mathbf{E} = -\left(\frac{B_0}{en_0}\right)(\imath\delta\mathbf{j} + \hat{\mathbf{e}}_{\mathbf{z}} \times \mathbf{j}) \tag{A.33}$$

Neglecting the displacement current term in equation A.31 and combining this result with equation A.30 and equation A.33 produces

$$-\left(\frac{B_0}{en_0\mu_0}\right)\{\imath\delta\nabla \times \nabla \times \mathbf{B} + \nabla \times [\hat{\mathbf{e}}_{\mathbf{k}} \times (\nabla \times \mathbf{B})]\} = \imath\omega\mathbf{B} \tag{A.34}$$

Applying the properties of the curl operation in the frequency domain, it can be demonstrated that $\nabla \times [\hat{\mathbf{e}}_{\mathbf{k}} \times (\nabla \times \mathbf{B})] = -\imath k(\nabla \times \mathbf{B})$, where k is the axial wave number in the assumption of perturbations of the type $\mathbf{A} = \mathbf{A}_0 + \tilde{A}\exp[\imath(kz + m\theta - \omega t)]$ for all physical quantities involved. Equation A.34 then becomes

$$-\left(\frac{B_0}{en_0\mu_0}\right)\{\imath\delta\nabla \times \nabla \times \mathbf{B} + \imath k\nabla \times \mathbf{B}\} = \imath\omega\mathbf{B} \tag{A.35}$$

This expression will be simplified through the electron plasma frequency $\omega_p^2 = n_0e^2/(\epsilon_0 m_e)$, the skin number $k_s = \omega_p/c$ and the low frequency whistler wave number defined by $\delta k_s^2 = \omega n_0\mu_0 e/B_0 = k_w^2$. Equation A.35 then becomes

$$\delta\nabla \times \nabla \times \mathbf{B} - k\nabla \times \mathbf{B} + k_w^2\mathbf{B} = \mathbf{0} \tag{A.36}$$

This is a vector-valued, second-order homogeneous ordinary differential equation with the characteristic equation

$$\delta\beta^2 - k\beta + k_w^2 = 0 \tag{A.37}$$

which produces the roots

$$\beta_{1,2} = \frac{k \mp \sqrt{k^2 - 4\delta k_w^2}}{2\delta} = \left(\frac{k}{2\delta}\right)\left[1 \mp \sqrt{1 - 4\delta\left(\frac{k_w^2}{k^2}\right)}\right] \tag{A.38}$$

Applying the binomial expansion to the square root term in the right side of the equation, the following simplified approximation can be obtained

$$\beta_{1,2} \approx \left(\frac{k}{2\delta}\right)\left\{1 \mp \left[1 - 2\delta\left(\frac{k_w^2}{k^2}\right)\right]\right\} \approx \left\{\begin{array}{l}\frac{k_w^2}{k}\\ \frac{k}{\delta} + \frac{k_w^2}{k}\end{array}\right. \tag{A.39}$$

Typically, $k_w^2/k \ll 1$ and therefore $\beta_2 \approx k/\delta$. Solution β_1 corresponds to the *helicon* of H-mode, while β_2 is the *Trivelpiece-Gould* or TG-mode.

The limit of the H-mode for the zero-electron mass limit is

$$\beta_H = \frac{k_w^2}{k} = \frac{\omega}{k}\frac{n_0 e \mu_0}{B_0} \equiv \alpha \tag{A.40}$$

which is the typical dispersion relation for helicon plasma waves with β_H a total wave number and k the wave number component in the direction of $\mathbf{B}$.

The TG-mode expression produces,

$$\omega = \Omega_c \cos\theta \tag{A.41}$$

which clearly defines the TG-mode as an electron cyclotron wave which is typically present at the boundary edges of the system and is more relevant a low values of the magnetic field $\mathbf{B}$.

The general solution of the ODE from equation A.36 can be obtained through the factorization

$$(\beta_1 - \nabla\times)\,(\beta_2 - \nabla\times)\,\mathbf{B} = 0 \tag{A.42}$$

where $\mathbf{B} = \mathbf{B_1} + \mathbf{B_2}$ where $\nabla \times \mathbf{B}_j = \beta_j \mathbf{B}_j$ for $j = 1, 2$. Taking the curl of these expressions, vector Helmholtz equations can be obtained for each one of the mode as $\nabla^2 \mathbf{B}_j + \beta_j^2 \mathbf{B}_j = 0$. This equation can be solved in cylindrical coordinates to obtain the expressions for the fields $\mathbf{B}$ and $\mathbf{E}$. The complete derivation is described in the published works by Chen et al. ([5, 32, 33, 36]).

Appendix B

Modeling of cylindrical magnetized plasmas

B.1. Introduction

The derivation of the 2D fluid-dynamic model for cylindrical magnetized plasmas will be presented, following the work of Ahedo and Navarro-Cavallé ([2, 3, 80]. These expressions are based in the fluid momentum conservation equations for a steady-state plasma in cylindrical coordinates. Through a variable separation process, specific models are developed for the description of the relevant plasma parameters as a function of the radial and axial coordinates.

B.2. Derivation

B.2.1. General Fluid Equations

The derivation starts with the contiuity and momentum equations for the plasma. The continuity equation can be expressed as

$$\nabla \cdot (n_e \mathbf{u}_e) = \nabla \cdot (n_i \mathbf{u}_i) = -\nabla \cdot (n_n \mathbf{u}_n) = n_e \left(n_n R_{ion} - \nu_w \right) \tag{B.1}$$

which expresses that the divergence of the momentum of electrons (or ions) is the opposite to the corresponding term for the neutrals, and that all these terms can be explained through the *ionization rate of reaction* $n_n R_{ion}$ (where R_{ion} has units of volume per unit time) and the *rate of wall recombination* ν_w. n_j and $\mathbf{u}_j$ are respectively the density and velocity vectors of species $j = e, i, n$.

The continuity equations for the plasma can be expressed as

$$\nabla \cdot (m_j n_j \mathbf{u}_j \mathbf{u}_j) = -\nabla \mathbf{p}_j + q_j n_j \left(-\nabla \phi + \mathbf{u}_j \times \mathbf{B} \right) - \mathbf{S}_j \tag{B.2}$$

where $\nabla \mathbf{p}_j$ is the pressure gradient term for species j, $p_j = n_j T_j$ with T_j is the temperature of species j in energy units, q_j is the charge per particle for species j (where $q_i = e$, $q_e = -e$ and $q_n = 0$) $-\nabla\phi$ is the gradient of the electric potential, $\mathbf{B} = B_0 \hat{\mathbf{e}}_z$ is the constant axial magnetic field along coordinate z, and the term $\mathbf{S}_j$ collects the collisional processes corresponding to species j. The previous expression can be expanded as follows,

$$n_j m_j \left[\frac{\partial \mathbf{u}_j}{\partial t} + (\mathbf{u}_j \cdot \nabla)\,\mathbf{u}_j \right] = -\nabla \mathbf{p}_j + q_j n_j \left(-\nabla\phi + \mathbf{u}_j \times \mathbf{B} \right) - \mathbf{S}_j \tag{B.3}$$

The expression between brackets in the left side of the previous equation is the material derivative or convective derivative of the particule velocity vector $\mathbf{u}_j$. Its proper derivation is presented at the end of this Appendix in section B.2.5.

B.2.2. Model Assumptions

The derivation of the cylindrical plasma models is based on the the set of assumptions listed in Table B.1.

Table B.1: Assumptions introduced in the derivation of the cylindrical magnetized plasma models.

	Assumption	Implication
1	Axial symmetry.	$\partial/\partial\theta = 0$
2	Cold neutrals, axial neutral velocity.	$T_n \ll T_i, T_e$ and $\mathbf{u}_n = u_n \hat{\mathbf{e}}_z$
3	Cold plasma approximation.	$T_i \ll T_e \Rightarrow p_i \ll p_e$
4	Longitudinal ambipolarity.	$\mathbf{j} = j_\theta \hat{\mathbf{e}}_\theta \Rightarrow u_{ir} = u_{er} = u_r$ and $u_{iz} = u_{ez} = u_z$
5	Variable separation for the density function.	$n(r,z) = n_z(z) n_r(r,z)$
		with $n_r(r,z)$ non-dimensional and $\int_0^R n_r(r,z) r dr = R^2/2$
6	Variable separation for $\phi(r,z)$, null potential at axis.	$\phi(r,z) = \phi_z(z) + \phi(r,z)$ and $\phi_r(0,z) = 0$
7	Magnetic effects on ions are negligible.	$u_{i\theta} \ll u_{e\theta} = u_\theta$
8	Negligible longitudinal electron inertia.	Inertia terms (left side terms) on coordinates r and z negligible in equation B.3.
	Azimuthal electron inertia retained.	Non-zero inertia terms (left side terms) on coordinate θ in equation B.3.
9	Radial variations predominant for $n_r, \phi_r, u_r, u_\theta$.	$\partial n_r/\partial z \ll \partial n_r \partial r$
		$\partial \phi_r/\partial z \ll \partial \phi_r/\partial r$
		$\partial u_j/\partial z \ll \partial u_j/\partial r$ for $j = r, \theta$
	Axial variations predominant for u_z.	$\partial u_z/\partial u_r \ll \partial u_z/\partial z$
10	Steady-state conditions.	$\partial/\partial t = 0$

By applying this set of assumptions and expanding the convective derivatives from equation B.3, three sets of equations can be obtained, for each one of the species present in the plasma and corresponding to the radial r, azimuthal θ and axial z coordinates, as well as the corresponding expression for the continuity equation. The equations corresponding to the electrons are

$$
\begin{aligned}
0 &= e\left(\frac{\partial \phi}{\partial r}\right) - eB_0 u_{\theta e} - T_e\left(\frac{\partial n}{\partial r}\right) - m_e n_n \left(R_{ion} + R_{en}\right) u_r & \text{(B.4)} \\
m_e\left[u_r\left(\frac{\partial u_\theta}{\partial r}\right) + \frac{u_\theta u_r}{r}\right] &= eu_r B_0 - m_e n_n \left(R_{ion} + R_{en}\right) u_\theta - m_e n R_{ei} u\theta & \text{(B.5)} \\
0 &= ne\left(\frac{\partial \phi}{\partial z}\right) - T_e\left(\frac{\partial n}{\partial z}\right) - m_e n n_n \left(R_{ion} + R_{en}\right)\left(u_z - u_n\right) & \text{(B.6)} \\
\left(\frac{1}{r}\right)\frac{\partial}{\partial r}\left(rnu_r\right) + \frac{\partial}{\partial z}\left(nu_z\right) &= nn_n R_{ion} - n\nu_w & \text{(B.7)}
\end{aligned}
$$

where $\nu_w = \nu_w(z)$ is the *wall recombination frequency*, a parameter describing the rate of production of neutrals at the system boundaries as they are impacted by ions and neutrals. $R_{ion}, R_{ei}, R_{en}, R_{in}$ are respectively the collisional rates for ionization, and electron-ion, electron-neutral and ion-neutral collisions. Ahedo et al. provide a set of approximations to these collisional rates as a function of the electron temperature T_e, which are listed below.

$$
\begin{aligned}
R_{ion} &= \sqrt{\frac{8T_e}{\pi m_e}}\sigma_{ion}\left[1 + \frac{T_e E_{ion}}{\left(T_e + E_{ion}\right)^2}\right]\exp\left(-\frac{E_{ion}}{T_e}\right) & \text{(B.8)} \\
R_{en} &= \sqrt{\frac{8T_e}{\pi m_e}}\sigma_{en} & \text{(B.9)} \\
R_{ei} &= \left(\frac{T_e}{1\ eV}\right)^{-3/2} \ln\Lambda \cdot (9.2 \times 10^{-14}\ \mathrm{m^3 s^{-1}}) & \text{(B.10)} \\
R_{in} &= c_{in}\left(k_2 - k_1 \log_{10} c_{in}\right)^2 & \text{(B.11)}
\end{aligned}
$$

where, in the case of argon gas, the constant parameters are given by $E_{ion} = 15.76$ eV, $\sigma_{ion} = 2.8 \times 10^{-20}$ m^2, $\sigma_{en} = 15 \times 10^{-20}$ m^2, $k_2 = 10.5 \times 10^{-10}$ m, and $k_1 = 1.67 \times 10^{-10}$ m. The paramter $c_{in} = |\mathbf{u}_i - \mathbf{u}_n|$ must be given in units of m/s. For scenarios of constante T_e, most of these collisional rates will be constant as well. Alternative correlations for these collisional rates have also been published by Gudmundsson ([55]) and are presented at the end of Appendix C.

The corresponding set of equations for the ions are

$$
\begin{aligned}
m_i u_r\left(\frac{\partial u_r}{\partial r}\right) &= -e\left(\frac{\partial \phi}{\partial r}\right) - m_i n_n\left(R_{in} + \frac{\nu_w}{n_n}\right)u_r & \text{(B.12)} \\
m_i u_z\left(\frac{\partial u_z}{\partial z}\right) &= -e\left(\frac{\partial \phi}{\partial z}\right) - m_i n_n\left(R_{in} + \frac{\nu_w}{n_n}\right)\left(u_z - u_n\right) & \text{(B.13)}
\end{aligned}
$$

When applying the corresponding assumptions, the equation for the θ coordinate for the ions becomes degenerate and has been omitted from the previous set. The continuity equation has also been omitted as it is the same as B.7.

The set of equations for the neutrals take only the axial coordinate and the continuity equation,

$$
\begin{aligned}
u_n \left(\frac{\partial u_n}{\partial z}\right) &= n\left(R_{in} + \frac{\nu_w}{n_n}\right)(u_n - u_z) && \text{(B.14)}\\
\frac{\partial}{\partial z}(n_n u_n) &= -n n_n R_{ion} + n\nu_w && \text{(B.15)}
\end{aligned}
$$

where the term involving neutral-electron collisions has been dropped in equation B.14 since $m_n \gg m_e$ and the effects on the neutral inertia are negligible.

B.2.3. Radial Model

Derivation

Taking the radial component of the continuity equation B.7 and applying assumption 5 produces the expression

$$
\left(\frac{1}{r}\right)\frac{\partial}{\partial r}(r n_r u_r) = n_r \nu_w \tag{B.16}
$$

Adding equations B.4 and B.12 produces

$$
u_r\left(\frac{\partial u_r}{\partial r}\right) = -u_B^2\left[\frac{\partial(\ln r)}{\partial r}\right] - \left(\frac{eB_0}{m_i}\right)u_\theta + \left(\frac{m_e}{m_i}\right)\left(\frac{u_\theta^2}{r}\right) - n_n\left(R_{ion} + R_{in}\right)u_r \tag{B.17}
$$

Equation B.5 produces

$$
u_r\left(\frac{\partial u_\theta}{\partial r}\right) = \left(\frac{eB_0}{m_e}\right)u_r - \left[n_n\left(R_{en} + R_{ion}\right) + n_r R_{ei}\right]u_\theta - \frac{u_\theta u_r}{r} \tag{B.18}
$$

When considering that $u_r(\partial u_r/\partial r) \ll u_\theta^2/r$ and also that the effect electron-neutral collisional processes is negligible when compared to the electrostatic, magnetic and pressure terms in the momentum equation, equation B.4 becomes

$$
e\left(\frac{\partial \phi_r}{\partial r}\right) = T_e\frac{\partial}{\partial r}\left[\ln\left(n_r\right)\right] + eB_0 u_\theta - \left(\frac{m_e u_\theta^2}{r}\right) \tag{B.19}
$$

Equations B.17 through B.19 form the basis of the radial model.

Rescaling

The radial model will now be rescaled using the auxiliary variables $u'_\theta = u_\theta \sqrt{m_e/m_i}$, the Bohm velocity $u_B = \sqrt{Te/m_i}$ and the lower hybrid frequency $\omega_{lh} = eB_0/\sqrt{m_i m_e}$.

Combining equations B.17 and B.19

$$u_r \left(\frac{\partial u_r}{\partial r} \right) = - \left(\frac{e}{m_i} \right) \left(\frac{\partial \phi_r}{\partial r} \right) - n_n \left(R_{in} + R_{ion} \right) u_r \tag{B.20}$$

Equation B.19 produces

$$\left(\frac{e}{m_i} \right) \left(\frac{\partial \phi_r}{\partial r} \right) = u_B^2 \left[\frac{\partial \left(\ln n_r \right)}{\partial r} \right] + \omega_{lh} u'_\theta - \frac{{u'_\theta}^2}{r} \tag{B.21}$$

Equation B.18 produces

$$u_r \left(\frac{\partial u'_\theta}{\partial r} \right) = \omega_{lh} u_r - \left[n_n \left(R_{en} + R_{ion} \right) + n_r R_{ei} \right] u'_\theta - \left(\frac{u'_\theta u_r}{r} \right) \tag{B.22}$$

Combining equations B.16, B.21 and B.22 produces

$$\left[\left(\frac{u_B^2}{u_r} \right) - u_r \right] \left(\frac{\partial u_r}{\partial r} \right) = \omega_{lh} u'_\theta + n \left(R_{in} + R_{ion} \right) u_r + \nu_w \left(\frac{u_B^2}{u_r} \right) - \left(\frac{1}{r} \right) \left({u'_\theta}^2 + u_B^2 \right) \tag{B.23}$$

The previous four equations constitute the rescaled radial model.

Non-dimensional Model

The previous rescaled model will now be normalized through the following variable substitution: $\hat{\omega}_{lh} = \omega_{lh}(R/u_B)$, $\hat{u'_\theta} = u'_\theta/u_B$, $\hat{u_r} = u_r/u_B$, $\hat{r} = r/R$, $\hat{\phi} = \phi/T_e$, $\hat{\nu_w} = \nu_w R/u_B$, and $\hat{n} = n/n_{r0}$ with n_{r0} the reference on-axis plasma density.

Equation B.16 produces the non-dimensional expression for the radial continuity equation,

$$\left(\frac{1}{\hat{r}} \right) \frac{\partial}{\partial \hat{r}} \left(\hat{r} \hat{n_r} \hat{u_r} \right) = \hat{n_r} \hat{\nu_w} \tag{B.24}$$

Equation B.23 produces

$$\left[\frac{1}{\hat{u_r}} - \hat{u_r} \right] \left(\frac{\partial \hat{u_r}}{\partial \hat{r}} \right) = \hat{\omega_{lh}} \hat{u_\theta} + \hat{\nu_i} \hat{u_r} + \left(\frac{\hat{\nu_w}}{\hat{u_r}} \right) - \left(\frac{{\hat{u_\theta}}^2}{\hat{r}} \right) - \frac{1}{\hat{r}} \tag{B.25}$$

Equation B.22 produces

$$\hat{u_r}\left(\frac{\partial \hat{u_r}}{\partial \hat{r}}\right) = \hat{\omega_{lh}}\hat{u_r} - \hat{\nu_e}\hat{u_\theta} - \left(\frac{\hat{u_\theta}\hat{u_r}}{\hat{r}}\right) \tag{B.26}$$

Equation B.21 produces

$$0 = -\left[\frac{\partial\left(\ln\hat{n}\right)}{\partial\hat{r}}\right] + \frac{\partial\hat{\phi}}{\partial\hat{r}} - \hat{\omega_{lh}}\hat{u_\theta} + \frac{u_\theta^2}{\hat{r}} \tag{B.27}$$

Equation B.20 produces

$$\left(\frac{\partial\hat{\phi}}{\partial\hat{r}}\right) = -\left(\frac{\partial\hat{u_r}}{\partial\hat{r}}\right) - \hat{\nu_i}\hat{u_r} \tag{B.28}$$

Equations B.24 through B.28 constitute the non-dimensional radial model. Boundary conditions for this model express that the following parameters are null at the $\hat{r} = 0$ coordinate, $\hat{u_r} = \hat{u_\theta} = \hat{\phi} = \ln\left(\hat{n}\right) = 0$, and the Bohm Sheath Criterion $\hat{u_r}(\hat{r} \to 1) \approx 1$.

Asymptotical Model

Asymptotical expressions can be found for the case of highly magnetized cylindrical plasmas, where $\hat{\omega_{lh}} \gg 1$ and $\hat{\nu_e}, \hat{\nu_i} \approx O(1)$. The electron inertia terms can then be removed from the left side of equation B.27 and the ambipolar potential term $\hat{\phi}$ can also be removed.

Equation B.27 produces then

$$0 = -\left[\frac{\partial\left(\ln\hat{n_r}\right)}{\partial\hat{r}}\right] - \hat{\omega_{lh}}\hat{u_\theta} \tag{B.29}$$

Equation B.26 produces then

$$\hat{u_r} = \left(\frac{\hat{\nu_e}}{\hat{\omega_{lh}}}\right)\hat{u_\theta} \tag{B.30}$$

Combining equations B.24, B.29 and B.30 prduces the expression

$$\left(\frac{\partial^2\hat{n_r}}{\partial\hat{r}^2}\right) + \left(\frac{1}{\hat{r}}\right)\left(\frac{\partial\hat{n_r}}{\partial\hat{r}}\right) + a_0^2\hat{n_r} = 0 \tag{B.31}$$

where $a_0^2 = (\hat{\nu_w}/\hat{\nu_e})\hat{\omega_{lh}}^2$. This is a Bessel equation, with the following solution

$$\hat{n_r} = J_0\left(a_o \hat{r}\right) \tag{B.32}$$

where J_0 is the Bessel function of the first kind of order zero, and $a_0 \approx 2.405$ is the first zero of J_0. Combining equations B.32 and B.29, and applying the recursive properties of Bessel functions and their derivatives, the following expression can be obtained

$$\hat{u_\theta} = \frac{a_0}{\hat{\omega_{lh}}}\left[\frac{J_1\left(a_0 \hat{r}\right)}{J_0\left(a_0 \hat{r}\right)}\right] \tag{B.33}$$

Equations B.32, B.33 and B.30 constitute the asymptotic radial model for magnetized plasmas, providing expressions for the parameters $\hat{n}$, $\hat{u_\theta}$ and $\hat{u_r}$.

B.2.4. Axial Model

Derivation

Combining equations B.7 and B.15 and projecting it onto the axial coordinate, the following expression is obtained

$$\frac{\partial}{\partial z}\left(n_z u_z + n_n u_n\right) = 0 \tag{B.34}$$

Integrating along the axial coordinate, an expression is found for the axial flow of heavy particles

$$n_z u_z + n_n u_n = g_0 \tag{B.35}$$

where $g_0 = \dot{m}/(m_i \pi R^2)$ is the axial flow of heavy particles (ions or neutrals) through the cylindrical cross-section of the system.

Projecting equation B.7 into the axial coordinate produces

$$\frac{\partial}{\partial z} = n_z\left(n_n R_{ion} - \nu_w\right) \tag{B.36}$$

Adding equations B.6 and B.13, the following expression can be obtained

$$u_z\left(\frac{\partial u_z}{\partial z}\right) = -u_B^2 \frac{\partial}{\partial z}\left[\ln\left(n_z\right)\right] - n_n\left(R_{in} + R_{ion}\right)\left(u_z - u_n\right) \tag{B.37}$$

Projecting equation B.14 into the axial coordinate (where $n_r = 1$) produces

$$u_n \left(\frac{\partial u_n}{\partial z} \right) = -n_z \left[R_{in} \left(u_n - u_z \right) + \left(\frac{\nu_w}{n_n} \right) u_n \left(1 - \alpha_w \right) \right] \tag{B.38}$$

where $\alpha_w u_n$ is the effective axial velocity of the neutrals created from recombination processes at the system boundary wall.

Substracting equation B.13 from equation B.6, applying assumption 5 and taking $m_e/m_i \ll 1$ produces

$$T_e \frac{\partial}{\partial z} \left[\ln \left(n_z \right) \right] = e \left(\frac{\partial \phi_z}{\partial z} \right) \tag{B.39}$$

Multiplying equation B.37 by the term u_z and combining with equation B.36 produces

$$\left(u_B^2 - u_z^2 \right) \left(\frac{\partial u_z}{\partial z} \right) = n_n u_z \left(R_{in} + R_{ion} \right) \left(u_z - u_n \right) + u_B^2 \left(n_n R_{ion} - \nu_w \right) \tag{B.40}$$

Now, multiplying equation B.37 by the term n_z produces

$$\left(u_B^2 - u_z^2 \right) \left(\frac{\partial n_z}{\partial z} \right) = -n_z \left[u_z \left(n_n R_{ion} - \nu_w \right) + n_n \left(R_{in} + R_{ion} \right) \left(u_z - u_n \right) \right] \tag{B.41}$$

Equation B.38 produces

$$n_n u_n \left(\frac{\partial u_n}{\partial z} \right) = n_z \left[u_n \nu_w \left(\alpha_w - 1 \right) + \left(u_z - u_n \right) n_n R_{in} \right] \tag{B.42}$$

Equations B.39 through B.42 form the basis of the Axial model. Boundary conditions for this model are defined at the upstream (closed) and downstream (open) ends of the cylindrical analysis domain: $u_{n,us} = u_{n0}$, $u_{z,us} = -u_B$, $u_{z,ds} = u_B$.

Non-dimensional Model

The Axial model will be normalized using the following variable substitutions: $\hat{z} = z/L$, $\hat{n_z} = n_z/n_0$, $\hat{n_n} = n_n/n_{n0}$, $\hat{u_z} = u_z/u_B$, $\hat{u_n} = u_n/u_{n0}$, $\hat{\nu_w} = \nu_w R/u_B$, and by introducing the terms $L_\star = u_B/(R_{ion} n_{n0})$ as the *effective ionization mean free path*, $n_0 = g_0/u_B$ as the *reference plasma density* and $n_{n0} = g_0/u_{n0}$ as the *reference neutral density*.

Equation B.40 then produces the normalized expression

$$\left(1 - \hat{u_z}^2 \right) \left(\frac{\partial \hat{u_z}}{\partial \hat{z}} \right) = \left(\frac{L}{L_\star} \right) \left[\hat{n_n} \hat{u_z} \left(\frac{R_{in}}{R_{ion}} + 1 \right) \left(\hat{u_z} - \frac{u_{n0} \hat{u_n}}{u_B} \right) + \hat{n_n} \right] - \left(\frac{L}{R} \right) \hat{\nu_w} \tag{B.43}$$

Equation B.41 produces the expression

$$\left(1-\hat{u_z}^2\right)\left(\frac{\partial \hat{n_z}}{\partial \hat{z}}\right) = -\left(\frac{L}{L_\star}\right)\hat{n_n}\hat{n_z}\left[\hat{u_z}+\left(\hat{u_z}-\frac{u_{n0}\hat{u_n}}{u_B}\right)\left(\frac{R_{in}}{R_{ion}}+1\right)\right]+\left(\frac{L}{R}\right)\hat{n_z}\hat{\nu_w}\hat{u_z} \tag{B.44}$$

Equation B.42 produces the expression

$$\hat{n_n}\hat{u_n}\left(\frac{\partial \hat{u_n}}{\partial \hat{z}}\right) = \hat{n_z}\left[\hat{n_n}\left(\frac{Lu_Bn_0}{L_\star n_{n0}u_{n0}}\right)\left(\hat{u_z}-\frac{u_{n0}\hat{u_n}}{u_B}\right)\left(\frac{R_{in}}{R_{ion}}\right)+\hat{u_n}\hat{\nu_w}\left(\alpha_w-1\right)\left(\frac{Ln_0}{Rn_{n0}}\right)\right] \tag{B.45}$$

Equation B.35 produces the expression

$$\hat{n_n} = 1-\hat{n_z}\hat{u_z} \tag{B.46}$$

The normalized Axial model is constituted by equations B.43 to B.46.

Asymptotical Model

The asymptotical model is based on the assumption that T_e and B_0 are large enough that the following relationships are valid: $\nu_w/(n_nR_{ion}) \ll 1$, $R_{in,s}/R_{ion} \ll u_{n0}/u_B \ll 1$, $\alpha_w = 1$ and $\hat{\nu_w} \to 0$. The process of constructing the asymptotical axial model requires two succesive variable substitutions. The first auxiliary variable ζ is defined through the expression

$$\frac{\partial \hat{z}}{\partial \zeta} = 1-\hat{u_z}^2 \tag{B.47}$$

Equation B.43 then produces

$$\frac{\partial \hat{u_z}}{\partial \zeta} = \left(\frac{L}{L_\star}\right)\hat{n_n}\left(\hat{u_z}^2+1\right) \tag{B.48}$$

Equation B.44 produces

$$\frac{\partial \hat{n_z}}{\partial \zeta} = -2\left(\frac{L}{L_\star}\right)\hat{n_n}\hat{n_z}\hat{u_z} \tag{B.49}$$

Equation B.45 is reduced to the expression $\partial\hat{u_n}/\partial\hat{z} = 0$, which implies $\hat{u_n} \equiv 1$.

Equation B.46 produces the expression

$$\hat{n_n} = 1 - \hat{n_z}\hat{u_z} \tag{B.50}$$

The second variable substitution relies on the auxiliary variable ξ defined through the expression

$$\frac{\partial \xi}{\partial \zeta} = \left(\frac{L}{L_\star}\right)\hat{n_n} \tag{B.51}$$

Equation B.48 then produces the expression

$$\hat{u_z} = \tan \xi \tag{B.52}$$

Combining equation B.49 with the boundary condition $u_{z,ds} = u_B$ at the downstream boundary produces the expression

$$\hat{n_z} = 2\eta_u \cos^2(\xi) \tag{B.53}$$

where the parameter $\eta_u = n_{z,ds}/n_0$ is analog to the *propellant utilization* defined for electric plasma thrusters.

Equation B.46 produces

$$\hat{n_n} = 1 - \eta_u \sin(2\xi) \tag{B.54}$$

The expression for the axial coordinate $\hat{z}$ is obtained from expanding the expression for the chain rule including both variable substitutions, $\partial\hat{z}/\partial\xi = (\partial\hat{z}/\partial\zeta)(\partial\zeta/\partial\xi)$. This produces the expression

$$\frac{\partial \hat{z}}{\partial \xi} = \left(\frac{L_\star}{L}\right)\left[\frac{1 - \tan^2(\xi)}{1 - \eta_u \sin(2\xi)}\right] \tag{B.55}$$

The left side of the previous equation can be integrated in the interval $\hat{z} \in [-1, \hat{z}]$, while the right side is integrated within the interval $\xi \in [-\pi/4, \xi]$. This produces the expression

$$\frac{z + L}{L_\star} = \int_{-\frac{\pi}{4}}^{\xi}\left[\frac{1 - \tan^2(\xi')}{1 - \eta_u \sin(2\xi')}\right] d\xi' \tag{B.56}$$

The parameter η_u can be obtained implicitly by considering the conditions at the downstream boundary, where $z = 0$ and $\xi = \pi/4$. Equations B.52 through B.54, plus equation B.56 constitute the asymptotic axial model for magnetized cylindrical plasmas.

The algorithm for the solution of the axial model can be summarized in the following steps,

1. From the input parameters $T_e, L, m_i, m_e, R_{ion}, n_{n0}, g_0$ the value of $L/L_\star$ can be obtained.

2. Considering the conditions at the downstream boundary, equation B.56 implicitly defines η_u.

3. Equation B.56 can now be used to define the mapping $\xi(\hat{z})$.

4. Equations B.52 through B.54 can be used to obtain $\hat{u_z}, \hat{n_z}, \hat{n_n}$.

B.2.5. Vector Calculus Formulas

The Material or Convective Derivative in Cylindrical Coordinates

The convective derivative of a vector-valued function $\mathbf{u} = [u_r(r,\theta,z,t)]\hat{\mathbf{e}}_r + [u_\theta(r,\theta,z,t)]\hat{\mathbf{e}}_\theta + [u_z(r,\theta,z,t)]\hat{\mathbf{e}}_z$ can be calculated in cylindrical coordinates as follows,

$$\left[\frac{\partial \mathbf{u}}{\partial t} + (\mathbf{u}\cdot\nabla)\,\mathbf{u}\right] = \frac{\partial \mathbf{u}}{\partial t} + \frac{\partial \mathbf{u}}{\partial r}\frac{\partial r}{\partial t} + \frac{\partial \mathbf{u}}{\partial \theta}\frac{\partial \theta}{\partial t} + \frac{\partial \mathbf{u}}{\partial z}\frac{\partial z}{\partial t} \tag{B.57}$$

where the first term on the right side of the equation does not require the derivation of the corresponding unit vectors, as it is computed at a fixed spatial location. That means,

$$\frac{\partial \mathbf{u}}{\partial t} = \frac{\partial u_r}{\partial t}\hat{\mathbf{e}}_r + \frac{\partial u_\theta}{\partial t}\hat{\mathbf{e}}_\theta + \frac{\partial u_z}{\partial t}\hat{\mathbf{e}}_z \tag{B.58}$$

The remaining terms in the right side of equation B.57 do need to contemplate the spatial derivatives of the unit vectors. The second term can then be simplified as,

$$\frac{\partial \mathbf{u}}{\partial r}\frac{\partial r}{\partial t} = u_r\left[\frac{\partial u_r}{\partial r}\hat{\mathbf{e}}_r + \frac{\partial u_\theta}{\partial r}\hat{\mathbf{e}}_\theta + \frac{\partial u_z}{\partial u_r}\hat{\mathbf{e}}_z\right] \tag{B.59}$$

The third term in the right side of equation B.57 produces the expression

$$\frac{\partial \mathbf{u}}{\partial \theta}\frac{\partial \theta}{\partial t} = \frac{u_\theta}{r}\left[\left(\frac{\partial u_r}{\partial \theta} - u_\theta\right)\hat{\mathbf{e}}_r + \left(u_r + \frac{\partial u_\theta}{\partial \theta}\right)\hat{\mathbf{e}}_\theta + \frac{\partial u_z}{\partial \theta}\hat{\mathbf{e}}_z\right] \tag{B.60}$$

The fourth term in the right side of equation B.57 produces the expression

$$\frac{\partial \mathbf{u}}{\partial z}\frac{\partial z}{\partial t} = u_z\left[\frac{\partial u_r}{\partial z}\hat{\mathbf{e}}_z + \frac{\partial u_\theta}{\partial z}\hat{\mathbf{e}}_\theta + \frac{\partial u_z}{\partial z}\hat{\mathbf{e}}_z\right] \tag{B.61}$$

Finally, substituting equations B.58, B.59, B.60 and B.61 in equation B.57 produces the final expression for the convective derivative of the function $\mathbf{u}$ in cylindrical coordinates,

$$\left[\frac{\partial \mathbf{u}}{\partial t} + (\mathbf{u}\cdot\nabla)\,\mathbf{u}\right] = \left[\frac{\partial u_r}{\partial t} + u_r\frac{\partial u_r}{\partial r} + \frac{u_\theta}{r}\frac{\partial u_r}{\partial \theta} - \frac{u_\theta^2}{r} + u_z\frac{\partial u_r}{\partial z}\right]\hat{\mathbf{e}}_r + \left[\frac{\partial u_\theta}{\partial t} + u_r\frac{\partial u_\theta}{\partial r} + \frac{u_\theta}{r}\frac{\partial u_\theta}{\partial \theta} + \frac{u_\theta u_r}{r} + u_z\frac{\partial u_\theta}{\partial z}\right]\hat{\mathbf{e}}_\theta + \left[\frac{\partial u_z}{\partial t} + u_r\frac{\partial u_z}{\partial r} + \frac{u_\theta}{r}\frac{\partial u_z}{\partial \theta} + u_z\frac{\partial u_z}{\partial z}\right]\hat{\mathbf{e}}_z \tag{B.62}$$

Appendix C

Modeling of Power Balance within Magnetized Cylindrical Plasmas

C.1. Introduction

A derivation of the expressions for the power balance for cylindrical magnetized plasmas, adapted for the particular scenario of helicon plasma sources, is presented in this Appendix. This model is based upon the work by Ahedo et al. ([3]) and Vidal et al. ([113]), and complements the 2D model for cylindrical magnetized plasmas presented in Appendix B.

C.2. Derivation

The power balance expression can be obtained from the expression for the conservation of momentum for all plasma species. Vidal et al. ([113]) presents it as

$$\frac{\partial}{\partial t}\left(n_j \varepsilon_j\right) + \nabla \cdot \left[\left(\varepsilon_j + T_j\right) \mathbf{\Gamma}_j\right] = -\nabla \cdot \mathbf{Q}_j + q_j \mathbf{\Gamma}_j \cdot \mathbf{E} + S_j - n_j \theta_j \tag{C.1}$$

where the subindexes $j = \{i, e, n\}$ correspond to ions, electrons and neutrals. n_j is the particle density of species j; $\varepsilon_j = (3/2)T_j + (1/2)m_j u_j^2$ is the mean energy per particle of species j; T_j is the temperature of species j in energy units; m_j and u_j are, correspondingly, the mass and mean scalar velocity of species j; $\mathbf{\Gamma}_j = n_j \mathbf{u}_j$ is the particle flux of species j; $\mathbf{Q}_j$ is the heat flux or particle j; $\mathbf{E}$ is the electric field; S_j is the external input power per unit volume absorbed by species j; and θ_j is the power dissipated by species j through collisional processes.

A series of assumptions can now be applied, matching those presented in the derivation of the cylindrical plasma models of Appendix B.

- The analysis is done in steady state conditions, therefore $(\partial/\partial t) = 0$.

- The cold plasma approximation is applied, therefore $T_i \approx 0$.
- The electron temperature is assumed constant, $T_e \approx$ *constant*. This implies $Q_j = 0$.

The previous set of assumptions eliminate the time-dependent term from the left side of equation C.1, and the first term of its right side. The remaining terms can be re-arranged in order to produce the following expression presented by Ahedo et al. ([3])

$$\nabla \cdot \dot{\mathbf{P}} = \mathbf{j} \cdot \mathbf{E} + \dot{P}_{in} - \dot{P}_{ion} \tag{C.2}$$

where the term $\dot{P}_{in} = \sum_j S_j$ is the total external power input to the system per unit volume.

The vector term $\dot{\mathbf{P}}_\mathbf{j}$ combines the internal, kinetic and pressure energy terms and has units of power per unit area,

$$\mathbf{P}_j = \sum_j \left[\left(\frac{3T_j}{2} + \frac{m_j u_j^2}{2} + T_j \right) n_j \mathbf{u_j} \right] \tag{C.3}$$

In the previous equation, the expressions corresponding to ions and neutrals will not present the terms including the temperature T_j. All these expressions will have components in the three cylindrical coordinates (r, θ, z).

The fist term on the right side of equation C.2 can be substituted using the following expression stating the fact that no external electric field is applied to the plasma, and that there are no current sources within the system ($\nabla \cdot \mathbf{j} = 0$),

$$\nabla \cdot (\phi \mathbf{j}) = \phi \nabla \cdot \mathbf{j} + \mathbf{j} \cdot \nabla \phi = -\mathbf{j} \cdot \mathbf{E} \tag{C.4}$$

The third term of the right side equation C.2 expresses the contribution of all collisional interactions, including ionization and excitation processes. It can be expressed through the ionization rate of reaction R_{ion} and the collisional energy per ion-electron pair created E'_{ion}, a term which will be detailed in the next section of the present Appendix.

$$\dot{\mathbf{P}}_{ion} = E'_{ion} n n_n R_{ion} = \nabla \cdot \left(E'_{ion} n \mathbf{u}_i \right) \tag{C.5}$$

Combining the vector derivatives of expressions C.4 and C.5, the expression from equation C.2 becomes

$$\nabla \cdot \left[\dot{\mathbf{P}} + E'_{ion} n \mathbf{u_i} + \phi \mathbf{j} \right] = \dot{P}_{in} \tag{C.6}$$

Integrating this expression over the whole volume of the system and applying Gauss's Divergence Theorem, the proper Power Balance Criterion is obtained

$$P_{ion} + P_{wall} + P_{beam} = P_{in} \tag{C.7}$$

where each term corresponds to a surface integral describing the flux of energy through the system boundaries due to the different terms involved.

The term P_{ion} combines all the contributions from collisional, excitation and ionization processes and can be estimated as

$$P_{ion} = E'_{ion}\left(\frac{\dot{m}_{iT}}{m_i}\right) \tag{C.8}$$

where $\dot{m}_{iT}$ is the total ion mass flow through the boundaries of the system. In the present case of a cylindrical magnetized plasma it can be calculated through the expression $\dot{m}_{iT} = \dot{m}_{us} + \dot{m}_{ds} + \dot{m}_{wall}$ where the terms on the right side correspond to the mass fluxes through the upstream ("us") and downstream ("ds") boundaries and the "wall" term correponds to the mass flux through the inner surface of the cylindrical boundary. m_{iT} can then be calculated through the following expression

$$\dot{m_{iT}} = m_i \pi R^2 u_B n_{us} + m_i \pi R^2 u_B n_{ds} + m_i(2\pi R u_B)\int_{-L}^{0} n(R,z)dz \tag{C.9}$$

where $u_B = \sqrt{T_e/m_i}$ is the ion Bohm velocity; n_{us} and n_{ds} are the mean plasma densities along the upstream and downstream boundaries of the system; and $n_{R,z}$ is the plasma density along the sheath edge on the plasma-facing surface of the cylindrical boundary.

The mean plasma densities along the upstream and downstream system boundaries can be estimated through surface integrals at these locations applied to the expressions derived in the 2D cylindrical magnetized plasma model. The mean plasma density at the upstream boundary can be obtained from

$$n_{us} = \left(\frac{1}{\pi R^2}\right)\iint_{us} n(r,-L)rdrd\theta = \left(\frac{2}{R^2}\right)\int_0^R n_r(r)n_z(-L)n_0 rdr \tag{C.10}$$

where $n_r(r)$ is the normalized radial density from the Radial model, $n_z(z)$ is the normalized axial density from the Axial model and n_0 is the reference plasma density; all of these terms have been described in Appendix B. In a similar approach, the mean plasma density through the downstream boundary can be described by

$$n_{ds} = \left(\frac{1}{\pi R^2}\right)\iint_{ds} n(r,0)rdrd\theta = \left(\frac{2}{R^2}\right)\int_0^R n_r(r)n_z(0)n_0 rdr \tag{C.11}$$

The term P_{wall} from equation C.7 combines the contributions of the flux of particle energy through the upstream and cylindrical boundaries of the system (its "*walls*"). It can be calculated from the expression

$$P_{wall} = 2\pi R \int_{-L}^{0} \dot{\mathbf{P}}(R,z) \cdot \hat{e}_r dz - 2\pi \int_{0}^{R} \dot{\mathbf{P}}(r,-L) \cdot \hat{e}_z r dr \tag{C.12}$$

where $\hat{e}_r$ and $\hat{e}_z$ are the unit vectors from the cylindrical coordinate system. The second term from the right side in the previous expression has a negative sign, since the particle flux through the upstream boundary has the opposite direction from $\hat{e}_z$.

The term P_{beam} is obtained in a very similar approach to P_{wall}, analyzing the flux of particle energies through the downstream open end of the system,

$$P_{beam} = 2\pi \int_{0}^{R} \dot{\mathbf{P}}(r,0) \cdot \hat{e}_z r dr \tag{C.13}$$

C.3. The term E'_{ion}

The calculation of the term P_{ion} in the power balance expression relies on the term E'_{ion}, defined as the energy dissipated by collisional, excitation and ionization processes per electron-ion pair created. This term is very specific to the particular species under analysis. The expressions presented here are those corresponding to singly-ionized argon plasmas.

The derivation of the power balance criterion presented by Ahedo et al. ([3]) suggests the used of an expression fitted to the data published by Dugan ([46]). The following description is based on the more recent work by Gudmundsson ([55]), as suggested by Lieberman and Lichtenberg ([71]).

The Gudmundsson model is based on collision rate data for argon ions at the low electron temperatures relevant for typical helicon plasma sources ($1\,\text{eV} < T_e < 10\,\text{eV}$). These later authors define this term as the *collisional energy lost per ion-electron pair created* $E'_{ion} = \varepsilon_c$, and define it as

$$\varepsilon_c = \varepsilon_{iz} + \sum_j \varepsilon_{ex,j} \frac{k_{ex,j}}{k_{iz}} + \frac{k_{el}}{k_{iz}} \frac{3m_e}{m_i} T_e \tag{C.14}$$

where ε_{iz} is the ionization energy for singly-charged ions ($\varepsilon_{iz} \approx 15.76$ eV for Ar^+ ions), $\varepsilon_{ex,j}$ and $k_{ex,j}$ are respectively the threshold energies and rate coefficients for the different excitation processes (represented by the subindex j), k_{iz} is the ionization rate coefficient, and k_{el} is the rate coefficient for elastic collisions between electrons and ions.

Gudmundsson compiles rate coefficients for different types of excitation reactions. The corresponding values and formulas for the terms $\varepsilon_{ex,j}$ and $k_{ex,j}$ for each one of them are presented in Table C.1.

Table C.1: Threshold energies $\varepsilon_{ex,j}$ and rate coefficients $k_{ex,j}$ corresponding to the excitation transitions of argon atoms. Obtained from the compilation published by Gudmundsson ([55]).

Final State	$\varepsilon_{ex,j}$ (eV)	$k_{ex,j}$ (m^3/s)
$^3\mathrm{P}_2$	11.5	$5.02 \times 10^{-15} \exp(-12.64/T_e)$
$^3\mathrm{P}_1$	11.6	$1.91 \times 10^{-15} \exp(-12.60/T_e)$
$^3\mathrm{P}_0$	11.7	$1.35 \times 10^{-15} \exp(-12.42/T_e)$
$^1\mathrm{P}_1$	11.8	$2.72 \times 10^{-16} \exp(-12.14/T_e)$
$4p$	13.2	$2.12 \times 10^{-14} \exp(-13.13/T_e)$
$4s, 4s'$	11.8	$1.45 \times 10^{-14} \exp(-12.96/T_e)$
$5s, 3\overline{d}, 5s', 3d'$	14.2	$1.22 \times 10^{-14} \exp(-17.80/T_e)$
$4d, 6s, 4\overline{d}, 4d', 6s'5d, 7s, 5\overline{d}$	15.0	$7.98 \times 10^{-15} \exp(-19.05/T_e)$
Higher states	15.5	$8.29 \times 10^{-15} \exp(-18.14/T_e)$

The ionization rate coefficient can be obtained from the expression

$$k_{iz} = (2.9 \times 10^{-14}) {T_e}^{0.50} \exp(-17.8/T_e) \tag{C.15}$$

for the temperature range $1 \text{ eV} < T_e < 10$ eV. Finally, the rate coefficient for elastic collisions can be found from

$$\ln(k_{el}) = -31.3879 + 1.6090 \ln(T_e) + 0.0618[\ln(T_e)]^2 - 0.1171[\ln(T_e)]^3 \tag{C.16}$$

Appendix D

Python Scripts

This Appendix contains the Python scripts used to implement the simulations discussed in chapter 4.

D.1. Description of the software implementation

The models discussed in chapter 4 of this thesis have been implemented as scripts in the Python[1], using the numerical libraries NumPy[2] and SciPy[3].

The scripts produced belong to three different categories: class definitions, parameter sets and execution scripts. The definition of these categories and the list of scripts is detailed in Table D.1. The execution scripts are the only programs designed to be directly invoked by the user.

[1] https://www.python.org
[2] https://numpy.org
[3] https://scipy.org

Table D.1: List of the Python scripts designed to implement the simulations from chapters 4 and 5.

Category	**Script Name**	**Description**
Class Definition	AhedoOOP.py	Definition of classes related to the 2D cylindrical magnetized plasma model by Ahedo et al. ([2, 3]). It also includes methods for the power balance simulation for the helicon plasma source.
	SheathsOOP.py	Definition of classes related to the plasma sheath models described by Lieberman and Lichtenberg ([71]).
	EcksteinSputteringOOP.pdf	Definition of classes related to the sputtering models described by Eckstein et al. [48].
Parameter Set	HeliconParSets.py	Sets of experimental parameters from helicon plasma sources to be used with *AhedoOOP.py*.
	SputteringPars.py	Sets of experimental parameters and fitting coefficients to be used in conjunction with *EcksteinSputteringOOP.py*. Fitting coefficients obtained from Behrisch et al. ([9]).
Execution Script	helicon_tests.py	Utility procedural script implementing unit tests of the radial, axial and power balance models from *AhedoOOP.py* and sputtering simulations from *EcksteinSputteringOOP.py*.
	HeliconErosionSim.py	Main simulation routine used to create the data sets plotted in section 4.3.
	HeliconPowerBalance.py	Main simulation routine used to create the power balance results shown in section 5.3.

```
#!/usr/bin/python

# *******************************************************
# Implementation of magnetized cylindrical plasma model
# from [ahedo13] and [ahedo09]
#
# OOP HELICON CLASS, Argon
#
# JIDVG, 2021
# *******************************************************

# Python and local ibraries
import numpy as np
import scipy.optimize as opt
import scipy.integrate as integrate
import scipy.special as special

# %%%%%%%%%%%%%%%%%%%%%%%%%%%%%%%%%%%%%%%%%%%%%%%%%%%%%%%%%%%%%%%%%%%%%%%%%%%%%%%%%%%%%%%%%%%%%%%%%%%%%%%%%%%%%%%%%%%%%%%%%
# Helicon Parameter structure definition
class HeliconPars:
        # Set of specific parameters required to define a particular instance of a magnetized cylindrical plasma

        # INIT method
        # Internal attributes are declared empty, for the user to override later
        # FIXME Include parameters required for calculation of collision rates.
        def __init__(self):
                self.R = 0.0                                    # Chamber radius                        [m]
                self.L = 0.0                                    # Chamber length                        [m]
                self.B0 = 0.0                                   # Axial magnetic field intensity        [T]
                self.mdot = 0.0                                 # Neutral injection mass flow           [kg / s]
                self.un0 = 0.0                                  # Neutral axial speed at injection      [m/s]
                self.nn0 = 0.0                                  # Neutral density at injection          [m^-3]
                self.Te = 0.0                                   # Constant electron temperature         [eV]
                self.Rion = 0.0                                 # Ionization rate                       [m3/s]
                self.Ren = 0.0                                  # e-n collision rate                    [m3/s]
                self.Rin = 0.0                                  # i-n collision rate                    [m3/s]
                self.Rei = 0.0                                  # e-i collision rate                    [m3/s]
                self.Z_p = 0.0                                  # Atomic number of ion species
                self.Aion = 0.0                                 # Standard atomic mass of ion species

                # Physical constants
                self.kB = 1.3807e-23                            # Boltzmann's constant                  [J/K]
                self.ee = 1.6022e-19                            # Elementary charge                     [C]
                self.m_e = 9.1094e-31                           # Electron mass                         [kg]
                self.m_p = 1.6726e-27                           # Proton mass                           [kg]

                # Argon parameters required for collision rates [ahedo13]
                self.Eion = 0.0                                 # First ionization energy, Argon                [eV]
                self.sigma_ion = 0.0                            # Ionization cross section, Argon               [m2]
                self.sigma_en = 0.0                             # e-n collision cross section, Argon            [m2]
                self.Rin_k2 = 0.0                               # Constant k2 for calculation of Rin, Argon     [m]
                self.Rin_k1 = 0.0                               # Constant k1 for calculation of Rin, Argon     [m]
                self.clambda = 0.0                              # Coulomb logarithm, average value according to [ahedo13] and [NRL Plasma Formulary]

                # Argon parameters required for calculation of energy cost per ion-electron pair [gudmundsson02]

                # Threshold energies for electron impact rate coefficients, Ar
                self.kthr01 = 0.0                                       # [eV]
                self.kthr02 = 0.0                                       # [eV]
                self.kthr03 = 0.0                                       # [eV]
                self.kthr04 = 0.0                                       # [eV]
                self.kthr05 = 0.0                                       # [eV]
                self.kthr06 = 0.0                                       # [eV]
                self.kthr07 = 0.0                                       # [eV]
```

```
                self.kthr08 = 0.0                                       # [eV]
                self.kthr09 = 0.0                                       # [eV]

                print ("Parameter definition complete.")


# ============================================================================================================================
# Helicon class definition
class HeliconModel:
        # Magnetized cylindrical plasma model by [ahedo09] and [ahedo13]

        # %%%%%%%%%%%%%%%%%%%%%%%%%%%%%%%%%%%%%%%%%%%%%%%%%%%%%%%%%%%%%%%%%%%%%%%%%%%%%%%%%%%%%%%%%%%%%%%%%%%%%%%%%%%%%%%%%%%%%%%%%%
        # INIT method
        def __init__(self, heliconpars, rrres, zzres):

                # Definition of local instance base input parameters
                self.R = heliconpars.R
                self.L = heliconpars.L
                self.B0 = heliconpars.B0
                self.mdot = heliconpars.mdot
                self.un0 = heliconpars.un0
                self.nn0 = heliconpars.nn0
                self.Te = heliconpars.Te
                #self.Rion = heliconpars.Rion
                #self.Ren = heliconpars.Ren
                #self.Rin = heliconpars.Rin
                #self.Rei = heliconpars.Rei
                self.Z_p = heliconpars.Z_p
                self.Aion = heliconpars.Aion
                self.rres = rrres
                self.zzres = zzres

                self.kB = heliconpars.kB
                self.ee = heliconpars.ee
                self.m_e = heliconpars.m_e
                self.m_p = heliconpars.m_p


                # Argon parameters required for collision rates [ahedo13]
                self.Eion = heliconpars.Eion
                self.sigma_ion = heliconpars.sigma_ion
                self.sigma_en = heliconpars.sigma_en
                self.Rin_k2 = heliconpars.Rin_k2
                self.Rin_k1 = heliconpars.Rin_k1
                self.clambda = heliconpars.clambda

                # Threshold energies for electron impact rate coefficients, Ar
                self.kthr01 = heliconpars.kthr01                        # [eV]
                self.kthr02 = heliconpars.kthr02                        # [eV]
                self.kthr03 = heliconpars.kthr03                        # [eV]
                self.kthr04 = heliconpars.kthr04                        # [eV]
                self.kthr05 = heliconpars.kthr05                        # [eV]
                self.kthr06 = heliconpars.kthr06                        # [eV]
                self.kthr07 = heliconpars.kthr07                        # [eV]
                self.kthr08 = heliconpars.kthr08                        # [eV]
                self.kthr09 = heliconpars.kthr09                        # [eV]

                # Initialiation of output vectors

                # Definition of linear space spanning zz coordinate
                self.zz = np.linspace(-self.L, 0, self.zzres)
                self.zzhat = self.zz / self.L
                # Empty vector to contain corresponding outputs
                self.xixi = np.zeros(np.size(self.zz))
```

```
        self.uz_cs = np.zeros(np.size(self.zz))
        self.n_n0 = np.zeros(np.size(self.zz))
        self.nn_nn0 = np.zeros(np.size(self.zz))
        # Definition of linear space spanning rr coordinate
        self.rr = np.linspace(0, self.R*0.99999, self.rres)
        self.rrhat = self.rr / self.R
        self.nr_nr0 = np.zeros(np.size(self.rrhat))
        self.ur_cs = np.zeros(np.size(self.rrhat))
        self.utheta_ce = np.zeros(np.size(self.rrhat))

        # Call ParInit() method
        self.ParInit()

        # Ionization and collision rate calculations according to [ahedo13]
        self.CollRateCalculation()

        # Calculation of parameters derived from the ionization and collision rates
        self.CollDerivedParameters()

    # %%%%%%%%%%%%%%%%%%%%%%%%%%%%%%%%%%%%%%%%%%%%%%%%%%%%%%%%%%%%%%%%%%%%%%%%%%%%%%%%%%%%%%%%%%%%%%%%%%%%%%%%%%%%%%%%%%%%
    # ParInit method: initialization of internal parameters...
    def ParInit(self):

        print('Calculating internal parameters...')

        # Calculation of derived internal parameters

        self.m_i = self.Aion * self.m_p                             # Argon ion mass                        [kg]
        self.cs = np.sqrt(self.Te * self.ee / self.m_i)             # Bohm speed                            [m/s]
        self.ce = np.sqrt(self.Te * self.ee / self.m_e)             # Electron sound speed                  [m/s]
        # self.g0 = self.un0 * self.nn0                             # Axial mass flow rate                  [1 / m2*s]
        self.g0 = self.mdot / (self.m_i * np.pi * self.R**2)        # Axial ion flow rate                   [1 / m2*s]
        self.n0 = self.g0 / self.cs                                 # Reference plasma density at backwall  [m^-3]
        self.omega_e = self.ee * self.B0 / self.m_e                 # electron cyclotron frequency          [1/s]
        self.omega_i = self.ee * self.B0 / self.m_i                 # ion cyclotron frequency               [1/s]
        self.wlh_d = (self.ee * self.B0) / np.sqrt(self.m_e * self.m_i) # Lower hybrid frequency            [1/s]
        self.wr_d = self.cs / self.R                                # radial transit frequency              [1/s]

        self.wlh = self.wlh_d / self.wr_d                           # Normalized lower hybrid frequency

        self.alpha_ion = 1.4 + 0.4*np.exp(0.7 * self.Eion / self.Te)    # Ionization cost factor                            [ahedo13, dugan67]
        self.Eion_eff = self.alpha_ion * self.Eion                  # Effective ionization energy           [eV]            [ahedo13]


    # %%%%%%%%%%%%%%%%%%%%%%%%%%%%%%%%%%%%%%%%%%%%%%%%%%%%%%%%%%%%%%%%%%%%%%%%%%%%%%%%%%%%%%%%%%%%%%%%%%%%%%%%%%%%%%%%%%%%
    # Ionization and collision rate calculation according to [ahedo13]
    # Routine independent of ParInit() to allow manual adjustments of these parameters
    def CollRateCalculation(self):
        # Calculation of ionization and collision rates [m3 / s]
        # [ahedo13] equations A1-A5
        self.Rion = np.sqrt(8*self.Te*self.ee / (np.pi * self.m_e)) * self.sigma_ion * (1 + (self.Te*self.Eion / (self.Te + self.Eion)**2)) * np.exp(-self.Eion/self.Te)
        self.Ren = np.sqrt(8*self.Te*self.ee / (np.pi * self.m_e)) * self.sigma_en
        self.Rei = self.Te**(-3/2) * self.clambda * 9.2e-14
        self.Rin = self.cs * (self.Rin_k2 - self.Rin_k1*np.log10(self.cs))**2

        # ================================================================================
        # Calculation of energy cost per ion-electron pair, argon [gudmundssen02]
        self.k01 = 5.02e-15*np.exp(-12.64/self.Te)                          # [m3/s]
        self.k02 = 1.91e-15*np.exp(-12.60/self.Te)                          # [m3/s]
        self.k03 = 1.35e-15*np.exp(-12.42/self.Te)                          # [m3/s]
        self.k04 = 2.72e-16*np.exp(-12.14/self.Te)                          # [m3/s]
        self.k05 = 2.12e-14*np.exp(-13.13/self.Te)                          # [m3/s]
```

```
        self.k06 = 1.45e-14*np.exp(-12.96/self.Te)                    # [m3/s]
        self.k07 = 1.22e-14*np.exp(-17.80/self.Te)                    # [m3/s]
        self.k08 = 7.98e-15*np.exp(-19.05/self.Te)                    # [m3/s]
        self.k09 = 8.29e-15*np.exp(-18.14/self.Te)                    # [m3/s]

        # Ionization rate coefficient (up to 10 eV)
        self.kiz = 2.9e-14 * self.Te**(0.50) * np.exp(-17.8/self.Te)

        # Rate coefficient for elastic collisions
        self.kel = np.exp(-31.3879 + 1.6090*np.log(self.Te) + 0.0618*(np.log(self.Te))**2 - 0.1171*(np.log(self.Te))**3)

        # Collisional energy lost per ion-electron par created
        # self.E_c = self.Eion + (1/self.kiz) * (self.kthr01*self.k01 + self.kthr02*self.k02 + self.kthr03*self.k03 + self.kthr04*self.k04 + self.kthr05*self.k05 + self.kthr06*self.k06 + self.kthr07*self.k07 + self.kthr08*self.k08 + self.kthr09*self.k09) + (self.kel/self.kiz)*(3*self.m_e/self.m_i)*self.Te
        #
        # 20220628 - 4.4X factor added to account for missing interactions at low-temperature which prevent the simulation from matching experimental data
        # 20220629 - 0.5X factor added to account for missing interactions at low-temperature which prevent the simulation from matching experimental data
        self.E_c = 1.0*(self.Eion + (1/self.kiz) * (self.kthr01*self.k01 + self.kthr02*self.k02 + self.kthr03*self.k03 + self.kthr04*self.k04 + self.kthr05*self.k05 + self.kthr06*self.k06 + self.kthr07*self.k07 + self.kthr08*self.k08 + self.kthr09*self.k09) + (self.kel/self.kiz)*(3*self.m_e/self.m_i)*self.Te)

    # %%%%%%%%%%%%%%%%%%%%%%%%%%%%%%%%%%%%%%%%%%%%%%%%%%%%%%%%%%%%%%%%%%%%%%%%%%%%%%%%%%%%%%%%%%%%%%%%%%%%%%%%%%%%%%%%%%
    def CollDerivedParameters(self):
        print('Calculating parameters derived from ionization and collision rates...')

        # Calculation of parameters derived from the ionization and collision rates
        # Must be called anytime these parameters are changed

        self.vion_d = self.nn0 * self.Rion                          # ionization frequency              [1/s]
        self.ven_d = self.nn0 * self.Ren                            # e-n collision frequency           [1/s]
        self.vin_d = self.nn0 * self.Rin                            # i-n collision frequency           [1/s]
        self.vei_d = self.nn0 * self.Rei                            # e-i collision frequency           [1/s]
        self.vi_d = self.vin_d + self.vion_d                        # combined ion collision freq.      [1/s]
        self.ve_d = self.ven_d + self.vei_d + self.vion_d           # combined e collision freq.        [1/s]

        self.vion = self.vion_d / self.wr_d
        self.vi = self.vi_d / self.wr_d
        self.ve = self.ve_d / self.wr_d

        # Axial model parameters
        self.Lstar = self.cs / (self.Rion * self.nn0)               # effective ionization mean-free path   [m]
        self.Lratio = self.L / self.Lstar

    # %%%%%%%%%%%%%%%%%%%%%%%%%%%%%%%%%%%%%%%%%%%%%%%%%%%%%%%%%%%%%%%%%%%%%%%%%%%%%%%%%%%%%%%%%%%%%%%%%%%%%%%%%%%%%%%%%%
    # Axial model method
    def AxialModel(self):
        # [ahedo13] equations 18, 19, 20

        # ***************************************************************************************************************************
        # Obtain eta_u, propellant utilization figure of merit, using [ahedo13] equation 20,
        # SciPy's scipy.integrate.quad integration routine and scipy.optimize.minimize_scalar optimization

        # Actual definite integral from [ahedo13] equation 20
        def axial_int_eta_integral_opt(eta_u):
            result = integrate.quad(lambda xi: (1.0-(np.tan(xi)**2.0)) / (1.0-eta_u*np.sin(2.0*xi)), -np.pi/4.0, np.pi/4.0, limit=100)
            # print("[ahedo13] equation 20: ", np.abs(result[0] - self.Lratio))
            return np.abs(result[0] - self.Lratio)                  # Use of np.abs function ensures we're minimizing towards zero

        # Run optimization routine to find value of eta_u as an implicit function of Lratio from [ahedo13] equation 20
        # Optimization bounded for reasonable values: 0.000001 < eta_u < 1.5
        eta_u_optresult = opt.minimize_scalar(axial_int_eta_integral_opt, bounds=(0.5,1.5), method='bounded')
```

```python
        # eta_u_optresult = opt.minimize_scalar(axial_int_eta_integral_opt)
        self.eta_u = eta_u_optresult.x

        # Calculation of plasma density at exit axial position E
        self.n_E = self.eta_u * self.g0 / self.cs


        # ****************************************************************************************************************************
        # Definition of function xi(z), by optimization of [ahedo19] equation 19
        # by using SciPy's scipy.integrate.quad integration routine and scipy.optimize.minimize_scalar optimization


        # RHS integral from [ahedo13] equation 20
        def axial_int_xi_integral_opt(xi_inp, eta_u, zz_inp):
            resultxi = integrate.quad(lambda xivar: (1.0-(np.tan(xivar)**2.0)) / (1.0-eta_u*np.sin(2.0*xivar)), -np.pi/4.0, xi_inp, limit=100)
            # print zz_inp, xi_inp, resultxi[0] - (zz_inp + L)/Lstar
            return np.abs(resultxi[0] - (zz_inp + self.L)/self.Lstar)

        # Run optimization routine to find value of xi(zz) from [ahedo13] equation 19.
        for zindex in range(0, np.size(self.zz)):
            # print 'Xi iteration number: ', zindex
            # print 'z value: ', zz[zindex]

            xi_optresult = opt.minimize_scalar(axial_int_xi_integral_opt, bounds=(-np.pi/4.0, np.pi/4), method='bounded', args=(self.eta_u, self.zz[zindex]))
            # xi_optresult = opt.minimize_scalar(axial_int_xi_integral_opt, args=(eta_u, zz[zindex]))

            self.xixi[zindex] = xi_optresult.x
            # print xi_optresult.message
            # print 'Xi result: ',xixi[zindex], '\n'

        # ****************************************************************************************************************************
        # Calculation of non-dimensional parameters (uz/cs), (n/n0), (nn/nn0)

        # Non-dimensional axial plasma velocity (uz/cs)
        self.uz_cs = np.tan(self.xixi)

        # Non-dimensional axial plasma density
        self.n_n0 = 2*self.eta_u*(np.cos(self.xixi)**2)

        # Non-dimensional axial neutral density
        self.nn_nn0 = 1 - self.eta_u*np.sin(2*self.xixi)

        # Method's output parameters
        # return self.uz_cs, self.n_n0, self.nn_nn0
        print("Calculation of axial model COMPLETE.")

        # ==========================================================================================================
        # DEBUG FIXME
        # from IPython import embed; embed()

    # %%%%%%%%%%%%%%%%%%%%%%%%%%%%%%%%%%%%%%%%%%%%%%%%%%%%%%%%%%%%%%%%%%%%%%%%%%%%%%%%%%%%%%%%%%%%%%%%%%%%%%%%%%%%%%%%
    # Radial Model method, a function of ZZ position
    def RadialModel(self):
        # Non-dimensional radial model
        # [ahedo09] equation 26, [ahedo13] equation 13

        # Argument parameter for Bessel solution of radial model
        a0 = special.jn_zeros(0,1)[0]
        vw = (a0**2) * (self.wr_d / self.wlh_d)**2 * self.ve_d
        # a0 = wlh*np.sqrt(vw/ve)

        # Non-dimensional radial plasma density
```

```
        self.nr_nr0 = special.jv(0, a0*self.rrhat)

        # Non-dimensional radial plasma velocity. FIXME Setting boundary condition (ur/cs)=1 at (r=R)
        self.ur_cs = (a0 * self.ve_d * self.wr_d / self.wlh_d**2)*(special.jv(1, a0 * self.rrhat) / special.jv(0, a0 * self.rrhat))
        self.ur_cs[-1] = 1

        # Non-dimensional azimuthal plasma velocity
        self.utheta_ce = (self.wlh_d/self.ve_d) * self.ur_cs

        # Method's output parameters
        # return rrhat, nrnr0, urcs
        print("Calculation of radial model COMPLETE.")



    # %%%%%%%%%%%%%%%%%%%%%%%%%%%%%%%%%%%%%%%%%%%%%%%%%%%%%%%%%%%%%%%%%%%%%%%%%%%%%%%%%%%%%%%%%%%%%%%%%%%%%%%%%%%%%%%%%%%
    # PowerBalance method.
    # Implementation of power balance expressions of [ahedo13] removing the magnetic nozzle; some concepts derived from [vidal99]
    def PowerBalance(self, Te, P_inp):

        print('\nStarting power balance calculations....')

        # =========================================================================================================
        # 0. Update system and execute of radial and axial models with current parameters
        self.Te = Te

        print('Starting calculations for Te =', Te, ' eV')

        # Update model calculated parameters
        self.ParInit()
        self.CollRateCalculation()
        self.CollDerivedParameters()

        # Execution of Axial and Radial models
        self.AxialModel()
        self.RadialModel()

        # Creation of 2D density map out of Axial and Radial models
        # Replication of radial model along the axial coordinate, setting the nr0 parameter in the Radial model as the n0 parameter from the Axial model
        # Implemented as a vector multiplication. Resultant matrix has rres rows, zres columns, defining the geometrical coordinates (z, r)
        # [ahedo13] calculation produces results normalized to n0, therefore the resulting matrix is multiplied by this factor to obtain physical units
        #
        # nmesh.shape = (rres, zres)
        nmesh = (self.nr_nr0.reshape(self.rres, 1) @ self.n_n0.reshape(1, self.zzres)) * self.n0
        nnmesh = np.tile(self.nn_nn0.reshape(1, self.zzres)*self.nn0, (self.rres, 1))

        # Maps of ion, electron and neutral velocities
        ur_vector = self.ur_cs * self.cs
        utheta_vector = self.utheta_ce * self.ce
        uz_vector = self.uz_cs * self.cs

        # Velocity vectors are tiled into arrays of dimension (rres, zzres), consistent with nmesh.
        ur_mesh = np.tile(ur_vector.reshape(self.rres,1), (1, self.zzres))
        utheta_mesh = np.tile(utheta_vector.reshape(self.rres,1), (1,self.zzres))
        uz_mesh = np.tile(uz_vector.reshape(1, self.zzres), (self.rres, 1))
        un_mesh = np.ones((self.rres, self.zzres)) * self.un0

        # Calculation of velocity magnitude meshes for ions and electrons and neutrals
        u_i_mag = np.sqrt(ur_mesh*ur_mesh + uz_mesh*uz_mesh)
        u_e_mag = np.sqrt(ur_mesh*ur_mesh + uz_mesh*uz_mesh + utheta_mesh*utheta_mesh)
        u_n_mag = un_mesh
```

```
        # Extraction of density values at boundary surfaces
        n_zboundary = nmesh[:,0]                        # First array column corresponds to zz = -L (material boundary)
        n_rboundary = nmesh[-1,:]                       # Last array row corresponds to rr = R
        n_Eboundary = nmesh[:,-1]                       # Last array column corresponds to zz = 0 (open end of HPS)


        # Calculation of Pdot function (internal energy + kinetic energy + pressure term)
        #
        # Pdot_r: only ions and electrons have a radial component to their velocity. Dimensions: (rres, zzres)
        # Te expressed in joules
        Pdot_r = (nmesh * ur_mesh) * ( 5*self.Te*self.ee/2 + self.m_e * (u_e_mag**2)/2 + self.m_i*(u_i_mag**2)/2)
        #
        # Pdot_z: all species have an axial component to their velocity. Dimensions: (rres, zzres)
        # Te expressed in joules
        Pdot_z = (nmesh * uz_mesh) * ( 5*self.Te*self.ee/2 + self.m_e * (u_e_mag**2)/2 + self.m_i*(u_i_mag**2)/2) + (nnmesh*un_mesh*self.m_i
*(u_n_mag**2)/2)

        # Power Balance equation ([ahedo13], equation 34)
        # P_ion + P_wall + P_beam = Pinp

        print('Calculation of parameter meshes and Pdot function complete....')

        # ===========================================================================================
        # 1. Calculation of term P_ion

        # 1.1 Calculation of mdot_upstream (total ion mass flow on upstream boundary)
        #
        # Average plasma density along upstream boundary ("endplate")
        n_B_avg = (2 / self.R**2) * integrate.trapezoid(n_zboundary * self.rr, dx=(self.rr[1]-self.rr[0]))
        #
        mdot_upstream = self.m_i * np.pi * self.R**2 * self.cs * n_B_avg
        print ('Mdot Upstream:', mdot_upstream, ' kg/s')

        # 1.2 Calculation of mdot_downstream (total ion mass flow on downstream boundary end)
        #
        # Average plasma density along downstream boundary ("plasma jet leaving the HPS")
        n_E_avg = (2 / self.R**2) * integrate.trapezoid(n_Eboundary * self.rr, dx=(self.rr[1]-self.rr[0]))
        #
        mdot_downstream = self.m_i * np.pi * self.R**2 * self.cs * n_B_avg
        print ('Mdot Downstream:', mdot_downstream, ' kg/s')

        # 1.3 Calculation of mdot_wall (total ion mass flow on inner surface of dielectric cylinder)
        mdot_wall = self.m_i * 2 * np.pi * self.R * integrate.trapezoid(n_rboundary * self.cs, dx=(self.zz[1]-self.zz[0]))
        print ('Mdot Wall:', mdot_wall, ' kg/s')

        # 1.4 Calculation of total ion mass flow on all boundaries
        mdot_iT = mdot_upstream + mdot_downstream + mdot_wall
        print ('Mdot Total:', mdot_iT, ' kg/s')

        print ('Mdot Calculation error:', self.mdot - mdot_iT, ' kg/s;', (self.mdot-mdot_iT)*100/self.mdot, ' %')

        # 1.5 Calculation of P_ion [W]
        # P_ion = self.Eion_eff * self.ee * (mdot_iT / self.m_i)                        # Using [dugan67]
        P_ion = self.E_c * self.ee * (mdot_iT / self.m_i)                               # Using [gudmudssen02]

        print('Calculation of P_ion complete:', P_ion, ' W')

        # ===========================================================================================
        # 2. Calculation of term P_wall
        # P_wall = (2*np.pi*self.R) * integrate.trapezoid(Pdot_r[-1,:], self.zz, dx=(self.zz[1]-self.zz[0])) - (2*np.pi) * integrate.trapezo
id(-Pdot_z[:,0]*self.rr, self.rr, dx=(self.rr[1]-self.rr[0]))
        P_wall_radialB = (2*np.pi*self.R) * integrate.trapezoid(Pdot_r[-1,:], dx=(self.zz[1]-self.zz[0]))
        P_wall_upstreamB = - (2*np.pi) * integrate.trapezoid(Pdot_z[:,0]*self.rr, dx=(self.rr[1]-self.rr[0]))
```

```
            P_wall = P_wall_radialB + P_wall_upstreamB

            print('Calculation of P_wall complete:', P_wall, ' W')

            # ==========================================================================================
            # 3. Calculation of term P_beam
            # P_beam = (2*np.pi) * integrate.trapezoid(Pdot_z[:,-1], self.rr, dx=(self.rr[1]-self.rr[0]))
            P_beam = (2*np.pi) * integrate.trapezoid(Pdot_z[:,-1]*self.rr, dx=(self.rr[1]-self.rr[0]))

            print('Calculation of P_beam complete:', P_beam, ' W')


            # ==========================================================================================
            # 4. Calculation of sum P_ion + P_wall + P_beam
            # Return unsigned difference between power balance calculation and input power

            print('Estimation of dissipated power:', P_ion+P_wall+P_beam, ' W')
            print('Minimization target:', np.abs((P_ion + P_wall + P_beam) - P_inp), ' W;', np.abs((P_ion + P_wall + P_beam) - P_inp)*100/P_inp, ' %'
)

            # ==========================================================================================
            # 5. DEBUG FIXME
            # from IPython import embed; embed()

            # Return error function in percentage
            return np.abs((P_ion + P_wall + P_beam) - P_inp)*100/P_inp
```

```
#! /usr/bin/python

# %%%%%%%%%%%%%%%%%%%%%%%%%%%%%%%%%%%%%%%%%%%%%%%%%%%%%%%%%%%%%%%%%%%%%%%%%%%%%%%%%%%%%%
# Calculations for DC and RF sheaths according to [lieberman05]
#
# JIDVG, 2022
# %%%%%%%%%%%%%%%%%%%%%%%%%%%%%%%%%%%%%%%%%%%%%%%%%%%%%%%%%%%%%%%%%%%%%%%%%%%%%%%%%%%%%%

# ********************************************************************************
# Python libraries
import numpy as np

# ********************************************************************************
# DC Sheath Class, [lieberman05] chapter 6
# Includes the low-frequency RF sheath regime (short ion transit time), [lieberman05] chapter 11.5

class DCSheath:

        # %%%%%%%%%%%%%%%%%%%%%%%%%%%%%%%%%%%%%%%%%%%%%%%%%%%%%%%%%%%%%%%%%%%%%%%%%%%%%%%%%%%%%%%%%%%%%%%%%%%%%%%%%%%
        # __INIT__ method
        def __init__(self, Te, ion_m, ee_n):

                # Assignment of input parameters to internal variables
                self.Te = Te                                                                    # electron temperature [eV]
                self.ion_m = ion_m                                                              # ion mass [amu]
                self.ee_n = ee_n                                                                # bulk electron density [m^-3]

                # Local physical constants
                self.ee_m = 9.1094e-31                                                          # electron mass [kg]
                self.ee_q = 1.6022e-19                                                          # electron charge [C]
                self.pp_m = 1.6726e-27                                                          # proton mass [kg]
                self.kB = 1.3807e-23                                                            # Boltzmann's constant [J/K]
                self.epsilon0 = 8.8542e-12                                                      # permittivity of free space [F/m]

                # Calculation of base parameters
                self.uB = np.sqrt(self.ee_q * self.Te / (self.ion_m * self.pp_m))               # Bohm velocity [m/s]
                self.lambdaD = np.sqrt(self.epsilon0 * self.Te / (self.ee_n * self.ee_q))       # Debye length [m]

                # Calculation of parameters for the case of a floating wall
                self.ion_flux = self.ee_n * self.uB                                             # Ion flux to wall [m^-2 sâM-^A»1]
                self.wall_potential_float = -self.Te * np.log(np.sqrt(self.ion_m / (2*np.pi*(self.ee_m/self.pp_m))))          # Potential at a floating wall [V]


        # %%%%%%%%%%%%%%%%%%%%%%%%%%%%%%%%%%%%%%%%%%%%%%%%%%%%%%%%%%%%%%%%%%%%%%%%%%%%%%%%%%%%%%%%%%%%%%%%%%%%%%%%%%%
        # Child Law DC Sheath. [lieberman05] section 6.3.
        def ChildLawSheath(self, V0):

                # Potential associated to Child's Law Sheath
                self.Child_V0 = V0

                # Sheath thickness according to Child's Law
                self.Child_s = (np.sqrt(2)/3) * self.lambdaD * (2*V0/self.Te)**(3/4)
```

```python

        # Characteristic velocity within the sheath
        self.Child_v0 = np.sqrt(2*self.ee_q*V0/ (self.ion_m*self.pp_m))

        # Ion transit time within the sheath
        self.Child_tau = 3*self.Child_s/self.Child_v0


    # %%%%%%%%%%%%%%%%%%%%%%%%%%%%%%%%%%%%%%%%%%%%%%%%%%%%%%%%%%%%%%%%%%%%%%%%%%%%%%%%%%%%%%%%%%%%%%%%%%%%%%%%%%%%%%%%
    # Low-Frequency RF Sheath Class, [lieberman05] chapter 11.5
    def LowFreqRFSheath(self, V0, Vbias, V_RF, f_RF):

        # Calculate Child's Law sheath parameters
        self.ChildLawSheath(V0)

        # Calculate angular frequency from input frequency
        omega_RF = 2 * np.pi * f_RF

        # Validation of short ion transit time scenario
        # Assumptions are valid if Child_tau < (1/omega_RF)
        if (self.Child_tau > 1/f_RF).any == True:

            # Abort calculations if Short Ion Transit Time assumption is invalid
            print('Short ion transit time assumption is not met.')
        else:
            # Low-frequency RF calculations: ion energy IED
            # [lieberman05] equations 11.6.6 and 11.6.7 excluding the flow rate term (n_s * u_B)

            # [liebeman05] equation 11.6.6
            self.LowFreq_IED = (1.0 / np.pi) / np.sqrt(V_RF**2 - (Vbias - V0)**2)

            # Add monoenergetic term at the V0 = Vbias position within the IED ([lieberman05] equation 11.6.7)
            # Validate first if calculation is done for a complete IED (size greater than 1)
            # then modify only row where V0 = Vbias
            # [lieberman05] equation 11.5.13 used to calculate omega*t_a
            if (self.LowFreq_IED.size > 1 ):
                self.LowFreq_IED[self.Child_V0 == Vbias] = ( (np.pi - 2 * np.arcsin(Vbias/V_RF)) / (2 * np.pi) )


```

```python
#!/usr/bin/python

# *******************************************************************************
# 20220122
# JIDVG
# Sputtering yield calculations based on "Sputtering Yields" chapter from  Behrisch & Eckstein, 2007
#
# OOP Implementation
# *******************************************************************************

# *******************************************************************************
# Python libraries
import math
import numpy as np


# *******************************************************************************
# Parameter class

class SputteringPars:
        # Set of parameters required to model sputtering interaction between an ion and an elemental
        # surface, based on [eckstein03]

        # INIT method
        def __init__(self):

                self.ion_z = 0.0                # Impacting ion atomic number                   []
                self.ion_m = 0.0                # Impacting ion atomic mass                     [amu]
                self.ion_E0 = 0.0               # Impacting ion energy                          [eV]
                self.ion_sbe = 0.0              # Impacting ion surface binding energy          [eV]
                self.target_z = 0.0             # Target material atomic number                 []
                self.target_m = 0.0             # Target material atomic mass                   [amu]
                self.target_sbe = 0.0           # Target material surface binding energy        [eV]
                self.target_rho = 0.0           # Target material volumetric mass density       [kg/m3]
                self.alpha = 0.0                # Angle of incidence wrt surface normal         [deg]

                self.lam = 0.0                  # lambda fitting parameter from [eckstein03]
                self.q = 0.0                    # q fitting parameter from [eckstein03]
                self.mu = 0.0                   # mu fittiing parameter from [eckstein03]
                self.f = 0.0                    # f fitting parameter from [eckstein03]:
                self.c = 0.0                    # c fitting parameter from [eckstein03]
                self.b = 0.0                    # b fitting parameter from [eckstein03]
                self.E_thr = 0.0                # threshold energy for sputtering               [eV]
                self.ETF = 0.0                  # Thomas-Fermi energy unit                      [eV]
                self.sbe_gamma = 0.0            # SBE / gamma ratio                             []

                self.AngularData = 0            # Array to capture fitting parameters for angular dependency

# *******************************************************************************
# Main class

class SputteringModel:

        # %%%%%%%%%%%%%%%%%%%%%%%%%%%%%%%%%%%%%%%%%%%%%%%%%%%%%%%%%%%%%%%%%%%%%%%%%%%%%%%
        # INIT method
        def __init__(self, sputteringpars):

                # Transfer model arguments to internal variables
                self.ion_z = sputteringpars.ion_z
                self.ion_m = sputteringpars.ion_m
                self.ion_E0 = sputteringpars.ion_E0
                self.ion_sbe = sputteringpars.ion_sbe
                self.target_z = sputteringpars.target_z
                self.target_m = sputteringpars.target_m
```

```python
        self.target_sbe = sputteringpars.target_sbe
        self.target_rho = sputteringpars.target_rho
        self.lam = sputteringpars.lam
        self.q = sputteringpars.q
        self.mu = sputteringpars.mu
        self.f = sputteringpars.f
        self.c = sputteringpars.c
        self.b = sputteringpars.b
        self.E_thr = sputteringpars.E_thr
        self.ETF = sputteringpars.ETF
        self.sbe_gamma = sputteringpars.sbe_gamma
        self.AngularData = sputteringpars.AngularData

        # Definition of local physical constants
        self.aB = 0.529177              # Bohr radius                                                [A]
        self.ee2 = 14.39                # square of the electron charge in LSS units                 [eV-A]
        self.amu = 1.6726e-27           # Proton mass                                                [kg]
        self.Avogadro = 6.022e23        # Avogadro's constant

        # Flag to recognize calculation of NormalIncidence
        self.normal_calculated = 0


    # %%%%%%%%%%%%%%%%%%%%%%%%%%%%%%%%%%%%%%%%%%%%%%%%%%%%%%%%%%%%%%%%%%%%%%%%%%%%%%
    # Calculation of threshold energy according to [bohdansky80]
    def ThresholdEnergy(self):

        # Determination of ion-target mass ratio
        if ((self.ion_m / self.target_m) <= 0.3):

            # Light ion approximation
            print('Light ion approximation')
            gamma = (4*self.ion_m*self.target_m) / ((self.ion_m * self.target_m)**2)
            return self.target_sbe / (gamma * (1- gamma))
        else:

            # Heavy ion approximation
            print('Heavy ion approximation')
            return self.target_sbe * 8 * (self.ion_m / self.target_m)**(5/2)


    # %%%%%%%%%%%%%%%%%%%%%%%%%%%%%%%%%%%%%%%%%%%%%%%%%%%%%%%%%%%%%%%%%%%%%%%%%%%%%%
    # NormalIncidence method
    def NormalIncidence(self):
        # [eckstein03] equation 5, [garcia94] for validation of formulae

        # Lindhard screening length (confirmation) [eckstein03] equation 4
        self.aL2 = ((9.*np.pi**2.)/128.)**(1./3.) * self.aB / (np.sqrt(self.ion_z**(2./3.) + self.target_z**(2./3.)))

        # Thomas-Fermi energy unit (confirmation)
        self.ETF2 = (((self.ion_m + self.target_m) / self.target_m) * ((self.ion_z * self.target_z * self.ee2) / self.aL2 ))

        # Reduced energy (confirmation) [eckstein03] equation 3
        # Data tables in [behrisch08] provide ETF as epsilon, headings not clear
        # self.epsilon2 = self.ion_E0 / self.ETF2
        self.epsilon2 = self.ion_E0 / self.ETF2

        # Nuclear stopping power for KrC potential [eckstein03] equation 2
        self.sn = (0.5 * np.log(1.0 + 1.2288*self.epsilon2)) / (self.epsilon2 + 0.1728*np.sqrt(self.epsilon2) + 0.008*self.epsilon2**(0.1504
))

        # Sputtering rate
        self.y_sput_normal = self.q * self.sn * ( ((self.ion_E0/self.E_thr) - 1.0)**self.mu) / ( self.lam + ((self.ion_E0/self.E_thr) - 1.0)
**self.mu )
```

```python

                # Set flag to 1
                self.normal_calculated = 1


        # %%%%%%%%%%%%%%%%%%%%%%%%%%%%%%%%%%%%%%%%%%%%%%%%%%%%%%%%%%%%%%%%%%%%%%%%%%%%%%
        # AngleIncidence method
        def AngleIncidence(self):
                # [eckstein03] equation 8

                # If NormalIncidence has not been calculated, do that first
                if (self.normal_calculated == 0):
                        self.NormalIncidence()

                # alpha_0 reference angle value                 [rad]
                self.alpha_0 = np.pi - np.arccos( np.sqrt( 1 / (1 + self.ion_E0 / self.ion_sbe) ) )

                # Convert input angle alpha to radians
                self.alpha_rad = self.alpha * np.pi / 180.0

                # Angle-dependent sputtering rate
                self.y_sput_angle = self.y_sput_normal * ( np.cos ( (self.alpha_rad * np.pi / self.alpha_0 / 2 )**self.c ) )**(-self.f) * np.exp( se
lf.b * (1 - 1 / np.cos((self.alpha_rad * np.pi / self.alpha_0 / 2)**self.c)))



# ***********************************************************************************
```

```python
#!/usr/bin/python

# *******************************************************
# Set of parameters for test helicon devices.
#
# JIDVG, 2022
# *******************************************************

# Import required modules
from AhedoOOP import *


# %%%%%%%%%%%%%%%%%%%%%%%%%%%%%%%%%%%%%%%%%%%%%%%%%%%%%%%%%%%%%%%%%%%%%%%%%%%%%%%%%%%%%%%%%%%%%%%%%%%%%%%%%%%%%%%%%%%%%%%%%
#
# INPUT OF MODEL PARAMETERS
#
# **********************************************************************************************
# INPUT model parameters
# **********************************************************************************************

# General parameters to apply to all models
general_rr_res = 500
general_zz_res = 1000

# -------------------------------------------------------------------------------------------------------------
# Parameters from [navarro12a]
navarro12pars = HeliconPars()

navarro12pars.R = 0.01                                   # Chamber radius                        [m]
navarro12pars.L = 0.10                                  # Chamber length                        [m]
navarro12pars.B0 = 0.06                                 # Axial magnetic field intensity        [T]
navarro12pars.mdot = 1e-7                               # Neutral injection mass flow           [kg / s]
navarro12pars.un0 = 350.0                               # Neutral axial speed at injection      [m/s]
navarro12pars.nn0 = 1.5e19                              # Neutral density at injection          [m^-3]
navarro12pars.Te = 10.0                                 # Constant electron temperature         [eV]
navarro12pars.Z_p = 18.0                                # Atomic number of ion species
navarro12pars.Aion = 40.0                               # Standard atomic mass of ion species

# Argon parameters required for collision rates [ahedo13]
navarro12pars.Eion = 15.76                              # First ionization energy, Argon                [eV]
navarro12pars.sigma_ion = 2.8e-20                       # Ionization cross section, Argon               [m2]
navarro12pars.sigma_en = 15e-20                         # e-n collision cross section, Argon            [m2]
navarro12pars.Rin_k2 = 10.5e-10                         # Constant k2 for calculation of Rin, Argon     [m]
navarro12pars.Rin_k1 = 1.67e-10                         # Constant k1 for calculation of Rin, Argon     [m]
navarro12pars.clambda = 15                              # Coulomb logarithm, average value according to [ahedo13] and [NRL Plasma Formulary]

navarro12 = HeliconModel(navarro12pars, general_rr_res, general_zz_res)
# -------------------------------------------------------------------------------------------------------------


# -------------------------------------------------------------------------------------------------------------
# Parameters from [ahedo13]
ahedopars = HeliconPars()

ahedopars.R = 0.02                                      # Chamber radius                        [m]
ahedopars.L = 0.10                                      # Chamber length                        [m]
ahedopars.B0 = 0.06                                     # Axial magnetic field intensity        [T]
ahedopars.mdot = 1e-7                                   # Neutral injection mass flow           [kg / s]
ahedopars.un0 = 400.0                                   # Neutral axial speed at injection      [m/s]
ahedopars.nn0 = 1.5e19                                  # Neutral density at injection          [m^-3]
ahedopars.Te = 10.0                                     # Constant electron temperature         [eV]
ahedopars.Z_p = 18.0                                    # Atomic number of ion species
ahedopars.Aion = 40.0                                   # Standard atomic mass of ion species
```

```
# Argon parameters required for collision rates [ahedo13]
ahedopars.Eion = 15.76                                   # First ionization energy, Argon                [eV]
ahedopars.sigma_ion = 2.8e-20                            # Ionization cross section, Argon               [m2]
ahedopars.sigma_en = 15e-20                              # e-n collision cross section, Argon            [m2]
ahedopars.Rin_k2 = 10.5e-10                              # Constant k2 for calculation of Rin, Argon     [m]
ahedopars.Rin_k1 = 1.67e-10                              # Constant k1 for calculation of Rin, Argon     [m]
ahedopars.clambda = 15                                   # Coulomb logarithm, average value according to [ahedo13] and [NRL Plasma Formulary]

ahedo = HeliconModel(ahedopars, general_rr_res, general_zz_res)
# ----------------------------------------------------------------------------------------------------------------



# ----------------------------------------------------------------------------------------------------------------
# Parameters from VX-CR [castro13, Amaya Navarro 2014]
vxcrpars = HeliconPars()

vxcrpars.R = 0.045                                       # Chamber radius                        [m]
vxcrpars.L = 0.226                                       # Chamber length                        [m]
vxcrpars.B0 = 0.1                                        # Axial magnetic field intensity        [T]
vxcrpars.mdot = 200*2.973e-8                             # Neutral injection mass flow           [kg / s]                mdot = 200 sccm [castro13]

vxcrpars.un0 = vxcrpars.mdot / (1.2891e-5 * np.pi * vxcrpars.R**2)
                                                         # Neutral axial speed at injection      [m/s]                   rho = 1.2891e-5 [NIST], T = 25 C, mdot = rho*A*un0

# vxcrpars.mdot = 6e-6                                   # Neutral injection mass flow           [kg / s]
# vxcrpars.un0 = 5.589e4                                 # Neutral axial speed at injection      [m/s]                   rho = 1.784, T = 25 C, mdot = rho*A*un0
vxcrpars.nn0 = 1.943e20                                  # Neutral density at injection          [m^-3]                  from P = 6e-3 torr and T = 25 C             [castro13]
                                                         #                                                               nn0 = P / (k_B * T)
vxcrpars.Te = 3.0                                        # Constant electron temperature         [eV]                    avg Te from [castro13]        FIXME 4 eV
vxcrpars.Z_p = 18.0                                      # Atomic number of ion species
vxcrpars.Aion = 40.0                                     # Standard atomic mass of ion species

# Argon parameters required for collision rates [ahedo13]
vxcrpars.Eion = 15.76                                    # First ionization energy, Argon                [eV]
vxcrpars.sigma_ion = 2.8e-20                             # Ionization cross section, Argon               [m2]
vxcrpars.sigma_en = 15e-20                               # e-n collision cross section, Argon            [m2]
vxcrpars.Rin_k2 = 10.5e-10                               # Constant k2 for calculation of Rin, Argon     [m]
vxcrpars.Rin_k1 = 1.67e-10                               # Constant k1 for calculation of Rin, Argon     [m]
vxcrpars.clambda = 15                                    # Coulomb logarithm, average value according to [ahedo13] and [NRL Plasma Formulary]

# Threshold energies for electron impact rate coefficients, Ar
vxcrpars.kthr01 = 11.5                                   # [eV]
vxcrpars.kthr02 = 11.6                                   # [eV]
vxcrpars.kthr03 = 11.7                                   # [eV]
vxcrpars.kthr04 = 11.8                                   # [eV]
vxcrpars.kthr05 = 13.2                                   # [eV]
vxcrpars.kthr06 = 11.8                                   # [eV]
vxcrpars.kthr07 = 14.2                                   # [eV]
vxcrpars.kthr08 = 15.0                                   # [eV]
vxcrpars.kthr09 = 15.5                                   # [eV]


vxcr = HeliconModel(vxcrpars, general_rr_res, general_zz_res)
# ----------------------------------------------------------------------------------------------------------------


# ----------------------------------------------------------------------------------------------------------------
# Parameters from PISCES-RF, Ar+ operation [thakur21b]
piscesRF_Arpars = HeliconPars()
```

```
piscesRF_Arpars.R = 0.06                                  # Chamber radius                          [m]
piscesRF_Arpars.L = 0.65                                  # Chamber length                          [m]
piscesRF_Arpars.B0 = 0.09                                 # Axial magnetic field intensity          [T]
piscesRF_Arpars.mdot = 60*2.973e-8                        # Neutral injection mass flow             [kg / s]                mdot = 60 sccm

piscesRF_Arpars.un0 = piscesRF_Arpars.mdot / (1.784 * np.pi * piscesRF_Arpars.R**2)
                                                          # Neutral axial speed at injection        [m/s]                   rho = 1.784, T = 25
C, mdot = rho*A*un0

piscesRF_Arpars.nn0 = 1.0e20                              # Neutral density at injection            [m^-3]                  [thakur21b]
piscesRF_Arpars.Te = 5.0                                  # Constant electron temperature           [eV]                    [thakur21b]
piscesRF_Arpars.Z_p = 18.0                                # Atomic number of ion species
piscesRF_Arpars.Aion = 40.0                               # Standard atomic mass of ion species

# Argon parameters required for collision rates [ahedo13]
piscesRF_Arpars.Eion = 15.76                              # First ionization energy, Argon                  [eV]
piscesRF_Arpars.sigma_ion = 2.8e-20                       # Ionization cross section, Argon                 [m2]
piscesRF_Arpars.sigma_en = 15e-20                         # e-n collision cross section, Argon              [m2]
piscesRF_Arpars.Rin_k2 = 10.5e-10                         # Constant k2 for calculation of Rin, Argon       [m]
piscesRF_Arpars.Rin_k1 = 1.67e-10                         # Constant k1 for calculation of Rin, Argon       [m]
piscesRF_Arpars.clambda = 15                              # Coulomb logarithm, average value according to [ahedo13] and [NRL Plasma Formulary]

piscesRF_Ar = HeliconModel(piscesRF_Arpars, general_rr_res, general_zz_res)
# ---------------------------------------------------------------------------------------------------------------

# ---------------------------------------------------------------------------------------------------------------
# Parameters from CSDX, Ar+ operation [burin05]
CSDX_Arpars = HeliconPars()

CSDX_Arpars.R = 0.06                              # Chamber radius                          [m]
CSDX_Arpars.L = 0.65                              # Chamber length                          [m]
CSDX_Arpars.B0 = 0.1                              # Axial magnetic field intensity          [T]
CSDX_Arpars.mdot = 60*2.973e-8                    # Neutral injection mass flow             [kg / s]                mdot = 60 sccm; FIXME no dat
a on [burin05]

CSDX_Arpars.un0 = CSDX_Arpars.mdot / (1.784 * np.pi * CSDX_Arpars.R**2)
                                                  # Neutral axial speed at injection        [m/s]                   rho = 1.784, T = 25 C, mdot
= rho*A*un0

CSDX_Arpars.nn0 = 1.0e20                          # Neutral density at injection            [m^-3]                  [thakur21b]
CSDX_Arpars.Te = 3.0                              # Constant electron temperature           [eV]                    [thakur21b]
CSDX_Arpars.Z_p = 18.0                            # Atomic number of ion species
CSDX_Arpars.Aion = 40.0                           # Standard atomic mass of ion species

# Argon parameters required for collision rates [ahedo13]
CSDX_Arpars.Eion = 15.76                          # First ionization energy, Argon                  [eV]
CSDX_Arpars.sigma_ion = 2.8e-20                   # Ionization cross section, Argon                 [m2]
CSDX_Arpars.sigma_en = 15e-20                     # e-n collision cross section, Argon              [m2]
CSDX_Arpars.Rin_k2 = 10.5e-10                     # Constant k2 for calculation of Rin, Argon       [m]
CSDX_Arpars.Rin_k1 = 1.67e-10                     # Constant k1 for calculation of Rin, Argon       [m]
CSDX_Arpars.clambda = 15                          # Coulomb logarithm, average value according to [ahedo13] and [NRL Plasma Formulary]

CSDX_Ar = HeliconModel(CSDX_Arpars, general_rr_res, general_zz_res)
# ---------------------------------------------------------------------------------------------------------------

# ---------------------------------------------------------------------------------------------------------------
# Parameters from UTHX, Ar+ operation [berisford10]
UTHX_Arpars = HeliconPars()

UTHX_Arpars.R = 0.06                              # Chamber radius                          [m]
UTHX_Arpars.L = 0.4                               # Chamber length                          [m]
UTHX_Arpars.B0 = 0.06                             # Axial magnetic field intensity          [T]
UTHX_Arpars.mdot = 55*2.973e-8                    # Neutral injection mass flow             [kg / s]                mdot = 60 sccm
```

```
UTHX_Arpars.un0 = UTHX_Arpars.mdot / (1.784 * np.pi * UTHX_Arpars.R**2)
                                                        # Neutral axial speed at injection      [m/s]                   rho = 1.784, T = 25 C, mdot = rho*A*un0

UTHX_Arpars.nn0 = 6.59e19                               # Neutral density at injection          [m^-3]                  n = p / (k_B*T); p data from [berisford10]
UTHX_Arpars.Te = 3.8                                    # Constant electron temperature         [eV]                    [berisford10]
UTHX_Arpars.Z_p = 18.0                                  # Atomic number of ion species
UTHX_Arpars.Aion = 40.0                                 # Standard atomic mass of ion species

# Argon parameters required for collision rates [ahedo13]
UTHX_Arpars.Eion = 15.76                                # First ionization energy, Argon                [eV]
UTHX_Arpars.sigma_ion = 2.8e-20                         # Ionization cross section, Argon               [m2]
UTHX_Arpars.sigma_en = 15e-20                           # e-n collision cross section, Argon            [m2]
UTHX_Arpars.Rin_k2 = 10.5e-10                           # Constant k2 for calculation of Rin, Argon     [m]
UTHX_Arpars.Rin_k1 = 1.67e-10                           # Constant k1 for calculation of Rin, Argon     [m]
UTHX_Arpars.clambda = 15                                # Coulomb logarithm, average value according to [ahedo13] and [NRL Plasma Formulary]

UTHX_Ar = HeliconModel(UTHX_Arpars, general_rr_res, general_zz_res)
# ------------------------------------------------------------------------------------------------------------


# ------------------------------------------------------------------------------------------------------------
# Parameters from UC3M - HTP05, Ar+ operation [navarro18]
HTP05_Arpars = HeliconPars()

HTP05_Arpars.R = 0.015                                  # Chamber radius                        [m]
HTP05_Arpars.L = 0.2                                    # Chamber length                        [m]
HTP05_Arpars.B0 = 0.0800                                # Axial magnetic field intensity        [T]
HTP05_Arpars.mdot = 50*2.973e-8                         # Neutral injection mass flow           [kg / s]                mdot = 50 sccm

HTP05_Arpars.un0 = HTP05_Arpars.mdot / (1.784 * np.pi * HTP05_Arpars.R**2)
                                                        # Neutral axial speed at injection      [m/s]                   rho = 1.784, T = 25 C, mdot = rho*A*un0

HTP05_Arpars.nn0 = 7.086e17                             # Neutral density at injection          [m^-3]                  n = p / (k_B*T); p=2.917e-8 bar data from [navarro18]
HTP05_Arpars.Te = 4.5                                   # Constant electron temperature         [eV]                    [navarro18]
HTP05_Arpars.Z_p = 18.0                                 # Atomic number of ion species
HTP05_Arpars.Aion = 40.0                                # Standard atomic mass of ion species

# Argon parameters required for collision rates [ahedo13]
HTP05_Arpars.Eion = 15.76                               # First ionization energy, Argon                [eV]
HTP05_Arpars.sigma_ion = 2.8e-20                        # Ionization cross section, Argon               [m2]
HTP05_Arpars.sigma_en = 15e-20                          # e-n collision cross section, Argon            [m2]
HTP05_Arpars.Rin_k2 = 10.5e-10                          # Constant k2 for calculation of Rin, Argon     [m]
HTP05_Arpars.Rin_k1 = 1.67e-10                          # Constant k1 for calculation of Rin, Argon     [m]
HTP05_Arpars.clambda = 15                               # Coulomb logarithm, average value according to [ahedo13] and [NRL Plasma Formulary]

HTP05_Ar = HeliconModel(HTP05_Arpars, general_rr_res, general_zz_res)
# ------------------------------------------------------------------------------------------------------------

# ------------------------------------------------------------------------------------------------------------
# Parameters from TohokuHX, Ar+ operation [takahashi17]
TohokuHX_Arpars = HeliconPars()

TohokuHX_Arpars.R = 0.065/2                             # Chamber radius                        [m]
TohokuHX_Arpars.L = 0.200                               # Chamber length                        [m]
TohokuHX_Arpars.B0 = 0.03                               # Axial magnetic field intensity        [T]
TohokuHX_Arpars.mdot = 24*2.973e-8                      # Neutral injection mass flow           [kg / s]                mdot = 24 sccm

TohokuHX_Arpars.un0 = TohokuHX_Arpars.mdot / (1.784 * np.pi * TohokuHX_Arpars.R**2)
                                                        # Neutral axial speed at injection      [m/s]                   rho = 1.784, T = 25 C, mdot
```

```
    = rho*A*un0

TohokuHX_Arpars.nn0 = 2.6e19                    # Neutral density at injection          [m^-3]                  n = p / (k_B*T); p data from
  [navarro18]
TohokuHX_Arpars.Te = 6                          # Constant electron temperature         [eV]                    [navarro18]
TohokuHX_Arpars.Z_p = 18.0                      # Atomic number of ion species
TohokuHX_Arpars.Aion = 40.0                     # Standard atomic mass of ion species

# Argon parameters required for collision rates [ahedo13]
TohokuHX_Arpars.Eion = 15.76                    # First ionization energy, Argon                [eV]
TohokuHX_Arpars.sigma_ion = 2.8e-20             # Ionization cross section, Argon               [m2]
TohokuHX_Arpars.sigma_en = 15e-20               # e-n collision cross section, Argon            [m2]
TohokuHX_Arpars.Rin_k2 = 10.5e-10               # Constant k2 for calculation of Rin, Argon     [m]
TohokuHX_Arpars.Rin_k1 = 1.67e-10               # Constant k1 for calculation of Rin, Argon     [m]
TohokuHX_Arpars.clambda = 15                    # Coulomb logarithm, average value according to [ahedo13] and [NRL Plasma Formulary]

TohokuHX_Ar = HeliconModel(TohokuHX_Arpars, general_rr_res, general_zz_res)
# ---------------------------------------------------------------------------------------------------------------
```

```python
#!/usr/bin/python

# *******************************************************
# Parameter sets for Eckstein sputtering simulations
#
# JIDVG, 2022
# *******************************************************

# Import required Python modules
from EcksteinSputteringOOP import *

# %%%%%%%%%%%%%%%%%%%%%%%%%%%%%%%%%%%%%%%%%%%%%%%%%%%%%%%%%%%%%%%%%%%%%%%%%%%%%%%%%%%%%%%%%%%%%%
# INPUT OF MODEL PARAMETERS

# %%%%%%%%%%%%%%%%%%%%%%%%%%%%%%%%%%%%%%%%%%%%%%%%%%%%%%%%%%%%%%%%%%%%%%%%%%%%%%%%%%%%%%%%%%%%%%
# MODEL #1
# Xenon Ions on Nickel Substrate --> Validation set from [eckstein03] figure 1a.
# FIXME No angular parameter data for this combination on [behrisch07]
XeNiPars = SputteringPars()

XeNiPars.ion_z = 54.0                   # Impacting ion atomic number                   []
XeNiPars.ion_m = 131.293                # Impacting ion atomic mass                     [amu]
XeNiPars.ion_E0 = 1000.0                # Impacting ion energy                          [eV]
XeNiPars.ion_sbe = 0.0                  # Impacting ion surface binding energy          [eV]
XeNiPars.target_z = 28.0                # Target material atomic number                 []
XeNiPars.target_m = 58.6934             # Target material atomic mass                   [amu]
XeNiPars.target_sbe = 4.46              # Target material surface binding energy        [eV]
XeNiPars.target_rho = 8908              # Target material volumetric mass density       [kg/m3]
XeNiPars.alpha = 0.0                    # Angle of incidence wrt surface normal         [deg]

XeNiPars.lam = 1.3503                   # lambda fitting parameter from [eckstein03]
XeNiPars.q = 20.8797                    # q fitting parameter from [eckstein03]
XeNiPars.mu = 2.3649                    # mu fittiing parameter from [eckstein03]
XeNiPars.f = 0.0                        # f fitting parameter from [eckstein03]:
XeNiPars.c = 0.0                        # c fitting parameter from [eckstein03]
XeNiPars.b = 0.0                        # b fitting parameter from [eckstein03]
XeNiPars.E_thr = 21.27                  # threshold energy for sputtering               [eV]
XeNiPars.ETF = 7.29221e5                # Thomas-Fermi energy unit                      [eV]
XeNiPars.sbe_gamma = 5.22               # SBE / gamma ratio                             []


XeNiModel = SputteringModel(XeNiPars)
# %%%%%%%%%%%%%%%%%%%%%%%%%%%%%%%%%%%%%%%%%%%%%%%%%%%%%%%%%%%%%%%%%%%%%%%%%%%%%%%%%%%%%%%%%%%%%%

# %%%%%%%%%%%%%%%%%%%%%%%%%%%%%%%%%%%%%%%%%%%%%%%%%%%%%%%%%%%%%%%%%%%%%%%%%%%%%%%%%%%%%%%%%%%%%%
# MODEL #2
# Ar+ Ions on Aluminum Substrate --> Validation set from [behrisch07] figure 11, page 85
# Angular paramteres chosen for E0 = 200 eV
ArAlPars = SputteringPars()

ArAlPars.ion_z = 18.0                   # Impacting ion atomic number                   []
ArAlPars.ion_m = 39.948                 # Impacting ion atomic mass                     [amu]
ArAlPars.ion_E0 = 1000.0                # Impacting ion energy                          [eV]
ArAlPars.ion_sbe = 1e-18                # Impacting ion surface binding energy          [eV]
ArAlPars.target_z = 13.0                # Target material atomic number                 []
ArAlPars.target_m = 26.961              # Target material atomic mass                   [amu]
ArAlPars.target_sbe = 3.36              # Target material surface binding energy        [eV]
ArAlPars.target_rho = 2700              # Target material volumetric mass density       [kg/m3]
ArAlPars.alpha = 0.0                    # Angle of incidence wrt surface normal         [deg]

ArAlPars.lam = 0.4713                   # lambda fitting parameter from [eckstein03]
ArAlPars.q = 4.7928                     # q fitting parameter from [eckstein03]
ArAlPars.mu = 2.0810                    # mu fittiing parameter from [eckstein03]
ArAlPars.f = 5.4733                     # f fitting parameter from [eckstein03]
```

```
ArAlPars.c = 0.8298                    # c fitting parameter from [eckstein03]
ArAlPars.b = 2.5849                    # b fitting parameter from [eckstein03]
ArAlPars.E_thr = 21.5497               # threshold energy for sputtering              [eV]
ArAlPars.ETF = 6.28194e4               # Thomas-Fermi energy unit                     [eV]
ArAlPars.sbe_gamma = 3.49              # SBE / gamma ratio                            []

# Angular Sputtering fitting parameters as a function of ion energy [behrisch07]
# [ion_E0 f b c y_sput_normal ion_sbe]
ArAlPars.AngularData = np.array([[100.0, 14.7601, 8.5471, 0.6703, 1.17e-1, 0.00],
                                [500.0, 6.7055, 3.4612, 0.8024, 9.10e-1, 0.00],
                                # [1000.0, 5.4733, 2.5849, 0.8298, 1.37e0, 0.00],
                                [1050.0, 4.4893, 1.7504, 0.8913, 1.17e0, 0.00],
                                [10000.0, 3.3890, 1.0004, 0.8667, 2.39e0, 0.00]])

ArAlModel = SputteringModel(ArAlPars)
# %%%%%%%%%%%%%%%%%%%%%%%%%%%%%%%%%%%%%%%%%%%%%%%%%%%%%%%%%%%%%%%%%%%%%%%%%%%%%%%%%%%%%%%%%%%%%%%

# %%%%%%%%%%%%%%%%%%%%%%%%%%%%%%%%%%%%%%%%%%%%%%%%%%%%%%%%%%%%%%%%%%%%%%%%%%%%%%%%%%%%%%%%%%%%%%%
# MODEL #3
# Ar+ Ions on Aluminum Substrate --> Validation set from [behrisch07] figure 11, page 85
ArSiPars = SputteringPars()

ArSiPars.ion_z = 18.0                  # Impacting ion atomic number                  []
ArSiPars.ion_m = 39.948                # Impacting ion atomic mass                    [amu]
ArSiPars.ion_E0 = 1000.0               # Impacting ion energy                         [eV]
ArSiPars.ion_sbe = 0.0                 # Impacting ion surface binding energy         [eV]
ArSiPars.target_z = 14.0               # Target material atomic number                []
ArSiPars.target_m = 28.085             # Target material atomic mass                  [amu]
ArSiPars.target_sbe = 4.70             # Target material surface binding energy       [eV]
ArSiPars.target_rho = 2329             # Target material volumetric mass density      [kg/m3]
ArSiPars.alpha = 0.0                   # Angle of incidence wrt surface normal        [deg]

ArSiPars.lam = 0.2770                  # lambda fitting parameter from [eckstein03]
ArSiPars.q = 3.2299                    # q fitting parameter from [eckstein03]
ArSiPars.mu = 1.5284                   # mu fittiing parameter from [eckstein03]
ArSiPars.f = 0.0                       # f fitting parameter from [eckstein03]:
ArSiPars.c = 0.0                       # c fitting parameter from [eckstein03]
ArSiPars.b = 0.0                       # b fitting parameter from [eckstein03]
ArSiPars.E_thr = 32.8380               # threshold energy for sputtering              [eV]
ArSiPars.ETF = 6.67979e4               # Thomas-Fermi energy unit                             [eV]
ArSiPars.sbe_gamma = 4.85              # SBE / gamma ratio                            []


ArSiModel = SputteringModel(ArSiPars)
# %%%%%%%%%%%%%%%%%%%%%%%%%%%%%%%%%%%%%%%%%%%%%%%%%%%%%%%%%%%%%%%%%%%%%%%%%%%%%%%%%%%%%%%%%%%%%%%

# %%%%%%%%%%%%%%%%%%%%%%%%%%%%%%%%%%%%%%%%%%%%%%%%%%%%%%%%%%%%%%%%%%%%%%%%%%%%%%%%%%%%%%%%%%%%%%%
# MODEL #4
# Tungsten self-sputtering
WWPars = SputteringPars()

WWPars.ion_z = 74.0            # Impacting ion atomic number                  []
WWPars.ion_m = 183.84          # Impacting ion atomic mass                    [amu]
WWPars.ion_E0 = 1000.0         # Impacting ion energy                         [eV]
WWPars.ion_sbe = 8.68          # Impacting ion surface binding energy         [eV]
WWPars.target_z = 74.0         # Target material atomic number                []
WWPars.target_m = 183.84       # Target material atomic mass                  [amu]
WWPars.target_sbe = 8.68       # Target material surface binding energy       [eV]
WWPars.alpha = 0.0             # Angle of incidence wrt surface normal        [deg]

WWPars.lam = 2.2697            # lambda fitting parameter from [eckstein03]
WWPars.q = 18.6006             # q fitting parameter from [eckstein03]
WWPars.mu = 3.1273             # mu fittiing parameter from [eckstein03]
WWPars.f = 5.6049              # f fitting parameter from [eckstein03]:
```

```
WWPars.c = 0.7587               # c fitting parameter from [eckstein03]
WWPars.b = 3.0949               # b fitting parameter from [eckstein03]
WWPars.E_thr = 24.9885          # threshold energy for sputtering              [eV]
WWPars.ETF = 1.99860e6          # Thomas-Fermi energy unit                     [eV]
WWPars.sbe_gamma = 8.68         # SBE / gamma ratio                            []


WWModel = SputteringModel(WWPars)
# %%%%%%%%%%%%%%%%%%%%%%%%%%%%%%%%%%%%%%%%%%%%%%%%%%%%%%%%%%%%%%%%%%%%%%%%%%%%%%%%%%%%%%%%%%%%%%%


# %%%%%%%%%%%%%%%%%%%%%%%%%%%%%%%%%%%%%%%%%%%%%%%%%%%%%%%%%%%%%%%%%%%%%%%%%%%%%%%%%%%%%%%%%%%%%%%
# MODEL #5
# Ar+ Ions on SiO2 ==> Interpolated values for target material
ArSiO2Pars = SputteringPars()

ArSiO2Pars.ion_z = 18.0                 # Impacting ion atomic number                     []
ArSiO2Pars.ion_m = 39.948               # Impacting ion atomic mass                       [amu]
ArSiO2Pars.ion_E0 = 1000.0              # Impacting ion energy                            [eV]
ArSiO2Pars.ion_sbe = 1e-18              # Impacting ion surface binding energy            [eV]
ArSiO2Pars.target_z = 11.0              # AVG Target material atomic number               []
ArSiO2Pars.target_m = 22.042            # AVG Target material atomic mass                 [amu]
ArSiO2Pars.target_sbe = 3.653           # AVG Target material surface binding energy      [eV]
ArSiO2Pars.target_rho = 2648            # Target material volumetric mass density         [kg/m3]
ArSiO2Pars.alpha = 0.0                  # Angle of incidence wrt surface normal           [deg]

# Lambda, q, mu and E_thr obtained from scipy.optimize.curve_fit LSQ routine
ArSiO2Pars.lam = 7.41718485             # lambda fitting parameter from [eckstein03]      FIXME 0.2770
ArSiO2Pars.q = 3.63577036               # q fitting parameter from [eckstein03]           FIXME 3.2299
ArSiO2Pars.mu = 2.33880581              # mu fittiing parameter from [eckstein03]         FIXME 1.5284
ArSiO2Pars.f = 0.0                      # f fitting parameter from [eckstein03]:
ArSiO2Pars.c = 0.0                      # c fitting parameter from [eckstein03]
ArSiO2Pars.b = 0.0                      # b fitting parameter from [eckstein03]
ArSiO2Pars.E_thr = 32.8380              # threshold energy for sputtering                 [eV]    FIXME 32.8380
ArSiO2Pars.ETF = 6.67979e4              # Thomas-Fermi energy unit                                [eV]
ArSiO2Pars.sbe_gamma = 4.85             # SBE / gamma ratio                               []

# Angular Sputtering fitting parameters as a function of ion energy [behrisch07]
# [ion_E0 f b c y_sput_normal ion_sbe]
# ArSiO2Pars.AngularData = np.array([[100.0, 14.7601, 8.5471, 0.6703, 1.17e-1, 0.00],
#                                [500.0, 6.7055, 3.4612, 0.8024, 9.10e-1, 0.00],
#                                [1050.0, 4.4893, 1.7504, 0.8913, 1.17e0, 0.00],
#                                [10000.0, 3.3890, 1.0004, 0.8667, 2.39e0, 0.00]])

ArSiO2Model = SputteringModel(ArSiO2Pars)
# %%%%%%%%%%%%%%%%%%%%%%%%%%%%%%%%%%%%%%%%%%%%%%%%%%%%%%%%%%%%%%%%%%%%%%%%%%%%%%%%%%%%%%%%%%%%%%%


# %%%%%%%%%%%%%%%%%%%%%%%%%%%%%%%%%%%%%%%%%%%%%%%%%%%%%%%%%%%%%%%%%%%%%%%%%%%%%%%%%%%%%%%%%%%%%%%
# MODEL #6
# Ar+ Ions on Al2O3 ==> Interpolated values for target material
ArAl2O3Pars = SputteringPars()

ArAl2O3Pars.ion_z = 18.0                # Impacting ion atomic number                     []
ArAl2O3Pars.ion_m = 39.948              # Impacting ion atomic mass                       [amu]
ArAl2O3Pars.ion_E0 = 1000.0             # Impacting ion energy                            [eV]
ArAl2O3Pars.ion_sbe = 1e-18             # Impacting ion surface binding energy            [eV]
ArAl2O3Pars.target_z = 10.5             # AVG Target material atomic number               []
ArAl2O3Pars.target_m = 21.485           # AVG Target material atomic mass                 [amu]
ArAl2O3Pars.target_sbe = 3.36           # AVG Target material surface binding energy      [eV]
ArAl2O3Pars.target_rho = 3987           # Target material volumetric mass density         [kg/m3]
ArAl2O3Pars.alpha = 0.0                 # Angle of incidence wrt surface normal           [deg]

# Lambda, q and mu obbtained from scipy.optimize.curve_fit LSQ, E_thr obtained from Ar -> Al
```

```
ArAl2O3Pars.lam = 14.55347763          # lambda fitting parameter from [eckstein03]    FIXME 0.15
ArAl2O3Pars.q =  3.732629              # q fitting parameter from [eckstein03]         FIXME 1.5
ArAl2O3Pars.mu = 0.39654893            # mu fittiing parameter from [eckstein03]       FIXME 2.0810
ArAl2O3Pars.f = 5.4733                 # f fitting parameter from [eckstein03]
ArAl2O3Pars.c = 0.8298                 # c fitting parameter from [eckstein03]
ArAl2O3Pars.b = 2.5849                 # b fitting parameter from [eckstein03]
ArAl2O3Pars.E_thr = 21.55              # threshold energy for sputtering               [eV]
ArAl2O3Pars.ETF = 6.28194e4            # Thomas-Fermi energy unit                      [eV]
ArAl2O3Pars.sbe_gamma = 3.49           # SBE / gamma ratio                             []

# Angular Sputtering fitting parameters as a function of ion energy [behrisch07]
# [ion_E0 f b c y_sput_normal ion_sbe]
# ArAl2O3Pars.AngularData = np.array([[100.0, 14.7601, 8.5471, 0.6703, 1.17e-1, 0.00],
#                                [500.0, 6.7055, 3.4612, 0.8024, 9.10e-1, 0.00],
#                                [1050.0, 4.4893, 1.7504, 0.8913, 1.17e0, 0.00],
#                                [10000.0, 3.3890, 1.0004, 0.8667, 2.39e0, 0.00]])

ArAl2O3Model = SputteringModel(ArAl2O3Pars)
# %%%%%%%%%%%%%%%%%%%%%%%%%%%%%%%%%%%%%%%%%%%%%%%%%%%%%%%%%%%%%%%%%%%%%%%%%%%%%%%%%%%%%%%%%%%%%%


# %%%%%%%%%%%%%%%%%%%%%%%%%%%%%%%%%%%%%%%%%%%%%%%%%%%%%%%%%%%%%%%%%%%%%%%%%%%%%%%%%%%%%%%%%%%%%%%
# MODEL #7
# Ar+ Ions on Si3N4 ==> Interpolated values for target material
ArSi3N4Pars = SputteringPars()

ArSi3N4Pars.ion_z = 18.0               # Impacting ion atomic number                   []
ArSi3N4Pars.ion_m = 39.948             # Impacting ion atomic mass                     [amu]
ArSi3N4Pars.ion_E0 = 1000.0            # Impacting ion energy                          [eV]
ArSi3N4Pars.ion_sbe = 1e-18            # Impacting ion surface binding energy          [eV]
ArSi3N4Pars.target_z = 10.5            # AVG Target material atomic number             []
ArSi3N4Pars.target_m = 21.045          # AVG Target material atomic mass               [amu]
ArSi3N4Pars.target_sbe = 4.811         # AVG Target material surface binding energy    [eV]
ArSi3N4Pars.target_rho = 3170          # Target material volumetric mass density       [kg/m3]
ArSi3N4Pars.alpha = 0.0                # Angle of incidence wrt surface normal         [deg]

# Lambda, q and mu obbtained from scipy.optimize.curve_fit LSQ, E_thr obtained from Ar -> Si
ArSi3N4Pars.lam = 10.0                 # lambda fitting parameter from [eckstein03]
ArSi3N4Pars.q = 3.47721093             # q fitting parameter from [eckstein03]
ArSi3N4Pars.mu = 1.36261146            # mu fittiing parameter from [eckstein03]
ArSi3N4Pars.f = 0.0                    # f fitting parameter from [eckstein03]:
ArSi3N4Pars.c = 0.0                    # c fitting parameter from [eckstein03]
ArSi3N4Pars.b = 0.0                    # b fitting parameter from [eckstein03]
ArSi3N4Pars.E_thr = 32.838             # threshold energy for sputtering               [eV]
ArSi3N4Pars.ETF = 6.67979e4            # Thomas-Fermi energy unit                              [eV]
ArSi3N4Pars.sbe_gamma = 4.85           # SBE / gamma ratio                             []

# Angular Sputtering fitting parameters as a function of ion energy [behrisch07]
# [ion_E0 f b c y_sput_normal ion_sbe]
# ArSi3N4Pars.AngularData = np.array([[100.0, 14.7601, 8.5471, 0.6703, 1.17e-1, 0.00],
#                                [500.0, 6.7055, 3.4612, 0.8024, 9.10e-1, 0.00],
#                                [1050.0, 4.4893, 1.7504, 0.8913, 1.17e0, 0.00],
#                                [10000.0, 3.3890, 1.0004, 0.8667, 2.39e0, 0.00]])

ArSi3N4Model = SputteringModel(ArSi3N4Pars)
# %%%%%%%%%%%%%%%%%%%%%%%%%%%%%%%%%%%%%%%%%%%%%%%%%%%%%%%%%%%%%%%%%%%%%%%%%%%%%%%%%%%%%%%%%%%%%%
```

```python
#!/usr/bin/python

# ***************************************************************************************************
# helicon_tests.py
#
# Routine for the creation of particular plots or models
# ***************************************************************************************************


# Python module packages required for execution
import numpy as np
import matplotlib.pyplot as plt
import matplotlib.colors as colors
import scipy.interpolate as interp

# Model-specific packages
from AhedoOOP import *
import SheathsOOP as Sheaths
from EcksteinSputteringOOP import *

# Files containing parameter sets
import HeliconParSets
import SputteringPars

plt.rcParams["text.usetex"] = True
plt.rcParams["font.size"] = 8

# **************************************************************************************************
# SIMULATION CONTROL
#
# FIXME Selection of specified models

# Helicon Model
ThisHeliconModel = HeliconParSets.vxcr

# Sputtering Model, estimation of threshold energy for compound target
ThisSputteringModel = SputteringPars.ArAl2O3Model
# ThisSputteringModel.E_thr = ThisSputteringModel.ThresholdEnergy()


# Output data file names
datafile = "vxcr"
sputtfile = "ArAl2O3"

# Selection of plots or actions
plot_radial = 1
plot_radial_nrscan = 0
plot_axial = 1
plot_axial_nscan = 0
plot_colormesh = 0
plot_colormesh_velocity = 0
plot_sensitivity = 0
plot_simple_plotter = 0
plot_sputt_normal = 0
plot_sputt_angular = 0
plot_sputt_2D = 0
plot_gudmundsson = 0

save_radial_nrscan = 0
save_axial_nscan = 0
save_sputt_normal = 0
# **************************************************************************************************
```

```
# ***********************************************************************************************
# MODIFICATION TO MODEL PARAMETERS
# ThisHeliconModel.Rion = 2.5e-15
# ThisHeliconModel.ParInit()                            # Initialize parameters
# ThisHeliconModel.CollRateCalculation()                # Calculate collision and ionization rates. FIXME Only if Te is modified
# ThisHeliconModel.CollDerivedParameters()              # Initialize collisional parameters

# ***********************************************************************************************
# MODEL EXECUTION
ThisHeliconModel.RadialModel()
ThisHeliconModel.AxialModel()

# %%%%%%%%%%%%%%%%%%%%%%%%%%%%%%%%%%%%%%%%%%%%%%%%%%%%%%%%%%%%%%%%%%%%%%%%%%%%%%%%%%%%%%%%%%%%%%%%%%%%%%%%%%%%%%%%%%%%%%%%%%
# PLOT MODEL RESULTS
#

# ---------------------------------------------------------------------------------------------------------------
# Axial model
if plot_axial == 1:
        figaxial, axsaxial = plt.subplots(4, 1, figsize=(3,12), sharex=True, tight_layout=True)
        figaxial.suptitle('Axial model')
        axsaxial[0].plot(ThisHeliconModel.zzhat, ThisHeliconModel.n_n0)
        axsaxial[0].set_ylabel(r'n / n$_0$')

        axsaxial[1].plot(ThisHeliconModel.zzhat, ThisHeliconModel.nn_nn0)
        axsaxial[1].set_ylabel(r'n$_n$ / n$_{n0}$')

        axsaxial[2].plot(ThisHeliconModel.zzhat, ThisHeliconModel.uz_cs)
        axsaxial[2].set(ylim=(-1,1))
        axsaxial[2].set_ylabel(r'u$_z$ / c$_s$')

        axsaxial[3].plot(ThisHeliconModel.zzhat, ThisHeliconModel.xixi/np.pi)
        axsaxial[3].set(ylim=(-0.25,0.25))
        axsaxial[3].set_ylabel(r'$\xi / \pi$')
        axsaxial[3].set_xlabel(r'$\hat{z}$')

        for ax in figaxial.get_axes():
                ax.label_outer()

        figaxial.set_dpi(300.0)

        figaxial.show()
        figaxial.savefig('AxialModelpng', dpi=300.0)

# ---------------------------------------------------------------------------------------------------------------
# Radial model
if plot_radial == 1:
        figradial, axsradial = plt.subplots(3, 1, figsize=(3,9), sharex=True, tight_layout=True)
        figradial.suptitle('Radial model')
        axsradial[0].semilogy(ThisHeliconModel.rrhat, ThisHeliconModel.nr_nr0)
        axsradial[0].set_ylabel(r'n$_r$ / n$_{r0}$')
        # axsradial[0].set_aspect('equal', 'box')

        axsradial[1].plot(ThisHeliconModel.rrhat, ThisHeliconModel.ur_cs)
        axsradial[1].set_ylabel(r'u$_r$ / c$_s$')
        axsradial[1].set(ylim=(0,1))
        # axsradial[1].set_aspect('equal', 'box')

        axsradial[2].plot(ThisHeliconModel.rrhat, ThisHeliconModel.utheta_ce)
        axsradial[2].set_ylabel(r'u$_\theta$ / c$_e$')
        axsradial[2].set_xlabel(r'$\hat{r}$')
        axsradial[2].set(ylim=(0,1))
        # axsradial[2].set_aspect('equal', 'box')
```

```
        for ax in figradial.get_axes():
                ax.label_outer()

        figradial.set_dpi(300.0)
        figradial.show()
        figradial.savefig('RadialModelpng', dpi=300.0)

# -------------------------------------------------------------------------------------------------------------
# Radial density scan
if plot_radial_nrscan == 1:
        figradial, axsradial = plt.subplots(figsize=(4,4), tight_layout=True)
        figradial.suptitle('Radial model')
        axsradial.semilogy(ThisHeliconModel.rrhat, ThisHeliconModel.nr_nr0)
        axsradial.set(ylabel=r'$n_r / n_{r0}$')
        axsradial.set(xlabel=r'$\hat{r}$')

        figradial.set_dpi(300.0)
        figradial.show()

# -------------------------------------------------------------------------------------------------------------
# Axial density scan
if plot_axial_nscan == 1:
        figaxiall, axsaxiall = plt.subplots(figsize=(4,4), tight_layout=True)
        figaxiall.suptitle('Axial model')
        axsaxiall.plot(ThisHeliconModel.zzhat, ThisHeliconModel.n_n0)
        axsaxiall.set(ylabel=r'$n / n_0$')
        axsaxiall.set(xlabel=r'$\hat{z}$')

        figaxiall.set_dpi(300.0)
        figaxiall.show()


# -------------------------------------------------------------------------------------------------------------
# Axial density scan
if plot_simple_plotter == 1:
        figsimple, axssimple = plt.subplots(figsize=(4,4), tight_layout=True)
        # FIXME Set here plot parameters
        axssimple.plot(ThisHeliconModel.zzhat, ThisHeliconModel.xixi)
        axssimple.set(ylabel=r'$\xi$')
        axssimple.set(xlabel=r'$\hat{z}$')
        # axssimple.xaxis.set_major_locator(plt.MultipleLocator(np.pi / 8))
        # axssimple.xaxis.set_minor_locator(plt.MultipleLocator(np.pi / 16))
        # axssimple.xaxis.set_major_formatter(plt.FuncFormatter(multiple_formatter()))
        figsimple.set_dpi(300.0)
        figsimple.show()

# -------------------------------------------------------------------------------------------------------------
# Save radial density scan data
if save_radial_nrscan == 1:
        np.savez(datafile, rrhat=ThisHeliconModel.rrhat, nr_nr0=ThisHeliconModel.nr_nr0)

# -------------------------------------------------------------------------------------------------------------
# Save axial density scan data
if save_axial_nscan == 1:
        np.savez(datafile, zzhat=ThisHeliconModel.zzhat, n_n0=ThisHeliconModel.n_n0)

# -------------------------------------------------------------------------------------------------------------
## Contour map of plasma density
if plot_colormesh == 1:
        # Creation of meshgrid
        zmesh, rmesh = np.meshgrid(ThisHeliconModel.zzhat, ThisHeliconModel.rrhat)

        # Creation of density mesh data
        nmesh = ThisHeliconModel.nr_nr0.reshape(ThisHeliconModel.rres, 1) @ ThisHeliconModel.n_n0.reshape(1, ThisHeliconModel.zzres)
```

```python

    # Creation of plot
    figmesh, axsmesh = plt.subplots(figsize=(4,4), tight_layout=True)

    pmesh = axsmesh.pcolormesh(zmesh, rmesh, np.log10(nmesh), cmap=plt.get_cmap('jet'))
    axsmesh.contour(zmesh, rmesh, np.log10(nmesh), ((-1.2, -0.8, -0.4, 0.0, 0.2, 0.4, 0.5)))

    axsmesh.set_xlabel('$\hat{z}$')
    axsmesh.set_ylabel('$\hat{r}$')
    axsmesh.set_ylim(0.4, 1.0)

    cbar = figmesh.colorbar(pmesh)
    cbar.set_label('$\log_{10}(n/n_0)$')

    figmesh.set_dpi(300.0)
    plt.show()
    figmesh.savefig('colormesh.png', dpi=300.0)

# ------------------------------------------------------------------------------------------------------------
## Contour map of plasma density
if plot_colormesh_velocity == 1:
    # Creation of coordinate meshgrid
    zmesh, rmesh = np.meshgrid(ThisHeliconModel.zzhat, ThisHeliconModel.rrhat)

    # Maps of ion, electron and neutral velocities
    ur_vector = ThisHeliconModel.ur_cs
    uz_vector = ThisHeliconModel.uz_cs

    # Velocity vectors are tiled into arrays of dimension (rres, zzres), consistent with nmesh.
    ur_mesh = np.tile(ur_vector.reshape(ThisHeliconModel.rres,1), (1, ThisHeliconModel.zzres))
    uz_mesh = np.tile(uz_vector.reshape(1, ThisHeliconModel.zzres), (ThisHeliconModel.rres, 1))

    # Calculation of velocity magnitude meshes for ions and electrons and neutrals
    u_i_mag = np.sqrt(ur_mesh*ur_mesh + uz_mesh*uz_mesh)

    # ============================================================================================
    # Calculation of radial ion velocity plot
    figradial, axsradial = plt.subplots(figsize=(4,4), tight_layout=True)

    pradial = axsradial.pcolormesh(zmesh, rmesh, np.log(ur_mesh), cmap=plt.get_cmap('jet'))

    axsradial.set_xlabel(r'$\hat{z}$')
    axsradial.set_ylabel(r'$\hat{r}$')
    cbar = figradial.colorbar(pradial)
    cbar.set_label('r$\log(u_r/c_s)$')

    figradial.set_dpi(300.0)
    plt.show()
    figradial.savefig('colormesh_velocity_radial.png', dpi=300.0)

    # ============================================================================================
    # Calculation of radial ion velocity plot
    figaxial, axsaxial = plt.subplots(figsize=(4,4), tight_layout=True)

    paxial = axsaxial.pcolormesh(zmesh, rmesh, np.log(uz_mesh), cmap=plt.get_cmap('jet'))

    axsaxial.set_xlabel(r'$\hat{z}$')
    axsaxial.set_ylabel(r'$\hat{r}$')
    cbar = figaxial.colorbar(paxial)
    cbar.set_label(r'$\log(u_z/c_s)$')

    figaxial.set_dpi(300.0)
    plt.show()
    figaxial.savefig('colormesh_velocity_axial.png', dpi=300.0)
```

```

        # ==========================================================================================
        # Creation of ion velocity magnitude plot
        figmesh, axsmesh = plt.subplots(figsize=(4,4), tight_layout=True)

        # pmesh = axsmesh.pcolormesh(zmesh, rmesh, np.log(u_i_mag), cmap=plt.get_cmap('jet'))
        pmesh = axsmesh.pcolormesh(zmesh, rmesh, u_i_mag, cmap=plt.get_cmap('jet'))

        axsmesh.set_xlabel(r'$\hat{z}$')
        axsmesh.set_ylabel(r'$\hat{r}$')
        cbar = figmesh.colorbar(pmesh)
        cbar.set_label(r'$u_i/c_s$')

        figmesh.set_dpi(300.0)
        plt.show()
        figmesh.savefig('colormesh_velocity_magnitude.png', dpi=300.0)


# ----------------------------------------------------------------------------------------------------------------
## Sensitivity of axial model to different plasma parameters

if plot_sensitivity == 1:

        par_field = np.linspace(5e-16, 1e-15, 10)                              # FIXME Iteration space is set here.
        steps_total = par_field.size

        nn0data_sensitivity = np.zeros((ThisHeliconModel.zzhat.size, steps_total))      # FIXME Array size selection
        sens_data = np.zeros((steps_total))                                  # FIXME Array for simple plots

        # Iterate values of selected parameter and store density data
        for step in range(steps_total):
                print('\nStep', step, ', computing for parameter value: ', par_field[step])
                ThisHeliconModel.Rion = par_field[step]                     # FIXME Parameter to iterate is set here
                ThisHeliconModel.ParInit()                                  # Initialize parameters
                ThisHeliconModel.CollDerivedParameters()                    # Initialize collisional parameters
                ThisHeliconModel.AxialModel()                               # Axial Model
                # ThisHeliconModel.RadialModel()                            # Radial Model
                nn0data_sensitivity[:,step] = ThisHeliconModel.n_n0         # FIXME Parameter to plot
                # sens_data[step] = ThisHeliconModel.Lstar
                # print("Lstar: ", ThisHeliconModel.Lstar, "; Lratio: ", ThisHeliconModel.Lratio)
                # print("Rion: ", ThisHeliconModel.Rion)

        # Creation of sensitivity plot
        fig_sens, axs_sens= plt.subplots(figsize=(4,4), tight_layout=True)

        # axs_sens.semilogx(par_field, sens_data)

        # FIXME Set plot properties here
        for dataplot in range(sens_data.size):
                axs_sens.plot(ThisHeliconModel.zzhat, nn0data_sensitivity[:,dataplot], label=par_field[dataplot])
                # axs_sens.plot(ThisHeliconModel.rrhat, nn0data_sensitivity[:,dataplot], label=par_field[dataplot])

        axs_sens.set(xlabel=r'$\mathbf{\hat{z}}$')
        axs_sens.set(ylabel=r'$\mathbf{n / n_{0}}$')

        # axs_sens.set(xlabel=r'$R_{ion}$')
        # axs_sens.set(ylabel=r'$L_\star$')

        axs_sens.legend()

        fig_sens.set_dpi(300.0)
        fig_sens.show()
        fig_sens.savefig('sensitivity.png', dpi=300)                          # FIXME filename

```

```

## END OF PLOT SECTION
## %%%%%%%%%%%%%%%%%%%%%%%%%%%%%%%%%%%%%%%%%%%%%%%%%%%%%%%%%%%%%%%%%%%%%%%%%%%%%%%%%%%%%%%%%%%%%%%%%%%%%%%%%%%%%%%%%%%%%%%%%%

# %%%%%%%%%%%%%%%%%%%%%%%%%%%%%%%%%%%%%%%%%%%%%%%%%%%%%%%%%%%%%%%%%%%%%%%%%%%%%%%%%%%%%%%%%%%%%%%%%%%%%%%%%%%%%%%%%%%%%%%%%%
# SPUTTERING: NORMAL INCIDENCE
# Sputtering Yield at Normal Incidence as a function of Impacting Ion Energy
if plot_sputt_normal == 1:

        # Define energy span [eV] and create variables
        E0Range = np.logspace(1.0, 5.0, num=1000)                       # FIXME Select incoming ion energy range
        YSputtRange = np.zeros(np.size(E0Range))

        for index in range(0, np.size(E0Range)):
                ThisSputteringModel.ion_E0 = E0Range[index]
                ThisSputteringModel.NormalIncidence()
                YSputtRange[index] = ThisSputteringModel.y_sput_normal

        # Filter out NaN values from E0Range and YSputtRange
        YSputtRange_f = YSputtRange[~np.isnan(YSputtRange)]
        E0Range_f = E0Range[~np.isnan(YSputtRange)]

        # Calculation of Polynomial Fit
        Polyfit = np.polynomial.polynomial.polyfit(np.log(E0Range_f), YSputtRange_f, deg=5)

        # **********************************************************************************************************************
        # SputtFig01
        sputtfig, sputtax1 = plt.subplots(figsize=(4,4), tight_layout=True)

        sputtax1.loglog(E0Range, YSputtRange, 'r.', markerfacecolor='none', label='[eckstein03] formula')
        sputtax1.loglog(E0Range, np.polynomial.polynomial.Polynomial(Polyfit)(np.log(E0Range)), 'b-', label='Calculated Fit')
        sputtax1.set_ylabel('Sputtering Yield (atoms/ion)')
        sputtax1.set_xlabel('Incident Ion Energy (eV)')
        sputtax1.legend()
        sputtax1.grid()
        # sputtax1.set_xlim(left=2e3, right=5e4)
        # sputtax1.set_ylim(bottom=1e-1, top=1e1)

        sputtfig.set_dpi(300.0)
        sputtfig.show()
        sputtfig.savefig('sputt_normal.png', dpi=300.0)

        # **********************************************************************************************************************
        # SputtFig02
        sputtfig02, sputtax02 = plt.subplots(figsize=(4,4), tight_layout=True)

        sputtax02.plot(E0Range, YSputtRange, 'r.', markerfacecolor='none', label='[eckstein03] formula')
        sputtax02.plot(E0Range, np.polynomial.polynomial.Polynomial(Polyfit)(np.log(E0Range)), 'b-', label='Calculated Fit')
        sputtax02.set_ylabel('Sputtering Yield (atoms/ion)')
        sputtax02.set_xlabel('Incident Ion Energy (eV)')
        sputtax02.legend()
        sputtax02.grid()
        sputtax02.set_xlim(left=0.0, right=1000.0)
        # sputtax02.set_ylim(bottom=1e-1, top=1e1)

        sputtfig02.set_dpi(300.0)
        sputtfig02.show()

        if save_sputt_normal == 1:
                np.savez(sputtfile, E0Range=E0Range, YSputtRange=YSputtRange, Polyfit=Polyfit)


# %%%%%%%%%%%%%%%%%%%%%%%%%%%%%%%%%%%%%%%%%%%%%%%%%%%%%%%%%%%%%%%%%%%%%%%%%%%%%%%%%%%%%%%%%%%%%%%
# ANGULAR INCIDENCE
```

```
# Sputtering Yield as a function of Angle of Incidence of the impacting ion
if plot_sputt_angular == 1:

        # Set incident ion energy
        ThisSputteringModel.ion_E0 = 1000.0
        ThisSputteringModel.NormalIncidence()
        # ThisSputteringModel.y_sput_normal = 2.13e-5

        # Range of test angles
        AlphaRange = np.linspace(0, 90, 182)                                    # Select range of angles
        YSputtAngleRange = np.zeros(np.size(AlphaRange))

        for index in range(0, np.size(AlphaRange)):
                ThisSputteringModel.alpha = AlphaRange[index]
                ThisSputteringModel.AngleIncidence()
                YSputtAngleRange[index] = ThisSputteringModel.y_sput_angle

        # SemiLog plot
        fig, ax3 = plt.subplots()
        ax3.semilogy(AlphaRange, YSputtAngleRange, 'r*', label='[eckstein03] formula')
        ax3.set_ylabel('Sputtering Yield (atoms/ion)')
        ax3.set_xlabel('Incident Ion Angle (deg)')
        ax3.set_title('SemiLog Plot')
        ax3.legend()
        plt.show()

# %%%%%%%%%%%%%%%%%%%%%%%%%%%%%%%%%%%%%%%%%%%%%%%%%%%%%%%%%%%%%%%%%%%%%%%%%%%%%%%%%%%%%%%%%%%%%%%%%%%%%%%%
# SPUTTERING YIELD AS A FUNCTION OF ION ENERGY AND ANGLE OF INCIDENCE
# Linear Interpolation / Extrapolation of available data for Angular Sputtering fitting parameters
# [behrisch07]

if plot_sputt_2D == 1:

        # Define energy span [eV] and create variables
        E0Range = np.logspace(1.0, 5.0, num=1000)                       # FIXME Select incoming ion energy range

        # Range of test angles
        AlphaRange = np.linspace(0, 90, 182)                                    # Select range of angles

        # Create array to hold interpolated data
        ThisModelAngularDataInterp = np.zeros((np.size(E0Range), 6))

        # Use SciPy's interp1d routine for interpolation
        ThisModelAngularDataInterp[:,0] = E0Range
        ThisModelAngularDataInterp[:,1] = interp.interp1d(ThisSputteringModel.AngularData[:,0], ThisSputteringModel.AngularData[:,1], fill_value='extrapolate')(E0Range)
        ThisModelAngularDataInterp[:,2] = interp.interp1d(ThisSputteringModel.AngularData[:,0], ThisSputteringModel.AngularData[:,2], fill_value='extrapolate')(E0Range)
        ThisModelAngularDataInterp[:,3] = interp.interp1d(ThisSputteringModel.AngularData[:,0], ThisSputteringModel.AngularData[:,3], fill_value='extrapolate')(E0Range)
        ThisModelAngularDataInterp[:,4] = interp.interp1d(ThisSputteringModel.AngularData[:,0], ThisSputteringModel.AngularData[:,4], fill_value='extrapolate')(E0Range)
        ThisModelAngularDataInterp[:,5] = interp.interp1d(ThisSputteringModel.AngularData[:,0], ThisSputteringModel.AngularData[:,5], fill_value='extrapolate')(E0Range)

        # Arrays for data storage. Dimensions = [ alpha ion_E0 ]
        SputtData2D = np.zeros((np.size(AlphaRange), np.size(E0Range)))

        # Iterate over energy levels and angles to calculate sputtering yield
        for column in range(0, np.shape(SputtData2D)[1]):
                for row in range(0, np.shape(SputtData2D)[0]):
                        # Set model parameters according to current ion_E0 and alpha
                        ThisSputteringModel.ion_E0 = ThisModelAngularDataInterp[column, 0]
                        # [ion_E0 f b c y_sput_normal ion_sbe]
```

```python
                    ThisSputteringModel.f = ThisModelAngularDataInterp[column, 1]
                    ThisSputteringModel.b = ThisModelAngularDataInterp[column, 2]
                    ThisSputteringModel.c = ThisModelAngularDataInterp[column, 3]
                    ThisSputteringModel.y_sput_normal = ThisModelAngularDataInterp[column, 4]
                    ThisSputteringModel.ion_sbe = ThisModelAngularDataInterp[column, 5]

                    ThisSputteringModel.alpha = AlphaRange[row]
                    ThisSputteringModel.AngleIncidence()
                    SputtData2D[row, column]  = ThisSputteringModel.y_sput_angle

        # Creation of meshgrid
        AlphaMesh, E0Mesh = np.meshgrid(AlphaRange, ThisModelAngularDataInterp[:,0])

        # Replace NaN data in SputtData2D with zeroes
        SputtData2D = np.nan_to_num(SputtData2D, copy=False)

        # Replace negative values in SputtData2D with zeroes
        SputtData2D[SputtData2D<0.0] = np.finfo(float).eps

        # Creation of plot
        FigMesh, (AxsMesh0) = plt.subplots(figsize=(4,4), tight_layout=True)
        # AxsPColorMesh = AxsMesh0.contour(np.log10(E0Mesh), AlphaMesh, SputtData2D.transpose(), levels=100, linewidths=0.5, colors='k')
        AxsPColorMesh = AxsMesh0.pcolormesh(np.log10(E0Mesh), AlphaMesh, SputtData2D.transpose(), edgecolors='k', norm=colors.LogNorm(vmin=1e-4, vma
x=1e3), cmap=plt.get_cmap('jet'), shading='gouraud')
        # plt.pcolormesh(np.log10(E0Mesh), AlphaMesh, np.log10(SputtData2D.transpose()), cmap=plt.get_cmap('jet'), shading='auto')

        AxsMesh0.set_title(r'Ar$^{+} \; \rightarrow \;$ Al')
        AxsMesh0.set_ylabel(r'$\alpha$ [deg]', fontsize=12)
        AxsMesh0.set_xlabel(r'$\log_{10} (E_0)$ [eV]', fontsize=12)
        AxsMesh0.set_aspect('auto', 'box')
        AxsCbar = FigMesh.colorbar(AxsPColorMesh)
        AxsCbar.set_label(r'Y$_{sputt}$ [atoms/ion]', fontsize=12)

        FigMesh.set_dpi(300.0)

        FigMesh.savefig('ArAlSputteringYield.png', dpi=300, format='png')

        plt.show()
# ---------------------------------------------------------------------------------------------------------------------
# Plot of varepsilon_c calculation from [gudmundsson02]
if plot_gudmundsson == 1:

        Te_field = np.linspace(1.0, 10.0, num=100)                      # FIXME Iteration space is set here.
        steps_total = Te_field.size

        varepsilon_data = np.zeros((steps_total))                       # FIXME Array for simple plots

        # Iterate values of selected parameter and store density data
        for step in range(steps_total):
                print('\nStep ', step, ', computing for parameter value: ', Te_field[step])
                ThisHeliconModel.Te = Te_field[step]                    # FIXME Parameter to iterate is set here
                ThisHeliconModel.ParInit()                              # Initialize parameters
                ThisHeliconModel.CollRateCalculation()
                ThisHeliconModel.CollDerivedParameters()                # Initialize collisional parameters
                varepsilon_data[step] = ThisHeliconModel.E_c            # FIXME Parameter to plot

        # Creation of plot
        fig_varepsilon, axs_varepsilon= plt.subplots(figsize=(4,4), tight_layout=True)

        axs_varepsilon.loglog(Te_field, varepsilon_data)

        axs_varepsilon.set(xlabel=r'$T_e$ (eV)')
        axs_varepsilon.set(ylabel=r'$\varepsilon_c$ (eV)')
        axs_varepsilon.set_ylim(10, 1e4)
```

```
        # axs_varepsilon.set_xlim(1, 10)
        axs_varepsilon.grid()

        fig_varepsilon.set_dpi(300.0)
        fig_varepsilon.show()
        fig_varepsilon.savefig('gudmundsson.png', dpi=300)                          # FIXME filename


## END OF PLOT SECTION
## %%%%%%%%%%%%%%%%%%%%%%%%%%%%%%%%%%%%%%%%%%%%%%%%%%%%%%%%%%%%%%%%%%%%%%%%%%%%%%%%%%%%%%%%%%%%%%%%%%%%%%%%%%%%%%%%%%%%%%%%%%%%%%
```

```
#!/usr/bin/python

# %%%%%%%%%%%%%%%%%%%%%%%%%%%%%%%%%%%%%%%%%%%%%%%%%%%%%%%%%%%%%%%%%%%%%%%%%%%%%%%%%%%%%%%%%%%%%%%
#
# Simulation of erosion phenomena within Helicon Plasma Sources
#
# JIDVG, 2022
#
# Dependence on:                        - AhedoOOP.py
#                                       - SheathsOOP.py
#                                       - EcksteinSputteringOOP.py
#
#
# Parameter sets on:                    - HeliconPars.py
#                                       - SputteringPars.py
# %%%%%%%%%%%%%%%%%%%%%%%%%%%%%%%%%%%%%%%%%%%%%%%%%%%%%%%%%%%%%%%%%%%%%%%%%%%%%%%%%%%%%%%%%%%%%%%

# Python module packages required for execution
import numpy as np
import matplotlib.pyplot as plt
import matplotlib.colors as colors
import scipy.interpolate as interp

# Model-specific packages
from AhedoOOP import *
import SheathsOOP as Sheaths
from EcksteinSputteringOOP import *

# Files containing parameter sets
import HeliconParSets
import SputteringPars


# ************************************************************************************************
# SIMULATION CONTROL

# DEBUG enable
DebugMSG = 1


# Selection of specified models

# Helicon Model
ThisHeliconModel = HeliconParSets.vxcr


# Sputtering Model
# ThisSputteringModel = SputteringPars.ArSiO2Model
SputterModels = ["ArSiO2", "ArAl2O3", "ArSi3N4"]
# SputterModels = ["ArAl2O3"]

# Output data file name
DataFileRoot = 'vxcr_'

# Control of sensitivity routine
SensPar = "Te"
SensParRange = [3.0, 5.0, 10.0]
# SensParRange = [3.0]

# RF Low Frequency Sheath Simulation
RF_NatFreq = 13.56e6                        # RF Sheath Natural Frequency           [Hz]
RF_AngFreq = 2*np.pi*RF_NatFreq             # RF Sheath Angular Frequency           [rad/s]
RF_PeakVoltage = 135                        # RF Sheath sine wave peak voltage      [V]
RF_rres = 1000                              # Fixed resolution of voltage span for IED
```

```python
# ************************************************************************************************


# %%%%%%%%%%%%%%%%%%%%%%%%%%%%%%%%%%%%%%%%%%%%%%%%%%%%%%%%%%%%%%%%%%%%%%%%%%%%%%%%%%%%%%%%%%%%%%%%
# FUNCTION RF_EtchRateCalculation() to compute the estimated Etch Rate due to the low-voltage RF Sheath under the antenna straps
def RF_EtchRateCalculation(HelModel, SputtModel, ee_nref):
        # Creation of Sheath Model
        ThisSheathModel = Sheaths.DCSheath(HelModel.Te, HelModel.Aion, ee_nref)         # FIXME Sheath model reads ion mass in amu

        # Estimation of Ion Energy Distribution (IED) function due to the Low-Frequency RF Sheath
        RF_V0_Range = np.linspace(0.0, RF_PeakVoltage, RF_rres)
        ThisSheathModel.LowFreqRFSheath(RF_V0_Range, 0.0, RF_PeakVoltage, RF_AngFreq)
        RF_IED = ThisSheathModel.LowFreq_IED

        # Create a single matrix for the IED
        RF_IED_Array = np.column_stack((RF_V0_Range, RF_IED))

        # Estimation of normal sputtering yield distribution along RF voltage range
        Normal_Y_Range = np.zeros(np.size(RF_V0_Range))

        for index in range(0, np.size(RF_V0_Range)):
                SputtModel.ion_E0 = RF_V0_Range[index]
                SputtModel.NormalIncidence()
                Normal_Y_Range[index] = SputtModel.y_sput_normal

        # Filter out INF values from IED and NAN values from Normal_Y_Range
        intrange = ~np.isinf(RF_IED) * ~np.isnan(Normal_Y_Range)

        # Compute average sputtering rate
        RF_Y_Avg = integrate.trapezoid(Normal_Y_Range[intrange] * RF_IED[intrange], RF_V0_Range[intrange], dx=(RF_V0_Range[1]-RF_V0_Range[0]))

        # Compute average incident ion energy
        RF_V0_Avg = integrate.trapezoid(RF_V0_Range[intrange] * RF_IED[intrange], RF_V0_Range[intrange])


        if DebugMSG==1:
                print('\nAVG RF sheath potential: \t', RF_V0_Avg, 'V')
                print('AVG RF sputtering rate: \t', RF_Y_Avg, 'atoms/ion')

        # Return relevant values
        return RF_V0_Range, RF_IED, Normal_Y_Range, RF_Y_Avg



# %%%%%%%%%%%%%%%%%%%%%%%%%%%%%%%%%%%%%%%%%%%%%%%%%%%%%%%%%%%%%%%%%%%%%%%%%%%%%%%%%%%%%%%%%%%%%%%%
# FUNCTION HeliconEtchCalculation() used to compute etch rate at system boundaries
def HeliconEtchCalculation(HelModel, SputtModel):

        # ************************************************************************************************
        # STEP I. Execution of 2D Cylindrical Plasma Model [ahedo13]
        HelModel.AxialModel()                   # Axial Model
        HelModel.RadialModel()                  # Radial Model

        # Creation of 2D density map out of Axial and Radial models
        # Replication of radial model along the axial coordinate, setting the nr0 parameter in the Radial model as the n0 parameter from the Axial model
        # Implemented as a vector multiplication. Resultant matrix has rres rows, zres columns, defining the geometrical coordinates (z, r)
        # [ahedo13] calculation produces results normalized to n0, therefore the resulting matrix is multiplied by this factor to obtain physical units
        nmesh = (HelModel.nr_nr0.reshape(HelModel.rres, 1) @ HelModel.n_n0.reshape(1, HelModel.zzres)) * HelModel.n0

        if DebugMSG==1:
                print('\nMaximum value of nmesh:', np.max(nmesh), ' m^-3')
                print('Minimum value of nmesh:', np.min(nmesh), ' m^-3')
```

```python

        # ***************************************************************************************
        # STEP II. Validation that mesh resolution is within the Debye length at the regions near the surfaces

        # Extraction of density values at boundary surfaces
        n_zboundary = nmesh[:,0]                        # First array column corresponds to zz = -L (material boundary) FIXME Verify z=0 coordinate
        n_rboundary = nmesh[-1,:]                       # Last array row corresponds to rr = R

        if DebugMSG==1:
                print('\nDensity values along z boundary: \tMAX=', np.max(n_zboundary), 'm^-3, \tMIN=', np.min(n_zboundary), 'm^-3')
                print('Density values along r boundary: \tMAX=', np.max(n_rboundary), ' m^-3, \tMIN=', np.min(n_rboundary), 'm^-3\n')

        # Calculate whether mesh resolution is smaller than Debye length

        # Analysis of Debye length and radial resolution at the z_max simulation boundary
        ZBoundarySheathModel = Sheaths.DCSheath(HelModel.Te, HelModel.Aion, n_zboundary)        # FIXME Sheath model reads ion mass in amu

        # %%%%%%%%%%%%%%%%%%%%%%%%%%%%%%%%%%%%%%%%%%%%%%%%%%%%%%%%%%%%%%%%%%%%%%%%%%%%%%%%%%%%%%%%%%%%
        # Print warning if axial resolution is larger than minimum Debye length at axial boundary
        if (ZBoundarySheathModel.lambdaD.min() - (HelModel.L / HelModel.zzres) < 0):
                print('\nInsufficient axial resolution for sputtering analysis at z=0 axial boundary.')

        # %%%%%%%%%%%%%%%%%%%%%%%%%%%%%%%%%%%%%%%%%%%%%%%%%%%%%%%%%%%%%%%%%%%%%%%%%%%%%%%%%%%%%%%%%%%%
        # Analysis of Debye length and radial resolution at the z_max simulation boundary
        RBoundarySheathModel = Sheaths.DCSheath(HelModel.Te, HelModel.Aion, n_rboundary)        # FIXME Sheath model reads ion mass in amu

        # Print warning if radial resolution is larger than minimum Debye length at radial boundary
        if (RBoundarySheathModel.lambdaD.min() - (HelModel.R / HelModel.rres) < 0):
                print('\nInsufficient radial resolution for sputtering analysis at r=R radial boundary.')

        # ***************************************************************************************
        # STEP III.
        # Analysis of wall sputtering due to the potential obtained by the floating wall. Z boundary.

        # Floating wall assumption

        # Set incident ion energy within sputtering model as the floating wall potential obtained due to the formation of the sheath
        SputtModel.ion_E0 = -ZBoundarySheathModel.wall_potential_float

        # Calculation of sputtering yield due to normal incidence
        SputtModel.NormalIncidence()

        # Calculation of etch rate at the boundary; FIXME error corrected in molar mass calculation
        ZBoundaryEtchRate = n_zboundary * ZBoundarySheathModel.uB * SputtModel.y_sput_normal * (SputtModel.target_m * 1.0e-3) / (SputtModel.target_rho * SputtModel.Avogadro)

        if DebugMSG==1:
                print('\nSheath potential at z boundary: \tMAX=', np.max(SputtModel.ion_E0), 'V, \tMIN=', np.min(SputtModel.ion_E0), 'V')
                print('Bohm velocity along z boundary: \tMAX=', np.max(ZBoundarySheathModel.uB), 'm/s, \tMIN=', np.min(ZBoundarySheathModel.uB), 'm/s')
                print('Sputtering yield along z boundary: \tMAX=', np.max(SputtModel.y_sput_normal), 'atoms/ion, \tMIN=', np.min(SputtModel.y_sput_normal), 'atoms/ion')
                print('Target material molar mass:\t\t', SputtModel.target_m * 1.0e-3, ' kg/mol')
                print('Particle flow towards z boundary: \tMAX=', np.max(n_zboundary * ZBoundarySheathModel.uB), 'm^-2s^-1, \tMIN=', np.min(n_zboundary * ZBoundarySheathModel.uB), 'm^-2s^-1')
                print('Estimated etch rate in z boundary: \tMAX=', np.max(ZBoundaryEtchRate), 'm/s, \tMIN=', np.min(ZBoundaryEtchRate), 'm/s\n')

        # ***************************************************************************************
        # STEP IV.
        # Analysis of wall sputtering due to the potential obtained by the floating wall. R boundary.

        # Floating wall assumption

        # Set incident ion energy within sputtering model as the floating wall potential obtained due to the formation of the sheath
        SputtModel.ion_E0 = -RBoundarySheathModel.wall_potential_float
```

```python

        # Calculation of sputtering yield due to normal incidence
        SputtModel.NormalIncidence()

        # Calculation of etch rate at the boundary; FIXME error corrected in molar mass calculation
        RBoundaryEtchRate = n_rboundary * RBoundarySheathModel.uB * SputtModel.y_sput_normal * (SputtModel.target_m * 1.0e-3) / (SputtModel.target_rho * SputtModel.Avogadro)

        if DebugMSG==1:
                print('\nSheath potential at r boundary: \tMAX=', np.max(SputtModel.ion_E0), 'V, \tMIN=', np.min(SputtModel.ion_E0), 'V')
                print('Bohm velocity along r boundary: \tMAX=', np.max(RBoundarySheathModel.uB), 'm/s, \tMIN=', np.min(RBoundarySheathModel.uB), 'm/s')
                print('Sputtering yield along r boundary: \tMAX=', np.max(SputtModel.y_sput_normal), 'atoms/ion, \tMIN=', np.min(SputtModel.y_sput_normal), 'atoms/ion')
                print('Target material molar mass:\t\t', SputtModel.target_m * 1.0e-3, ' kg/mol')
                print('Particle flow towards r boundary: \tMAX=', np.max(n_rboundary * RBoundarySheathModel.uB), 'm^-2s^-1, \tMIN=', np.min(n_rboundary * RBoundarySheathModel.uB), 'm^-2s^-1')
                print('Estimated etch rate in r boundary: \tMAX=', np.max(RBoundaryEtchRate), 'm/s, \tMIN=', np.min(RBoundaryEtchRate), 'm/s\n')

        # ***********************************************************************************************
        # STEP V.
        # Analysis of wall sputtering due to the low-frequency RF sheath beneath the external helicon antenna straps, following [berisford10]

        # Calculation of MAXIMUM density value along radial boundary for RF sheath calculation
        max_ee_n = np.max(n_rboundary)

        This_V0_Range, This_RF_IED, This_Normal_Y_Range, This_RF_Y_Avg = RF_EtchRateCalculation(HelModel, SputtModel, max_ee_n)        # Execution of low-freq RF sheath etch calculations

        # Calculation of low-frequency RF sheath etch rate at the radial boundary; FIXME error corrected in molar mass calculationg
        RF_EtchRate = n_rboundary * RBoundarySheathModel.uB * This_RF_Y_Avg * (SputtModel.target_m * 1.0e-3) / (SputtModel.target_rho * SputtModel.Avogadro)

        if DebugMSG==1:
                print('\nSheath potential at r boundary (RF): \tMAX=', np.max(This_RF_IED), 'V, \tMIN=', np.min(This_RF_IED), 'V')
                print('Bohm velocity along z boundary: \tMAX=', np.max(RBoundarySheathModel.uB), 'm/s, \tMIN=', np.min(RBoundarySheathModel.uB), 'm/s')
                print('Sputtering yield along r boundary (RF): \tMAX=', np.max(This_RF_Y_Avg), 'atoms/ion, \tMIN=', np.min(This_RF_Y_Avg), 'atoms/ion')
                print('Target material molar mass:\t\t', SputtModel.target_m * 1.0e-3, ' kg/mol')
                print('Particle flow towards r boundary (RF): \tMAX=', np.max(n_rboundary * RBoundarySheathModel.uB), 'm^-2s^-1, \tMIN=', np.min(n_rboundary * RBoundarySheathModel.uB), 'm^-2s^-1')
                print('Estimated etch rate in r boundary: \tMAX=', np.max(RF_EtchRate), 'm/s, \tMIN=', np.min(RF_EtchRate), 'm/s\n')

        # ***********************************************************************************************
        # STEP VI.
        # Function return variables.
        return ZBoundaryEtchRate, RBoundaryEtchRate, -ZBoundarySheathModel.wall_potential_float, -RBoundarySheathModel.wall_potential_float, This_V0_Range, This_RF_IED, This_Normal_Y_Range, This_RF_Y_Avg, RF_EtchRate

# %%%%%%%%%%%%%%%%%%%%%%%%%%%%%%%%%%%%%%%%%%%%%%%%%%%%%%%%%%%%%%%%%%%%%%%%%%%%%%%%%%%%%%%%%%%%%%%%%%%%%%%%%%%%%%%%%%%%%%%%
# FUNCTION EtchPlots() used to plot etch rates at system boundaries
def EtchPlots(HelModel, ZEtchRate, REtchRate):

        fig_floatingetch, axs_floatingetch = plt.subplots(2, 1)
        fig_floatingetch.suptitle('Etch rates computed due to floating potential at system physical boundaries.')

        axs_floatingetch[0].plot(HelModel.rrhat, ZEtchRate)
        axs_floatingetch[0].set(ylabel='Etch Rate (m/s)', xlabel='r/R')

        axs_floatingetch[1].plot(HelModel.zzhat, REtchRate)
        axs_floatingetch[1].set(ylabel='Etch Rate (m/s)', xlabel='z/L')

        fig_floatingetch.tight_layout()

        fig_floatingetch.savefig('AxialRadialEtchRates.png', dpi=300, bbox_inches='tight')
        # fig_floatingetch.show()
```

```
# %%%%%%%%%%%%%%%%%%%%%%%%%%%%%%%%%%%%%%%%%%%%%%%%%%%%%%%%%%%%%%%%%%%%%%%%%%%%%%%%%%%%%%%%%%%%%%%%%%%%%%%%%%%%%%%%
# FUNCTION SaveData() used to save relevant variables to datafile
def SaveData(HelModel, SputtModel, ZEtchRate, REtchRate, FloatPot, YSputtNormal, Outfile):
        np.savez(Outfile, rrhat=HelModel.rrhat, zzhat=HelModel.zzhat, ZEtchRate=ZEtchRate, REtchRate=REtchRate, FloatPotential=FloatPot, y_sput_normal=YSputtNormal)



# %%%%%%%%%%%%%%%%%%%%%%%%%%%%%%%%%%%%%%%%%%%%%%%%%%%%%%%%%%%%%%%%%%%%%%%%%%%%%%%%%%%%%%%%%%%%%%%%%%%%%%%%%%%%%%%%
# FUNCTION Sensitivity() to execute sensitivity analysis
def EtchRateSensitivity(HelModel, SputtModel, ParName, ParRange):

        # Set of values for parameter iteration
        par_field = ParRange
        ParSteps = len(ParRange)

        # Initialize output matrices
        ZEtchRateData = np.zeros((HelModel.rrhat.size, ParSteps))
        REtchRateData = np.zeros((HelModel.zzhat.size, ParSteps))
        ZFloatPotentialData = np.zeros((HelModel.rrhat.size, ParSteps))
        RFloatPotentialData = np.zeros((HelModel.zzhat.size, ParSteps))
        RF_V0Range_Data = np.zeros((RF_rres, ParSteps))
        RF_IED_Data = np.zeros((RF_rres, ParSteps))
        RF_Normal_Y_Range_Data = np.zeros((RF_rres, ParSteps))
        RF_Y_Avg_Data = np.zeros(ParSteps)
        RF_EtchRate_Data = np.zeros((HelModel.zzhat.size, ParSteps))


        # Iteration of values for parameter ParName
        for step in range(ParSteps):
                print("Calculations for parameter value", step)

                # Select RF V_peak value according to Te
                if HelModel.Te==3.0:
                        RF_PeakVoltage=111.30
                elif HelModel.Te==5.0:
                        RF_PeakVoltage=165.66
                elif HelModel.Te==10.0:
                        RF_PeakVoltage=301.56

                exec('HelModel.' + ParName + '=par_field[step]')                # Assignment of corresponding value to selected ParName
                HelModel.ParInit()                # Parameter initialization
                HelModel.CollRateCalculation()
                HelModel.CollDerivedParameters()

                HelModel.AxialModel()                # Execution of Ahedo 2D model
                HelModel.RadialModel()
                print("Ahedo model execution complete.")

                ThisZEtchRate, ThisREtchRate, ThisZFloatPot, ThisRFloatPot, ThisV0Range, ThisIED, ThisYRange, ThisYAvg, ThisRFEtchRate = HeliconEtchCalculation(HelModel, SputtModel)
                # Exection of boundary etch rate calculations
                print("Etch rate calculations completed.")
                print("RF sheath etch rate calculations completed.")

                ZEtchRateData[:, step] = ThisZEtchRate
                REtchRateData[:, step] = ThisREtchRate
```

```
                ZFloatPotentialData[:, step] = ThisZFloatPot
                RFloatPotentialData[:, step] = ThisRFloatPot
                RF_V0Range_Data[:, step] = ThisV0Range
                RF_IED_Data[:, step] = ThisIED
                RF_Normal_Y_Range_Data[:, step] = ThisYRange
                RF_Y_Avg_Data[step] = ThisYAvg
                RF_EtchRate_Data[:, step] = ThisRFEtchRate


        # At the end of the loop, return matrices
        return ZEtchRateData, REtchRateData, ZFloatPotentialData, RFloatPotentialData, HelModel.rrhat, HelModel.zzhat, RF_V0Range_Data, RF_IED_Data,
 RF_Normal_Y_Range_Data, RF_Y_Avg_Data, RF_EtchRate_Data
# END EtchRateSensitivity()



# %%%%%%%%%%%%%%%%%%%%%%%%%%%%%%%%%%%%%%%%%%%%%%%%%%%%%%%%%%%%%%%%%%%%%%%%%%%%%%%%%%%%%%%%%%%%%%%%%%%
# MAIN LOOP - Single Iteration
# ZBoundaryEtchRateExt, RBoundaryEtchRateExt = HeliconEtchCalculation()
# EtchPlots(ZBoundaryEtchRateExt, RBoundaryEtchRateExt)
# SaveData(ZBoundaryEtchRateExt, RBoundaryEtchRateExt, Datafile)


# %%%%%%%%%%%%%%%%%%%%%%%%%%%%%%%%%%%%%%%%%%%%%%%%%%%%%%%%%%%%%%%%%%%%%%%%%%%%%%%%%%%%%%%%%%%%%%%%%%%
# MAIN LOOP - Sensitivity
for SputtChoice in SputterModels:
        print("Calculations for", SputtChoice, "sputtering model")

        ThisSputteringModelName = 'SputteringPars.' + SputtChoice + 'Model'
        exec('ThisSputteringModel = ' + ThisSputteringModelName)

        ThisZEtchRateData, ThisREtchRateData, ThisZFloatPotentialData, ThisRFloatPotentialData, This_rrhat, This_zzhat, ThisV0RangeData, ThisIEDData
, ThisNormalYData, ThisYAvgData, ThisRFEtchData = EtchRateSensitivity(ThisHeliconModel, ThisSputteringModel, SensPar, SensParRange)
        print("Sensitivity analysis completed.")

        OutFile = DataFileRoot + SputtChoice

        # FIXME Implement RF Sheath calculations here, add saved data to NPZ files

        np.savez(OutFile, ZEtchRateData=ThisZEtchRateData, REtchRateData=ThisREtchRateData, ZFloatPotentialData=ThisZFloatPotentialData, RFloatPoten
tialData=ThisRFloatPotentialData, rrhat=This_rrhat, zzhat=This_zzhat, V0RangeData=ThisV0RangeData, IEDData=ThisIEDData, NormalYData=ThisNormalYData,
 YAvgData=ThisYAvgData, RFEtchData=ThisRFEtchData)
```

```python
#!/usr/bin/python3

# *****************************************************************************************************
# HeliconPowerBalance.py
#
# Routine implementing the power balance expressions for Helicon Plasma Sources from [ahedo13]
# Some concepts implemented from [vidal99].
# *****************************************************************************************************


# Python module packages required for execution
import numpy as np
import matplotlib.pyplot as plt
import matplotlib.colors as colors
import scipy.interpolate as interp
import scipy.optimize as opt

# Model-specific packages
from AhedoOOP import *
import SheathsOOP as Sheaths
from EcksteinSputteringOOP import *

# Files containing parameter sets
import HeliconParSets
import SputteringPars

plt.rcParams["text.usetex"] = True
plt.rcParams["font.size"] = 6

# ****************************************************************************************************
# SIMULATION CONTROL
#
# FIXME Selection of specified models

# Helicon Model
ThisHeliconModel = HeliconParSets.vxcr

# Sputtering Model, estimation of threshold energy for compound target
ThisSputteringModel = SputteringPars.ArAl2O3Model
# ThisSputteringModel.E_thr = ThisSputteringModel.ThresholdEnergy()


# Output data file names
datafile = "vxcr"
sputtfile = "ArAl2O3"

# RF Input Power
RF_in = 3000                                    # [W]
RF_range = np.linspace(2000, 5000, 7)           # [W]

# mdot Range
# in units of [sccm] transformed to [kg/s]
mdot_range = np.linspace(200, 1000, 5)*2.973e-8

# Selection of plots or actions
power_balance_optimization = 1
power_balance_sweep = 0

# ****************************************************************************************************

# ----------------------------------------------------------------------------------------------------------
## Implementation of [ahedo13] por balance model adapted to just the HPS
if power_balance_optimization == 1:

```

```
    # Run optimization algorithm to find value fo Te that minimizes np.abs((Pion + Pwall + Pbeam) - RF_in)
    Te_opt_result = opt.minimize_scalar(ThisHeliconModel.PowerBalance, bounds=(2.75, 6.0), args=(RF_in), method='bounded')

    # Report result
    if Te_opt_result.success:
        print('Estimated Te:\t', Te_opt_result.x, ' eV')
        print('Objective function:\t ', Te_opt_result.fun, ' %')
    else:
        print('Optimization failed')

# ---------------------------------------------------------------------------------------------------------------------
if power_balance_sweep == 1:

    PB_data = np.zeros((RF_range.size * mdot_range.size, 5))
    PB_RowCounter = 0

    # Iterate over mdot values
    for mdotCounter in range(mdot_range.size):
        # Iterate over RF power values
        for RFcounter in range(RF_range.size):
            print('\nStarting calculations for Pin=', RF_range[RFcounter], ' W;\tmdot=', mdot_range[mdotCounter], 'kg/s')

            # Update mdot value in Model
            ThisHeliconModel.mdot = mdot_range[mdotCounter]

            # Execute minimization routine with current value of RF power
            Te_opt_result = opt.minimize_scalar(ThisHeliconModel.PowerBalance, bounds=(2.75, 10.0), args=(RF_range[RFcounter]), method='bounded')

            # Report result
            if Te_opt_result.success:
                print('Estimated Te: ', Te_opt_result.x, ' eV')
            else:
                print('Optimization failed')

            # Save data in 3D array
            PB_data[PB_RowCounter, 0] = mdot_range[mdotCounter]
            PB_data[PB_RowCounter, 1] = RF_range[RFcounter]
            # PB_data[PB_RowCounter, 2] = (np.datetime64('now') - np.datetime64('1970-01-01T00:00:00')) / np.timedelta64(1, 's')
            PB_data[PB_RowCounter, 2] = Te_opt_result.x
            PB_data[PB_RowCounter, 3] = ThisHeliconModel.n0
            PB_data[PB_RowCounter, 4] = Te_opt_result.fun

            PB_RowCounter += 1


    # Save 3D array to file
    np.savez('PowerBalanceSweep', PB_data=PB_data)
```

Appendix E

Original Publications

This Appendix contains the published articles from chapters 3 and 4 in the orginal layout as published by the corresponding peer-reviewed journals.

frontiers | Frontiers in Physics

REVIEW
published: 26 April 2022
doi: 10.3389/fphy.2022.856221

Plasma-Surface Interactions Within Helicon Plasma Sources

Juan I. Del Valle[1,2]*, *Franklin R. Chang Diaz*[1] and *Víctor H. Granados*[2,3]

[1]Ad Astra Rocket Company Costa Rica, Liberia, Costa Rica, [2]Doctorado en Ciencias Naturales para el Desarrollo (DOCINADE) Program, Instituto Tecnológico de Costa Rica, Universidad Nacional de Costa Rica, Universidad Nacional a Distancia de Costa Rica, Cartago, Costa Rica, [3]Universidad Nacional, Heredia, Costa Rica

Helicon plasma sources do not require electrodes or grids directly immersed in the plasma, and also present an axial magnetic field confining the plasma discharge. These factors are believed to provide them with long operational lifetimes because of the reduced potential for surface etching. The physics of helicon waves, cylindrical magnetized plasmas, sheaths, and plasma-surface interactions are discussed in the context of this claim. Practical implementation aspects are also reviewed, along with relevant experimental results. It is shown that understanding the distribution of ion density within the source, the presence of induced potentials in its surfaces, and the physics of low-energy sputtering reactions is essential to properly model erosion phenomena within helicons, and consequently predict their performance in practical applications.

Keywords: helicon plasma, surface, erosion, sputtering, interactions

OPEN ACCESS

Edited by:
Agnes Granier, UMR6502 Institut des Matériaux Jean Rouxel (IMN), France

Reviewed by:
Kazunori Takahashi, Tohoku University, Japan
Alan A. Howling, Swiss Federal Institute of Technology Lausanne, Switzerland

***Correspondence:**
Juan I. Del Valle
juan@adastrarocket.com

Specialty section:
This article was submitted to Plasma Physics, a section of the journal Frontiers in Physics

Received: *16 January 2022*
Accepted: *17 February 2022*
Published: *26 April 2022*

Citation:
Del Valle JI, Chang Diaz FR and Granados VH (2022) Plasma-Surface Interactions Within Helicon Plasma Sources. Front. Phys. 10:856221. doi: 10.3389/fphy.2022.856221

1 INTRODUCTION

Helicon plasma sources (HPS) have attracted attention in recent decades because of their ability to produce high-density plasmas at low or moderate power levels and magnetic field intensities. For example, electron densities of more than $10^{12}\,cm^{-3}$ can be produced on helicon plasma sources operating at input power levels of around $1\,kW_e$ [1]. These properties make them suitable for practical applications in several fields. Within the research of plasma-material interactions at fusion-relevant conditions, HPSs have been used as a part of test facilities where candidate wall materials are subjected to the typical operating conditions in projected fusion devices [2, 3], up to heat flux levels exceeding $20\,MW/m^2$ [4]. Helicons have also been used in the plasma-processing of commercial materials and products [5, 6]. Within the field of electric space propulsion, helicon plasma thrusters have been actively developed in recent years [7–11]; helicons are also essential components of more advanced electric propulsion systems such as the VASIMR engine [12]. **Figure 1** shows some examples of devices based on helicon plasma sources.

Another key feature of HPSs is that they typically do not have electrodes or cathodes in direct contact with the plasma, but rely instead on external radio frequency (RF) systems to launch and couple the corresponding waves within the medium and excite the discharge. This differs from other common plasma sources such as glow or DC discharges, where the plasma risks contamination from the release of electrode material or the source may fail if this element erodes sufficiently. Avoiding direct contact between the plasma and such elements is particularly useful where a long operating lifetime is desired for the plasma source, either because long duty cycles will be required in the application (as in commercial plasma-processing devices), high power densities are required (as in linear devices used for the research of suitable materials for fusion-relevant conditions), or because these previous conditions combine with the impossibility to access the device in the case of component failure (as in electric space thrusters).

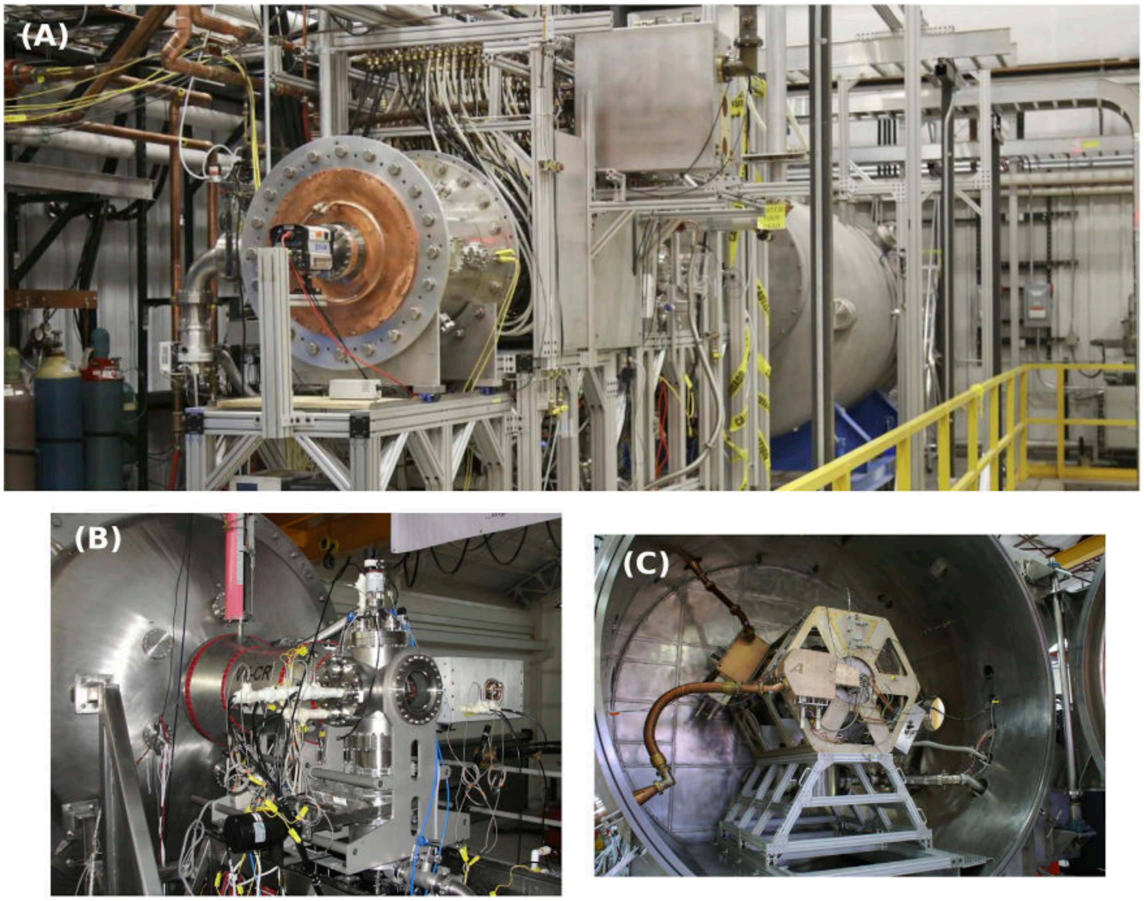

FIGURE 1 | Examples of applications of Helicon Plasma Sources. **(A)** The Proto-MPEX linear device for the study of plasma-material interactions at fusion-relevant conditions [3]. Courtesy of Oak Ridge National Laboratory, U.S. Dept. of Energy. **(B)** The VX-CR research helicon plasma source [61]. Courtesy of Ad Astra Rocket Company Costa Rica, Liberia, Costa Rica. **(C)** The VASIMR VX-200SS high-power propulsion engine [12]. Courtesy of Ad Astra Rocket Company, Webster, TX, United States.

Despite this advantage particular to the discharge excitation mechanism, practical implementations of HPSs do contain other confinement surfaces which are in direct contact with the plasma. The performance of helicon sources depends on the specific properties of these surfaces as well, and their ability to withstand the conditions they are subjected to throughout the operating lifetime of the source. These issues are therefore also important when considering the long-term viability of helicon plasma sources in their intended applications, and are the subject of the present review.

This article is structured as follows. **Section 2** discusses the physics behind helicon plasma waves and recent results on the modeling of cylindrical magnetized plasmas. **Section 3** then reviews the theory of plasma-surface interactions as it applies to helicon plasma sources. **Section 4** describes practical aspects of helicon plasma source design and implementation, as they relate to the plasma-surface interaction phenomena. Finally, **section 5** summarizes this review's findings and offers perspectives for the advancement of the research and design of reliable, robust helicon plasma sources with long operational lifespans.

2 PHYSICS OF HELICON PLASMA SOURCES

2.1 Helicon Plasma Waves

Helicon waves are a category of right-hand polarized (RHP) plasma waves which propagate along DC magnetic fields in bounded systems. They are related to so-called *whistler* waves, which have been studied in atmospheric physics since the early twentieth century. Whistlers and helicon waves belong to the group of right-hand polarized (RHP) waves propagating parallel to a magnetic field, in the frequency range $\omega_{ci} \ll \omega \ll \omega_{ce}$ (where ω_{ci} is the ion cyclotron frequency and ω_{ce} is the electron cyclotron frequency), together with electron cyclotron waves. **Figure 2** shows the location of whistlers and helicon plasma waves within a ω-k diagram representing RHP cold plasma waves.

A historical perspective for the first twenty years of helicon research has been given by Chen and Boswell [13, 14]. The following twenty-year period has been covered in more recent reviews by Chen [15] and Shinohara [1]. Theoretical treatments of the physics behind helicon waves have been produced, among

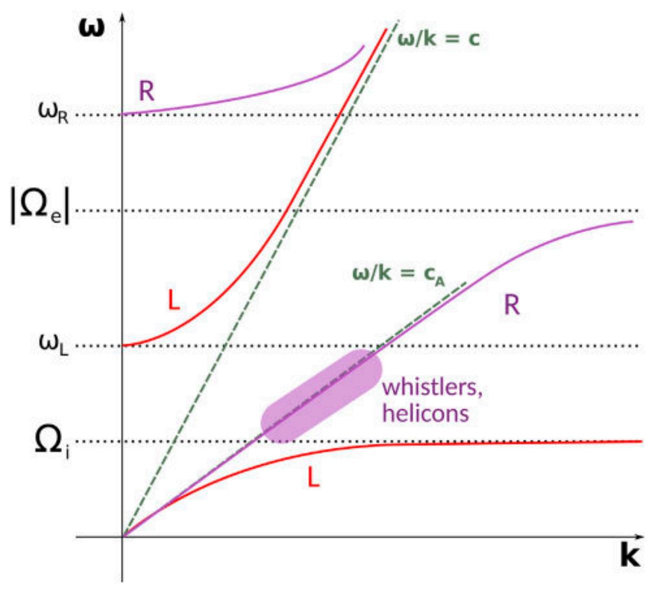

FIGURE 2 | Location of whistlers and helicon plasma waves, among cold plasma waves propagating parallel to the externally-applied magnetic field.

others, by Klozenberg et al. [16], Chen [17], and Chen and Arnush [18, 19].

A basic dispersion relation can be obtained for helicon plasma waves from simplifying the Appleton-Hartree expression for quasi-longitudinal right-handed cold plasma waves [20, 21], propagating at an angle θ from an axial, static magnetic field $\mathbf{B} = B_0\hat{\mathbf{e}}_\mathbf{z}$,

$$\beta = \frac{\omega}{k}\frac{n_0 e\mu_0}{B_0} \tag{1}$$

where $\beta^2 = k^2 + k_\perp^2$ is the total wave number, $k = \beta\cos\theta$ and $k_\perp$ are the parallel and perpendicular components of the wave number, and n_0 is the plasma density. This expression, despite being a simplification, provides an intuitive insight on the relationship between the magnetic field B_0, the density n_0, the wave frequency ω, and the wave number β, and can be used as a starting point when designing or analyzing a HPS.

A more detailed description of helicon waves can be obtained from Maxwell's equations by neglecting ion motions and the displacement current, as originally shown by Klozenberg et al. [16]. When the effects of electron inertia are retained within the analysis [14, 18, 22] two solutions are obtained for the dispersion relation,

$$\beta_{1,2} = \frac{k}{2\delta}\left[1 \mp \left(1 - \frac{4\delta k_\omega^2}{k^2}\right)^{1/2}\right] \tag{2}$$

where $\delta = \omega/\omega_{ce}$ is the ratio between the wave frequency and the electron cyclotron frequency $\omega_{ce} = eB_0/m_e$, and $k_\omega^2 = \omega\omega_p^2/\omega_c c^2 = \omega n_0 e\mu_0/B_0 \equiv \alpha k$ is the wavenumber for low-frequency whistler waves along B_0 in free space, with $\alpha = \beta$ the wave number previously described in **Eq. 1**. ω_p is the electron plasma frequency at density n_0. δ is neglected when the effects of the electron mass are omitted or for frequencies $\omega \ll \omega_{ce}$.

Eq. 2 describes two solutions for the wave dispersion relation, which can be simplified as shown in **Eq. 3**.

$$\beta_{1,2} \approx \frac{k}{2\delta}\left[1 \mp \left(1 - \frac{2\delta k_\omega^2}{k^2}\right)\right] \approx \begin{cases} k_\omega^2/k \\ k/\delta \end{cases} \tag{3}$$

Solution β_1 corresponds to the zero electron mass limit, and describes the helicon wave ("H") from **Eq. 1**. The second solution $\beta_2 = \beta_2 \cos\theta\omega_{ce}/\omega$ describes a wave with frequency $\omega = \omega_{ce}\cos\theta$, which is an electron cyclotron wave propagating at an angle to the magnetic field. This is the Trivelpiece-Gould mode ("TG"), first described in bounded systems by Trivelpiece and Gould [23]. The TG mode co-exists with the H mode, and becomes relevant at lower values of B_0. The TG mode is thought to play a relevant role in the damping mechanism of helicon plasma sources and to contribute to its high ionization efficiency via mode-conversion processes [24].

Eq. 3 describes the dispersion relation for both the H-mode and the TG mode. Expressions for the magnetic and electric fields (**B**, **E**) have been derived for different geometries as described in the early works on helicons [16, 25] as well as in more recent literature [14, 17, 22]. These expressions depend as well on the boundary conditions chosen for the analysis and on whether these boundaries are modelled as conductors or not [18]. Practical implementations of HPSs are typically linear devices implemented as cylindrical enclosures made of dielectric materials, as will be described in **section 4**.

The expressions obtained from **Eqs. 1**, **3**, as well as the detailed derivations of the **B** and **E** fields that can be obtained for a particular configuration and geometry, can be used as an initial approximation to understand the regimes of H and TG modes that can be propagated in a given configuration, and establish a baseline estimation of the expected density distribution in a given HPS device.

One particular advantage of HPSs stemming from the fundamental physics of helicon waves is the ability of these devices to couple RF waves at the core of dense plasmas, enabled by the presence of the axial magnetic field and the propagation of the H-mode. This fact presents an advantage over other types of plasma sources, such as inductively-coupled plasmas (ICPs) where the penetration of RF waves into the plasma is limited by its skin-depth, or electron-cyclotron sources (ECR), where microwaves cannot propagate below the O-mode cutoff frequency (the electron plasma frequency ω_{pe}).

An investigation on the mechanisms which enable the initiation of the high-density helicon mode (the H-mode), based on modeling and experimental work, has been carried out by Carter et al. [26], including indirect evidence of the deposition of RF power at the high-density core in a helicon plasma source.

2.2 Cylindrical Magnetized Plasmas

Section 2.1 described helicon plasma waves and derived their dispersion relation in various scenarios. The general behavior of magnetized plasmas in cylindrical geometries will now be

TABLE 1 | Relevant models developed for cylindrical magnetized plasmas which are applicable to the study of Helicon Plasma Sources.

References	Tonks [28]	Ewald et al. [90]	Fruchtman et al. [29]	Sternberg et al. [30]	Ahedo et al. [32]
Dimensionality	1D	1D	2D	1D	2D
Symmetry	Azimuthal, Longitudinal	Azimuthal, Longitudinal	Azimuthal	Azimuthal, Longitudinal	Azimuthal
Inertia					
Electrons	N/A	No	No	No	Yes, except longitudinal
Ions	N/A	Yes	Yes	Yes	Yes
Quasineutrality	Yes	Yes	Yes	Yes	Yes, except within sheath
Isothermality					
Electrons	Yes	Yes	Yes	Yes	Yes
Ions	Yes	Yes, $T_i \approx T_n$	Yes, $T_i = 0$	Yes, $T_i = 0$	Yes, $T_i \ll T_e$

analyzed, which is relevant to the characterization of practical HPSs as described in **section 4**.

The problem of describing the bulk behavior of a plasma discharge has been addressed since the early stages of the development of plasma physics. In the classical paper by Tonks and Langmuir [27], expressions were derived for the distribution of the electric potential in an arc discharge, for various geometries including cylindrical coordinates. Scenarios were analyzed for different regimes of ion collisionality and ionization rates. This work also contains a treatment of the plasma-material boundary at the edge of the plasma discharge, pointing to the discontinuity of the bulk model within the plasma sheath.

In a later paper, Tonks [28] studied the effects of the magnetic field in an arc plasma. One of the cases described was the positive column plasma immersed within a longitudinal magnetic field, the same typical configuration applied nowadays to most helicon plasma sources. A radial model is developed based on classical diffusion theory. More recent models for cylindrical magnetized plasmas have been developed by Fruchtman et al. [29] and Sternberg et al. [30]. These works introduced the use of 2D fluid models in cylindrical coordinates (with the assumption of azimuthal symmetry), the separation of variables in order to decouple the expressions for the radial and axial coordinates, and the analysis of different degrees of magnetization. Differences between these authors rely on the assumptions chosen to simplify their models. The previous works were further adapted and extended by Ahedo et al. [31, 32], who developed a 2D model for cylindrical magnetized plasmas as part of their work on describing the plasma dynamics within helicon plasma thrusters. The properties of these models have been summarized in **Table 1**.

These descriptions of cylindrical magnetized plasmas can be used to approximate the distribution of key parameters within the discharge, such as the density distribution, the velocity of ions and electrons, and the plasma potential. As an example, the complete model developed by Ahedo et al. [31, 32] is described by a set of four radial equations and five more for the axial dimension. These take as inputs information regarding the ion species taking part in the discharge, collisional rates related to the ionization and interactions between ions, electrons and neutrals, and constant parameters such as the magnitude of the axial magnetic field B_0 and the isothermal electron temperature T_e.

The dispersion relations found for helicon plasma waves in **section 2.1** can be used to obtain reference values for parameters such as the peak density value in the discharge. This information

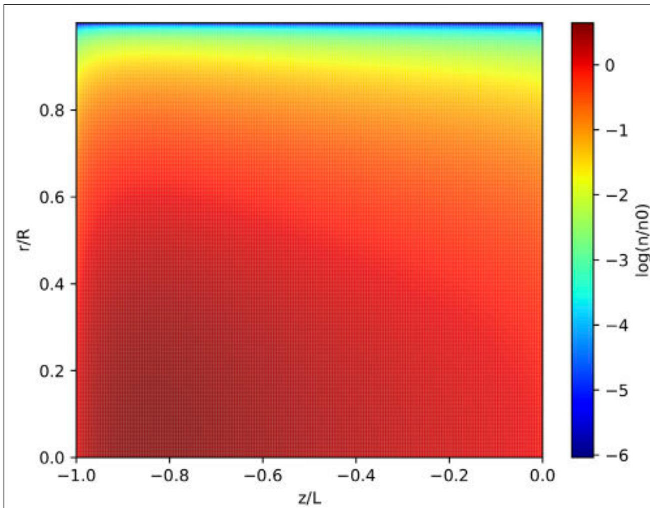

FIGURE 3 | Estimation of 2D plasma density distribution in the VX-CR research HPS, obtained through the model developed by Ahedo et al. [31, 32]. Geometry and plasma parameters were obtained from [61, 88, 91]. Density values are normalized with respect to the background neutral Argon density, $n_{n0} \approx 2 \times 1020$ m^{-3}. The VX-CR source is composed of a dielectric ceramic tube with R = 0.045 m and L = 0.226 m.

can be coupled with the description obtained from a 2D fluid model in order to project the distribution of plasma density, kinetic energy, and plasma potential throughout the discharge. Understanding the values of these parameters at the boundaries of the system, where the plasma comes into contact with solid materials, is essential to describe the interaction phenomena taking place in this region. **Figure 3** shows an example of the models from Refs. [31, 32] being used to estimate the 2D plasma distribution within a particular HPS, the VX-CR device. Data from these models can be used to obtain the plasma conditions at the radial ($r \to R$) and axial ($z \to -L$) boundaries, which then enable the analysis of the interaction between the plasma discharges and the physical confinement materials.

3 PLASMA-SURFACE PHENOMENA IN HPS

Solid materials often constitute the physical boundaries of plasmas, and the interaction between the surface atoms and the bulk plasma

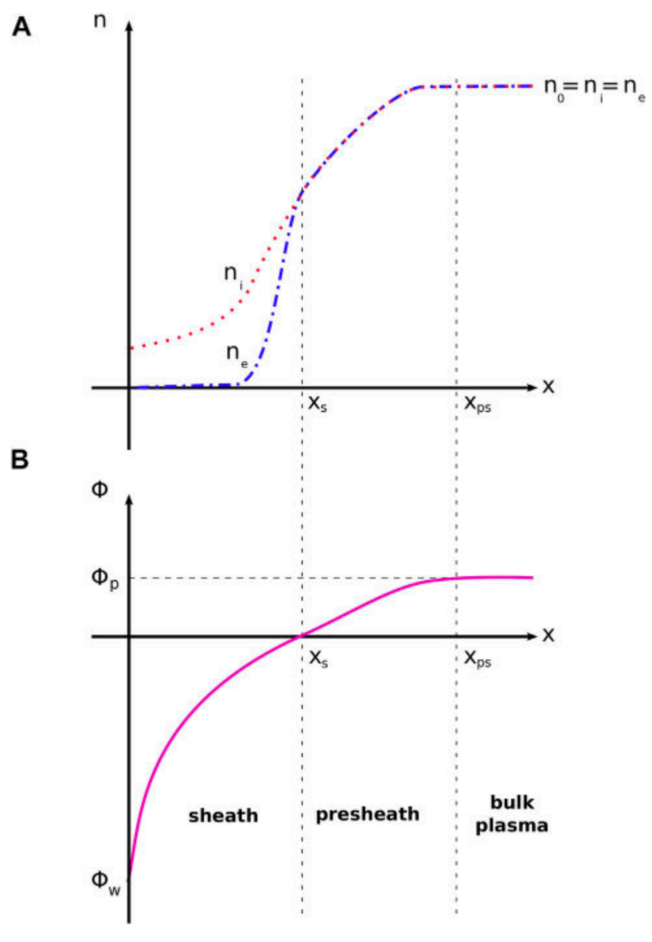

FIGURE 4 | Regions in the transition between the bulk plasma and a surface in contact with a plasma, such as the inner confinement surfaces in a HPS or the surface of an electrostatic probe immersed in the plasma. Graph **(A)** shows the behavior of the electron and ion density, while graph **(B)** shows the electric potential. The surface is located at $x = 0$. The bulk plasma region is located at $x > x_{ps}$, where the plasma is quasineutral and its potential is the plasma potential Φ_p. The presheath is the region $x_s < x < x_{ps}$ where both the plasma density and potential decrease gradually as $x \to x_s$. The sheath properly begins at the point $x = x_s \approx \lambda_{De}$, where the ions acquire the Bohm velocity $u_i = u_B = -(k_B T_e/m_i)^{1/2}$. Quasineutrality is broken, the electron density quickly decreases to zero and the potential drops gradually towards the wall potential Φ_w at $x = 0$.

can have a significant effect on the behaviour of the latter. In the case of typical HPSs, the dielectric containment surfaces are the only regions of direct interaction between the plasma and material surfaces. This is a particular advantage over other plasma generation technologies in which electrodes or cathodes have to be immersed within the plasma discharge, as they constitute additional regions of potential failure limiting the operational lifetime of the device. It is therefore relevant to understand the fundamental principles behind the most typical plasma-surface interactions within HPSs, in order to characterize them and to design strategies for their control or mitigation.

3.1 Plasma Sheaths

3.1.1 DC Sheaths

Sheath is the region near a material boundary in contact with a plasma where the bulk quasineutrality breaks due to the buildup of charge at the surface. In low-temperature plasmas, such as those typically found in HPSs, the more mobile electrons produce a negative charge at the surface and, therefore, a positive sheath where the ion density is larger than the electron density, $n_i > n_e$. Sheaths typically have a scale in the order of the Debye length, $\lambda_D = (\epsilon_0 T_e / e n_0)^{1/2}$. Sheaths have been studied since the early days of plasma physics, with the term originally coined by Irving Langmuir [33].

The process by which the quasineutrality in the bulk plasma transitions into the sheath is gradual, and three distinct regions can be identified as shown in **Figure 4**. The quasineutral density within the bulk plasma ($n_i = n_e = n_0$) begins to decrease in the vicinity of the boundary, in a region called the pre-sheath where the bulk density and the plasma potential both decrease. The scale of the pre-sheath is of the order of the ion mean free path (λ_i). The plasma then enters the sheath proper, at which point the quasineutrality does break and the electron density diminishes at a much faster rate than the ion density. The plasma potential decreases until reaching the wall potential, which is typically lower than the bulk plasma potential.

An important property of the transition from the plasma to the sheath is the Bohm Sheath Criterion, which establishes a condition on the minimum energy of the ions as they enter the sheath. The derivation of this criterion is based upon the assumptions of negligible ionization within the sheath itself, negligible electric field at the plasma edge, Maxwellian electrons with a density given by the Boltzmann relation, and cold ions with constant temperature [34, 35]. Its expression is provided by **Eq. 4** and states that the energy of the ions within the sheath is comparable to that of the electrons in the bulk plasma, and that their thermal velocities surpass the Bohm velocity $u_B^2 = (k_B T_e)/m_i$.

$$eV_0 \geq \frac{T_e}{2} \Rightarrow v_i \geq u_B \tag{4}$$

It is possible to find expressions for the potential obtained by the surface wall due to the formation of the sheath. For the case of collisionless sheaths, **Eq. 5** describes the wall potential with respect to the plasma potential at the sheath-presheath point of transition for the case of floating surfaces immersed within the plasma [35], a condition typical of certain types of probes as well as the boundary surfaces of HPSs.

$$\Phi_w = -\left(\frac{k_B T_e}{e}\right) \ln \sqrt{\frac{m_i}{2\pi m_e}} \tag{5}$$

This value is directly proportional to the electron temperature, and a constant factor related to the ion/electron mass ratio. It is also possible to obtain expressions for the approximate width of the sheath, as well as expressions for these values when the sheath is collisional or the material surface is biased with a particular voltage [35].

The behavior of the plasma as it enters and traverses the sheath is critical to the understanding of the phenomena occurring at the boundary surfaces, as these depend on the energy of the ions and electrons reaching it.

3.1.2 RF or Capacitive Sheaths

In devices where radiofrequency (RF) waves, plasmas, and materials coexist, the RF wave field dominates the formation and properties of the sheath near the boundary surfaces, allowing the appearance of potentials that surpass those typical of DC sheaths dominated by thermal effects. This phenomenon is defined as an RF plasma sheath, and it presents specific implications in the design of capacitive plasma sources, in material processing applications and within RF subsystems in fusion devices. An early treatise on this subject was presented by Butler and Kino [36], and a more recent review on this topic has been presented by Myra [37] with a particular emphasis on magnetically confined fusion systems.

RF sheaths present several features not found in the previously described DC sheaths. Plasmas interact with electrodes driven by oscillating currents I_{rf}, characterized by a frequency ω_{rf}. The sheaths created in the boundary region between the bulk plasma and these electrodes have a time-varying thickness correlated to the oscillation in the driving electrical parameters. Similar to the DC case, quasineutrality breaks within the sheath with the electron density becoming very low or even negligible. Lieberman and Lichtenberg [35] show simplified models for the case of simple, plane-parallel capacitive discharges, where assumptions help to gain a better understanding on the phenomena involved.

For idealized cases where the driving frequency is larger than the ion plasma frequency, $\omega_{\mathrm{rf}}^2 \gg \omega_{pi}^2$, the ions react to the time-averaged potentials in the bulk plasma and not to the driving RF frequency. On the other hand, electrons do respond to the driving RF current, given the particular condition $\omega_{pe}^2 \gg \omega_{\mathrm{rf}}^2 (1 + \nu_m^2/\omega_{\mathrm{rf}}^2)$, with ν_m being the electron-neutral collision frequency. The current travelling through the RF sheaths is then mostly displacement current produced by the time-varying electric field (given the very low electron density within the sheaths), unlike inside the bulk plasma where electrons react to the RF field and are able to carry the current through conduction. The analysis of an RF sheath depends on several factors, including the geometry of the problem, whether collisions are present within the sheath (when the ion mean free path, λ_i is smaller than the sheath thickness), and the frequency applied by the RF source. For the very high frequency (VHF) range, high ($n_e \approx 10^{17} m^{-3}$) plasma densities can be achieved with moderate power input, and this has been exploited in commercial devices used for materials processing [22].

In the particular case where $\omega_{\mathrm{rf}} < \omega_i$, with $\omega_i = 2\pi/\tau_i$ and τ_i being the ion transit time through the sheath, the ions within the sheath are able to respond to the time-varying RF field and a low-frequency RF sheath is formed [35]. These differ from the high-frequency case since current conduction through the sheath is dominated by resistive effects and not by the displacement of the time-varying electric potential. Besides, the voltage at the capacitive electrodes becomes rectified within portions of the RF cycle, losing its sinusoidal character. In this low-frequency regime, ions react to the sheath as in the case of a high-voltage DC sheath, and the energy they obtain is a non-linear function of the time-varying voltage within the RF cycle [35].

RF sheaths are relevant to HPSs since they are present in the regions near the conductors of the antenna system used to produce the helicon discharge, where the plasma reacts to the time-varying field of the RF cycle. Despite the advantage presented by the fact that the antenna can be located outside of the discharge chamber, these RF sheaths are able to accelerate ions traversing the RF sheath with energies that can surpass those obtained in the boundary DC sheaths present in other regions within the source. This fact has critical implications for the subsequent analysis of plasma-material interactions within HPSs.

3.2 Plasma-Surface Interactions

Plasma-surface interactions (PSIs) or plasma-material interactions (PMIs) comprehend the different phenomena that occur when ions, electrons, and neutrals within a plasma reach a material boundary. These interactions might produce effects on both the plasma itself as well as on the boundary. PSIs are essential in the field of plasma materials processing, and are also critical to the successful development of practical fusion devices [38, 39], as most designs include open magnetic flux surfaces where the plasma directly impinges the physical boundaries. They are also crucial in the advancement of electric propulsion technologies, where the lifetime of the thrusters directly depends on the erosion rate of those critical surfaces directly in contact with the plasma discharge or the plume of the thruster [40, 41].

Several processes can occur at the physical boundaries of a helicon plasma. Positive ions traversing the sheath typically become neutralized, in a process that either produces an excited neutral, or a neutral plus the emission of a secondary electron (Auger emission [35]). Secondary electron emission has been found to play a role in the sheath dynamics of certain types of low-energy plasma discharges, such as capacitively-coupled plasmas [42].

Another fundamental process is sputtering, the removal of material from a solid surface material due to the impact of an energetic impinging particle, typically ions in the case of plasma discharges. It is one of the most relevant phenomena occurring at the boundary surfaces of plasma discharges, since it can be responsible for significant erosion of said surfaces if the adequate conditions are met. **Figure 5** depicts the basic mechanisms behind the most relevant PSI phenomena encountered in the study of HPSs.

Theoretical treatments of the phenomenon of sputtering are provided by Sigmund [43], Bohdansky [44], Yamamura [45], Eckstein [46], and Behrisch et al. [47]. Most models describe the process as the result of collisional cascades in the surface layer of the target material, in which the momentum of the impacting ion is transferred to an atom in the target material's lattice through elastic collisions. The random arrangement of the position of both particles implies that an oblique collision is likely. The impacted target atom, in turn, collides with other neighboring particles triggering the cascade. With sufficient energy in the original impacting ion, eventually the collisional cascade will provide one of the atoms in the surface layer with an energy level surpassing the surface binding energy of the material [48], and a momentum directed outside of the surface. The atom will then be sputtered from the surface.

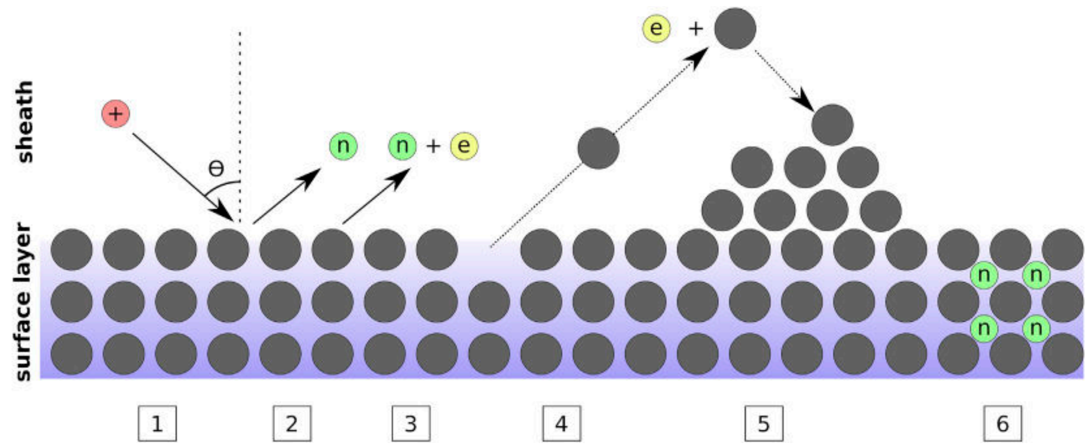

FIGURE 5 | Simplified diagram of the plasma-surface interaction phenomena most relevant to the study of HPSs. The plasma sheath region is depicted at the top of the diagram, while the top layers of the plasma-facing surface lattice are represented at its bottom, where the surface atoms are represented by solid circles. (1) represents the impacting ion, approaching the surface at an angle θ with respect to its normal, and with an energy E_0. When the ion energy does not surpass the threshold energy for sputtering $E_0 < E_{thr}$, the ion may become neutralized by a surface electron releasing a reflected neutral as shown in (2). In some cases, an additional electron may be released [secondary or Auger emission, (3)]. When $E_0 > E_{thr}$, collisional cascades within the top surface lattice are sufficient to expel a surface atom and sputtering occurs (4). The sputtered surface atoms might become ionized as they traverse the sheath, in which case they will be accelerated by the sheath potential back towards the surface and *redeposition* of material may occur (5). If the ion impact energy is sufficiently large, $E_0 \gg E_{thr}$, the ions may become neutralized and *implanted* within the surface lattice (6).

Simulation of the sputtering process based on the first principles from classical mechanics is possible, by using the technique of Molecular Dynamics [49, 50]. Other popular simulation packages are based on the Monte Carlo statistical method, such as TRIM. SP [51] and SRIM [52]. Sputtering yield estimations obtained by the use of these software packages are strongly dependent on the chosen input parameters, and have been shown to differ from experimental values in certain ranges [53].

The fundamental parameter in sputtering models is the sputtering yield, Y_{sputt}, defined as the number of surface atoms sputtered off the surface per incident impacting ion. Y_{sputt} is mainly a function of the ion species and surface material, the ion energy, and the angle of incidence between the surface normal and the ion's velocity vector. Below a particular threshold energy level, E_{thr}, ion impacts are not able to sputter surface atoms and $Y_{sputt} = 0$.

Several models have been developed to produce estimations for the sputtering yield, each particular to the species involved in the process, and the angle of incidence and energy E_0. Lieberman and Lichtenberg [35] report expressions valid for large atomic species within certain boundaries of their atomic number ratio. Eckstein and Preuss [46] proposed the model shown on **Eq. 6**, which is valid for ions impacting the surface at a normal angle of incidence.

$$Y(E_0) = q s_n^{KrC}(E_0) \frac{\left(\frac{E_0}{E_{thr}} - 1\right)^{\mu}}{\lambda + \left(\frac{E_0}{E_{thr}} - 1\right)^{\mu}} \tag{6}$$

where the krypton-carbon interaction potential s_n^{KrC} [46, 54] is used as an adequate mean value for different participating species and describes the nuclear stopping cross section. This parameter is defined as follows,

$$s_n^{KrC}(\varepsilon) = \frac{0.5 \ln(1 + 1.228\,8\varepsilon)}{\varepsilon + 0.172\,8\sqrt{\varepsilon} + 0.008\varepsilon^{0.150\,4}} \tag{7}$$

The reduced energy ε is obtained as follows,

$$\varepsilon = E_0 \frac{M_t}{M_i + M_t} \frac{a_L}{Z_i Z_t e^2} \tag{8}$$

where the subindexes i and t are used to describe the atomic numbers Z and atomic masses M of the projectile ion and target surface atoms, respectively. a_L is the Lindhard screening length [55],

$$a_L = \left(\frac{9\pi^2}{128}\right)^{1/3} a_B \left(Z_i^{2/3} + Z_t^{2/3}\right)^{-1/2} \tag{9}$$

where a_B is the Bohr atomic radius.

The remaining free parameters q and λ from **Eq. 6** can be found in [47] for a variety of impacting ions, target materials, and ion energies.

When ions impact on a boundary surface not in a perpendicular direction, but instead at an angle α with respect to the surface normal, the calculation of the sputtering yield needs to take this geometry into account. Eckstein and Preuss [46] proposed the formula in **Eq. 10**,

$$Y(E_0, \alpha) = Y(E_0, 0) \left\{ \cos\left[\left(\frac{\alpha}{\alpha_0}\frac{\pi}{2}\right)^c\right]\right\}^{-f} \exp\left\{ b\left(1 - \frac{1}{\cos\left[\left(\frac{\alpha}{\alpha_0}\frac{\pi}{2}\right)^c\right]}\right)\right\} \tag{10}$$

where

$$\alpha_0 = \pi - \arccos\sqrt{\frac{1}{1 + \left(E_0/E_{sp}\right)}} \geq \frac{\pi}{2} \tag{11}$$

E_{sp} is a binding energy characteristic of impacting ions, and c and f are fitting parameters. Behrisch and Eckstein [47] have compiled tables for these formulae for the most common ions and target materials.

For the case of surface materials consisting of alloys or compounds of different elements, the sputtering yield will be different for each different species present in the target surface. For the steady state with a sufficiently high flux of incident ions, the sputtering yields will distribute according to the stochiometric concentration of each species within the target compound. However, this distribution is not kept for small fluences of impinging ions, and the phenomenon of preferential sputtering occurs.

For binary target materials, containing two elemental species i and j, the sputter preferentiality δ can be defined [47] as a ratio of the elemental sputtering yields Y_i, Y_j and their stochiometric concentrations c_i, c_j,

$$\delta = \frac{Y_i}{Y_j}\frac{c_j}{c_i} \tag{12}$$

δ can also be estimated as follows,

$$\delta = \left(\frac{M_j}{M_i}\right)^{2m}\left(\frac{U_j}{U_i}\right)^{1-2m} \tag{13}$$

where M_i, M_j are the atomic masses, U_i, U_j the surface binding energies, and m is a power exponent describing the interaction potential.

When a plasma encounters a solid surface, such as at the boundaries provided by the containment surfaces of a HPS, a sheath will be formed and ions will be accelerated according to the potential present at the wall. If the ions are able to increase their energy beyond the threshold energy E_{thr}, sputtering will occur and the surface will be modified. Combining this information with the density distribution obtained through experimental measurements or simulations, such as the fluid models described in **section 2.2**, an *etch* rate or *erosion* rate can be calculated for the surface. This value can be used to project the behavior of the HPS and establish limits to its useful lifetime in a particular practical application.

In practical applications, the etch rate E of a surface bombarded with energetic ions, measured as a ratio of the etch depth per unit of time, is calculated as a function of the incident ion flux Γ_i, the particular sputtering yield Y, and the mass density of the target surface ρ_t as shown in **Eq. 14**,

$$E = \frac{\Gamma_i Y M_{m,t}}{\rho_t N_A} \tag{14}$$

where $M_{m,t}$ is the molar mass of the target surface and N_A is Avogadro's constant. The calculation of the sputtering yield would take into account all the considerations discussed in this section. The incident ion flux Γ_i is determined by the particular conditions of the plasma discharge near the surface; for example, it can be approximated by applying the Bohm Sheath Criterion and specifying that $\Gamma_i = n_s u_B$ where n_s is the ion density at the entrance of the sheath and u_B the ion Bohm velocity.

4 RELEVANT ENGINEERING ASPECTS

Figure 6 shows a simplified 2-D cross section of a typical HPS built in a cylindrical geometry (excluding auxiliary vacuum vessels, diagnostics or nozzle elements which may exist in laboratory or thruster applications). A cylindrical dielectric tube is sealed at one of its ends by an endcap or barrier. Neutral gas is fed inside the cylinder from an external source. An axial magnetic field, parallel to the dielectric cylinder axis, is created by using solenoid coils or permanent magnets. An antenna is used to launch the helicon waves into the neutral medium; this antenna is typically placed outside of the exterior surface of the dielectric tube. The open end of the cylinder is commonly attached to an external chamber and a gas extraction system capable of maintaining the vacuum pressure within the source at the required limits. Considerations for the design and implementation of practical HPSs are discussed in detail in [22].

Given the fact that the antenna used to launch the helicon waves can be placed outside the plasma medium, surrounding the external surface of the dielectric cylinder, the plasma-facing surfaces of the endcap, the dielectric cylinder and any other purposely-designed limiter inner walls are the only material boundaries in direct contact with the plasma, and therefore the only ones potentially subject to plasma-material interactions. The axial magnetic field limits the diffusion of particles toward the cylinder's inner surfaces. The *upstream* section of typical HPSs, shown at the left of **Figure 6**, will usually contain another boundary surface and is a common location for the injection of the neutral gas required to sustain the plasma discharge. Depending on the specific geometry of a particular device, this section might be located in the vicinity of the helicon antenna or away from it, and the magnetic field might remain parallel to the axis of the source or diverge instead. The density of neutrals is usually higher in this region, promoting more frequent interactions with ions and removing momentum from them, which in turn has an effect on the energy they carry towards the boundary surfaces.

The careful selection of these materials interacting with the plasma discharge, as well as an adequate design of the HPS geometry, magnetic field, and antenna, can reduce the plasma density and particle energies near the inner surfaces of these elements and therefore mitigate their erosion due to material sputtering. This in turn provides HPSs with the potential of long operational lifetimes. This is a critical property in fields such as in-space electric propulsion, where thrusters based on HPSs are among the leading candidate technologies within electrode-less thrusters [56].

4.1 Plasma-Facing Materials in HPSs

Materials used for the construction of HPSs must comply with a number of often conflicting properties. RF-transparent materials are commonly used to manufacture the cylindrical tube, allowing for the efficient transmission of the RF waves produced by the

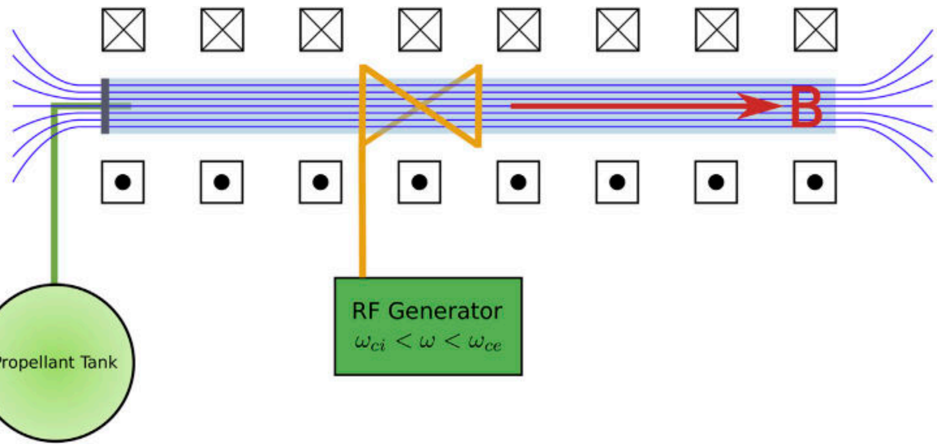

FIGURE 6 | Simplified representation of a typical implementation of a Helicon Plasma Source.

external antenna to the plasma medium. This requires materials with a low dissipation of RF energy, which is usually measured in terms of the loss tangent (tan δ). The amount of thermal energy dissipated by the boundary material is directly proportional to this loss tangent parameter, which is in itself proportional to the material temperature [57]. This can potentially create a positive feedback loop of RF energy losses within the boundary material, showing the importance of the material selection in practical HPSs.

From a practical engineering point of view, HPS materials should feature a high thermal conductivity, enabling the distribution and extraction of the heat loads produced by the inherent inefficiencies of the RF transmission and the ionization process within the source. Materials with a high thermal conductivity will allow the heat loads present in the material to spread axially and azimuthally, promoting the creation of a more even temperature distribution and reducing the appearance of thermal hotspots. This in turn contributes to the reduction of the amount of thermal energy dissipated as the RF energy traverses the boundary material. Thermal management of HPSs is a critical issue in practical implementations [58–62] and is essential for the development of high-power systems relying on HPSs, such as the VASIMR engine [63], the Proto-MPEX PMI research device [64], and the PISCES-RF steady-state helicon device [2].

De Faoite et al. [65] compiled a thorough review of the available data on the most relevant thermal and mechanical properties of dielectric technical ceramics commonly used in HPSs, focusing on those aspects relevant to the thermal management issues described above. The materials included in the analysis included alumina, aluminum nitride, berylia, quartz, sialon, and silicon nitride. A later work [66] presents linear regressions of these properties as a function of temperature, where adequate fits were found for some of them while also highlighting the limits of the publicly available data sets.

In order to assess the reliability of these dielectric materials under the boundary conditions present in inner confinement surfaces of HPSs, their sputtering parameters would have to be evaluated under similar conditions, using the models and techniques discussed in **section 3.2**. As an example, **Figure 7** compiles experimental and simulated data for the sputtering yields of singly charged argon ions impacting some of these dielectric materials commonly used in HPSs, as a function of the impacting ion energy and at normal incidence. These choices are typical for the materials used in the VX-CR research HPS [61].

As an indicative example, erosion phenomena will be estimated for a typical HPS operating with an electron temperature of $T_e \approx 5\,\mathrm{eV}$ and a density $n \approx 2 \times 10^{18}\,\mathrm{m}^{-3}$ in the regions near the surface of a floating dielectric confinement wall [67]. **Eq. 5** estimates that the wall potential becomes $\Phi_w = -23.5\,\mathrm{V}$. If the ions enter the sheath with negligible kinetic energy, it can be assumed this will be the incident energy at the wall, slightly larger than the corresponding threshold energy for sputtering $E_{thr} \approx 19\,eV$. If the wall material is alumina, **Eq. 6** produces a value of $Y \approx 0.06$ atoms/ion for the case of normal incidence to the surface and **Eq. 14** produces an approximate etch rate of $E = 17.62$ nm/s. If the wall thickness of this material is $t = 2.5$ mm, this means it would take $\Delta t = 141.9 \times 10^3\,\mathrm{s} = 39.4\,\mathrm{h}$ for the wall to erode (in a scenario where all conditions remain constant). If the confinement surface is made of quartz glass (silicon dioxide), the wall potential Φ_w would be below the threshold energy for sputtering for argon ions impinging on SiO_2, $E_0 < E_{thr} \approx 35\,\mathrm{eV}$, and no sputtering would occur.

If these conditions exist in the vicinity of the antenna straps of the HPS, where the RF energy is transmitted as a 13.56 MHz signal with a peak-to-peak voltage amplitude of $V_{pp} = 1\,\mathrm{kV}$ (and therefore a peak voltage of $V_p = 500\,\mathrm{V}$), the methods described by Berisford et al. [68] can be used to estimate an average sputtering rate given the ion energy distribution function for low-frequency RF sheaths [35]. In this particular case, an average sputtering yield of $Y_{avg} = 0.08$ is obtained for the case of Argon ions impacting the alumina surface. The corresponding etch rate would then be $E = 23.5$ nm/s, and it would take $\Delta t = 106{,}400\,\mathrm{s} = 29.56\,\mathrm{h}$ for the wall to erode. If the material is quartz, the RF sheath would be able to produce sputtering, with an average yield of $Y_{avg} = 0.06$, an etch rate of $E =$

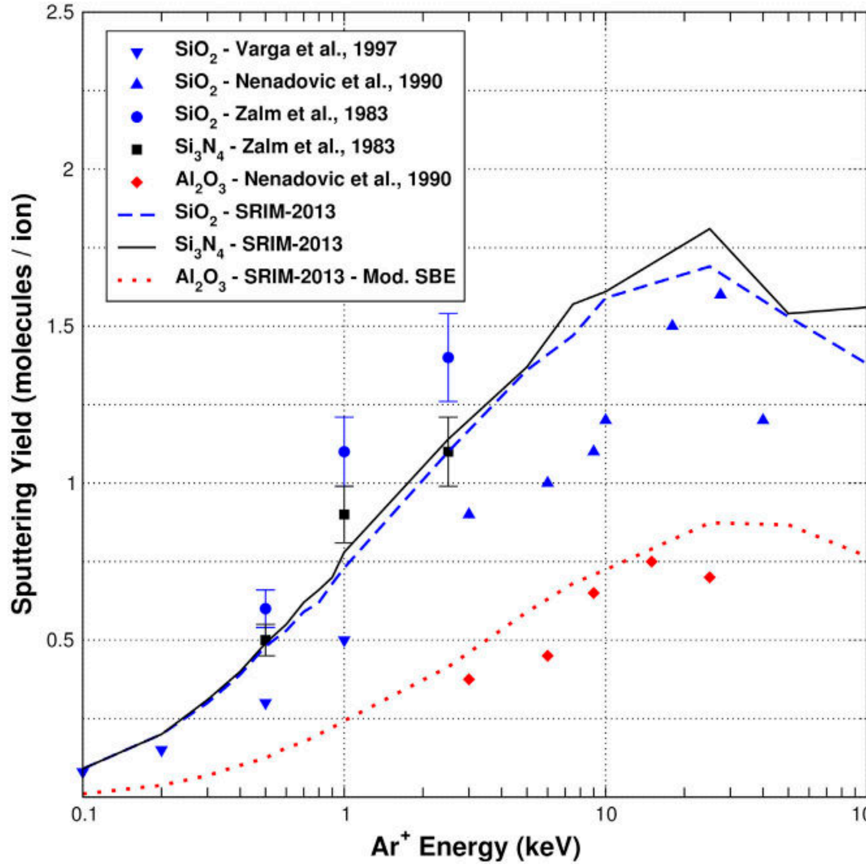

FIGURE 7 | Sputtering yields for Ar^+ ions impacting perpendicularly onto some of the compounds commonly used in the construction of HPSs. Experimental data is shown for SiO_2 [92–94], Al_2O_3 [93], and Si_3N_4 [92]; as well as computational results obtained with the SRIM-2013 package.

18.85 nm/s, and the surface would be eroded in Δt = 132,600 s = 36.84 h. These are extremely simplified estimations, where conditions remain constant during the whole process, and no variations in the sputtering yield are introduced due to surface modification or deviations from normal incidence as the surface degrades.

4.2 Relevant Experimental Work Regarding PSI Within HPSs

HPSs have been used as part of plasma processing devices since early in their development [5, 10]), generating plasmas with the adequate parameters in order to modify the surfaces of samples or substrates subjected to their discharge. However, few studies have been conducted on the effects of the plasma discharge itself upon the inner confinement surfaces of HPSs.

Among these, Aanesland et al. [69] reported on the effects of an additional, floating copper antenna immersed within the discharge itself. They describe the sputtering of copper atoms from this additional antenna, which are then redeposited on the inner surface of the dielectric discharge tube. At high power levels, they describe how the areas in this dielectric tube located under the straps of the external helicon antenna remain clean due to the re-sputtering of the deposited copper layer. They suggest this is an effect of the RF sheath created on the plasma-surface boundary, as previously discussed in **section 3.1.2**.

This same mechanism was observed by Berisford et al. [60], when researching the power distribution and erosion within the dielectric tube of a linear helicon device. These authors developed expressions to estimate the etch rates observed at these regions under the straps of the extenal helicon antenna, modelling the sheath present in these areas as a low-frequency RF scenario (refer to **section 3.1.2**) and averaging the sputtering yield according to the ion energy distribution throughout the RF cycle [35]. These findings were validated through experimental observations of the actual erosion in the dielectric cylinder used in their experiment. These authors were able to estimate the required particle flux at the regions under the helicon antenna conductor from the measured etch rates, and also by analyzing IR thermal data measured at the same location; both estimations agreed within a factor of two.

Barada et al. [70] investigated this phenomenon more thoroughly, experimentally confirming the existence of an increased negative DC bias under the straps of the external antenna in the inner surfaces of a HPS, and investigating how this wall potential is affected by variations in the helicon discharge parameters. Infra-red (IR) thermography measurements taken on the inner surface of the dielectric ceramic window of the PISCES-RF device [2] also provided indirect evidence of this phenomena, showing increased values of the plasma heat flux under the straps of the helicon antenna, particularly the conductor connected to the live (non-grounded) terminal of the RF power supply.

The use of Faraday shields has been explored as a means to mitigate the effect of capacitive coupling within inductively-coupled plasmas (ICPs), and their application to HPSs has been suggested for the same purpose [71]. The Faraday shield has been implemented as a cylindrical jacket made of conducting material, installed between the dielectric plasma confinement surface and the helical antenna used in the ICP reactor [72]. Longitudinal slits have to be cut along this shield, to enable the inductive fields to penetrate the discharge. Specific experiments applying this technique to HPSs have yet to be performed. This method could potentially improve the performance of HPSs by reducing the erosion rate due to capacitive coupling under the antenna straps; however, its effects on other aspects of the source such as thermal management, and discharge efficiency, have to be investigated.

Recent experiments by Beers et al. [73, 74] describe the analysis of the helicon discharge section of the Proto-MPEX device, where they combined a finite-element model describing the helicon discharge, an ad-hoc sheath model, and a transport code in order to analyze the production of impurities due to sputtering at the material boundaries. Their results confirm the experimental findings of Berisford et al. [60] and Barada et al. [70], showing the importance of the electrostatic potentials near the helicon antenna straps as a source of energetic ions impacting the radial boundaries. They also showed the difference between the operation in non-magnetized and magnetized regimes, as was also discussed by Ahedo et al. [32].

The effect of the strength and geometry of the magnetic field on the performance of HPSs has also been researched. The magnetic field has an effect on the density profile within the source. Lafleur et al. [75] show that its intensity affects the peak value of the plasma density in the helicon mode, and they show the existence of optimal configurations for given values of input RF power and magnetic field intensity. The axial magnetic configuration is also able to modify the performance of an HPS. Takahashi et al. [76–78] have described the distribution of momentum transfer between the plasma and different elements of the source, its relationship with the magnetic field configuration, and how it can affect the total thrust of a helicon plasma thruster. These experiments describe how the ions are able to impart an axial momentum to the inner wall of the dielectric confinement material, due to the fact that their velocity vector is not completely normal to the wall surface [78]. This method could be used to indirectly estimate the incident angle with the confinement surface as the ions traverse the sheath, a critical factor in the calculation of the sputtering yield, although it is shown how the radial component is responsible of the energy transfer towards the wall.

The profile of the magnetic field within a HPS can be designed to mitigate the consequences of plasma-wall interactions within the source. Caneses et al. [79] describe experiments where two configurations of the magnetic field within the Proto-MPEX high-power helicon device were used to demonstrate the usefulness of controlling where the last uninterrupted magnetic flux surface (LUFS) makes contact with the inner confinement surfaces of the source. They relocated this contact point away from the dielectric ceramic window towards a purposely-designed stainless steel cylindrical limiter surface, an element with a function analog to that of divertors in fusion devices. This design change reduced the thermal heat loads under the dielectric window associated with direct impingement of the plasma, since the magnetic geometry maintains the LUFS at a minimum distance of approximately 1 cm away from the boundary surfaces. The plasma density decays rapidly beyond this point, as the magnetic lines intersect the material boundaries more often. This technique of magnetic field shaping allows the Proto-MPEX to reduce the heat loads on the dielectric window, but its effects on the sputtering and erosion related to plasma-surface interaction have not been thoroughly investigated. However, the careful design of magnetic geometries is commonly used for this purpose on electric propulsion devices [80, 81].

Figure 8 summarizes the findings of these experiments with regard to the appearance of sputtering phenomena within the internal dielectric confinement surfaces of HPSs. Region (1) in the figure represents areas within these internal surfaces in direct contact with the plasma, where a sheath forms and the dielectric surface obtains a negative electric potential Φ_w as described by **Eq. 5**. The positive ions are then accelerated towards the wall with a surface flux determined by the product of the bulk plasma density n_0 and the Bohm velocity u_B they obtain when entering the sheath. The effect of the impinging ions on the dielectric surface can then be analyzed according to the sputtering models discussed in **subsection 3.2**, and effective surface etch rates may be computed. Region (2) in **Figure 8** describes the particular phenomena observed by Berisford et al. [60], Aanesland et al. [69], Barada et al. [70], and Beers et al. [73, 74], where the creation of RF sheaths on the internal surfaces directly under the helical antenna straps may create the conditions for high-voltage DC sheaths in the negative part of the cycle. In this scenario, average sputtering yields can be computed through the ion energy distribution within the negative portion of the RF cycle [35], and hence etch rates can be computed as well.

5 SUMMARY AND CONCLUSION

Helicon plasma sources (HPSs) hold great potential for the development of efficient, high-density plasma sources. One of their widely quoted advantages is the absence of cathodes or electrodes directly in contact with the plasma discharge. This fact limits any plasma-surface interactions to the inner surfaces of the dielectric confinement surfaces, where the diffusion of the plasma is limited by the action and geometry of the axial magnetic field, thus reducing the expected material erosion rates and providing these devices with a potentially long operational lifetime. This proposed advantage of HPSs, among others, is still the subject of debate [82, 83].

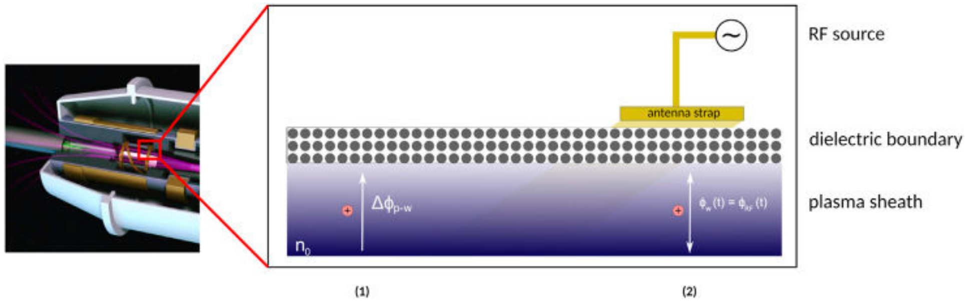

FIGURE 8 | Representation of the two main sputtering regimes present in helicon plasma sources, as previously reported in literature. **(1)** shows the conditions present at the boundary between the bulk plasma, with density n_0, and the internal dielectric boundaries within an HPS. Parameters such as this density and the electron temperature T_e define the conditions present within the plasma sheath, which accelerate the positive ions towards the wall through the plasma-wall potential $\Delta\Phi_{p-w}$ [35]. If the energy obtained by the ions at the material boundary surpasses the threshold energy E_{thr}, sputtering will then occur. **(2)** describes the situation particular to the areas under the antenna straps, which may be subjected to high capacitive voltages driven by the external RF subsystem [60, 70, 73]. Given sufficiently large voltages, the negative part of the antenna's RF cycle will accelerate the ions towards the surface with enough time to traverse the sheath, essentially behaving as a high-voltage DC sheath [60]. Once again, if the energy obtained by the ions surpasses the threshold limit, sputtering will occur.

The present review summarized the theory describing these interactions, beginning with the physics of helicon waves and cylindrical magnetized plasmas (**section 2**), followed by a description of the most relevant plasma-surface interaction phenomena within HPSs (**section 3**). Practical implementation aspects and relevant experimental results were presented in **section 4**.

Current research results point towards the existence of two main modes of plasma-surface interaction within HPSs. The first one is the diffusion of plasma towards the inner surfaces of these material boundaries, where the ions are then accelerated through DC sheaths and sputtering may occur if they are able to become energized above the corresponding threshold energy level. The eventual etch rate experienced by particular devices will depend on the plasma parameters near the boundaries, the species present in the plasma and the wall material, and the geometry of the magnetic field at each region. The second mode of interaction appears in the regions of the helicon dielectric window directly under the conductor straps of the antenna, where capacitive RF sheaths are created and accelerate the ions. Direct (profilometry and surface analysis) and indirect (IR thermography) evidence has confirmed the existence of this phenomenon, and it has also been investigated through modeling and simulations. Experimental results suggest that these RF sheaths appearing under the helicon antenna straps are responsible for the appearance of thermal hot spots and regions of concentrated erosion patterns in the inner surface of the dielectric windows of HPSs.

Despite recent advances in the description and understanding of these plasma-material interactions within helicon plasma sources, several topics are still open for research and experimentation. Current modeling efforts integrate different specific tools to simulate the interactions between the plasma discharge, the transport and diffusion of the plasma species throughout the simulation domain, the creation of DC and RF sheaths, and the interaction phenomena occurring at the material boundaries. As usual within the simulation of plasma phenomena, varying timescales, lengths and energy levels are involved. Integrated simulation efforts for the specific purpose of studying sputtering and impurity transport within HPSs are recent, and they could benefit from the development of purposely-designed integrated simulation tools for this task.

Specific models for sputtering phenomena on the dielectric ceramics commonly used in HPSs should be developed and validated through experimentation. Additionally, the interaction between the sputtered species, the original plasma, external impurities, and the boundary surfaces, including the formation of new compounds and molecules, appears to be a topic of relevance, as shown in the results obtained in the Proto-MPEX device [74] where these relationships were taken into account to better explain the observed experimental results.

The magnetic field geometry can be designed in order to displace the contact points between the plasma and its boundary surfaces and also to create a separation between the magnetic flux surface enveloping the plasma and the confinement materials. This strategy appears to have a potential effect in reducing the erosion phenomena within the HPS, as suggested by the effect it has shown in modifying and reducing the heat flux distribution in the Proto-MPEX experiment [79]. Yet this claim has not been thoroughly investigated. This experiment also demonstrated how cylindrical liners can be placed at the locations where the plasma does contact the boundary surfaces; when this occurs outside of the section where the helicon antenna is located, the requirement for an RF-transparent dielectric window can be removed and other materials with lower sputtering yields can be selected. However, the exact interactions between these liner materials, the plasma, and the sputtered impurities have to be investigated. This technique could offer some critical advantages for the creation of impurity-free plasmas in high-power helicon devices used to research fusion-relevant material interactions; however, they might introduce new unwanted issues in other applications where the physical lifetime of the hardware is the priority, such as in electric propulsion devices.

From an experimental perspective, the diagnostics able to measure the above-mentioned parameters can be improved. Given the linear nature of most helicon devices, access to the critical regions near the dielectric ceramic window and the RF antenna region is complex. High power density devices, such as the Proto-MPEX and Pisces-RF devices, or the VASIMR VX-200SS engine, create a hostile environment for most physical probes. Measurements have been done of the inner wall potential [70], the radial heat flux, and the UV radiation [60], yet these experiments were not conducted inside high-power, steady-state devices.

Measurements of the effects of sputtering within the inner surface of helicon confinement surfaces have been studied through profilometry [60] and x-ray photoelectron spectroscopy [74]. Extensive experience in this particular field has been obtained in the simulation and execution of long-duration experimental runs of electric propulsion devices [40, 84–86], but not in those which employ HPSs. Diagnostics such as optical profilometry [87] and coordinate-measuring machines [88] could also be applied to HPSs, particularly for the measurement of surface erosion after long-duration tests in high-power devices.

The engineering problem of managing the heat fluxes transferred by the plasma onto the inner confinement surfaces of HPSs is partially related to the plasma-surface interaction issues discussed throughout this review, since the direct impingement of energetic ions onto these surfaces is one of the mechanisms of heat transfer present in the sources. Some mitigation techniques previously discussed, such as shaping the magnetic field to control the points of direct contact between the plasma and these inner surfaces, can be applied to both phenomena. The role of the temperature on the erosion rate of these surfaces in contact with the plasma has not been investigated in the particular case of HPSs. The formation of nanostructures has been studied in the case of candidate materials for the divertors of projected fusion devices [89]; similar conditions might be achievable in high-power HPSs operating at steady-state for long periods of time, and whether these phenomena affect the sputtering of these inner confinement surfaces remains to be investigated.

The physics concepts presented here can be combined to establish a framework for analyzing the impact of plasma-material interactions within HPSs, and explore mitigation strategies suited for the development of high-power helicon sources, particularly for those applications where an extended operational lifetime of the system is a critical requirement. These concepts can be used to model the density distribution within the HPS and the existence of induced RF or DC bias voltages on its inner surfaces, which appear to be a significant factor in the appearance of local sputtering and deposition phenomena. A sufficient understanding of these phenomena will be required as the application of high-power, steady-state helicon sources continues to grow in the fields of materials processing, fusion research, and in-space electric propulsion.

AUTHOR CONTRIBUTIONS

JDV conceptualized the review and figures, and wrote the first draft of the manuscript. FCD and VG critically revised the manuscript. All authors read and approved the final submitted version of the article.

FUNDING

This research work was funded by Ad Astra Rocket Company Costa Rica. Financial support for the open-access publishing of this manuscript was provided by Universidad Nacional de Costa Rica (UNA). The authors declare that this study received funding from Ad Astra Rocket Company Costa Rica. The funder was not involved in the study design, collection, analysis, interpretation of data, the writing of this article or the decision to submit it for publication.

ACKNOWLEDGMENTS

The authors wish to acknowledge the contribution of Juan Francisco Caneses, who reviewed a draft of this manuscript and provided critical feedback and comments.

REFERENCES

1. Shinohara S. Helicon High-Density Plasma Sources: Physics and Applications. *Adv Phys X* (2018) 3:1420424. doi:10.1080/23746149.2017.1420424
2. Thakur SC, Simmonds MJ, Caneses JF, Chang F, Hollmann EM, Doerner RP, et al. PISCES-RF: a Liquid-Cooled High-Power Steady-State Helicon Plasma Device. *Plasma Sourc Sci. Technol* (2021) 30:055014. doi:10.1088/1361-6595/abef19
3. Rapp J, Biewer TM, Bigelow TS, Caughman JBO, Duckworth RC, Ellis RJ, et al. The Development of the Material Plasma Exposure experiment. *IEEE Trans Plasma Sci* (2016) 44:3456–64. doi:10.1109/tps.2016.2628326
4. Caneses JF, Lau C, Goulding RH, Bigelow TS, Biewer TM, Caughman JB, et al. Power Transport Efficiency during O-X-B 2nd Harmonic Electron Cyclotron Heating in a Helicon Linear Plasma Device. *Plasma Phys Controlled Fusion* (2021) 64:025005 (21pp). doi:10.1088/1361-6587/ac4525
5. Perry AJ, Vender D, Boswell R. The Application of the Helicon Source to Plasma Processing. *J Vac Sci Technol B* (1991) 9:310–7. doi:10.1116/1.585611
6. Wang S-B, Wendt AE. Control of Ion Energy Distribution at Substrates during Plasma Processing. *J Appl Phys* (2000) 88:643–6. doi:10.1063/1.373715
7. Charles C, Boswell R, Alexander P, Costa C, Sutherland O, Pfitzner L, et al. Operating the Helicon Double Layer Thruster in a Space Simulation Chamber. *IEEE Trans Plasma Sci* (2008) 36:1196–7. doi:10.1109/tps.2008.924425
8. Shabshelowitz A, Gallimore AD. Performance and Probe Measurements of a Radio-Frequency Plasma Thruster. *J Propulsion Power* (2013) 29:919–29. doi:10.2514/1.b34720
9. Shinohara S, Nishida H, Tanikawa T, Hada T, Funaki I, Shamrai KP. Development of Electrodeless Plasma Thrusters with High-Density Helicon Plasma Sources. *IEEE Trans Plasma Sci* (2014) 42:1245–54. doi:10.1109/tps.2014.2313633
10. Chen FF. A Compact Permanent-Magnet Helicon Thruster. *IEEE Trans Plasma Sci* (2015) 43:195–7. doi:10.1109/tps.2014.2361476
11. Takahashi K. Magnetic Nozzle Radiofrequency Plasma Thruster Approaching Twenty Percent Thruster Efficiency. *Scientific Rep* (2021) 11:1–12. doi:10.1038/s41598-021-82471-2
12. Chang Diaz F, Squire JP, Carter M, Corrigan A, Dean L, Farrias J, et al. An Overview of the VASIMR® Engine. In: 2018 Joint Propulsion Conference; 2018 July 9-11; Cincinnati, OH, USA. (2018). p. 4416.

13. Boswell RW, Chen FF. Helicons-the Early Years. *IEEE Trans Plasma Sci* (1997) 25:1229–44. doi:10.1109/27.650898
14. Chen FF, Boswell RW. Helicons-the Past Decade. *IEEE Trans Plasma Sci* (1997) 25:1245–57. doi:10.1109/27.650899
15. Chen F. Helicon Discharges and Sources: a Review. *Plasma Sourc Sci Tech* (2015) 24:014001 (25 pp). doi:10.1088/0963-0252/24/1/014001
16. Klozenberg JP, McNamara B, Thonemann PC. The Dispersion and Attenuation of Helicon Waves in a Uniform Cylindrical Plasma. *J Fluid Mech* (1965) 21:545–63. doi:10.1017/s0022112065000320
17. Chen FF. Plasma Ionization by Helicon Waves. *Plasma Phys Control Fusion* (1991) 33:339–64. doi:10.1088/0741-3335/33/4/006
18. Chen F, Arnush D. Generalized Theory of Helicon Waves - I - normal Modes. *Phys Plasmas* (1998) 4:3411. doi:10.1063/1.872483
19. Arnush D, Chen F. Generalized Theory of Helicon Waves - II - Excitation and Absorption. *Phyisics of Plasmas* (1998) 5(5):1239–1254. doi:10.1063/1.872782
20. Stix TH. *Waves In Plasmas*. New York, NY, USA: Springer Science & Business Media (1992).
21. Goldston RJ, Rutherford PH. *Introduction to Plasma Physics*. Bristol, UK: CRC Press (1995).
22. OA Popov ed. *High Density Plasma Sources: Design, Physics and Performance*. Park Ridge, NJ, USA: Noyes Publications (1995).
23. Trivelpiece AW, Gould RW. Space Charge Waves in Cylindrical Plasma Columns. *J Appl Phys* (1959) 30:1784–93. doi:10.1063/1.1735056
24. Shamrai KP, Taranov VB. Volume and Surface Rf Power Absorption in a Helicon Plasma Source. *Plasma Sourc Sci. Technol.* (1996) 5:474–91. doi:10.1088/0963-0252/5/3/015
25. Legéndy CR. Macroscopic Theory of Helicons. *Phys Rev* (1964) 135: A1713–A1724. doi:10.1103/physrev.135.a1713
26. Carter MD, Baity FW, Jr, Barber GC, Goulding RH, Mori Y, Sparks DO, et al. Comparing Experiments with Modeling for Light Ion Helicon Plasma Sources. *Phys Plasmas* (2002) 9:5097–110. doi:10.1063/1.1519539
27. Tonks L, Langmuir I. A General Theory of the Plasma of an Arc. *Phys Rev* (1929) 34:876–922. doi:10.1103/physrev.34.876
28. Tonks L. Theory of Magnetic Effects in the Plasma of an Arc. *Phys Rev* (1939) 56:360–73. doi:10.1103/physrev.56.360
29. Fruchtman A, Makrinich G, Ashkenazy J. Two-dimensional Equilibrium of a Low Temperature Magnetized Plasma. *Plasma Sourc Sci. Technol.* (2005) 14: 152–67. doi:10.1088/0963-0252/14/1/017
30. Sternberg N, Godyak V, Hoffman D. Magnetic Field Effects on Gas Discharge Plasmas. *Phys Plasmas* (2006) 13:063511. doi:10.1063/1.2214537
31. Ahedo E. Parametric Analysis of a Magnetized Cylindrical Plasma. *Phys Plasmas* (2009) 16:113503. doi:10.1063/1.3262529
32. Ahedo E, Navarro-Cavallé J. Helicon Thruster Plasma Modeling: Two-Dimensional Fluid-Dynamics and Propulsive Performances. *Phys Plasmas* (2013) 20:043512. doi:10.1063/1.4798409
33. Langmuir I. Oscillations in Ionized Gases. *Proc Natl Acad Sci* (1928) 14: 627–37. doi:10.1073/pnas.14.8.627
34. Allen J. The Plasma-Sheath Boundary: its History and Langmuir's Definition of the Sheath Edge. *Plasma Sourc Sci Tech* (2009) 18:014004. doi:10.1088/0963-0252/18/1/014004
35. Lieberman M, Lichtenberg A. *Principles of Plasma Discharges and Materials Processing*. Hoboken, NJ, USA: Wiley-Interscience (2005).
36. Butler HS, Kino GS. Plasma Sheath Formation by Radio-Frequency fields. *Phys Fluids* (1963) 6:1346–55. doi:10.1063/1.1706905
37. Myra J. A Tutorial on Radio Frequency Sheath Physics for Magnetically Confined Fusion Devices. *J Plasma Phys* (2021) 87:905870504. doi:10.1017/s0022377821000878
38. Rapp J, Biewer TM, Bigelow TS, Caneses JF, Caughman JBO, Diem SJ, et al. Developing the Science and Technology for the Material Plasma Exposure experiment. *Nucl Fusion* (2017) 57:116001. doi:10.1088/1741-4326/aa7b1c
39. Linsmeier C, Unterberg B, Coenen J, Doerner R, Greuner H, Kreter A, et al. Material Testing Facilities and Pprogram for Plasma-Facing Component Testing. *Nucl Fusion* (2017) 59(9):092012. doi:10.1088/1741-4326/aa4feb
40. Pérez-Grande D, Fajardo P, Ahedo E. Evaluation of Erosion Reduction Mechanisms in a Hall Effect Thruster. In: Joint Conference of 30th International Symposium on Space Technology and Science, 34th International Electric Propulsion Conference and 6th Nano-satellite Symposium; 2015 July 4-10; Hyogo-Kobe, Japan. (2015).
41. Brown NP, Walker MLR. Review of Plasma-Induced Hall Thruster Erosion. *Appl Sci* (2020) 10:3775. doi:10.3390/app10113775
42. Horváth B, Daksha M, Korolov I, Derzsi A, Schulze J. The Role of Electron Induced Secondary Electron Emission from SiO2surfaces in Capacitively Coupled Radio Frequency Plasmas Operated at Low Pressures. *Plasma Sourc Sci. Technol.* (2017) 26:124001. doi:10.1088/1361-6595/aa963d
43. Sigmund P. Theory of Sputtering. I. Sputtering Yield of Amorphous and Polycrystalline Targets. *Phys Rev* (1969) 184:383–416. doi:10.1103/physrev.184.383
44. Bohdansky J. A Universal Relation for the Sputtering Yield of Monatomic Solids at normal Ion Incidence. *Nucl Instr Methods Phys Res Section B: Beam Interactions Mater Atoms* (1984) 2:587–91. doi:10.1016/0168-583x(84)90271-4
45. Yamamura Y, Tawara H. Energy Dependence of Ion-Induced Sputtering Yields from Monoatomic Solids at normal Incidence (1995). Technical report. Japan: National Institute for Fusion Science.
46. Eckstein W, Preuss R. New Fit Formulae for the Sputtering Yield. *J Nucl Mater* (2003) 320:209–13. doi:10.1016/s0022-3115(03)00192-2
47. R Behrisch W Eckstein eds. *Sputtering by Particle Bombardment: Experiments and Computer Calculations from Threshold to MeV Energies*. Berlin, Germany: Springer-Verlag (2007).
48. Kelly R. The Surface Binding Energy in Slow Collisional Sputtering. *Nucl Instr Methods Phys Res Section B: Beam Interactions Mater Atoms* (1986) 18:388–98. doi:10.1016/s0168-583x(86)80063-5
49. Urbassek HM. Molecular-dynamics Simulation of Sputtering. *Nucl Instr Methods Phys Res Section B: Beam Interactions Mater Atoms* (1997) 122: 427–41. doi:10.1016/s0168-583x(96)00681-7
50. Kubota NA, Economou DJ, Plimpton SJ. Molecular Dynamics Simulations of Low-Energy (25-200 eV) Argon Ion Interactions with Silicon Surfaces: Sputter Yields and Product Formation Pathways. *J Appl Phys* (1998) 83:4055–63. doi:10.1063/1.367225
51. Biersack JP, Eckstein W. Sputtering Studies with the Monte Carlo Program TRIM.SP. *Appl Phys A* (1984) 34:73–94. doi:10.1007/bf00614759
52. Ziegler JF, Ziegler MD, Biersack JP. SRIM - the Stopping and Range of Ions in Matter (2010). *Nucl Instr Methods Phys Res Section B: Beam Interactions Mater Atoms* (2010) 268:1818–23. doi:10.1016/j.nimb.2010.02.091
53. Wittmaack K. Reliability of a Popular Simulation Code for Predicting Sputtering Yields of Solids and Ranges of Low-Energy Ions. *J Appl Phys* (2004) 96:2632–7. doi:10.1063/1.1776318
54. García-Rosales C, Eckstein W, Roth J. Revised Formulae for Sputtering Data. *J Nucl Mater* (1995) 218:8–17. doi:10.1016/0022-3115(94)00376-9
55. Lindhard J, Scharff M. Energy Dissipation by Ions in the Kev Region. *Phys Rev* (1961) 124:128–30. doi:10.1103/physrev.124.128
56. Charles C. Plasmas for Spacecraft Propulsion. *J Phys D: Appl Phys* (2009) 42: 163001. doi:10.1088/0022-3727/42/16/163001
57. Caughman J, Baity F, Bigelow T, Gardner W, Hoffman D, Forrester S, et al. Non-fusion Applications of Rf and Microwave Technology. In: The 11th Topical Conference on Radio Frequency Power in Plasmas; 1995 17–19 May; Palm Springs, California (USA), 355 (1996). p. 449–58.
58. Berisford DF, Bengtson RD, Raja LL, Cassady LD, Chancery WJ. Heat Flow Diagnostics for Helicon Plasmas. *Rev Sci Instrum* (2008) 79:10F515. doi:10.1063/1.2955710
59. Mulcahy JM, Browne DJ, Stanton KT, Chang Diaz FR, Cassady LD, Berisford DF, et al. Heat Flux Estimation of a Plasma Rocket Helicon Source by Solution of the Inverse Heat Conduction Problem. *Int J Heat Mass Transfer* (2009) 52: 2343–57. doi:10.1016/j.ijheatmasstransfer.2008.10.031
60. Berisford D, Bengston R, Raja L. Power Balance and wall Erosion Measurements in a Helicon Plasma, Sputtering. *Phys Plasmas* (2010) 17: 033503. doi:10.1063/1.3304184
61. Del Valle Gamboa J, Cortés S, Fonseca L, Oguilve-Araya J, Valverde J, Martínez C, et al. The VX-CR experiment: A thermal and Lifetime Testbed for the VASIMR^{TM} Engine. In: 32nd International Electric Propulsion Conference; 2011 September 11-15; Wiesbaden, Germany. IEPC-2011-155 (2011).
62. De Faoite D, Browne DJ, Del Valle Gamboa JI, Stanton KT. Inverse Estimate of Heat Flux on a Plasma Discharge Tube to Steady-State Conditions Using Thermocouple Data and a Radiation Boundary Condition. *Int J Heat Mass Transfer* (2014) 77:564–76. doi:10.1016/j.ijheatmasstransfer.2014.04.069

63. Squire JP, Carter M, Chang Diaz FR, Corrigan A, Dean L, Farrias J, et al. Steady-state Testing at 100 kW in the VASIMR® VX-200SS Project. In: AIAA Propulsion and Energy 2019 Forum; 2019 August 19-22; Indianapolis, IN, USA. (2019). p. 3810.
64. Showers M, Piotrowicz PA, Beers CJ, Biewer TM, Caneses J, Canik J, et al. Power Accounting of Plasma Discharges in the Linear Device Proto-Mpex. *Plasma Phys Control Fusion* (2018) 60:065001. doi:10.1088/1361-6587/aab7c8
65. De Faoite D, Browne D, Chang-Diaz F, Stanton K. A Review of the Processing, Composition and Temperature-dependent Mechanical and thermal Properties of Dielectric Technical Ceramics. *J Mater Sci* (2011) 47:4211–4235. doi:10.1007/s10853-011-6140-1
66. De Faoite D, Browne D, Stanton K. Regression Analysis of Temperature-dependent and thermal Properties of Dielectric Technical Ceramics. *J Mater Sci* (2012) 48:451–461. doi:10.1007/s10853-012-6759-6
67. Lee CA, Chen G, Arefiev AV, Bengtson RD, Breizman BN. Measurements and Modeling of Radio Frequency Field Structures in a Helicon Plasma. *Phys Plasmas* (2011) 18:013501. doi:10.1063/1.3533273
68. Berisford D. *Thermal Phenomena and Power Balance in a Helicon Plasma*. [Ph.D. thesis]. Austin (TX): University of Texas at Austin (2009).
69. Aanesland A, Charles C, Boswell RW, Fredriksen A. Sputtering Effects in a Helicon Plasma with an Additional Immersed Antenna. *Plasma Sourc Sci. Technol.* (2003) 12:85–8. doi:10.1088/0963-0252/12/1/311
70. Barada KK, Chattopadhyay PK, Ghosh J, Saxena YC, Bora D. Wall Charging of a Helicon Antenna Wrapped Plasma Filled Dielectric Tube. *Phys Plasmas* (2015) 22:013507. doi:10.1063/1.4906360
71. Takahashi K. Helicon-type Radiofrequency Plasma Thrusters and Magnetic Plasma Nozzles. *Rev Mod Plasma Phys* (2019) 3:1–61. doi:10.1007/s41614-019-0024-2
72. Hopwood J. Review of Inductively Coupled Plasmas for Plasma Processing. *Plasma Sourc Sci. Technol.* (1992) 1:109–16. doi:10.1088/0963-0252/1/2/006
73. Beers CJ, Green DL, Lau C, Myra JR, Rapp J, Younkin TR, et al. Rf Sheath Induced Sputtering on Proto-Mpex. I. Sheath Equivalent Dielectric Layer for Modeling the Rf Sheath. *Phys Plasmas* (2021) 28:093503. doi:10.1063/5.0054074
74. Beers CJ, Lau C, Rapp J, Younkin TR, Biewer TM, Bigelow T, et al. Rf Sheath Induced Sputtering on Proto-Mpex Part 2: Impurity Transport Modeling and Experimental Comparison. *Phys Plasmas* (2021) 28:103508. doi:10.1063/5.0065464
75. Lafleur T, Charles C, Boswell RW. Characterization of a Helicon Plasma Source in Low Diverging Magnetic fields. *J Phys D: Appl Phys* (2011) 44:055202. doi:10.1088/0022-3727/44/5/055202
76. Takahashi K, Chiba A, Komuro A, Ando A. Axial Momentum Lost to a Lateral wall of a Helicon Plasma Source. *Phys Rev Lett* (2015) 114:195001. doi:10.1103/physrevlett.114.195001
77. Takahashi K, Ando A. Enhancement of Axial Momentum Lost to the Radial wall by the Upstream Magnetic Field in a Helicon Source. *Plasma Phys Control Fusion* (2017) 59:054007. doi:10.1088/1361-6587/aa626f
78. Takahashi K, Sugawara T, Ando A. Spatially- and Vector-Resolved Momentum Flux Lost to a wall in a Magnetic Nozzle Rf Plasma Thruster. *Sci Rep* (2020) 10:1061–11. doi:10.1038/s41598-020-58022-6
79. Caneses JF, Beers C, Thakur SC, Simmonds MJ, Goulding RH, Lau C, et al. Characterizing the Plasma-Induced thermal Loads on a 200-kW Light-Ion Helicon Plasma Source via Infra-red Thermography. *Plasma Sourc Sci Tech* (2021) 30:075022. doi:10.1088/1361-6595/abf814
80. Mikellides IG, Katz I, Hofer RR, Goebel DM. Magnetic Shielding of a Laboratory Hall Thruster. I. Theory and Validation. *J Appl Phys* (2014) 115:043303. doi:10.1063/1.4862313
81. Hofer RR, Goebel DM, Mikellides IG, Katz I. Magnetic Shielding of a Laboratory Hall Thruster. II. Experiments. *J Appl Phys* (2014) 115:043304. doi:10.1063/1.4862314
82. Godyak V. On Helicon Thrusters: Will They Ever Fly? *J Appl Phys* (2020) 127:103301. doi:10.1063/1.5139998
83. Takahashi K, Charles C, Boswell RW, Takao Y, Fruchtman A, Navarro-Cavallé J, et al. Commentary: On Helicon Thrusters: Will They Ever Fly? *Front Phys* (2020) 8:277. doi:10.3389/fphy.2020.00277
84. Boyd I, Falk M. A Review of Spacecraft Material Sputtering by Hall Thruster Plumes. In: AIAA 37th Joint Propulsion Conference; 2001 July 8–11; Salt Lake City, Utah (USA) (2001). doi:10.2514/6.2001-3353
85. Eagle W, Boyd I, Trepp S, Sedwick R. The Erosion Prediction Impact on Current Hall Thruster Model Development. In: 44th AIAA/ASME/SAE/ASEE Joint Propulsion Conference & Exhibit; 2008 July 21-23; Hartford, CT. (2008). doi:10.2514/6.2008-5087
86. Shastry R, Herman D, Soulas G, Patterson M. NASA's Evolutionary Xenon Thruster (NEXT) Long-Duration Test as of 736 Kg of Propellant Throughput. In: 48th AIAA/AME/SAE/ASEE Joint Propulsion Conference and Exhibit; 2012 July 30 - August 01; Atlanta, GA. (2012). doi:10.2514/6.2012-4023
87. Gildea S, Matlock T. Martinez-sanchez WJ Mand Hargus. Erosion Measurements in a Diverging Cusped-Field Thruster. In: 32nd International Electric Propulsion Conference; 2011 September 11-15; Wiesbaden, Germany. IEPC-2011-149 (2011).
88. Del Valle Gamboa J, Castro J, Arce N, Chinchilla E, Echeverría E, Lezama D, et al. Measurement of the Dielectric wall Erosion in Helicon Plasma Thrusters: an Application to the VASIMR VX-CR experiment. In: 33rd International Electric Propulsion Conference; 2013 October 6-10; Washington, DC, USA. (2013).
89. Kajita S, Sakaguchi W, Ohno N, Yoshida N, Saeki T. Formation Process of Tungsten Nanostructure by the Exposure to Helium Plasma under Fusion Relevant Plasma Conditions. *Nucl Fusion* (2009) 49:095005. doi:10.1088/0029-5515/49/9/095005
90. Ewald HN, Crawford FW, Self SA. Steady-State Theory of an Intermediate-Pressure Discharge Column in a Magnetic Field. *J Appl Phys* (1967) 38:2753–61. doi:10.1063/1.1710000
91. Castro J, Del Valle J, Arce N, Chinchilla E, Echeverría E, Lezama D, et al. VASIMR VX-CR experiment: Status, Diagnostics and Plasma Plume Characterization. In: The 33rd International Electric Propulsion Conference; 2013 October 6-10; Washington, DC, USA. IEPC-2013-202. USA: The George Washington University (2013).
92. Zalm PC, Beckers LJ, Sanders FHM. On the Pole of Physical Sputtering in Reactive Ion Beam Etching. *Nucl Instr Methods Phys Res* (1983) 209-210:561–5. doi:10.1016/0167-5087(83)90853-0
93. Nenadovic T, Perraillon B, Bogdanov Z, Djordjevic Z, Milic M. Sputtering and Surface Topography of Oxides. *Nucl Instr Methods Phys Res B* (1990) 48:538–43.
94. Varga P, Neidhart T, Sporn M, Libiseller G, Schmid M, Aumayr F, et al. Sputter Yields of Insulators Bombarded with Hyperthermal Multiply Charged Ions. *Phys Scr* (1997) T73:307–10. doi:10.1088/0031-8949/1997/t73/100

Conflict of Interest: Authors JDV, FCD, and VG were employed by the company Ad Astra Rocket Company Costa Rica.

The remaining author declare that the research was conducted in the absence of any commercial or financial relationships that could be construed as a potential conflict of interest.

frontiers | Frontiers in Physics

TYPE Original Research
PUBLISHED 11 August 2022
DOI 10.3389/fphy.2022.950472

Check for updates

OPEN ACCESS

EDITED BY
Jayr Amorim,
Instituto de Tecnologia da Aeronáutica (ITA), Brazil

REVIEWED BY
Jon Tomas Gudmundsson,
University of Iceland, Iceland
Umair Siddiqui,
Phase Four, United States

*CORRESPONDENCE
Juan I. Del Valle,
juan@adastrarocket.com

SPECIALTY SECTION
This article was submitted to Low-Temperature Plasma Physics, a section of the journal Frontiers in Physics

RECEIVED 22 May 2022
ACCEPTED 05 July 2022
PUBLISHED 11 August 2022

CITATION
Del Valle JI, Granados VH and Chang Díaz FR (2022), Estimation of erosion phenomena within helicon plasma sources through a steady-state explicit analytical model.
Front. Phys. 10:950472.
doi: 10.3389/fphy.2022.950472

Estimation of erosion phenomena within helicon plasma sources through a steady-state explicit analytical model

Juan I. Del Valle [1,2]*, Víctor H. Granados [2,3] and Franklin R. Chang Díaz [1]

[1]Ad Astra Rocket Company Costa Rica, Liberia, Costa Rica, [2]Doctorado en Ciencias Naturales para el Desarrollo (DOCINADE) Program, Instituto Tecnológico de Costa Rica, Universidad Nacional de Costa Rica, Universidad Estatal a Distancia de Costa Rica, San Carlos, Costa Rica, [3]Universidad Nacional de Costa Rica, Heredia, Costa Rica

Helicon plasma sources produce high-density discharges without the need of electrodes in direct contact with the plasma, which is thought to provide them with long operational lifetimes. An explicit steady-state analytical model is described with the capability of depicting the 2D plasma density distribution, the sheath potentials and the estimated sputtering and etch rates along the plasma-facing components of the source. The individual constituting submodels are fitted against available experimental data, and the model is used to predict erosion rates within the VX-CR research helicon plasma source. Erosion within these components is dependent on the value of plasma density along the boundaries, the electron temperature and the particular ion-target material combination. The highest erosion rates are found along the upstream system boundary, followed by the regions near the helicon antenna straps where a capacitive RF sheath is formed. The assumptions and limitations of the model are discussed, and future improvements are proposed.

KEYWORDS

helicon plasma, erosion, sputtering, model, etching

1 Introduction

The use of helicon plasma sources (HPSs) [1] within different research and practical applications has gained traction because of their ability to produce high-density plasmas at low power levels and magnetic field intensities, and their capability to dissipate energy into the plasma deeper than other technologies such as capacitively-coupled (CC) or inductively-coupled (IC) discharges. Helicon sources have found usage within the materials processing industry, in electric propulsion devices, as ion sources for fusion systems, and within facilities researching the interactions between plasmas and materials at fusion-relevant conditions.

One of the claimed advantages of HPSs is the fact that the discharge is driven by radiofrequency (RF) waves emitted from an external helical antenna which does not contact the plasma directly, thereby discarding any damage to it as a potential failure mode. The erosion of electrodes and grids facing the plasma discharge is one of the key lifetime-limiting factors in practical devices relying on other plasma-generation techniques, and HPSs are therefore expected to exhibit long-lasting operational regimes. The presence of axial magnetic fields within HPSs also contributes to confine the plasma and reduce its diffusion towards the material boundaries. However, the erosion of these internal plasma-facing components due to the contact with the discharge has not been widely investigated in order to accurately estimate its effects. As these sources find their way into ever larger and more powerful devices, clearly understanding their limitations becomes key to the engineering of reliable and robust devices.

In a previous paper [2], we have contributed a review of this topic and the different phenomena involved in its analysis, and described past published work addressing erosion phenomena within HPS. Among those, Berisford et al. [3] conducted experimental measurements of the etching phenomena on the inside of a quartz tube used as dielectric boundary in a helicon source. They identified the voltages induced by the helicon antenna on the inner surface of the HPS dielectric cylindrical boundary as a key erosion mechanism, and correlated their predictions with experimental measurements to within an order of magnitude. Their work relied on simplified formulas for the sputtering of elemental targets by energetic ions and low-frequency RF sheaths, adapted for their particular HPS. Barada et al. [4] and Thakur et al. [5] also confirmed the relevance of this capacitive coupling phenomena in the regions near the location of the antenna straps. Recent work by Beers et al. [6, 7] developed a combined model integrating a finite-element simulation of the RF discharge, an ad-hoc sheath model and a transport code to estimate erosion and deposition rates in high-power deuterium discharges from the Proto-MPEX experiment, which were then compared to experimental measurements. Their approach to sputtering simplified the actual aluminum nitride (AlN) boundaries as pure aluminum, given their observations of aluminum enrichment in the surface after experimental runs. Their simulation provides an accurate and detailed prediction of sheath potentials, sputtering and deposition phenomena, and impurity transport within the HPS; its disadvantage is the complexity involved in the convergence of discrete 3D codes.

In the present work, we describe the development and validation of a modeling tool for the estimation of sputtering and etch rates within the plasma-facing components of a HPS. It combines individual analytical modules for analyzing the 2D distribution of plasma density within the source, the voltages produced by the sheaths in different regimes, and the sputtering phenomena and associated etching. The 2D plasma description and the sheath models adapt fluid-dynamic models previously published in the literature, while the sputtering package is also based on adapted empirical expressions developed to match available experimental data. The sputtering model was extended to provide the ability of simulating compound target materials. The combined model aims to simplify the estimation of average and peak erosion rates within HPSs, with the goal of providing a flexible tool that can be used to predict the performance of a particular device, to develop general erosion mitigation techniques for HPSs in general, and for the engineering analysis of practical helicon implementations.

This paper is organized as follows. Section 2 describes the individual components which form part of the simulation package. Section 3 describes the validation of each individual submodel against publicly-available experimental data sets; as well as the application of the combined tool to a particular HPS, the VX-CR device at Ad Astra Rocket Company Costa Rica. Section 4 analyzes these results and discusses the assumptions and limitations underlying the model, and section 5 summarizes the main findings of this work.

2 Mathematical models

This section describes the first-principle models underlying the implementation of the analysis tools developed for the investigation of erosion phenomena within helicon plasma sources.

Figure 1A) presents an idealized diagram of a helicon plasma source (HPS), showing its main components in a typical cylindrical configuration, as well as the coordinate system defining the simulation domain. Figure 1B), reproduced from [2], describes the two main modes of erosion phenomena within the plasma-facing components of HPSs, as described in the literature.

The models presented in the following subsections are independent of the particular ion species present in the plasma, although they do assume the discharge is produced with a single gas (not a mixture of gasees), which is singly-ionized (a typical case in most low-temperature helicon sources).

2.1 Dispersion relation for helicon waves

Helicon waves fall into the category of right-hand polarized (RHP) plasma waves, which propagate along constant magnetic fields in bounded systems. They are related to atmospheric whistler waves, and typically appear in the frequency range $\omega_{ci} \ll \omega \ll \omega_{ce}$, where ω is the excitation frequency and ω_{ci} and ω_{ce} are, respectively, the ion and electron cyclotron frequencies for the given configuration.

A description of the relation dispersion describing helicon plasma waves can be obtained from Maxwell's equations, applying the cold plasma approximation (non-thermal ions)

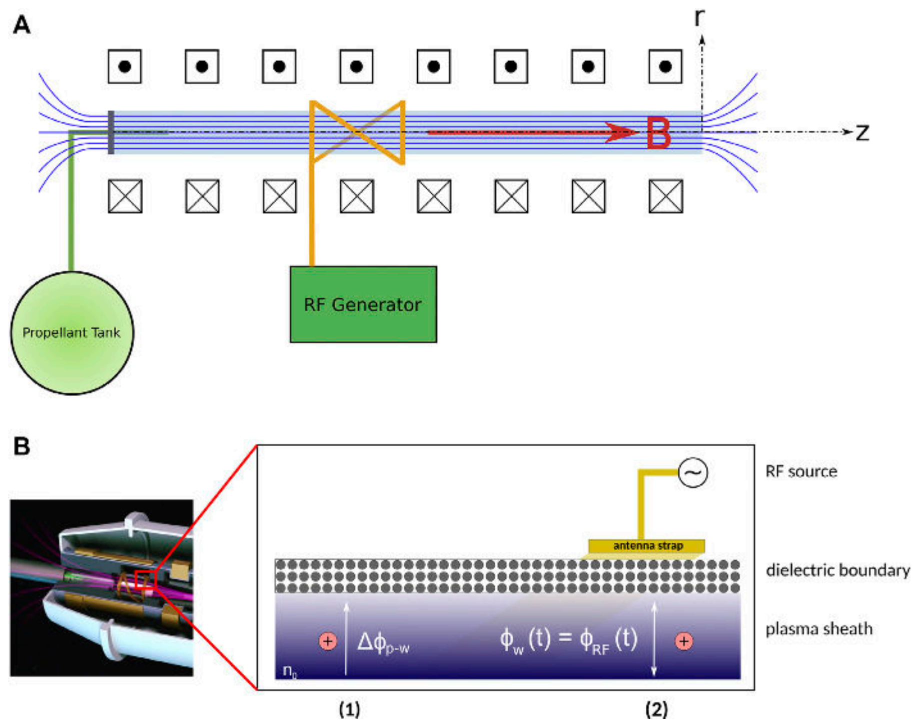

FIGURE 1
(A) A simplified diagram of a Helicon Plasma Source (HPS). **(B)** A representation of the main mechanisms of erosion present in Helicon Plasma Sources, reproduced from [2]. Region (1) describes the acceleration of ions towards the inner confinement surfaces due to the DC sheath and the floating negative potential present at the surface. Region (2) describes the acceleration of the ions due to the present of an external source of RF excitation, such as the terminals of the antenna used to excite the plasma discharge.

and neglecting the displacement current, as shown in detail by Chen and Arnush [8–10].

When electron inertia is retained in the derivation, the total wave number β of the wave is defined by

$$\beta_{1,2} = \frac{k}{2\delta}\left[1 \mp \left(1 - \frac{4\delta k_\omega^2}{k^2}\right)^{1/2}\right] \approx \frac{k_\parallel}{2\delta}\left[1 \mp \left(1 - \frac{2\delta k_\omega^2}{k_\parallel^2}\right)\right] \approx \begin{cases} k_\omega^2/k_\parallel \\ k_\parallel/\delta \end{cases} \tag{1}$$

where θ is the angle of propagation of the wave with respect to the constant, axial magnetic field $\mathbf{B} = B_0\hat{\mathbf{e}}_\mathbf{z}$, with components parallel and perpendicular to $\mathbf{B}$: $\beta^2 = k_\parallel^2 + k_\perp^2$, where $k_\parallel = \beta\cos\theta$ and $k_\perp = \beta\sin\theta$. The ratio $\delta = \omega/\omega_{ce}$ is the ratio between the wave frequency and the electron cyclotron frequency $\omega_{ce} = eB_0/m_e$, and $k_\omega^2 = \omega\omega_p^2/\omega_{ce}c^2 = \omega n_0 e\mu_0/B_0 \equiv \beta k_\parallel$ is the wavenumber for low-frequency whistler waves along B_0 in free space.

The first solution to Eq. 1, β_1, corresponds to the helicon or *H* mode obtained in the zero electron mass limit, when electron inertia is neglected. Solution β_2 corresponds to the Trivelpiece-Gould or *TG* mode, an electron cyclotron wave propagating at an angle to the magnetic field and a relevant damping mechanism in helicon plasma sources, particularly at low values of B_0.

The expression for the *H* mode β_1 can be expanded as

$$\beta_1 = \frac{\omega}{k_\parallel}\frac{n_0 e\mu_0}{B_0} = \frac{\omega}{\beta_1\cos\theta}\frac{n_0 e\mu_0}{B_0} \tag{2}$$

where n_0 corresponds to the electron density of the plasma where the wave is propagating, with e the electron charge and μ_0 the permeability of free space.

The previous equation provides a means to estimate the maximum value of the expected plasma density for a given helicon device as a function of the axial magnetic field intensity B_0, for given values of the excitation frequency ω, the parallel wave number $k_\parallel$ and the angle θ between the wave propagation vector and B_0. These last parameters can be determined through the source's RF subsystem and the antenna geometry.

For the typical scenario of a helicon plasma source of cylindrical geometry of radius R and exciting mode $m = 1$, the previous equation can be simplified [8, 11] to

$$n_0 = \left(\frac{p_0 k_\parallel}{R\omega e\mu_0}\right)B_0 \tag{3}$$

10.3389/fphy.2022.950472

where p_0 is the lowest root of the Bessel function of the first kind and order 0 ($J_1(p_0) = 0$, with $p_0 \approx 3.83$).

The actual distribution of plasma density within practical helicon plasma sources is seldom uniform, yet this expression enables the estimation of a reference value for the expected peak plasma density, which can be used with the subsequent models when describing the variation in all relevant plasma parameters.

2.2 2D fluid description of cylindrical magnetized plasmas in steady-state

The description of the plasma behavior within a helicon plasma source is provided by a 2D, two-fluid description of cylindrical plasmas in the presence of an axial magnetic field using the cylindrical coordinate set (r, θ, z). The chosen model is an implementation of the asymptotic magnetized regime proposed by Ahedo and Navarro-Cavallé [12], which describes a quasineutral, isothermal plasma with azimuthal symmetry and where the ion temperature is much lower than the electron temperature, $T_i \ll T_e$. The model is based in a series of assumptions and simplifications, including: steady-state, azimuthal symmetry, cold neutrals whose velocity u_n and density distribution n_n only depend on the axial position, longitudinal ambipolarity where the axial and radial velocities of ions and electrons are constant ($u_{iz} = u_{ez}$ and $u_{ir} = u_{er}$) and the ion azimuthal velocity is negligible $u_{i\theta} \ll u_{e\theta} = u_\theta$, among others chosen by the authors.

The model is described by a set of radial and axial equations. The radial submodel describes the behavior of the plasma at a given axial location z. The ratio between the plasma density n_r and its value at the cylinder axis $n_r(z, 0)$ can be described by the expression

$$\frac{n_r(z,r)}{n_r(z,0)} = J_0\left(a_0\frac{r}{R}\right) \tag{4}$$

where r is the radial coordinate, R is the maximum radius of the cylindrical plasma discharge, n_r is the quasineutral plasma density, J_0 is the Bessel function of the first kind of order 0 and $a_0 \approx 2.405$ is the first zero of J_0.

The radial component of the ion and electron velocity u_r is normalized by the ion sound speed $c_s = \sqrt{eT_e/m_i}$ and can be expressed as

$$\frac{u_r}{c_s} = a_0\left(\frac{\nu_e\omega_r}{\omega_{lh}^2}\right)\left[\frac{J_1(a_0 r/R)}{J_0(a_0 r/R)}\right] \tag{5}$$

where the term $\nu_e = \nu_{en} + \nu_{ei} + \nu_{ion}$ is a linear combination of the electron-neutral ν_{en} and electron-ion ν_{ei} collision frequencies as well as the ionization frequency ν_{ion}, $\omega_r = c_s/R$ is the radial transit frequency; $\omega_{lh} = eB_0/\sqrt{m_e m_i}$ is the lower-hybrid frequency and J_1 is the Bessel function of the first kind of order 1. The collision rates composing the term ν_e can be approximated as a function of T_e, as described in [12].

The electron azimuthal velocity u_θ is normalized by the electron thermal velocity $c_e = \sqrt{eT_e/m_e}$ and is described by the expression

$$\frac{u_\theta}{c_e} = (u_r/c_s)(\omega_{lh}/\nu_e). \tag{6}$$

Boundary conditions for the radial model preclude null plasma velocities and plasma potential $u_r = u_\theta = \phi_p = 0$, and a known plasma density $n(z, r) = n(0, r)$ at the cylinder axis $r = 0$. At the $r = R$ physical boundary, the Bohm sheath criterion states that $u_r(z, R) = c_s$.

The axial submodel describes the plasma parameters at the $r = 0$ coordinate as a function of the axial coordinate z. For the limit of large T_e, large B_0 and with ideal plasma recombination at the system physical boundaries (producing neutrals with the same axial velocity u_n), the ideal asymptotic model from Ahedo et al. [12] can be applied.

The axial neutral velocity u_n remains constant throughout the source,

$$u_n = u_{n0}. \tag{7}$$

The axial velocity of both ions and electrons, u_z, is normalized by the ion sound velocity c_s and defined in terms of the auxiliary variable ξ as follows

$$u_z/c_s = \tan\xi. \tag{8}$$

The plasma density n is described by the following expression

$$n/n_0 = 2\eta_u \cos^2\xi \tag{9}$$

where $n_0 = g_0/c_s$ is a reference plasma density, g_0 is the axial flow of heavy species (ions + neutrals) at the upstream boundary of the source $g_0 = \dot{m}/(m_i\pi R^2)$, $\dot{m}$ is the input mass flow to the system, and m_i is the mass of the ions. The parameter $\eta_u = n_{z=0}/n_0$ is the propellant utilization defined as the ratio between the plasma density at the downstream open boundary of the system, $n_{z=0}$, and n_0.

The axial neutral density n_n is defined as

$$n_n/n_{n0} = 1 - \eta_u \sin 2\xi \tag{10}$$

where $n_n0 = g_0/u_{n0}$ is a reference neutral density.

The axial variation of the auxiliary variable ξ is defined implicitly by the integral expression

$$\frac{z+L}{L_\star} = \int_{-\pi/4}^{\xi}\frac{1-\tan^2\xi'}{1-\eta_u\sin 2\xi'}d\xi' \tag{11}$$

where L is the axial length of the simulation space, $L_\star = c_s/(R_{ion}n_{n0})$ is an effective ionization mean free path, and R_{ion} is the ionization collision rate. An expressions for R_{ion} as a function of T_e is provided in [12].

The boundary conditions for the axial model include the given known values for the following parameters at both the upstream boundary $z = -L$ and the downstream exit plane $z = 0$: a given value for the flow of neutrals into the system, g_0; the reference neutral axial velocity $u_n(r, -L) = u_{n0}$; and the plasma velocity equal to the Bohm velocity at both the upstream and downstream axial boundaries, $u_z(r, -L) = -c_s$ and $u_z(r, 0) = c_s$. Setting $z = 0$ and $\xi = \pi/4$ in Eq. 11 defines the propellant utilization η_u as an implicit function of the ratio $L/L_\star$.

2.3 Sheath models

In the region where the plasma contacts a physical material boundary, the quasineutrality of the bulk discharges is broken due to the buildup of charge at the surface. This region is called a sheath, and its properties depend on both the parameters of the plasma as well as the material surface. The scale of the sheath is in the order of the Debye length, $\lambda_D = (\epsilon_0 T_e/en_0)^{1/2}$, and is typically much smaller than the characteristic dimensions of practical laboratory plasmas.

The transition between the bulk plasma and the material surface occurs through different regions or regimes. Prior to the actual sheath, the *pre-sheath* is located, where the plasma density and potential decrease but quasineutrality is still preserved. At the point where the sheath begins, the Bohm sheath criterion must be met, $u_i \geq c_s$. Within the sheath, quasineutrality breaks and the electron density decreases rapidly towards zero. The potential at the material wall Φ_w is therefore lower than the bulk plasma.

For the case of a floating dielectric material immersed into the plasma, the potential obtained at the wall can be described [13] as

$$\Phi_w = -T_e \ln \sqrt{\frac{m_i}{2\pi m_e}}. \tag{12}$$

It is a function of constant properties of the plasma species (the ion and electron masses, m_i and m_e), and the electron temperature T_e expressed in units of electric potential. Under the assumption that $T_i \approx 0$, ions entering the sheath will be accelerated towards the wall due to the potential difference $\Phi_p - \Phi_w$, where Φ_p is the plasma potential.

Other conditions could be present in the boundary material, such as grounded or biased surfaces at a potential Φ_{bias}, in which case the analysis would need to take into account the effect of the potential difference $\Phi_p - \Phi_{bias}$ in the acceleration of the ions.

For the case where radiofrequency (RF) waves are present near the interface of plasmas and materials, such as near the location of the antenna straps providing the excitation source in helicon plasma sources, an *RF plasma sheath* is created. When the driving RF frequencies are sufficiently high ($\omega_{rf} \gg \omega_{pi}$, with $\omega_{pi}^2 = (e^2 n_0)/(\epsilon_0 m_i)$ the ion plasma frequency), the ions are able to respond only to the time-averaged variations in the DC plasma potentials and not the instantaneous RF wave. The electrons in the bulk plasma are able to react to the RF wave potentials, yet most of the current in the sheath is displacement current, given its low electron density.

When the frequency of the RF wave is low enough, ions are able to respond to the RF wave and a *low frequency sheath* is formed. This condition requires that $\omega \ll \omega_i = \pi\omega_{pi}(2T_e/V_0)^{1/4}$, with V_0 the transient voltage of the RF wave [13]. During the RF cycle, the ions will be accelerated towards the surface due to the time-varying potential.

The ion energy distribution function $g_i(E)$ for a low-frequency RF sheath [13] is given by the expression

$$g_i(E) = \begin{cases} \dfrac{1}{\pi}\left[V_{rf}^2 - (V_{bias} - E)^2\right]^{-1/2} & E \neq V_{bias} \\ \dfrac{1}{2\pi}\left[\pi - 2\sin^{-1}\left(V_{bias}/V_{rf}\right)\right] & E = V_{bias} \end{cases} \tag{13}$$

where V_{rf} is the peak voltage amplitude of the RF wave, V_{bias} is any DC bias voltage applied to the surface, and E is the instantaneous voltage of the RF field. The distribution has a different expression for the case $E = V_{bias}$, to take into account the rectifying effect of the low-frequency sheath.

2.4 Sputtering phenomena

Plasma-surface interactions include all the phenomena that appear at the intersection between plasmas and a material boundary. Among those, sputtering is of significant interest to the fields of materials processing, fusion engineering and electric space propulsion. Sputtering is the removal of material from a solid surface due to the impact of energetic particles, and it plays a fundamental role in determining the lifetime of practical devices.

Sputtering depends on several parameters, including the properties of the impinging particles, the composition of the target material surface and the geometry of the impact. A simplified model for the geometry of the sputtering process [2] describes the incoming ion being accelerated by the potential drop on the sheath to an energy E_0 until it impacts the surface with an angle θ with respect to the surface normal. If the energy surpasses a threshold level for the occurrence of sputtering, $E_0 > E_{thr}$, a cascade of collisions within the target material will be able to provide sufficient momentum to one or several particles in the top layer of the target material, and allow them to overcome the surface binding energy E_{sb} and leave the surface.

Sputtering is described by the sputtering yield Y, defined as the number of surface particles sputtered from the target material surface per incoming ion. It depends on the properties of the impacting ion and the target material, the energy of the ion and the angle of incidence. Several models have been developed for the estimation of actual sputtering yields; the model chosen for this study is the one published by Eckstein and Preuss [14], which improves upon earlier work.

The sputtering yield Y when ions impact a surface at normal incidence ($\theta = 0$) is obtained with the expression

$$Y(E_0) = q s_n^{KrC}(E_0) \frac{\left(\frac{E_0}{E_{thr}} - 1\right)^{\mu}}{\lambda + \left(\frac{E_0}{E_{thr}} - 1\right)^{\mu}}. \tag{14}$$

It depends on three free parameters (q, λ and μ) used to fit the model to experimental data. Behrisch and Eckstein [15] have tabulated these parameters for a significant selection of sputtering scenarios involving monoatomic elemental targets. The term s_n^{KrC} is the krypton-carbon interaction potential,

$$s_n^{KrC}(\varepsilon) = \frac{0.5 \ln(1 + 1.2288\varepsilon)}{\varepsilon + 0.1728\sqrt{\varepsilon} + 0.008\varepsilon^{0.1504}} \tag{15}$$

which is used as an adequate mean value to describe the nuclear stopping cross section for the problem, for any combination of ion species and target materials (not necessarily involving carbon or krypton). The term ε is the reduced potential, which is calculated as

$$\varepsilon = E_0 \frac{M_t}{M_i + M_t} \frac{a_L}{Z_i Z_t e^2} \tag{16}$$

and depends on the parameter a_L, the Lindhard screening length,

$$a_L = \left(\frac{9\pi^2}{128}\right)^{1/3} a_B \left(Z_{ion}^{2/3} + Z_{tar}^{2/3}\right)^{-1/2} \tag{17}$$

where a_B is the Bohr atomic radius.

When the ion impact occurs at an angle, $0 < \theta \leq \pi/2$, Y can be described by the expression

$$Y(E_0, \theta) = Y(E_0, 0) \left\{\cos\left[\left(\frac{\theta}{\theta_0} \frac{\pi}{2}\right)^c\right]\right\}^{-f} \exp\left\{b\left(1 - \frac{1}{\cos\left[\left(\frac{\theta}{\theta_0}\frac{\pi}{2}\right)^c\right]}\right)\right\}. \tag{18}$$

It depends on the parameters b, c and f, which have also been tabulated in [15] for a variety of common scenarios.

The parameter θ_0 is calculated according to the expression

$$\theta_0 = \pi - \arccos\sqrt{\frac{1}{1 + \left(E_0 / E_{sp}\right)}} \geq \frac{\pi}{2} \tag{19}$$

where E_{sp} corresponds to the surface binding energy of the impacting ions; it is equal to the surface binding energy of the projectiles in the case of self bombardment, $E_{sp} = 0$ for noble gas ions impacting on the target, and $E_{sp} \approx 1$ eV for ions of the hydrogen isotopes [14].

2.5 Implementation

The models described in the previous subsections were implemented as an object-oriented (OOP) toolkit in the Python programming language (version 3.9), with extensive use of routines from the NumPy and SciPy packages. The OOP approach enables a modular design, which allows for the substitution of a particular submodel with an alternative version. The approximate running time for the sensitivity analysis simulations presented in Figures 9, 10 is less than 5 min, on a PC computer having quad-core Intel Core i5-5200 CPU at 2.20 GHz, 8 GB of RAM and running the Debian GNU/Linux operating system.

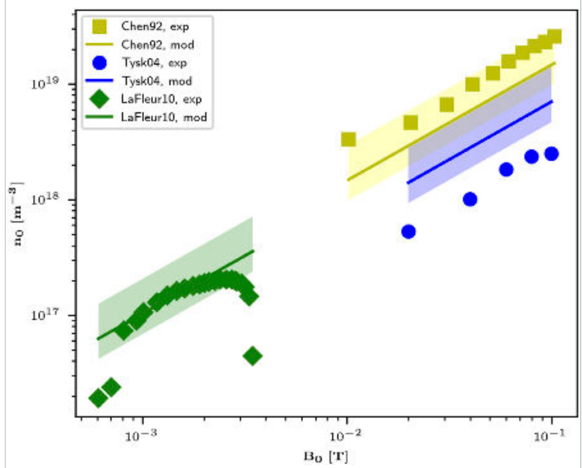

FIGURE 2
Comparison between the estimations provided by the helicon wave dispersion relation of Eq. 1 and experimental data published by Chen ([16]), [17] and [18]. The shaded regions correspond to variations in the estimation of n_e when considering the uncertainty in the estimation of λ, taken as $\pm$ 50%.

3 Results

3.1 Model validation

In order to adjust the parameters in the models described in Section 2 and to verify the accuracy of their estimations, publicly-available experimental data from a variety of suitable HPSs has been used for comparison. The chosen experimental data sets match the assumptions and configurations required by each submodel, and sufficient detail has been disclosed regarding the relevant physical and geometrical parameters of the source, enabling the use of the different mathematical expressions.

Figure 2 presents the estimations of n_e provided by Eq. 3 of Section 2.1 as a function of the axial magnetic field B_0, together with experimental data published by Chen [16], Tysk et al. [17] and LaFleur et al. [18]. The parameters obtained for these three validation cases of Figure 2 are listed in Table 1. The chosen data sets are all helicon devices tested with argon gas, using Boswell-

TABLE 1 Experimental parameters obtained for the data sets of Figure 2, used for the validation of the simplified helicon wave dispersion model of Eq. 3.

	Chen, 1992 [16]	Tysk, 2004 [17]	LaFleur, 2010 [18]
Ion species	Ar^{+}	Ar^{+}	Ar^{+}
L_{ant} (m)	0.12	0.12	0.1
λ (m)	0.24	0.24	0.2
$k_{\parallel}$ (rad/m)	26.18	15.71	31.42
R (m)	0.02	0.05	0.068
f ($\times 10^{6}$ Hz)	27.12	13.56	13.56
ω ($\times 10^{7}$ rad/s)	17.04	8.52	8.52

type double saddle antennas or half-helical antennas, which preferentially excite wavelengths of twice their lengths, $\lambda \approx 2 \times L_{ant}$. The parallel angular wave number $k_{\parallel}$ of Eq. 3 is then obtained as $k_{\parallel} = 2\pi/\lambda$. This estimation is only an approximation, and Figure 2 shows the range of estimated density values accounting for variations in the wavelength λ of ±50% as suggested by Light and Chen [19]. The linear relationship between n and B_0 present in all experimental data sets is closely matched by the model estimations, particularly for the Chen and LaFleur data sets.

The two separate fluid-models described in Section 2.2 are compared to experimental measurements in Figures 3, 4. The chosen versions of these models are the asymptotic, magnetized regimes. For the case of the radial model [12, 20], Figure 3 shows the normalized radial profile of the plasma density, compared to experimental data from the CSDX device published by Burin et al. [21], from the VX-CR device by Castro et al. [22] and from the PISCES-RF device by Thakur et al. [5, 23], from experimental runs using argon gas as the feedstock in all cases. The published experimental parameters obtained from these experimental data sets are described in Table 2. The reference plasma density n_{r0} is obtained from the peak density value at $r = 0$. In the case of the VX-CR device, the radial coordinates of the published density values in [22] have been adjusted to account for the expansion of the magnetic field lines (and the plasma plume) as they exit the HPS towards the point of measurement. As described by the original authors, the magnetized version of this radial model describes a slow decay of the radial plasma density, which falls rapidly near the radial boundary of the HPS; the experimental data confirms this behavior, with only the VX-CR data approximating the estimated trend. For the purposes of this research, the fact that this magnetized regime of the radial model may overestimate the plasma density near the surface boundary, allows for a more conservative estimation of the boundary etch rates.

The validation of the axial model of Eqs 7–11 with experimental data is presented in Figure 4, where the on-axis

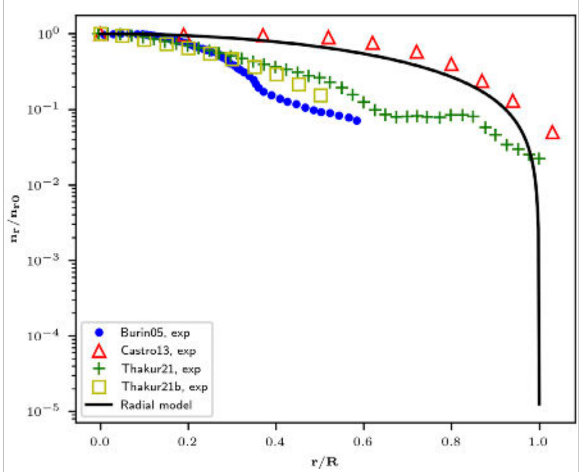

FIGURE 3
Comparison of the radial plasma density distribution estimated by Ahedo's radial model [12, 20] and experimental data published by Burin et al. [21], Castro et al. [22], and Thakur et al. [5, 23].

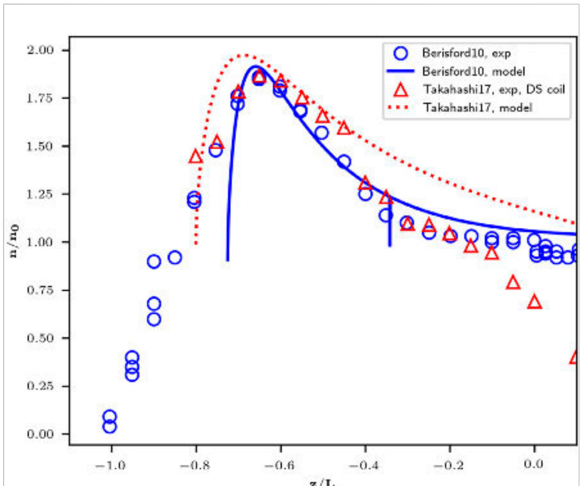

FIGURE 4
Comparison of the distribution of the on-axis plasma density as estimated by Ahedo's axial model [12] and experimental data published by Berisford et al. [3] and Takahashi et al. [24].

plasma density is presented as a function of the axial position inside the cylindrical dielectric containment surface. The experimental data sets are those published by Berisford et al. [3] and Takahashi et al. [24], which once again correspond to experiments running on argon gas. The source parameters used in the estimation are listed in Table 3. It was found that the axial model was able to predict the behavior of the axial density profile,

10.3389/fphy.2022.950472

TABLE 2 Experimental parameters obtained for the validation data sets of Figure 3, used for the validation of Ahedo's radial model in the magnetized case [20, 12], as shown in Eqs 4–6.

	Burin, 2005	Castro, 2013	Thakur, 2021	Thakur, 2021b
	[21]	[22]	[5]	[23]
Ion species	Ar^{+}	Ar^{+}	Ar^{+}	Ar^{+}
T_e (eV)	2.25	4.0	5.0	3.50
n_0 ($\times 10^{19}$ m^{-3})	2.35	0.388	2.45	1.93
R_0 (m)	0.1	0.045	0.1	0.1
B_0 (T)	0.1	0.1	0.09	0.09

TABLE 3 Experimental parameters obtained for the data sets used in Figure 4, for the validation of Ahedo's axial model in the asymptotic case [12].

	Berisford, 2010	Takahashi, 2017
	[3]	[24]
Ion species	Ar^{+}	Ar^{+}
L (m)	0.4	0.2
Δz (m)	−0.1	0.2
T_e (eV)	3.8	6.0
B_0 (T)	0.06	0.03
n_0 (m^{-3})	1.0×10^{19}	8.0×10^{17}

but an axial displacement $\Delta z = z_{\mathrm{exp}} - z_{\mathrm{mod}}$ was required to match the experimental data, where z_{exp} and z_{mod} are, respectively, the experimental axial coordinates and the ones used for the model calculations. The reference plasma density n_0 is obtained as the asymptotic on-axis density at the downstream boundary of the simulation domain (at the coordinate $z = 0$ following the convention of [12]). At this location, the Bohm criterion ($u_{z=0} = c_s$) is imposed as a boundary condition, setting the auxiliary variable $\xi = \pi/4$ according to Eq. 8. As the optimization process described for Eq. 11 when $z = 0$ converges to values $\eta_u \rightarrow 1$ for these two configurations (complete propellant utilization) Eq. 9 will tend towards a maximum value of 2 for the ratio n/n_0, which corresponds to the peak on-axis density and can be verified in the experimental data sets.

The sputtering model from [14] is compared to experimental data in Figure 5, for the particular case of argon ions impacting SiO_2 [13, 25–27], Al_2O_3 [13, 26] and Si_3N_4 [25] target materials. The sputtering yield is presented as a function of incident ion energy. These materials were chosen as they are some of the most widely used in the construction of practical HPSs, including the VX-CR device analyzed in the next subsection. Eckstein's model, as described by Eqs 14–18, is designed to model the interaction between elemental ions and surface materials. The fitting parameters available in the literature for these equations [15] only account for this type of target materials. Therefore, some of the required parameters were obtained by averaging the values of the constituting elements of the compound materials, following a technique originally proposed by Berisford et al. [3] when applying the particular sputtering model presented in [13]. Table 4 lists the parameters chosen to represent these compound materials. The atomic number Z_t, the atomic mass m_t and the surface binding energy SBE_t for each compound target material were found as a simple arithmetic average between the values corresponding to the two constituent elements in the lattice. *SBE* data was obtained from [13]. The threshold energy, a key parameter in the analysis of low-temperature devices such as typical laboratory HPSs, was selected as the corresponding value

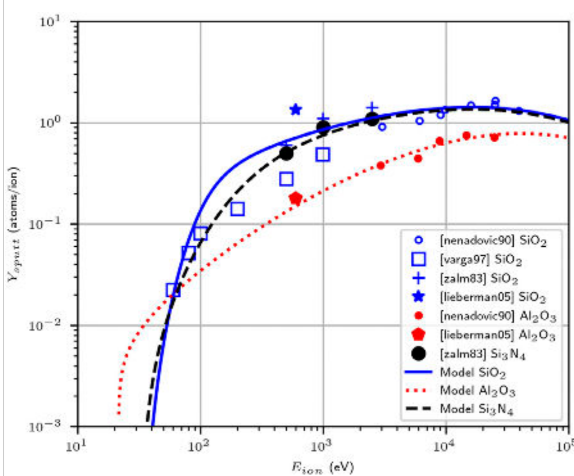

FIGURE 5
Estimation of the sputtering yield at normal incidence for argon ions impacting on different dielectric ceramic materials commonly used in HPSs, obtained from the model presented in Section 2.4. The fitting parameters used are those described in Table 4. The estimations are compared to the available experimental data points published for SiO_2 [13, 25–27], Al_2O_3 [13, 26] and Si_3N4 [25].

TABLE 4 Fitting parameters chosen to represent SiO_2, Al_2O_3 and Si_3N_4 within the sputtering estimation models presented in Figure 5. The values for the material properties and the fitting parameters were obtained through a combination of averaging and optimization techniques, as described in subsection 3.1.

	SiO_2	Al_2O_3	Si_3N_4
Z_t	11.0	10.5	10.5
m_t (amu)	22.042	21.485	21.045
SBE_t (eV)	3.653	3.36	4.811
E_{thr} (eV)	32.8380	21.55	32.838
ρ (kg/m^3)	2,648	3,987	3,170
λ	7.417	14.553	10.0
q	3.636	3.373	3.4777
μ	2.339	0.397	1.363

for argon atoms in normal incidence on pure *Si* in the case of SiO_2 and Si_3N_4, and that of pure *Al* for the case of Al_2O_3 [15]. The remaining fitting parameters λ, q and μ were obtained through a least-squares optimization algorithm.

3.2 Analysis and investigation of the VX-CR HPS

The VX-CR experiment [22, 28] is a research helicon plasma source (HPS) located at Ad Astra Rocket Company Costa Rica, designed for the study of thermal management and component lifetime issues in the first stage of the VASIMR® [29] engine. Figure 6A shows a simplified diagram of its operating configuration. It consists of a dielectric ceramic cylinder enclosed in a high vacuum chamber with a base pressure of 1.3×10^{-4} Pa. One end of this cylinder is sealed with a dielectric ceramic endcap, with openings to allow the injection of gas into the HPS. This cylinder is surrounded by a half-wavelength helical copper antenna, driven by an external RF subsystem able to deliver up to 13 kW$_e$ of radiofrequency energy to the plasma discharge. The open end of the dielectric cylinder is connected to a 14 m^3 exhaust vacuum chamber (not shown in Figure 6), with a baseline pressure of 1.3×10^{-1} Pa. An axial magnetic field is created through two solenoid coils, with the resulting magnetic field intensity profile depicted in Figure 6B. The dielectric boundary surfaces in the VX-CR are at a floating electric potential; this is not always the case for all HPSs, as these elements can be grounded [3] or biased to a particular voltage. Argon is the feedstock gas used in typical operations with the VX-CR and was used in the simulated results described in this subsection.

The models described in Section 2 and validated in Section 3.1 were used to estimate the erosion rates due to plasma-material interaction in the VX-CR device. Table 5 shows typical geometrical and operational parameters characteristic of experimental runs at the VX-CR device, at RF power levels between 1 kW$_e$ and 4 kW$_e$ and using argon gas. The three ceramic materials which have been used for the dielectric components of the device (the cylinder and its boundary endcap) are silicon dioxide (SiO_2), alumina (Al_2O_3) and silicon nitride (Si_3N_4). Figure 7A presents experimental measurements of the peak RF voltages at the helicon antenna straps as a function of the delivered RF forward power to the system; Figure 7B (adapted from [22]) describes estimations of the electron temperature T_e obtained from Langmuir probe data, also as a function of RF forward power.

Figure 8 shows the distribution of normalized plasma density inside the VX-CR HPS, as predicted by the models described in Section 2.2 for the scenario with $T_e = 5$ eV. A base density of $n_0 \approx 4.04 \times 10^{18}$ m^{-3} is predicted. The maximum estimated plasma density corresponds to $n_{\max} \approx 8.19 \times 10^{18}$ m^{-3}, while the mean plasma density is $n_{\mathrm{avg}} \approx 3.04 \times 10^{18}$ m^{-3}.

The estimated plasma density values shown in Figure 8 were used to obtain the approximate values along the upstream axial ($\hat{z} \to -1$) and radial ($\hat{r} \to 1$) boundaries of the dielectric cylinder. The radial and axial resolutions used in this particular simulation, Δr and Δz, are shown in Table 5; although they exceed the Debye lengths present in both simulation boundaries, the density values obtained along these regions, $n_{\hat{z}\to-1} = n_r[\hat{r}, \hat{z} = -1 + (\Delta z/L)]$ and $n_{\hat{r}\to1} = n_r[\hat{r} = 1 - (\Delta r/R), \hat{z}]$, have been used as reference values for the plasma density at these inner surfaces.

These density estimations along the radial and axial boundaries were used to calculate the etch rates along these surfaces due to the potential created at the wall by the sheath. The electron temperature T_e was used as an input to Eq. 12 in order to estimate the potential developed by the inner surfaces, under the assumption that they are floating (isolated from any induced voltages, as is the case in the VX-CR device). Under the cold ion approximation, this potential is taken as the energy obtained by the ions as they traverse the sheath. The sputtering yield was calculated for the case of normal incidence Eq. 14 along the axial and radial boundaries. The etch rate E, defined as the ratio of surface etch depth per unit of time, was calculated through the expression

$$E = \frac{\Gamma_i Y M_m}{\rho_t N_A} \tag{20}$$

where $\Gamma_i = n_b u_B$ is the incident ion flux (with n_b the plasma density along the boundary), M_m and ρ_t are the molar mass and mass density of the surface material and N_A is Avogadro's constant.

The results of the etch rate calculations are shown in Figure 9, where etch rate estimations are presented for the axial boundary (Figures A–C) and the radial boundary (Figures D–F). Results are shown for the three different dielectric materials previously analyzed (SiO_2, Al_2O_3 and Si_3N_4), and three chosen values of

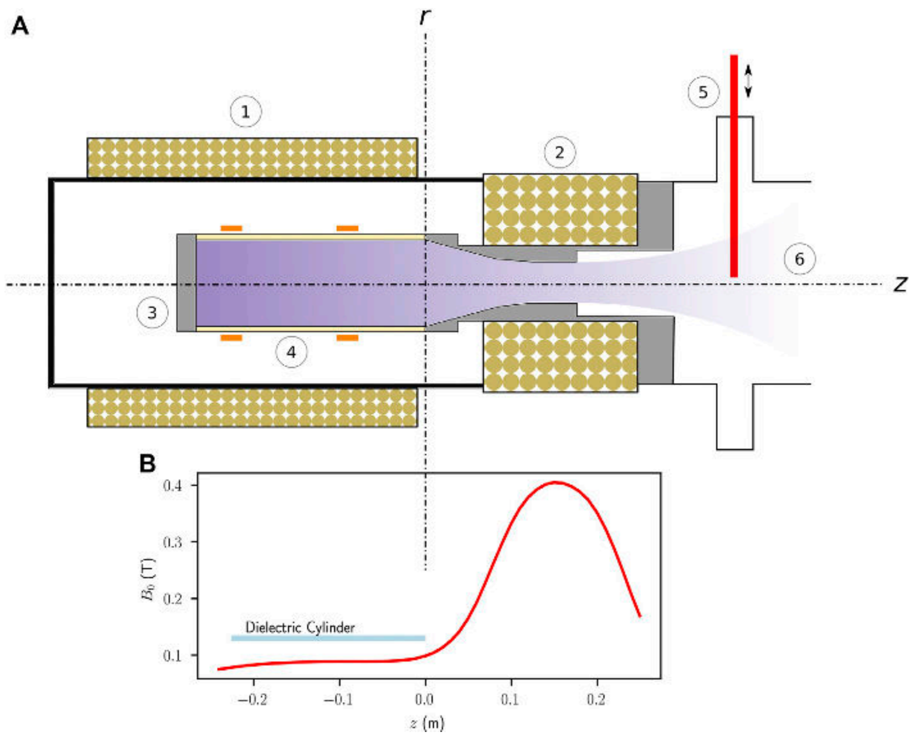

FIGURE 6
(A) Diagram of the VX-CR research helicon device. The axial magnetic field is produced through two solenoid coils, 1 in the HPS region and 2 located downstream of the source. The HPS itself is located inside a high-vacuum chamber to prevent arcing from the voltages present in the RF subsystem. 3 represents the upstream dielectric boundary of the source and this is the point where gas injection occurs (not shown). 4 represents the dielectric cylindrical boundary of the HPS, as well as the approximate location of the helicon antenna straps. 5 marks the location of a reciprocating Langmuir probe used to obtain ion current density and plasma density readings. 6 describes the downstream section of the HPS, interfaced to a vacuum chamber and a pumping system (not shown). **(B)** Experimental measurements of the magnetic field intensity B_0 at the HPS axis as a function of the z axial position. The coordinate system has its origin at the exit boundary of the HPS dielectric cylindrical boundary, following the convention established in section 2.2. Measurement uncertainties for the values of B_0 are less or equal than 0.0008 T.

TABLE 5 Geometrical and physical parameters used for the simulation results of the VX-CR device presented in Section 3.2. The values of T_e and $V_{\max,RF}$ correspond to three separate scenarios, and were obtained from the regression described in Figure 7.

Parameter	Value
R (m)	0.045
L (m)	0.226
B_0 (T)	0.1
T_e (eV)	3.0, 5.0, 10.0
$\dot{m}$ (kg/s)	1.785×10^{-3}
n_{n0} (m^{-3})	1.5×10^{20}
Δr (m)	9×10^{-5}
Δz (m)	2.26×10^{-4}
f_{RF} (Hz)	13.56×10^{6}
$V_{\max,RF}$ (V)	111.30, 165.66, 301.56
Ion species	Ar^+
Dielectric materials	SiO_2, Al_2O_3, Si_3N_4

the electron temperature. Since the simulation provides the ions with an energy equal to the floating potential obtained by the dielectric walls, the results depend on both T_e and the threshold energy for sputtering E_{thr} in each case. Figure 5 had shown that Al_2O_3 has a lower threshold energy than SiO_2 and Si_3N_4 according to the sputtering model, and that is the reason why the cases simulating silicon dioxide and silicon nitride present etching only at the higher values of the electron temperature, corresponding to the only scenarios where the wall floating potential produced by the plasma sheath is larger than E_{thr}. For the scenarios involving aluminum nitride, no sputtering occurs for the cases with T_e = 3.0 eV.

The low-frequency RF sheath model from [13], presented in Section 2.3, can be used to estimate the etch rate produced in certain regions of the radial boundary of the dielectric cylinder due to the vicinity of the helicon antenna straps. Table 5 presents the frequency f and peak voltage $V_{\max,RF}$ present in the helicon antenna straps of the VX-CR device. Using Eq. 13 and assuming

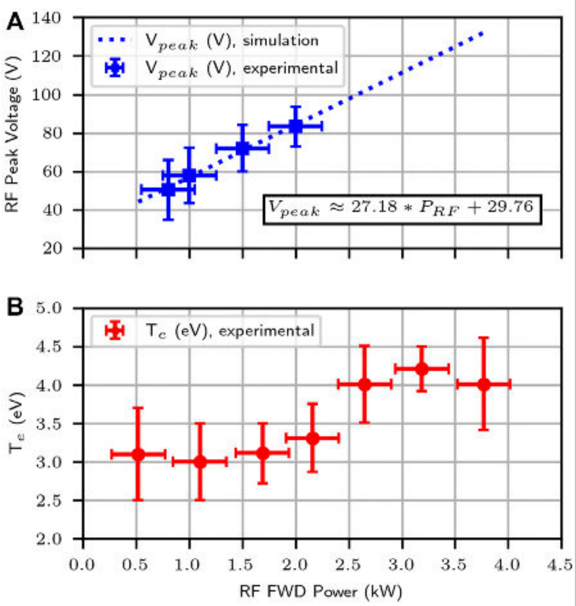

FIGURE 7
Experimental data obtained from the typical operation configuration of the VX-CR helicon plasma source, adapted from [22]. **(A)** shows the measurements of the peak voltage V_p in the VX-CR helicon antenna, measured at the external RF feed line, as a function of the measured RF forward power coupled into the system. A linear regression has been calculated for these data points, with the resulting expression shown in the plot. **(B)** shows the estimated values for the electron temperature T_e as a function of RF forward power, obtained from measurements with the reciprocating Langmuir probe. Experimental techniques and measurement uncertainties for these data points have been described in [22].

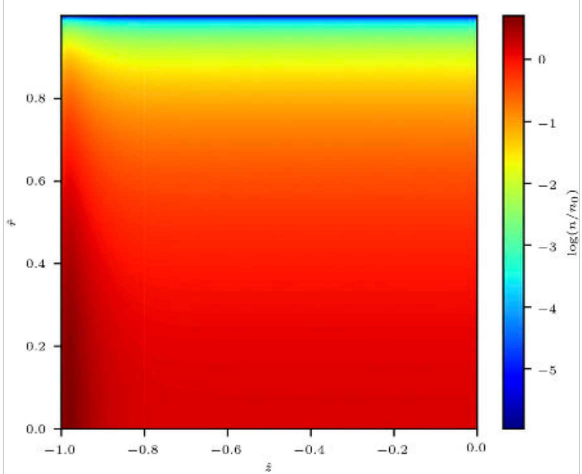

FIGURE 8
Estimated plasma density distribution in the VX-CR device [22, 28], as estimated by Ahedo's model [12, 20]. The relevant geometrical and physical parameters used for this simulation are listed in Table 5. The reference plasma density n_0 is calculated as the ratio of the axial flow rate of heavy species per unit area g_0 and the ion Bohm velocity, $n_0 = g_0/c_s$, and has a value of $n_0 \approx 4.04 \times 10^{18}$ m^{-3} in this particular simulation.

that the voltages present in the copper terminals of the antenna are directly induced in the nearby inner surfaces of the dielectric cylinder of the HPS (as suggested by the results presented by [3, 7]), the incident ion energy distribution can be calculated. Once again using the cold ion approximation and assuming the ions are accelerated at normal incident only by the RF sheath voltage, the mean sputtering yield $\bar{Y}$ due to the low-frequency RF sheath can be obtained as a function of the axial position along the inner surface of the dielectric cylinder through the expression

$$\bar{Y}(\hat{r} = 1, \hat{z}) = \int_0^{V_{\max,\mathrm{RF}}} Y(E) \cdot g_i(E, \hat{z}) \cdot dE. \tag{21}$$

The average value of the sputtering yield, $\bar{Y}$ can then be used within Eq. 20 to estimate the etch rate at any potential axial location of the helicon antenna straps along the radial boundary. The results are presented in Figure 10 for the same three candidate materials and T_e values as in Figure 9, where estimations are depicted for the etch rate along the entire radial boundary. Given the higher voltages induced by the RF subsystem in the helicon antenna, erosion is present in all configurations. These results are once again dependent on the sputtering threshold energy and the electron temperature. They are also a function of the voltages produced in the RF subsystem, which is an element external to the HPS and may differ between different practical implementations.

4 Discussion

4.1 Practical estimation of erosion within HPSs

The analysis of sputtering and erosion phenomena within HPSs is dependent on understanding the behavior of key properties of the plasma throughout the source and particularly in the vicinity of the physical boundary surfaces of interest, with density and temperature being the most relevant parameters. Published experimental results identify two main modes of plasma-material interaction relevant to the estimation of erosion rates in the plasma-facing components of HPSs, which were shown in Figure 1B. Region (1) in the figure describes the acceleration of ions towards the boundary surfaces due to the potential obtained by the floating wall due to the formation of the sheath; the ions will obtain the energy difference between the plasma potential and the wall potential, $\Delta\phi_{p-w} = \phi_p - \phi_w$. When using the cold ion approximation, $|\phi_p| \ll |\phi_w|$ is often assumed. This DC sheath is present along all plasma-facing boundary surfaces. Region (2) in the diagram describes the interaction

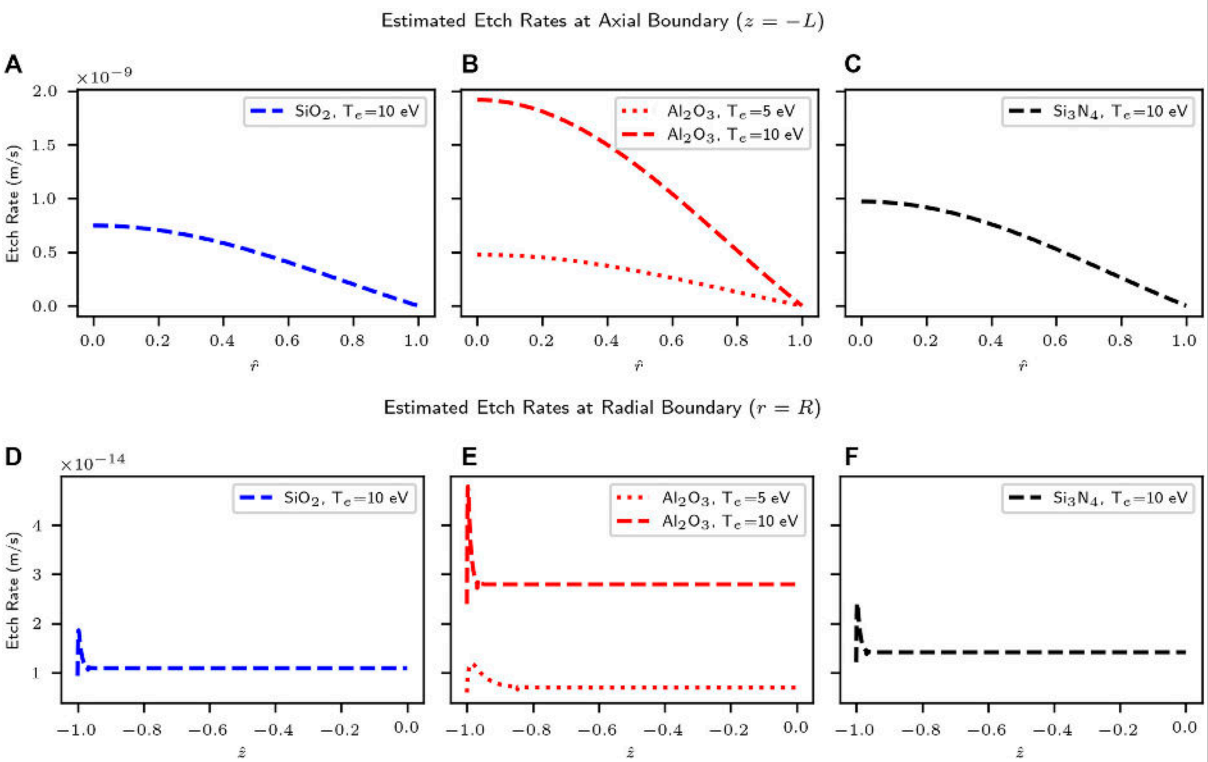

FIGURE 9
Estimated etch rates at the inner surfaces of the boundary dielectric containment material in the VX-CR device, as obtained through the combination of the density distribution, sheath and sputtering models described in Section 2. The etch rates for the axial ($z = -L$) boundary, the endplate located at the upstream end of the dielectric cylinder, are presented in the top row in plots **(A)**, **(B)** and **(C)**; the corresponding etch rates for the radial ($r = R$) boundary, the inner surface of the dielectric cylinder, are presented in the bottom row in plots **(D)**, **(E)** and **(F)**. Estimations are presented for three different dielectric ceramic materials (SiO_2, Al_2O_3 and Si_3N_4) and three reference values for the electron temperature T_e. Plots are shown only for those scenarios where the ion energies surpass the corresponding threshold energy for sputtering, $E_0 \geq E_{thr}$.

between the ions and the RF sheath produced by the oscillation voltages induced in the vicinity of the location of the helicon antenna straps, dependent on the operation of the RF subsystem external to the HPS. This particular type of sheath, present at specific discrete locations along the radial ($r \to R$) boundary surface, is able to induce potentials ϕ_{RF} at the wall typically much larger than those produced by the DC sheath. Practical implementations of HPS commonly rely on RF generators operating in the high-frequency band (6.78 MHz, 13.56 MHz and other typical commercial frequencies), which enable the use of the low-frequency sheath model described in Section 2.3 when the proper conditions are met.

The plasma density profile along the inner surfaces of the dielectric boundaries of a HPS has a direct influence on the magnitude of the rate of erosion throughout these regions, since the incident ion flow rate Γ_i is directly proportional to n_b. In the present approach, the distribution of plasma density has been obtained through the use of the uncoupled models of Section 2.2 for cylindrical geometries, which correspond to the asymptotic limit of the models presented by Ahedo et al. [12]. The radial model Eqs 4–6 produces the classical diffusion profile based on the zero-order Bessel function. Figure 3 shows how the simulated profile tends to overestimate the radial density value as $r \to R$ when compared to experimental data, which will produce conservative values of the ion flow rate towards the surface.

The axial model of Eqs 7–11 describes the axial distribution of plasma density along the central axis of the cylindrical geometry, as a function of the reference density $n_0 = g_0/c_s$ obtained from the axial flow rate of ions and/or neutrals $g_0 = \dot{m}/(m_i \pi R^2)$ and the Bohm velocity c_s. The axial density profile is dependent on the auxiliary coordinate ξ and the parameter $\eta_u = (n_{z=0}/n_0)$, which corresponds to the propellant utilization factor in electric propulsion applications. The mapping $\xi(z)$ to the physical dimension is obtained by analyzing Eq. 11 at the downstream boundary $z = 0$. The density distribution, provided by Eq 9, presents a maximum value determined by the location of $\xi = 0$ and located towards the upstream boundary of the simulation domain. The axial spread of this density

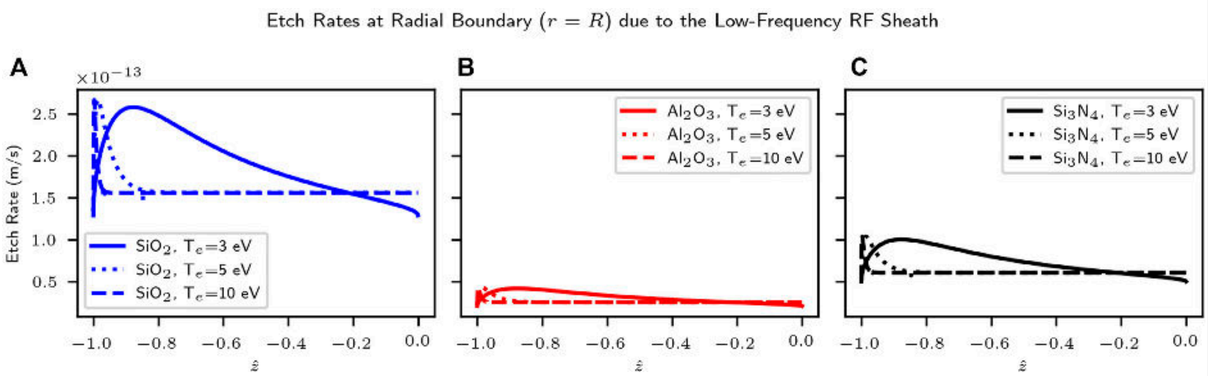

FIGURE 10
Estimation of the etch rate at the radial boundary $r = R$, the inner surface of the dielectric cylinder, due to the low-frequency RF sheath induced by the vicinity of the straps of the helicon antenna, using a method derived from the approach by Berisford et al. [3]. These plots represent the estimated etch rates for all possible locations of these external sources of RF excitation; actual devices typically have these antenna conductors at specific particular locations. Results are presented for three different candidate materials (SiO_2, Al_2O_3, Si_3N_4 corresponding to plots **(A–C)**), and three values to of the electron temperature T_e.

distribution is dependent on the parameter $L_\star$ appearing in Eq. 11. This parameter is inversely proportional to the ionization rate R_{ion}, which is a function of T_e; this rate and the collisional ones R_{ie}, R_{in} and R_{en} can be calculated following the formulas provided by [12].

The combination of the models discussed in Section 2 allows for a computationally-inexpensive approximation to sputtering and erosion phenomena within HPSs, as they use uncoupled steady-state fluid expressions for the axial and radial distribution. These are then combined to produce a complete 2D map of the density distribution such as the one in Figure 8. The density decay described by the radial model is combined with the density distribution profile along the cylinder axis provided by the axial model. The values at the cylinder boundaries can then be extracted and used as inputs to the sheath models of Section 2.3, in order to estimate the energy obtained by the ions as they impact the wall. The sputtering models are then used to predict the sputtering yields and corresponding etch rates.

Figures 9, 10 show how the estimated etch rates for the VX-CR device at the axial boundary (the upstream endplate at $z \to -L$) are about four orders of magnitude larger than the ones produced at the radial boundary for either the DC sheath scenario (plots d, e and f of Figure 9) or the low-frequency RF sheath estimation (Figure 10). This is a product of the larger density values present along that boundary surface, which is impacted along the whole range of the radial coordinate $0 < r < R$ at the axial location $z = -L$. For the case of the radial boundary ($r \to R$, the inner surface of the dielectric cylinder), the etching produced by the DC sheath potential (Figure 9D–F) is smaller than that produced by the voltages induced by the low-frequency RF sheath (Figure 10). This depends on the particular electrical configuration of the external RF subsystem. In the case of the VX-CR, the RF subsystem is designed to operate at high current levels in order to reduce the voltage magnitude in the RF feed lines. Nevertheless, the average voltages during the negative part of the sinusoidal RF cycle weighted according to the distribution function described in Eq. 13 are larger than those produced by the sheath at the floating walls. For the case of helicon systems with grounded boundary surfaces, the energy of the ions reaching the wall would depend on the magnitude of the plasma potential ϕ_p and the ion energy distribution function within the plasma, and it is even less likely that the acceleration through the sheath can produce any etching as previously described by Berisford et al. [3].

4.2 Model limitations and potential improvements

The accuracy of the etch rate estimations provided by the model are conditioned by the validity of its assumptions. The simple magnetic field configuration of Figure 1, with a constant axial B_0, is not the case for most practical HPS implementations. Devices with discrete solenoid cells might present a cusped profile, while other devices might include regions of higher intensity, mirror configurations and other scenarios. When the magnetic field lines intersect directly with the boundary surfaces, regions of direct impingement will produce localized spots of energy deposition and erosion [6, 7]. Since the radial model chosen is an asymptotic approximation for the magnetized regime, the radial density profile is not dependent on the magnetic field intensity and does not capture the effect of modifying B_0 on the radial ion diffusion.

The electron temperature T_e is assumed constant, and is an input parameter to both models. It plays a key role in defining the collisional rates and the sheath potentials. A constant T_e results from the steady-state condition of the discharge and sufficient electron confinement [20]. This value of T_e can be estimated from global input and output parameters of the HPS, such as the total power coupled through the RF subsystem and the particle flow rate through the system boundaries, by using a power balance model (such as the ones described in [12, 30, 31]). This would also enable the use of engineering models of the external RF subsystem for the calculation of the voltages present at the helicon antenna terminals as a function of the coupled RF power. These values could then be used as inputs to the RF sheath models for the estimation of sputtering and etching in the locations near the antenna straps.

The condition of constant axial B_0 is rarely accomplished in practical helicon devices with a cylindrical geometry, either because the magnetic field is not produced through a single magnetic cell or due to the deliberate configuration of variable magnetic field intensities with the purpose of producing mirror effects or modifying the performance of the source. If the field lines diverge and intersect the inner surface of the dielectric cylinder, the kinetic energy of the ions along the direction parallel to the field lines is compounded with the acceleration due to the sheath potentials, and significant etching may occur at the impact points [32]. A variable B_0 will also produce magnetic field lines which are not parallel to the dielectric cylinder axis at regions near the inner boundary surfaces, and the use of sheath models considering oblique magnetic fields [33] might be necessary.

The presence of a non-parallel magnetic field also contributes to the ions having an impact angle different than normal incidence, requiring the use of the angular sputtering formulas described in Section 2.4 instead of the simpler normal-incidence scenarios used in Figures 9, 10. Another aspect of the sputtering models that needs further research is the lack of accurate experimental data, and therefore the corresponding fitting parameters required by the sputtering expressions, for dielectric ceramic compounds at the low energy ranges typical of HPSs. Parameters such as the threshold energy E_{thr} play a critical role in the estimation of etching rates, yet most of the available data and models such as the ones in Section 2.4 have been developed in scenarios where ions impact monoatomic targets. The present approach averaged several parameters of Eqs 14–16 between the values corresponding to the constituting elements of the dielectric compounds; however the values for the threshold energy E_{thr} were obtained from those corresponding to argon ions impacting monoatomic silicon and aluminum, which resulted in the best correlations with published experimental sputtering data.

5 Conclusion

The development and validation of a set of modeling tools designed for the investigation of sputtering and erosion phenomena within the plasma-facing surfaces of a helicon plasma source (HPS) has been presented. It is based on the combination of a 2D fluid-based model for the distribution of plasma density within the HPS (based on the work of Ahedo et al. [12]), sheath models for the estimation of the wall potential in the case of floating surfaces and low-frequency RF fields [13], and a sputtering model based on the work of Eckstein et al. [14]. Relying on the use of steady-state analytical expressions derived from first-principles approximations or empirical models, it aims to provide computationally-inexpensive estimations of the etch rates along the inner boundary surfaces of a HPS. This information is critical for applications of HPSs where long operational times are desired, such as electric propulsion engines or high-power sources for the research of fusion-relevant plasma-material interactions.

The individual components of the model have been validated against published experimental data, centering on the case of argon discharges in sources using silicon dioxide, alumina and silicon nitride components as boundary surfaces. Since the chosen sputtering model was not developed to simulate compound materials, average values were used for the properties of the target material atoms, and the fitting parameters in the model were obtained through an optimization algorithm. The threshold energy for sputtering was selected as that of argon atoms impacting monoatomic silicon or aluminum. This approach yielded the best correlation with published data. This strategy can be adapted to other ion species and target materials, and represents an improvement of previously published techniques using empirical analytical models for the analysis of sputtering on dielectric compound materials such as the approach described in [3]. The subsequent analysis showed how the threshold energy for sputtering E_{thr} is a critical parameter for the analysis of etching within low-temperature devices such as HPSs.

Estimations of the etch rates due to particle sputtering were obtained for the VX-CR helicon plasma source, as a representative device conforming to the model's assumptions. The highest expected values were found at the upstream boundary, the circular endcap surface, where etch rates between 0.5 and 2.0 nm/s were obtained due to the acceleration of ions through the sheath at the axial upstream boundary. For the radial boundary (the inner plasma-facing surface of the dielectric cylinder), these values ranged between 0.5 and 5.0×10^{-14} m/s. Along this same boundary surface, etch rates produced by the low-frequency RF sheath acceleration are one order of magnitude higher, with averages between 0.25 and 2.5×10^{-13} m/s. These results confirm previous findings pointing towards the relevance of the voltages induced by the RF sheath under the antenna straps; but also point towards the importance of controlling the plasma density values in the regions near the upstream axial boundary of the system.

The model presented in this study can potentially be used to guide the physics and engineering design of more robust helicon sources with longer operational lifetime. A discussion is also presented regarding the limitations and possible improvements of this modeling approach, including the estimation of electron temperature from the power balance in the system, the consideration of variable magnetic field intensities and more refined sputtering models for the compounds of interest.

Data availability statement

The original contributions presented in the study are included in the article/Supplementary Material, further inquiries can be directed to the corresponding author.

Author contributions

JDV conceptualized the manuscript and figures, and wrote the first draft of the manuscript. FCD and VG critically revised the manuscript. All authors read and approved the final submitted version of the article.

Funding

This research work was funded by Ad Astra Rocket Company Costa Rica. Financial support for the open-access publishing of this manuscript was provided by the National University of Costa Rica (UNA).

Conflict of interest

Authors JDV and FCD were employed by the company Ad Astra Rocket Company Costa Rica.

The remaining author declares that the research was conducted in the absence of any commercial or financial relationships that could be construed as a potential conflict of interest.

Publisher's note

References

1. Chen F. Helicon discharges and sources: a review. *Plasma Sourc Sci Technol* (2015) 14:014001. doi:10.1088/0963-0252/24/1/014001

2. Del Valle JI, Chang Diaz FR, Granados VH. Plasma-surface interactions within helicon plasma sources. *Front Phys* (2022) 10:856221. doi:10.3389/fphy.2022.856221

3. Berisford D, Bengston R, Raja L. Power balance and wall erosion measurements in a helicon plasma. *Phys Plasmas* (2010) 17:033503. doi:10.1063/1.3304184

4. Barada KK, Chattopadhyay P, Ghosh J, Saxena Y, Bora D. Wall charging of a helicon antenna wrapped plasma filled dielectric tube. *Phys Plasmas* (2015) 22: 013507. doi:10.1063/1.4906360

5. Thakur SC, Simmonds MJ, Caneses JF, Chang F, Hollmann EM, Doerner RP, et al.PISCES-RF: A liquid-cooled high-power steady-state helicon plasma device. *Plasma Sourc Sci Technol* (2021) 30:055014. doi:10.1088/1361-6595/abef19

6. Beers CJ, Green DL, Lau C, Myra J, Rapp J, Younkin TR, et al.RF sheath induced sputtering on Proto-MPEX. I. sheath equivalent dielectric layer for modeling the RF sheath. *Phys Plasmas* (2021) 28:093503. doi:10.1063/5.0054074

7. Beers C, Lau C, Rapp J, Younkin T, Biewer T, Bigelow T, et al.RF sheath induced sputtering on Proto-MPEX part 2: Impurity transport modeling and experimental comparison. *Phys Plasmas* (2021) 28:103508. doi:10.1063/5.0065464

8. Chen F. Physics of helicon discharges. *Phys Plasmas* (1996) 3:1783–93. doi:10.1063/1.871697

9. Chen F, Arnush D. Generalized theory of helicon waves - I - normal modes. *Phys Plasmas* (1997) 4:3411–21. doi:10.1063/1.872483

10. Arnush D, Chen F. Generalized theory of helicon waves - II - excitation and absorption. *Phys Plasmas* (1998) 5:1239–54. doi:10.1063/1.872782

11. Chen F. Plasma ionization by helicon waves. *Plasma Phys Control Fusion* (1991) 33:339–64. doi:10.1088/0741-3335/33/4/006

12. Ahedo E, Navarro-Cavallé J. Helicon thruster plasma modeling: two-dimensional fluiddynamics and propulsive performances. *Phys Plasmas* (2013) 20:043512. doi:10.1063/1.4798409

13. Lieberman M, Lichtenberg A. *Principles of plasma discharges and materials processing*. New Jersey: Wiley-Interscience (2005).

14. Eckstein W, Preuss R. New fit formulae for the sputtering yield. *J Nucl Mater* (2003) 320:209–13. doi:10.1016/s0022-3115(03)00192-2

15. R Behrisch W Eckstein, editors. *Sputtering by particle bombardment: Experiments and computer calculations from threshold to MeV energies*. Berlin, Germany: Springer-Verlag (2007).

16. Chen FF. Experiments on helicon plasma sources. *J Vacuum Sci Technol A: Vacuum, Surf Films* (1992) 10:1389–401. doi:10.1116/1.578256

17. Tysk S, Denning M, Scharer J, Akhtar K. Optical, wave measurements, and modeling of helicon plasmas for a wide range of magnetic fields. *Phys Plasmas* (2004) 11:878–87. doi:10.1063/1.1642656

18. Lafleur T, Charles C, Boswell R. Plasma control by modification of helicon wave propagation in low magnetic fields. *Phys Plasmas* (2010) 17:073508. doi:10.1063/1.3460351

19. Light M, Chen F. Helicon wave excitation with helical antennas. *Phys Plasmas* (1995) 2:1084–93. doi:10.1063/1.871461

20. Ahedo E. Parametric analysis of a magnetized cylindrical plasma. *Phys Plasmas* (2009) 16:113503. doi:10.1063/1.3262529

21. Burin M, Tynan G, Antar G, Crocker N, Holland C. On the transition to drift turbulence in a magnetized plasma column. *Phys Plasmas* (2005) 12:052320. doi:10.1063/1.1889443

22. Castro J, Del Valle J, Arce N, Chinchilla E, Echeverría E, Lezama D, et al.VASIMR VX-CR experiment: Status, diagnostics and plasma plume characterization. In: The 33rd International Electric Propulsion Conference. Washington DC, USA: The George Washington University (2013). IEPC-2013-202.

23. Thakur SC, Paul M, Hollmann E, Lister E, Scime E, Sadhu S, et al.Ion heating in the pisces-rf liquid-cooled high-power, steady-state, helicon plasma device. *Plasma Sourc Sci Technol* (2021) 30:065010. doi:10.1088/1361-6595/abff10

24. Takahashi K, Ando A. Enhancement of axial momentum lost to the radial wall by the upstream magnetic field in a helicon source. *Plasma Phys Control Fusion* (2017) 59:054007. doi:10.1088/1361-6587/aa626f

25. Zalm P, Beckers L, Sanders F. On the pole of physical sputtering in reactive ion beam etching. *Nucl Instr Methods Phys Res* (1983) 209/210:561–5. doi:10.1016/0167-5087(83)90853-0

26. Nenadovic T, Perraillon B, Bogdanov Z, Djordjevic Z, Milic M. Sputtering and surface topography of oxides. *Nucl Instr Methods Phys Res Section B: Beam Interactions Mater Atoms* (1990) 48:538–43. doi:10.1016/0168-583x(90)90178-w

27. Varga P, Neidhart T, Sporn M, Libiselle G, Schmid M, Aumayr F, et al.Sputter yields of insulators bombarded with hyperthermal multiply charged ions. *Phys Scr* (1997) T73:307–10. doi:10.1088/0031-8949/1997/t73/100

28. Del Valle JI, Cortés S, Fonseca L, Oguilve-Araya J, Valverde J, Martínez C, et al.The VX-CR experiment: A thermal and lifetime testbed for the VASIMR™ engine. In: 32nd International Electric Propulsion Conference; Wiesbaden, Germany (2011). IEPC-2011-155.

29. Chang Diaz F, Squire JP, Carter M, Corrigan A, Dean L, Farrias J, et al.An overview of the VASIMR® engine. In: 2018 Joint Propulsion Conference; Cincinnati, OH (2018). p. 4416.

30. Lafleur T, Charles C, Boswell R. Electron temperature characterization and power balance in a low magnetic field helicon mode. *J Phys D Appl Phys* (2011) 44: 185204. doi:10.1088/0022-3727/44/18/185204

31. Vidal F, Johnston TW, Margot J, Chaker M, Pauna O. Diffusion modeling of an hf argon plasma discharge in a magnetic field. *IEEE Trans Plasma Sci IEEE Nucl Plasma Sci Soc* (1999) 27:727–45. doi:10.1109/27.774677

32. Caneses JF, Beers C, Thakur SC, Simmonds MJ, Goulding RH, Lau C, et al.Characterizing the plasma-induced thermal loads on a 200-kW light-ion helicon plasma source via infra-red thermography. *Plasma Sourc Sci Technol* (2021) 30:075022. doi:10.1088/1361-6595/abf814

33. Myra JR, D'Ippolito DA. Radio frequency sheaths in an oblique magnetic field. *Phys Plasmas* (2015) 22:062507. doi:10.1063/1.4922848